WIND EFFECTS ON PERMEABLE BUILDING ENVELOPES: A TWO-DIMENSIONAL EXPLORATORY STUDY

Dissertation

submitted to and approved by the

Department of Architecture, Civil Engineering and Environmental Sciences
University of Braunschweig – Institute of Technology

and the

Department of Civil and Environmental Engineering
University of Florence

in candidacy for the degree of a
Doktor-Ingenieur (Dr.-Ing.) /
Dottore di Ricerca in Civil and Environmental Engineering*)

by
Andrea Giachetti
born 18/09/1984
from Florence, Italy

Submitted on	25 August, 2017
Oral examination on	9 November, 2017
Professorial advisors	Prof. Klaus Thiele Prof. Gianni Bartoli Prof. Claudio Mannini

2018

*) Either the German or the Italian form of the title may be used.

To my best friend Stefano

Abstract

The definition of wind effects on buildings with permeable envelopes may represent a challenging task. Owing to a complex aerodynamic interaction, the relatively small cavity created between the building and the external screen may play a crucial role on the fluid-dynamic characterization of such buildings, thus on the envelope performances in terms of wind resistance and natural ventilation.

The present work deals with an exploratory two-dimensional study on systems composed by an open-gap airtight screen and a rectangular section. The aerodynamic interference caused by the presence of the screen has been investigated, trying to understand the role of each potential influencing factor. The effects produced by the concurrent presence of confined (in the cavity behind the screen) and unconfined (around the whole system) flows have been analyzed, in terms of wind induced forces and pressures. Moreover, the possibility of using simplified models to evaluate the internal pressures having the external ones on a section where the cavity has not been reproduced, namely the possible external and internal pressure decoupling, has been considered.

The studied geometries were characterized by a square or a rectangular 2:3 section, with a face entirely shielded by a relatively thin screen, spaced less than 1/10 of the cylinders cross-flow dimension. Despite the many contributions on bluff body aerodynamics concerning dual bluff bodies, and similar researches mainly oriented towards a drag reduction, to the author's knowledge, studies on configurations such as those considered in the present study have not been performed yet (in particular, considering screens with so small gap widths).

Experimental and Computational Fluid-Dynamic (CFD) simulations have been carried out with a complementary role. Wind tunnel tests have been conducted by varying the main parameters, namely the gap width, the screen typology, the wind direction, the shielded rectangular cylinder and the approaching flow characteristics. On the other hand, two-dimensional Unsteady Reynolds-Averaged Navier-Stokes (URANS) simulations have been performed on a selected case study to integrate the experimental results through flow visualizations and velocity measurements.

For a wind direction normal to the shielded face, the global aerodynamic parameters of the system are slightly affected by the presence of the open-gap screen. By contrast, the pressures on the lateral sides and on the rear face exhibit a different trend when the screen is present. In particular, CFD simulations showed that the screen causes the mean flow reattachment on the lateral body sides of the square section. However, the screen effects depend on the gap width, the shielded cross-section and the approaching flow turbulence.

Mean pressure coefficients in the cavity behind the screen are always negative, with values between -1.9 and -2.5, inducing a drag on the screen comparable to that of the considered sections without it. Significant effects also occur when the wind direction is varied, since the presence of the screen reduces the lift coefficient slope and increases the angle of flow reattachment.

The through cavity behind the airtight screen plays a crucial role: for winds normal to the face an oscillating flow occurs, driven by the vortex shedding and influencing the aerodynamics of the two-dimensional system. By contrast, if the flow in the cavity is prevented by an airtight compartmentation, the aerodynamic interaction does not occur, and the screen acts as a mere body elongation in the streamwise direction.

The present study can be considered as a precursor study for more complex three-dimensional geometries, such as those involving permeable building envelopes. Since further studies are necessary to properly define the wind effects on more realistic cases, a simple classification useful to plan future studies is also proposed in the present thesis.

Zusammenfassung

Die Definition von Windeinwirkungen auf Gebäude mit Vorgehängten hinter lüfteten Fassaden kann eine herausfordernde Aufgabe darstellen. Aufgrund einer komplexen aerodynamischen Wechselwirkung, könnte der relativ kleine Hohlraum zwischen dem Gebäude und des externen Schirms eine entscheidende Rolle bei der fluiddynamischen Charakterisierung solcher Gebäude und somit bei der Umschlagleistungen in Bezug auf Windwiderstand und natürliche Belüftung spielen.

Die vorliegende Arbeit befasst sich mit einer explorativen zweidimensionalen Untersuchung von Systemen, die aus einem luftdichten Schirm mit offener Luftspalte und einem rechteckigen Querschnitt bestehen. Die aerodynamische Interferenz, die durch das Vorhandensein des Schirms verursacht wird, wurde untersucht, um die Rolle jedes möglichen Einflussfaktors zu verstehen. Die untersuchten Formen waren durch einen quadratischen oder rechteckigen Querschnitt von 2: 3 gekennzeichnet, wobei eine Fläche vollständig durch ein relativ dünnen Schirm abgeschirmt war, der weniger als 1/10 der Zylinderquerströmungsdimension aufwies. Experimentelle und Computergestützte Fluid-Dynamische (CFD) Simulationen wurden mit einer komplementären Rolle durchgeführt. Windkanalversuche wurden durchgeführt, indem die Hauptparameter, nämlich die Spaltbreite, die Bildschirmtypologie, die Windrichtung, der abgeschirmte Rechteckzylinder und die sich nähernde Fließeigenschaften untersucht wurden.

Bei einer Windrichtung senkrecht zur abgeschirmten Fläche werden die globalen aerodynamischen Parameter des Systems durch das Vorhandensein des Bildschirms mit offenem Spalt geringfügig beeinflusst. Im Gegensatz dazu, zeigen die Drücke auf den Seiten und auf der Rückseite einen anderen Trend, wenn der Schirm vorhanden ist.

Insbesondere zeigten CFD-Simulationen eine oszillierende Strömung, die durch die Wirbelablösung und eine mittlere Strömungswiederbefestigung an den Außenseiten des quadratischem Querschnitt angetrieben wurde. Die Schirmeffekte hängen jedoch von der Spaltbreite, dem abgeschirmten Querschnitt und der sich annähernden Strömungsturbulenz ab. Signifikante Effekte treten auch auf, wenn die Windrichtung variiert wird, da das Vorhandensein des Schirms die Steigung des Auftriebskoeffizienten verringert.

ACKNOWLEDGEMENT

Firstly, I would like to express my sincere gratitude to my tutors Prof. Gianni Bartoli and Prof. Klaus Thiele for the support in my research project, for their patience and motivation. Their office door was always open and I will always carry with me our interesting discussions.

I would like to acknowledge also my co-tutor and friend Prof. Claudio Mannini. Without his passion for the research, his patience and scientific knowledge it was really hard to conclude this path. I will be always indebted to him for his tutoring activity and support.

My sincere thanks also goes to all the CRIACIV wind tunnel team, especially to Tommaso Massai for his astounding support, to Ninni Marra and Luca Pigolotti who really encouraged me continuously. Our stimulating discussions, our crazy periods of fun and stress were all fundamental parts of my research path.

I would like to thank all the colleagues that helped me during these three years, especially Vito, Emanuele, Pina, Federica and Dario for their friendship, Irene and Giovanni for their help with the CFD simulations and their warm support. Moreover, I would like to thank Giampiero Manara (Permasteelisa Group), Luca Patruno (University of Bologna) and Andrea Pasquali (University of Braunschweig) for their patience to my mails full of questions. I am grateful to BetaCAE System S.A. which kindly made the academic licenses of their software available. I must express my very profound gratitude to my grandmother Carla and all the rest of my family, Maria Luisa, my friends Stefano, Niccolò, Francesco and all the people who helped me in this adventure.

A special thanks goes to the music and the constant presence of God.

Index of Contents

List of figures

List of tables

List of symbols

B	bluff body dimension parallel to the flow
C_{bp}	base pressure coefficient (the term "base" refers to the middle point of the rear face of the bluff body)
C_D	drag force coefficient
C_{DRB}	rearbody drag coefficient
C_{DS}	mean drag coefficient on the screen.
C_L	lift force coefficient
C_p	pressure coefficient
C_{sep}	pressure coefficient at the separation point (closest to the upstream edge of the model)
Co	Courant number
$dC_L/d\alpha$	mean lift coefficient slope centered around the 0° wind direction
D	cross-flow characteristic dimension of the two-dimensional bluff body considered
f	oscillating flow frequency
f_v	Strouhal frequency
F_D	drag force
F_L	lift force
I_u	turbulence intensity of the approaching wind flow
k	kinetic energy of the turbulent fluctuations (turbulent kinetic energy)
k_{RF}	reduced frequency
L	gap depth between the screen and the bluff-body face
L_c	mean recirculating length
L_{chr}	characteristic length chosen to rewrite the equations in terms of non-dimensional quantities
L_m	length used to evaluate the force coefficients (*i.e.* for the experimental tests is the model length)
L_x , L_y	integral length scales, respectively along the x- and y-directions
n_w	dimension of a cell at the wall surface
p	pressure
Q	flow rate
Re	Reynolds number
$\mathrm{Re}_{loc,\max}$	local maximum value of Reynolds estimated in the present work
Re_{MAX}	Critical local Reynolds number based on the mean velocity in the cavity used by Loudon and Tordesillas (1998) instead of $\mathrm{Re}_{OSC,C}$

$\mathrm{Re}_{OSC,C}$	Critical local Reynolds number proposed by Ohmi and Iguchi (1982): a Reynolds number defined with local quantities of the internal flow
s_{ij}	strain-rate tensor
t_{ij}	viscous stress tensor
T	period of vortex shedding
u	instantaneous flow velocity (with components u, v, w)
u_*	characteristic non-dimensional velocity at the wall (the friction velocity)
U	averaged flow velocity
U_{bl}	potential flow velocity just outside the boundary layer
U_{chr}	characteristic velocity chosen to rewrite the equations in terms of non-dimensional quantities
U_∞	approaching mean flow velocity
Wo	Womersley number
y^+	dimensionless wall distance
α	wind direction
δ	boundary layer thickness
Δt_{ch}	characteristic time step
ΔP	pressure difference at the cavity extremities
ε	dissipation rate
μ	air viscosity
ρ	air density
ω_{chr}	characteristic frequency chosen to rewrite the equations in terms of non-dimensional quantities
ω	specific turbulent dissipation rate
Ω	absolute value of the vorticity
ν	kinematic viscosity
ν_T	kinematic eddy viscosity
ϕ	phase lags measured between the pressure taps behind the screen and the first tap on the lateral side close to the separation point

NOTE: The present list includes the most used symbols. Symbols adopted only once or related to the content of the Appendix are not included.

Chapter 1 – Introduction

The present study aims to investigate the aerodynamics of a two-dimensional system composed by an airtight screen attached to a rectangular cross-section. As sketched in Fig. 1.1, the study attempts to comprehend the wind effects caused by the presence of a screen which creates a through cavity, as a preparatory work for more realistic three-dimensional systems, such as buildings with permeable envelopes.

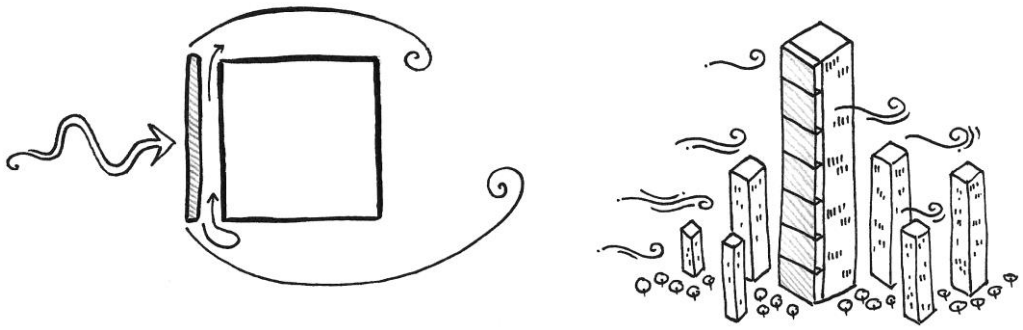

Fig. 1.1 - A picture to summarize the thesis approach. Courtesy of C. Torsoli (2017).

1.1 Motivations

Recently, many engineering problems have stimulated a renewed interest in bluff body aerodynamics, a field in which experimental, numerical and theoretical studies coexist describing the reciprocal effects between a body and the incoming flow experiencing boundary layer separation.

When the wind approaches a building with a permeable envelope, part of the flow moves in the cavity between the external screen and the building face. If the cavity flow and the external flow mutually interacts, the evaluation of the wind effects on this complex system may represent a quite complicated task.

From an aerodynamic point of view, a permeable envelope can be considered as an additional layer somehow held in front of the building face, at a relatively small distance. The interference between the screen and the body is such that they behave as a unique object, namely, a new fluid-interacting system. This is an interesting fluid-dynamic case study, for which additional studies are nowadays required in order to have a deeper insight.

Such a system may exhibit an aerodynamic behavior quite different from the one associated to the original bluff body without the screen. Thus, the role of each parameter affecting the system aerodynamics needs to be clarified. In particular, it is necessary to understand when the presence of the screen can be neglected and if the wind induced pressures in the cavity can be evaluated through simplified models.

The introduction of geometrical parameters of a lower order of magnitude with respect to the cross-flow body dimension, as the gap width, complicates the problem, and the combination of all the possible parameters leads to a wide number of possible cases. Hence, a detailed study on a simplified two-dimensional system is needed.

On the other hand, previous studies concerning very small changes on bluff body geometries (*e.g.* Lajos, 1986), demonstrated that the aerodynamics of these bodies can be remarkably affected by apparently negligible modifications, like the sharpness of the corners or the surface roughness (Fig. 1.2). Such studies support the interest in the investigation of such small geometrical parameters of the system.

The literature concerning screened bluff bodies is mainly focused on the drag reduction of the overall system, so that the considered screen distances are comparable with the body characteristic dimension (*e.g.* Koenig and Roshko, 1985, Cooper, 1988). Conversely, the current study deals with gap widths between 1/10 and 1/40 of the cross-wind section dimension. To the author's knowledge, rectangular cylinders with a flat plate (the screen) positioned in order to create such a small through cavity constitute geometries which are yet to be investigated.

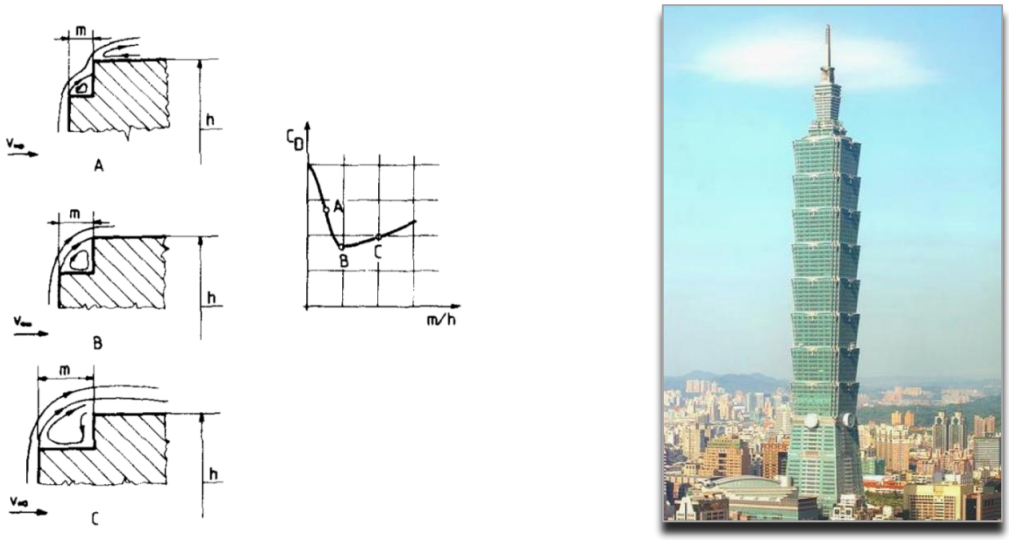

Fig. 1.2 - Drag reduction using a "step" an order of magnitude smaller than the characteristic body dimension on the front face: on the left, results of a two-dimensional study (Lajos, 1986); on the right the Taipei 101 tower in Taiwan represents an impressive practical application of corners modification to reduce wind loads (Irwin, 2008).

1.2 Objectives

The fluid-dynamic characterization of the two-dimensional system composed by an airtight screen and a rectangular cylinder, as schematized in Fig. 1.3, in which concurrent unconfined and a confined flows are involved, represents a complex task that requires the achievement of intermediate steps, as set out below.

One of the first goals is to understand if and how the presence of the screen modifies the aerodynamics of the bluff body, once the system is composed. If the screen does not affect the aerodynamic behavior, or its influence is negligible, the possibility to decouple the external and internal pressures in the cavity (*i.e.* to use the external pressures as boundary conditions to evaluate the internal ones) is considered.

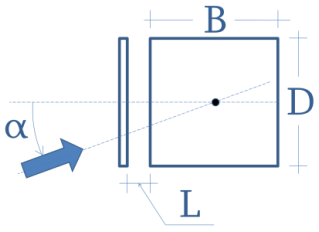

Fig. 1.3 - Sketch of the two-dimensional section studied: cross-flow characteristic dimension (*D*), gap depth (*L*), body dimension parallel to the flow (*B*) and wind direction (α).

Under this assumption, the system is studied in different configurations, with gap distances down to 1/40 of the body cross-flow characteristic dimension. The effects of a different screen typology, with an airtight interruption of the through cavity to prevent the flow passage, or with an opening on the external layer, are investigated. Parameters, such as the approaching flow turbulence and the wind direction, are varied in order to understand if the screen effects occur only under specific conditions. A peculiar fluid-dynamic behavior of the system is expected by varying potential influencing factors, and both the external and the internal flows are investigated through the measure of local and global aerodynamic coefficients.

In the present study the cavity behind the screen is connected to the outer flow through the lateral openings. The pressure at the extremities of the cavity tends to drive the cavity flow, and an internal flow motion may occur. If an oscillating flow occurs, the local Reynolds number and an additional non-dimensional parameter related to the oscillating frequency, namely the Womersley number, must be considered to define the flow regime. These two non-dimensional numbers allow the definition of the flow properties in terms of velocity profile and phase difference with respect to the driving pressure gradient. Investigations of the Reynolds and Womersley number effects have been studied to understand their influence on the global and local aerodynamic quantities, and the attempt to extend the range of investigated Womersley numbers through Computational Fluid Dynamics (CFD) simulations is discussed.

1.3 Methodologies

Experimental and numerical studies on two-dimensional body cross-sections are usually taken as a reference, and aimed to the comprehension of more complex (even three-dimensional) flow phenomena. As an example, the studies on circular cylinders (*e.g.* Bearman, 1969) are used for approaching the definition of the wind load on structures like chimneys (or similar), as well as those related to rectangular cylinders (*e.g.* Vickery, 1966), are the basis for tall buildings and bridges.

In order to achieve the targets established, experimental tests in the wind tunnel on section models and CFD simulations on two-dimensional sections were planned and executed. These two approaches have to be meant as complementary.

Aerodynamic forces were measured to evaluate the global effects possibly induced by the presence of the screen. Pressure distributions were measured on the screened body and evaluated on the screen (by means of CFD) to describe the system behavior in details through pressure signal statistics. In particular, the pressures around the mere screen were evaluated only using CFD, because it was not possible to equip this component of the physical model with pressure taps. Qualitative flow visualization were performed through CFD post-processing.

The study was carried out by varying the main parameters, such as Reynolds number (7.86×10^4 - 2.26×10^5), gap depth ($D/40 < L < D/10$) and the ratio of the body sides ($B/D = 1$ and $= 2/3$), as indicated in Fig. 1.3, according to wind tunnel or computational limitations. Moreover, wind direction ($0° < \alpha < 180°$) and turbulence properties of the approaching flow (smooth and turbulent $I_u \approx 13\%$) were also varied to understand their influence. Finally, in order to improve the comprehension of the through cavity role, two other types of screen configurations were experimentally tested: one with an additional vertical airtight compartmentation and one with an external opening on the screen.

It is to be noted that, only in very few specific conditions the flow around a tall building section can be considered in a very first approach as two-dimensional (Fig. 1.4), this is the reason why this study does not intend to give results directly applicable on a realistic three-dimensional case.

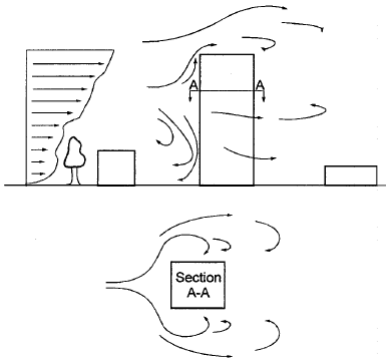

Fig. 1.4 - Horizontal section of a tall building at the stagnation point (Holmes, 2007).

1.4 Implications

The current two-dimensional aerodynamic study may be also considered as *exploratory* though preparatory for more complex three-dimensional geometries (Fig. 1.5). In particular, a rectangular prism with an airtight screen, and an internal laterally-opened cavity partitioned with horizontal airtight layers, is considered as the base case for the 2-D extrapolation discussed in the present work (Fig. 1.5 - c). This, in turn, may represent a more realistic system composed by a building with a permeable envelope, thus implying significant contributions to this technological field deriving from the main outcomes of the present study. This façade typology, to the author's knowledge, has received relatively little attention so far, but the system aerodynamics, and in particular the oscillating flow expected behind the screen, may open new possibilities in terms of natural ventilation and energy harvesting devices installation. Moreover, such a building envelope may exhibit a good fire performance, thanks to the horizontal airtight compartmentations. In Fig. 1.6 one of the few practical applications encountered is reported. The façade exhibited high performance in the building energy context. Indeed, the double-skin, side-opened façades of the Unipol Tower in Bologna (Italy) contributed to achieve the Gold level of LEED certification (Leadership in Energy and Environmental Design, Green Building Council).

Finally, in order to simplify the extension of the obtained results, a review of the research concerning wind effects on permeable envelopes together with a classification of possible case studies, useful to plan future research activities, are carried out. This part is reported in an appendix, to improve the thesis readability.

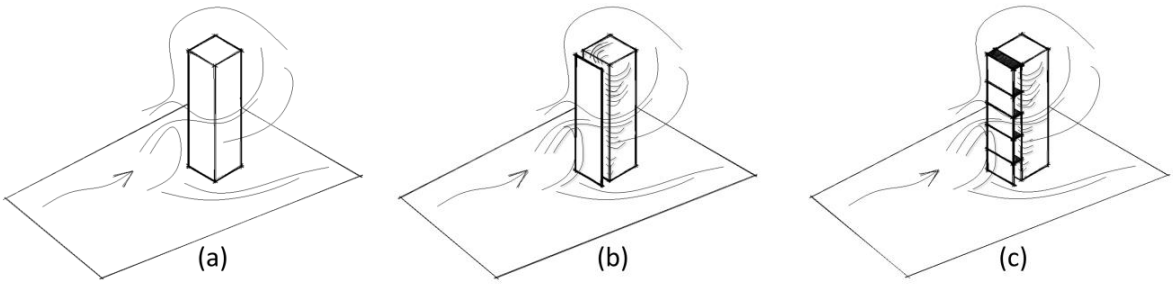

Fig. 1.5 - Sketches of the three-dimensional system flow: (a) without screen; (b) and (c) are respectively the case with an airtight screen without (b) and with (c) horizontal compartmentations.

Fig. 1.6 - A case study with characteristics of the selected reference façade typology: the Unipol Tower in Bologna (Italy). Pictures of the tower under construction (left, center) and completed (right).

1.5 Contributions and outline of the research work

In the following, a brief summary of the thesis contents is described. The flow chart reported in Fig. 1.7 summarizes the main points of the research work pointing out the interaction between the many different aspects analyzed in the present study.

In Chapter 2 a detailed review on fundamentals of bluff body aerodynamics without and with a screen is conducted. The main results obtained on regular two-dimensional rectangular cylinders with low side ratio are collected in order to point out the main flow features. The analysis of such basic works is extended to rectangular cylinders with modifications. It is shown how small changes to the geometry may remarkably affect the system aerodynamics.
The chapter also analyzes the few researches carried out on geometries similar to the object of the current work. It is also useful to contextualize the characteristics of the internal oscillating flows, a quite unusual topic in wind engineering.

In Chapter 3 the experimental campaign is described. This represents the most important part of the whole work. The experimental set-up is accurately described together with its limitations, and the obtained results are extensively analyzed.

In Chapter 4 CFD simulations are described. A case study, previously investigated by means of wind tunnel test, was selected to show how the use of numerical simulations could help to overcome some of the limits encountered during the experimental campaign.

In Chapter 5 the main conclusions are summarized, and possible future developments and outlooks of the thesis work are identified.

Towards future studies, a wind-effects based literature review on permeable building envelopes was carried out, as reported in Appendix 1. From the analysis of the state of art, the lack of a classification of possible façade configurations emerged. It was argued that this lack is related to the many geometric scales and parameters involved in the problem. The consequence is expressed, for example, by the wind loading codes inadequacy. Hence, a very first classification for permeable double-skin building envelopes merely based on the system aerodynamics is proposed.

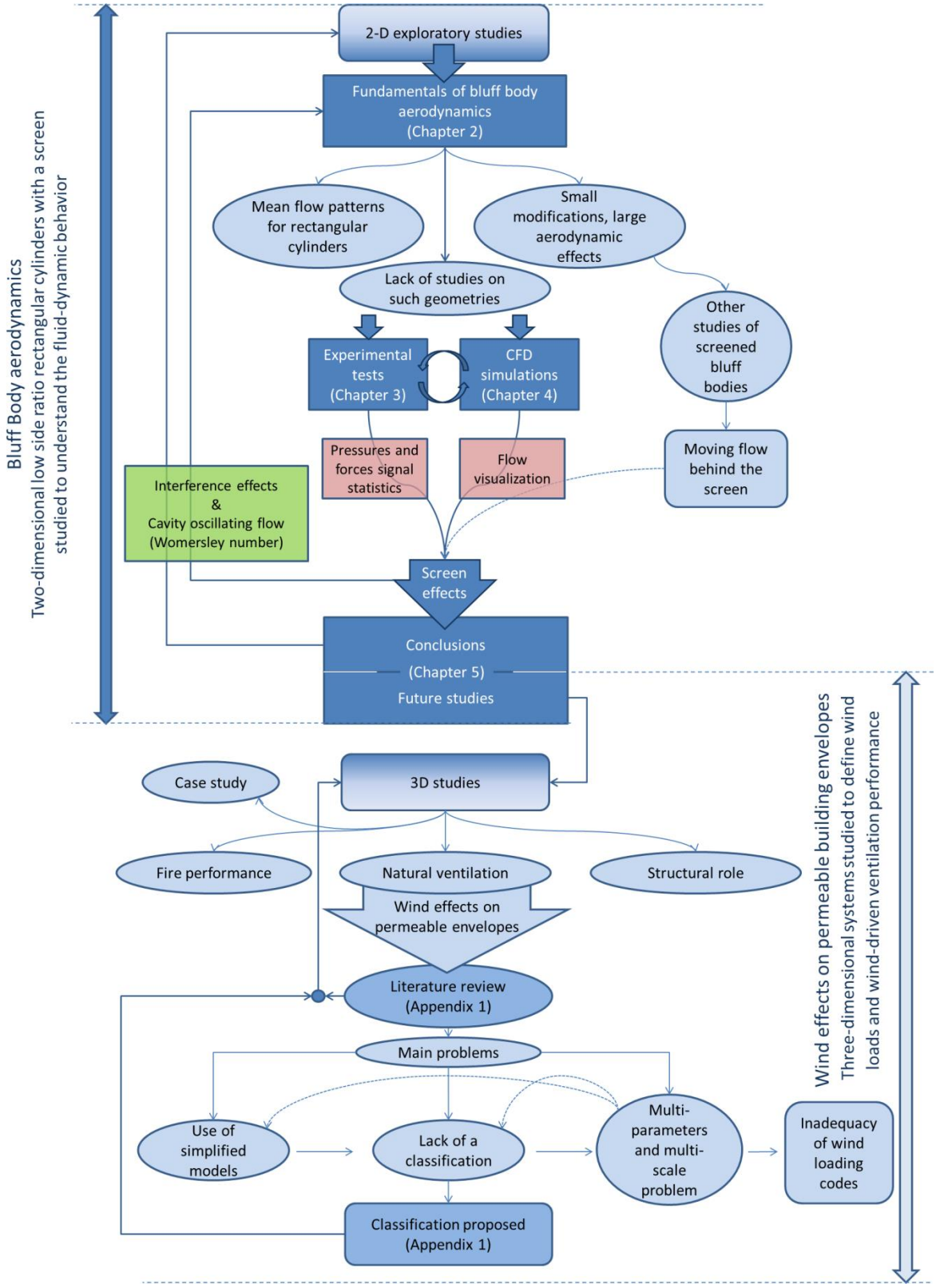

Fig. 1.7 - Thesis content diagram.

Chapter 2 – Fundamentals of bluff body aerodynamics

In the present chapter fundamentals of fluid dynamics involving a bluff body in a moving air fluid are proposed. The few points recalled (and discussed) are crucial for the correct physical interpretation of the results obtained by both the experimental and the numerical studies.

2.1 Basic bluff body flow features

The aerodynamics is defined as the study of the motion of air interacting with a solid body. Indeed, when a solid body is immersed in a flow, surface forces caused by pressure and viscous stresses act on the body, and mutually on the fluid. By integrating the surface forces around the whole body surface, the resulting fluid-dynamic force and moment are obtained.

Usually, in a two-dimensional flow domain, the resultant force is divided into two components based on the direction of the free-stream velocity vector (U_∞), namely drag and lift force (moment is intentionally neglected in the present work). The force component aligned with U_∞ is called *drag* (F_D) which, in turn, is given by two contributions: the pressure drag and the friction drag. The cross-flow force component is called *lift* (F_L). Based on a body characteristic dimension, as the cross-flow width (D), the approaching fluid density (ρ) and velocity (U_∞), the two force components are expressed through the relative non-dimensional drag and lift coefficients per unit length (L_m), respectively indicated as C_D and C_L:

$$C_D = \frac{F_D}{1/2 \rho U_\infty{}^2 D L_m} \qquad C_L = \frac{F_L}{1/2 \rho U_\infty{}^2 D L_m} \qquad \textit{(eq. 2.1)}$$

From an aerodynamic point-of-view, the bodies immersed in the moving fluid can be distinguished into two groups, namely, the *aerodynamic* (or streamlined) bodies and the *bluff* bodies. The following distinction is carried out referring to an incompressible two-dimensional flow at relatively high Reynolds numbers.

Aerodynamic bodies are characterized by small drag coefficients, mainly caused by friction drag. The flow around this typology of body develops a thin boundary layer that remains attached over almost the whole surface. This feature allows to an approximate estimation of the wind-induced forces, and explains the small wake behind such body typology compared to the characteristic cross-flow dimension. A standard aerodynamic body, namely, a two-dimensional symmetrical airfoil aligned with the free-stream, characterized by a velocity U_∞, is reported on the left side of Fig. 2.1. The pressure on the body surface at a certain location ($p(s)$) coincides with that in the potential flow just outside the boundary layer which, in turn, is directly related to the velocity in the same region ($U_{bl}(s)$). So that, the pressure distribution can be described through the pressure coefficient from the application of Bernoulli's theorem:

$$C_p(s) = \frac{p(s) - p_\infty}{1/2 \rho U_\infty^2} = 1 - \frac{U_{bl}^2(s)}{U_\infty^2} \qquad \textit{(eq. 2.2)}$$

Three representative points of the distribution can be considered. At the stagnation point, where velocity U_{bl} is null, the maximum pressure coefficient ($C_p = 1$) occurs. Conversely, the minimum pressure coefficient lies in correspondence of the widest cross-section point, where $U_{bl} > U_\infty$. Finally, at the end of the aerodynamic body, $U_{bl} \simeq U_\infty$ and the pressure coefficient results almost null.

The bluff bodies are characterized by drag coefficients one order of magnitude higher than the streamlined ones. In this case, the pressure drag is high enough to neglect the friction contribution. Indeed, a bluff body exhibits a more or less premature separation of the boundary layer from the surface, generating a wake in size comparable to the characteristic cross-flow body dimension (Buresti, 2012).
The pressure drag of a bluff body may be further divided into two contributions. The first is due to the forebody drag, *i.e.* pressure over the front part of the body with attached boundary layer. The second contribution, that is the afterbody (or rearbody) drag, results from the pressures on the surface portion lying inside the separate wake. Depending on the bluff body shape, the forebody drag can range from close to zero up to values comparable to the afterbody drag.

In bluff body aerodynamics the sharp-edged and round-edged bodies constitute two well separated groups. The circular cylinder represents the limit case of a round-edged body. In round-edged bodies the flow separation occurs at different locations depending also on the Reynolds number and surface roughness, while in sharp-edged bodies the separation is fixed at the edges. In this second group, parameters such as the body geometry and the free stream turbulence influence the wake characteristics without moving the location of the separation point.
Separated shear layers tends to roll up into vortices, causing, for example, the vortex shedding: for a steady, smooth, approaching flow, at Reynolds numbers sufficiently high (with $\mathrm{Re} = U_\infty D / \upsilon$), a symmetrical two-dimensional bluff body exhibits a regular alternate shedding of vortices from the two sides of the body. The double row of vortices of opposite sign shed is also known as the Kármán vortex street, so that the steady approaching flow becomes unsteady around the body. In particular, the flow can be considered as a periodic flow, with period equal to $T = 1/f_v$, where f_v is the frequency of vortex shedding, also named the Strouhal frequency. The critical Reynolds number above which the vortex shedding occurs depends on the body shape, characterized by a certain Strouhal value.
The vortex shedding causes even remarkable transversal forces also when the flow is aligned with the body axis-of-symmetry. During the alternate shedding, the lift force reaches a minimum and a maximum instantaneous peak value that may be of the same order of magnitude of the drag force. To consider these transversal force oscillations, the lift coefficient standard deviation parameter (C_L') is usually employed. However, the averaged lift coefficient at the end of a complete vortex shedding cycle results null.
The geometrical considerations on the bluff body corners obviously affects the main aerodynamic parameters, such as the C_D , the C_L and the Strouhal frequency (St). Generally, for Reynolds numbers typical of the wind engineering, and according to the briefly introduced dependency of the separation point with Reynolds number, a round-edged body may exhibit a *Re*-dependence Strouhal frequency. In contrast, for a sharp-edged body (with the flow perpendicular to a face) the frequency of vortex shedding results almost constant regardless of Reynolds number.
It is worth noting that this is valid only for Re numbers of practical use in wind engineering (usually $Re > 10^4$). For certain rectangular bluff bodies in specific Reynolds number ranges, the Strouhal numbers could depend on *Re* (*e.g.* Okajima, 1982).

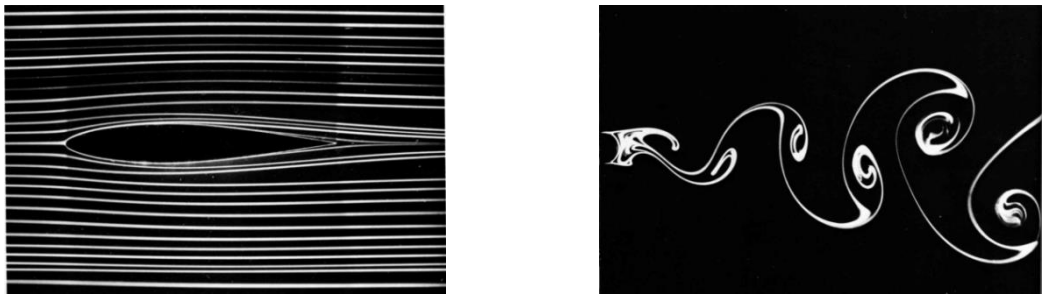

Fig. 2.1 - Two representative flow visualizations reported by Buresti, 2012. On the left, an aerodynamic (streamlined) body: a NACA 64A015 profile at Reynolds number (*Re*) equal to 7000. On the right, a bluff body: the circular cylinder at *Re* = 140 (Van Dyke, 1982).

2.2 Main flow characteristics around two-dimensional rectangular cylinders

The flow around a bluff body is characterized by two basic flow features: boundary layer separation (and reattachment, depending on the body shape), and formation of the Kármán vortex street (Nakamura, 1993). In the case of two-dimensional rectangular cylinders, the condition of wind perpendicular to the front is the starting configuration to describe such features.

Two-dimensional rectangular prisms could exhibit a drag, expressed through the non-dimensional drag coefficient, that varies non monotonically by increasing the side ratio. For a smooth approaching flow, Fig. 2.2-left shows the drag coefficients obtained in literature versus the side ratio in a range $0 < B/D < 2.8$ (Laneville and Yong, 1983). Fig. 2.2-right shows another peculiarity of two-dimensional rectangular cylinder by means of pressure distributions for different side ratio rectangles, showing that the variation of C_D for different side ratios depends mainly on the rearbody pressure drag (Da Matha Sant'Anna *et al.*, 1988). Indeed, as reported in the figure, pressure coefficient distributions on the front of various rectangular cylinders exhibit almost equal trends, while pressure distributions at the base develop differently. In particular, the Authors distinguished the cases A,B,C,D from the cases E,F,G based on the suction measured behind the separation point (high in the former, low in the latter). It is worth noting that the terms "base pressure" indicate the pressure at the central point of the body rear face (the base). The related coefficient is usually named "C_{bp}", though sometimes *base pressure* indicates the average of pressures measured over different points on the leeward face (*e.g.* Lee, 1975).

The relation between the drag coefficient and the side ratio can be ascribed, in first approximation, to the curvature of the streamlines close to the trailing edge (Fig. 2.3): starting from the C_D measured for a near-zero side ratio (flat plate perpendicular to the flow), the drag coefficient increases by increasing the streamwise body dimension (Fig. 2.2-left). At the same time, the size of the separated wave cavity reduces (filled by the body itself), while the streamlines curvature increases reaching a maximum at $B/D \approx 0.6$ (Nakaguchi *et al.*, 1968, Bearman and Trueman, 1972). Up to this side ratio, the mean flow does not feel the influence of the leeward corners, and the pressures at the base decrease down to the values to which corresponds the maximum drag coefficient ($B/D \approx 0.6$). This trend is reversed for higher values of the side ratio, because the vortices are forced by the trailing edge corners to form further downstream. According to Lyn and Rodi (1994), the near-field wake flow behind a bluff body is temporally and spatially extremely complex, with the interaction between the two separated shear layers and regions of irrotational flow entrained into the wake.

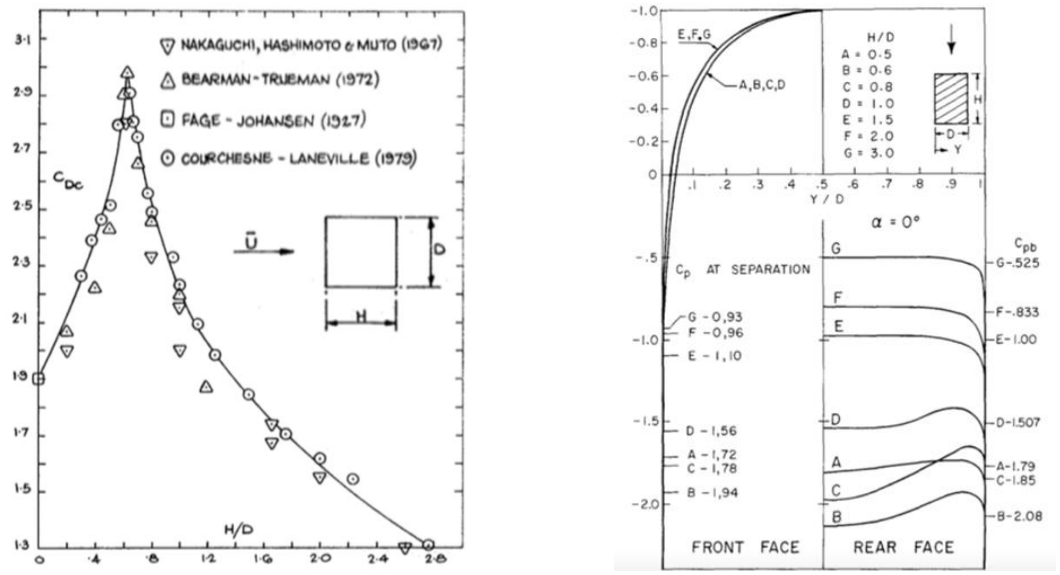

Fig. 2.2 - Drag force of rectangular cylinder for different side ratios with perpendicular flow: (left) some drag coefficients from literature (Laneville and Yong, 1983); (right) front and rear pressure distributions (Da Matha Sant'Anna *et al.*, 1988).

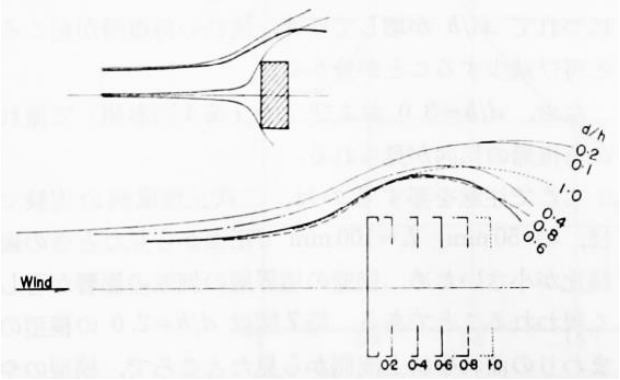

Fig. 2.3 - Shear layer curvature observed at different side ratios through flow visualization (Nakaguchi *et al.*, 1968).

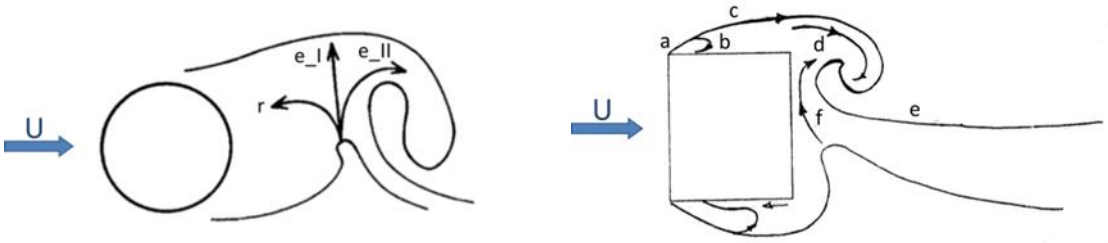

Fig. 2.4 - Mechanism of vortex formation behind a bluff body. On the left, the scheme proposed by Gerrard (1966) for a generic bluff body with low side ratio. Arrows showing a reverse flow (r) and entrainment in the wake (e_I and e_II). On the right, the scheme proposed by Laneville and Yong in 1983. Part of the initial vorticity (a) is absorbed by the bubble (b), while the unabsorbed continues in the shear layer (c). The vortex is created by the shear layer (d), and it is supplied with fluid from the wake (e) and entrainment from the opposite shear layer (f).

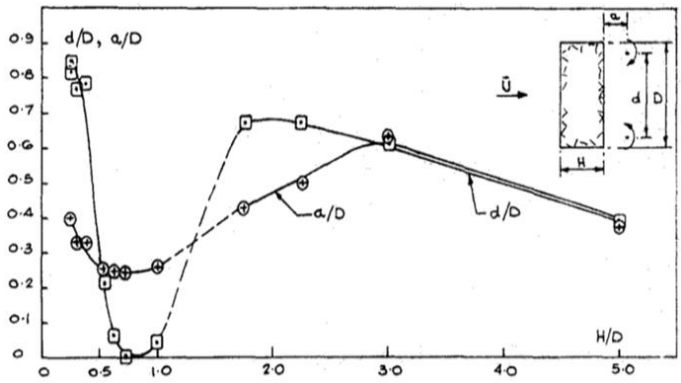

Fig. 2.5 - Parameters to describe the main flow features of two-dimensional rectangular cylinders in smooth flow: non-dimensional transversal relative distance of vortex centers (*d/D*) and non-dimensional streamwise distance from the base of vortex formation (*a/D*) (Laneville and Yong, 1983).

The main mechanism of vortex formation behind a generic bluff body was discussed by Gerrard in 1966 (Fig. 2.4-left). Later, Laneville and Yong (1983) proposed an interpretation of the same mechanism for the rectangular section (Fig. 2.4-right). According to the Authors, the main flow features can be clearly described focusing on the loci of the wake vortices, the wet length on the body side and the base pressure distribution, well described and quantified in the original papers. In particular, the normalized distance of vortex formation in the streamwise dimension (*a/D*), and width in the transversal dimension (*d/D*) are shown in Fig. 2.5 for different side ratios. The wet length represents the portion of the body side over which the separation bubble is attached.

Generally, at the sharp edge the boundary layer separates and part of its vorticity is absorbed by a growing separation bubble. For Laneville and Yong (1983), the separation bubble can be considered as a buffer region of variable size during a cycle, filled with fluid and vorticity, then released at maturity. The remaining part of vorticity continues in the shear layer, and it rolls in the forming vortices, in a proportion related to the cylinder side ratio. Then the vorticity and fluid contained in this shear layer interacts with the opposite vortex, or the adjacent one, depending again on the side ratio. Hence, when the vortex has been shed, the separation bubble reduces to its minimum size. At the end of the cycle, if the side ratio is low ($B/D < 3$), the vorticity and fluid released by the bubble entrain in the forming wake vortex., otherwise, if the reattachment occurs on the cylinder side ($B/D > 3$), the bubble exhausts its content in patches of vorticity.

Laneville and Yong highlighted some macroscopic (but not trivial) effects of the side ratio on the wake characteristics: the initial vorticity and the interaction between opposite forming vortex, are affected by the afterbody length of the body.

With the simple description of a vortex shedding cycle, it is possible to better understand the drag coefficient trend above described referring to Fig. 2.2-left. Based on the interpretation of time integrated patterns of flow visualization, they distinguished four possible fluid mechanical processes. The present work deals with the two central cases described in the original paper.

For a cylinder side ratio in the range $0.5 < B/D < 1$ the separation bubble extends from the separation point, even if the lateral side is not completely wet by the bubble. An important part of the vorticity contained in the initial shear layer feeds the bubble, which in turn interacts with a weakened shear layer. The vorticity contained in the bubble tends to produce a downwash effect which forces the wake vortex to roll up closer to the centerline. In this group lies one of the tested sections: the rectangular 2:3 section. According to the literature, for a side

ratio close to 0.6, the maximum drag coefficient occurs. Referring to Fig. 2.5, for rectangular cylinders included in this group, the loci of the vortex formation (*a/D*) are close to the rear body face, along the centerline. The vortex centers normalized transversal distance (*d/D*) is small compared to the other cases, and the typical U-shaped pressure distribution at the base occurs (Fig. 2 of the original paper). The streamlines close to the trailing edge exhibit very high curvature (Fig. 2.3).

In the present work, the case of a screen attached in front of a rectangular cylinder is studied. Its presence could act as a body elongation or it could create a more complex system. However, to understand the consequences of an elongation of a rectangular cylinder is fundamental to correctly interpret the results once the screen is fixed on. In particular, for cylinders with $1 < B/D < 3$, an increase of the side ratio tends to reduce the downwash effects caused by the separation bubble, so that the wake vortex formation locates away from the centerline (Fig. 2.5). The pressure distribution along the base is almost uniform and the pressures increased. The flow mechanisms in this side ratio range are quite complex, in fact they split up the standard vortex shedding regime (with fully separated flow) from the reattachment one. An intermittent reattachment is supposed to occur, albeit not detectable with the set-up used by the Authors. However, the absence of a secondary region on the leeward part of the lateral side, seems to preclude the possibility of a steady reattachment, while it suggests that at the end of its growth, a direct entrainment of the bubble in the wake vortex occurs.

2.2.1 Turbulence effects

The formation mechanisms around rectangular cylinders are usually presented for smooth flow and wind perpendicular to the windward face. In this specific configuration, the side ratio dependence on pressure distributions around the body, and, in turn, resulting drag coefficients, assumes a physical relevance. However, in order to give a comprehensive description, a further step consists to consider the free stream turbulence (referred as FST in the following).
The effects of turbulence on two-dimensional rectangular bluff bodies, was observed on their drag coefficients since early studies (*e.g.* McLaren *et al.*, 1969). At low angle of attack, a C_D reduction was observed increasing the turbulence, while the effect was reversed at large angles. Intensity and length scales are the main FST characteristics. In this topic, the FST is considered spatially uniform.

Turbulence intensity (I_u) is usually defined as the ratio of the r.m.s. velocity fluctuations of the streamwise component to the mean velocity. The turbulence characteristics depend on the oncoming flow, originating upstream, as it occurs, for instance, in the wind tunnel when a homogeneous turbulence grid is fixed upstream the tested model.
According to Kolmogorov theory, the length scales of vortices characterizing the turbulent flow are divided in three ranges responsible for the production, transfer and dissipation of energy contained. Integral length scales (L_x, L_y), describes the first range, and they are the most interesting for the purpose of this work. These scales are evaluated as the areas under the curves of spatial autocorrelation of the wind velocity components in the longitudinal (x) or transverse (y) directions, and are assumed to be representative of the average size of the most energetic turbulent eddies. Moreover, the integral scales could indicate the largest distance of velocity correlation between two distant points.

Usually, in the bluff body field, it is important to refer to the ratio between L_y (or L_x that it is easier to measure maintaining a similar physical meaning) and the characteristic body dimension (D). If $L_x/D >> 1$, the vortices with higher energy content are larger than the body itself. The FST will appear to the flow around the body as a time-varying flow in terms of magnitude and direction. In this case, the interaction between the FST and the body generated turbulence does not occur and the main FST effects can be estimated using the quasi-steady assumption.

In contrast, if $L_x/D << 1$, the turbulence interacts with the local flow. According to Bearman and Morel (1983), the overall effect of FST is often the result of the combination of three basic mechanisms, namely: (i) accelerated transition to turbulence in shear layers, (ii) enhanced mixing and entrainment, and (iii) distortion of FST itself by the mean flow. Effects as the anticipated transition to turbulence, the increased mixing and spreading rate, affect the shear layers behavior, namely, the body aerodynamics. Moreover, the FST is distorted by the blocking effects of a solid wall and by the mean flow field around the body in turn (Bearman, 1972). Therefore, the distorted turbulence in proximity of a bluff body may be quite different in structure from that of the approaching FST.

The importance of the streamlines curvature respect to the afterbody drag has been already discussed in the reference literature. The shear layer after the separation in correspondence of a sharp edge quickly become turbulent (Cherry *et al.,* 1984), so that the transition effect of the FST is not likely to be the dominant one at high Reynolds numbers. By contrast, the more important effect will be the enhancement of entrainment into the shear layers. This effect tends to increase the shear layer curvature. The main results on those bluff bodies with shapes characterized by fully separated flow ($B/D < 0.5$) is a reduction of the pressure at the base, *i.e.* an increased drag. For bluff bodies experiencing reattachment in smooth flow ($B/D > 3$), the increased entrainment anticipates the location of reattachment, thus reducing it by increasing the turbulence intensity. Bluff bodies with intermediate side ratio ($0.5 < B/D < 3$) exhibit a shear layer interaction with the rear body corners. So that, according to the effect previously described in smooth flow, the FST reduces the drag coefficient for these last two groups.

Fig. 2.6 shows how the mechanism by which the FST influences the flow past rectangular cylinders, resulting in a shift of the smooth drag coefficient trend (previously reported in Fig. 2.2-left). In fact, it has been reported that FST has the same effect on rectangular bluff bodies of a "body extension" in the streamwise direction (*e.g.* Nakamura, 1993).

Bearman and Morel (1983) concluded that the scale of turbulence is not a key parameter, as if it lied into the range between one order of magnitude smaller than the shear layer thickness, and one order larger than the typical body dimension. This lack of scale sensitivity was explained by the Authors assuming that there is a complex interaction between physical mechanisms involving small and large scales. Changing the length scale could strengthen some and weaken the other, thus leaving the resulting measured quantities substantially unchanged. On the contrary, Nakamura (1993) distinguishes two main turbulence scales: the scale comparable with, respectively, the shear layer thickness ($L_x/D \approx 0.1$) and the body size ($L_x/D \approx 1$). The Author found that there is a strong interaction between the body-scale turbulence and vortex shedding from bluff bodies, especially for short rectangular cylinders ($0.2 < B/D < 0.6$). Moreover, this interaction leads to opposite effects for two- or three- dimensional bodies. On the other hand, the small-scale turbulence is responsible to promote the shear-layer/edge interaction above described.

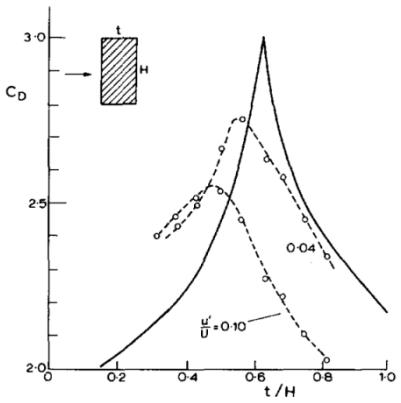

Fig. 2.6 - Drag of two-dimensional rectangular cylinder in smooth and turbulent streams: The continuous line represents the results obtained by Bearman and Trueman (1972) in smooth flow. The dashed curves, indicate the smooth and turbulent conditions studied by Courchesne and Laneville (1972).

The scales distinction pointed out by Nakamura is in accordance with some detailed works carried out on the formation of vortices behind bluff bodies. In particular, Gerrard (1966) concluded that there are two simultaneous characteristic lengths which participate at the oscillating wakes of bluff bodies: the scale of the formation region and the width to which the free shear layer diffuse.

The FST causes distinguishable effects also varying the wind angle of attack (α). The bluff bodies that in smooth flow at α = 0° exhibit a separated flow (B/D < 3), experience flow reattachment at a typical angle of attack. For instance, the flow around the square section reattaches for $\alpha \approx 13°$ in smooth flow, but it anticipates to $\alpha \approx 10°$ in turbulent flow (Lee, 1975). The FST effect, according to the interpretation of a "body elongation", consists in an earlier reattachment for bluff bodies with low side ratio.
FST is uniformly generated, both experimentally and numerically, by means grids or, only numerically, synthetic inlet boundary conditions. Issues concerning the correct turbulence reproduction were mentioned by Bearman and Morel (1983), and it has to be paid attention to them nowadays. The wide dispersion of data in turbulent flow reflects the complexity of this practical aspect.

2.2.2 The square section

Taking into account sharp-edged bodies, the square section can be considered the counter part of the circular cylinder for the round-edged ones. Therefore, a large number of experimental and numerical works are dedicated to the aerodynamics of this section. Some of them elucidated the flow mechanisms behind the above mentioned properties of shear layers and near-wake, as well as many contributions focused on the turbulence influence. A complete literature review on the square section is outside the scope of the current section. In the following, the main aerodynamic features of the two-dimensional section, based on selected papers, are proposed.
Vickery (1966) performed experimental tests to carry out a first comparison between smooth and turbulent flow. He concluded that, in the Reynolds range considered ($4\times10^4 < Re < 1.6\times10^5$), the square section produces considerably greater and more strongly correlated lift forces than the circular cross-section. An important reduction of lift fluctuation and drag coefficient in turbulent flow was measured, and the interaction between shear-layer and trailing edge caused by turbulence was discussed. Later, Lee (1975) focused the attention on the

turbulence effects for different turbulence intensities and length scales, also varying the angle of attack. He clearly showed that the mean pressure distribution changes on the body sides and the increased base pressure were caused by the FST interaction with the flow field around the body. He noticed that at the lateral sides of the body, for wind perpendicular to the face, a pressure recovery occurs for turbulence intensity $I_u \geq 6.5\%$. Generally speaking, the r.m.s. pressure distributions (C_p') at the base is reduced by the FST. On the body sides, FST does not modify the overall C_p' pattern, except for $I_u \geq 12.5\%$, where its rear peak in the distribution move forward to almost $0.5D$. According to Vickery (1966), the spectral analyses show a reduction of the vortex shedding effects (as the lift force) once the FST is introduced. A broadened band width centered on the Strouhal frequency, and a loss of energy at that frequency, were measured in turbulent flow.
Unexpected effects caused by an increase in I_u were observed by Namiranian and Gartshore (1988): in contrast with previous studies (*e.g.* Vickery, 1966), the Authors observed a steady increase in correlation lengths, for vortex excitation forces, experienced by the square section.
Recently, Lander *et al.* (2016) performed in-deep studies on the influence of FST on the square section, focusing on the shear layers role. In their work, most of the previously reported effects of FST on the section aerodynamics were reproduced and discussed. Instantaneous measurements were carried out so to complete steady observations already present in literature: specifically by using time-resolved particle image velocimetry (TRPIV). Some results are proposed in Fig. 2.7, in which a so called "elliptical vortices" transformation accompanied by an elongation in the streamwise direction is reported. The increased length of the wake was also associated with a reduction in the cross-stream velocity fluctuations. The paper elucidates many aspect concerning the shear layers behavior with enhanced FST. For instance, it was found the substantial increase in curvature towards the body, but no pronounced increase in the shear layer growth rate was observed.

Concerning the angle of attack variation, its influence was documented by observing the anticipated pressure recovery at the rear of the side face caused by the FST (Lee, 1975). This experimental evidence was explained by a twofold effect. On one hand, the thickening of the shear layer may cause the total enclosure of the separation bubble to occur at a smaller angle; on the other hand, the thicker shear layer may result in a smaller separation area with less local suction. Furthermore, the variation of base pressure with flow angle in smooth and turbulent condition confirmed the results from Vickery: for angles above the flow reattachment, the region of vortex formation is distanced from the body, thus the difference of C_{bp} measured with the two approaching flows is small. Detailed measurements for different angles of attack were also performed by Rockwell (1977). The tests were carried out in smooth flow, with two pressure taps on the lateral side, respectively close to the leading and the trailing edge. They found that the maximum pressure fluctuation amplitude, caused by vortex-shedding, occurs at $\alpha \approx 5°$.
As introduced at the beginning of the section, there is a vast literature on the square cylinder. The two-dimensional square section merges a simple geometry with a complex flow behavior, representing a, so to say, benchmark case of bluff body aerodynamics employed to validate experimental tests and numerical simulations. For the sake of completeness, two additional aspects need to be briefly mentioned.

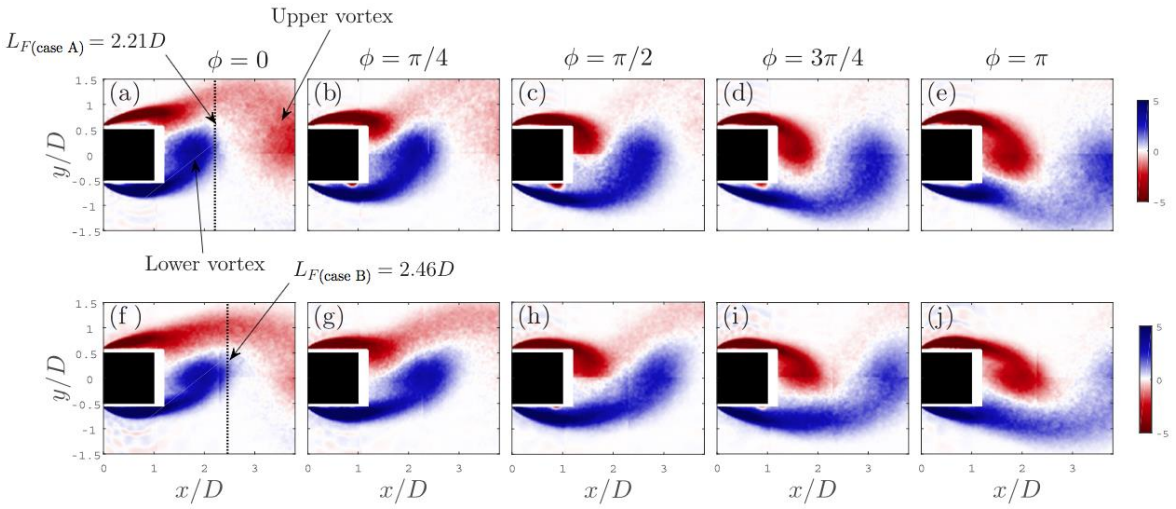

Fig. 2.7 - Phase-averaged normalized vorticity at five phases along the shedding cycle: upper row, smooth flow; lower row, turbulent flow. In the figure from Lander *et al.* (2016) are reported also the formation length (L_F) measured for the two approaching flow conditions.

A huge number of computational fluid dynamic (CFD) numerical simulations have been carried out so far. According to the approach of the current section, results obtained from experimental tests were recalled and employed to describe the main flow features around the square section because, historically, the CFD simulations made use of the square section as a benchmark to validate the simulations themselves (*e.g.* Murakami and Mochida, 1995, Bosch and Rodi, 1998, Yu and Kareem, 1998, Shur *et al.*, 2005, Oka and Ishihara, 2009, Raisee *et al.*, 2010). In this field, a milestone paper was carried out by Rodi in 1997. The Author reported and discussed the results of a LES (Large Eddy Simulations) Workshop, (organized by the Author together with Professor Ferziger of Stanford University). In the workshop, groups from different universities were invited to submit the results of CFD simulations for two case studies: one of these was the two-dimensional square section.

Despite the more recent development of CFD, respect to wind tunnel tests, the level achieved (*e.g.* Trias *et al.*, 2015) suggests that contributions of CFD in bluff body aerodynamics will became more and more important.

The second aspect concerns the proneness of the square section to the galloping instability phenomenon. The current study does not deal with aeroelastic tests, therefore in this introductory part the galloping phenomenon is not considered. However, the lift coefficient slope parameter together with the drag coefficient (Den Hartog criterion), was employed to evaluate the effect of the screen on the baseline sections (square and rectangle in Chapter 3).

2.3 Effects of bluff body cross-section modification

Studies on two-dimensional rectangular bluff bodies may help in understanding the main flow features of slender three-dimensional structures, such as bridges or tall buildings.

The comprehension of rectangular cylinders aerodynamics allows to design opportune adjustments to the original section, aiming for an increased aerodynamic performance of structures (*e.g.* a drag reduction). Thus, making an overview on several opportunely modified geometries, may be preparatory to investigate the effects caused by the presence of a screen fixed close to a rectangular section.

From here on simple cross sections, such as circular or square, are indicated as “original” (or “baseline”) whereas those presenting variations or addictions are called “modified”. It is worth

noting that each modified section proposed can be described in terms of shear layer curvature, wake width and body side-ratio (fully separated, trailing-edge interaction and reattachment of the flow). In line with the previous section, turbulence effects are also considered here, while section modifications, which involve the use of splitter plates to modify the body wake, are not dealt with hereafter.

According to Lajos (1986), the value of the forebody drag can be reduced by accelerating the flow over the front face. This can be achieved in different ways: for instance "streamlining" the forebody geometry, rounding up or beveling the leading edges. Moreover, the effects of various devices attached near the periphery of the front face were investigated by the Authors. The aerodynamic appendages fixed on the forebody exhibited a drag reduction down to 50%. The main results obtained in these two-dimensional exploratory studies, were also extended in the field of tall buildings, as pointed out in Kwok and Bailey (1987).
Anyway, most of literature studies on drag reduction were aimed to fuel consumption of vehicles reduction, by considering bluff bodies with high side ratio (commercial trucks applications). On the other hand, the results obtained inspired similar studies for civil engineering applications (*e.g.* Takeuchi, 1990). In fact, Tamura and Miyagi (1999) compared the effects of chamfered and rounded corners on a square cylinder and a three-dimensional prism, investigating also the effects of turbulence. For both, the modified two- and three-dimensional models, it was observed an overall reduction of the drag force and lift fluctuations. For all the tested cases in smooth flow, the lift coefficient slope centered in 0° (wind perpendicular to the model face) was negative. In turbulent flow, the rounded section only reached a positive lift coefficient slope. The Authors concluded that irrespectively to the approaching flow (smooth or turbulent), the original square section and the modified one with chamfered corners exhibited a flow pattern of complete separation. In contrast, the model with rounded corners in turbulent flow was characterized by separation with reattachment. The modified sections exhibited also an increased vortex shedding frequency compared to the original case. They observed the corner-modifications sensitivity also in the three-dimensional case, although the measured effects were smaller than in the two-dimensional case. Additional results on the square section with rounded corners can be found in Carassale *et al.* (2014).
Another method of drag reduction and, more generally, of aerodynamics modification, is based on the turbulence manipulation of the approaching flow (*e.g.* Narashima and Sreenivasan, 1988). The FST effects discussed in the previous section suggested the researchers to employ additional elements in the system designed to generate turbulence. The effects caused by the introduction of a small rod in front of a circular cylinder were studied by Prasad and Williamson (1997), while Igarashi (1997) considered the same effects on the square section. Both the studied bodies exhibited flow patterns modifications, as pointed out from the substantial drag reduction achieved. Moreover, the two studies investigated the optimal configuration for drag reduction by varying the rod dimension and its distance to the body (parametric study).
Many other methods for the drag reduction has been proposed during the years. Munshi *et al.* (1999), and, later, Beaudoin *et al.* (2006), investigated the effect of corners with a moving surface in order to actively modify the body aerodynamics. Other solutions tended to use passive flow features to reduce the drag (Fig. 2.8), deflecting the flow in order to reduce the shear layer curvature and/or increasing the base pressure (*e.g.* Hirst *et al.*, 2015).

A fascinating study in the field of tall buildings was performed by Menicovich *et al.*, (2014), by proposing an innovative approach to integrate active air flow control into the building envelopes, in order to modify the tall building aerodynamics. In their work, an active system of jets modified the building aerodynamics without varying the original building shape.
On the other hand, Hassanli *et al.* (2017) proposed an innovative building envelope able to interact with the building aerodynamics (aspect previously studied in Hu *et al.*, 2016), to exploit the internal flows for energy harvesting devices. The Authors assumed the building envelope to be a screen in different configuration of external openings with the cavity opened both laterally and on top. The three-dimensionality of the problem did not allow to simplify the problem as two-dimensional but it demonstrated the possibility to modify the system building+façade aerodynamics with passive internal flows. Their work showed that a screen fixed close to a rectangular prism can interfere with the overall aerodynamics, also when the gap width is small compared to the building characteristic dimension (D). In particular, the tests were performed with an open gap width equal to $D/22.5$.

2.3.1 Some studies concerning bluff bodies with a screen

The modification of a bluff body shape through small scale adjustments may cause important aerodynamics modification, depending on the location of the modifications. This can occur also with a screen fixed in front of the building structure, where the openings of the cavity (between the façade and the building) lie behind the edges, namely, the separation point.
Nevertheless, there is a lack of literature in bluff body aerodynamics concerning a system where the screen is fixed very close to the body spaced by a through cavity.
The effect of a flat plate fixed in front of a semi-infinite circular cylinder (having the length dimension parallel to the oncoming flow direction) was investigated by Koenig and Roshko (1985), although, the aim of the work was oriented to parameterize screen dimension and distance in order to reduce the system drag as much as possible. By combining the results, four drag regimes (A,B,C,D in Fig. 2.9) were distinguished, with the related boundary configurations (see AB, CB, etc. in Fig. 2.9). Gap widths of the same order of magnitude as those tested in the current work were not investigated, but interesting considerations were discussed, such as on the rotating flow effect behind the screen.
Cooper (1988) performed wind tunnel tests on a square cylinder having a forebody plate held in front of the windward face. He also tested different configurations by varying the plate width and the gap width, always searching for a drag reduction. Measurements were carried out for different angles of attack reaching gap a width of $D/11$. The model was equipped only with a force balance, so that no pressure data were recorded.

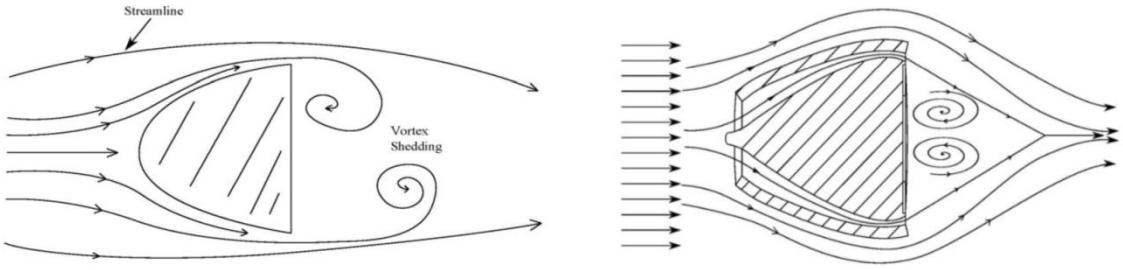

Fig. 2.8 - Main flow structure around a generic bluff body (left) and expected results (right) after passive flow modifications (Hirst *et al.*, 2015).

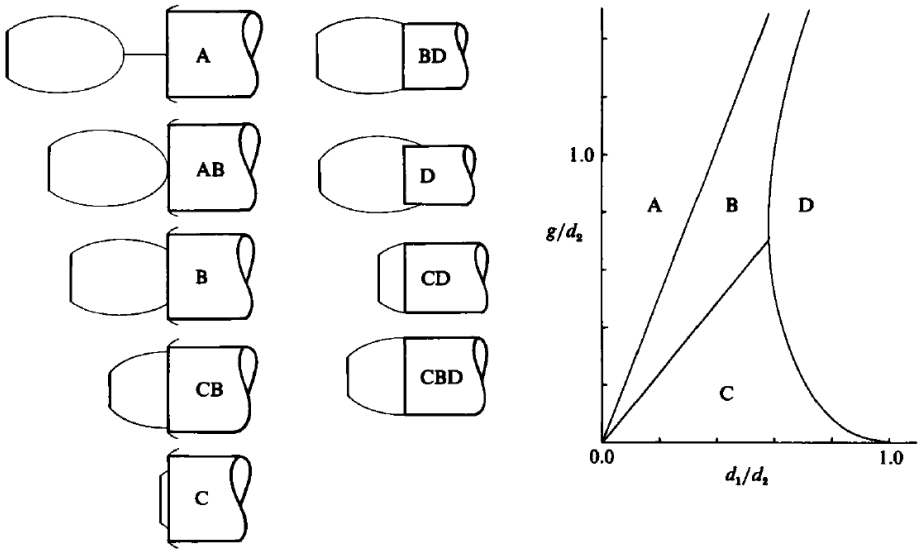

Fig. 2.9 - Patterns obtained from intersections of a disk-wake profile and a semi-infinite cylinder (Koenig and Roshko, 1985). In their study both the gap width (g) and the screen dimension (d_1) respect to the body chord (d_2) are varied.

In case the cross-flow body dimension equals that of the flat plate, such geometry coincides with the current work reference case. The smallest gap width tested by Cooper is almost equal to the largest one tested in the current work. However, as pointed out in Chapter 3, the results obtained are not in line with Cooper's paper. In Fig. 2.10, it is possible to appreciate a reduction of the drag coefficient compared to the case without forebody plate, and a negligible effect on the lift coefficient slope. Unfortunately there is not enough information to assess the reliability of these results, but the drag coefficient of the square section without the screen equal to 1.82 at 0° indicates some criticalities of the set up adopted by Cooper. Considering the small dimensions of the model (side length equal to 19mm), it is possible that it was not suitable to appreciate the plate effect at a distance of 1.7mm (*D*/11).

Finally, it is worth recalling the work performed by Bentley and Nichols (1990) in which the vortex fields around dual bluff bodies were mapped. In this case the geometry of the problem was still similar to the one tested in the current work, but the minimum gap width tested was *D*/2.5, which is far away from the one of interest in the field of building façade. Nevertheless, interesting remarks were reported after the comparison between the case without and with a vertical compartmentation of the cavity. The Authors observed that the movement of air through the gap widths tested was crucial to vortex shedding enhancement (Fig. 2.11). Similar considerations were reported by Hu *et al.* (2016), by observing that, for wind perpendicular to the airtight screen, with the open gap cavity, "*the flow within the double-skin façade appears to be in unison with the vortex shedding frequency and hence reinforces the vortex shedding process*".

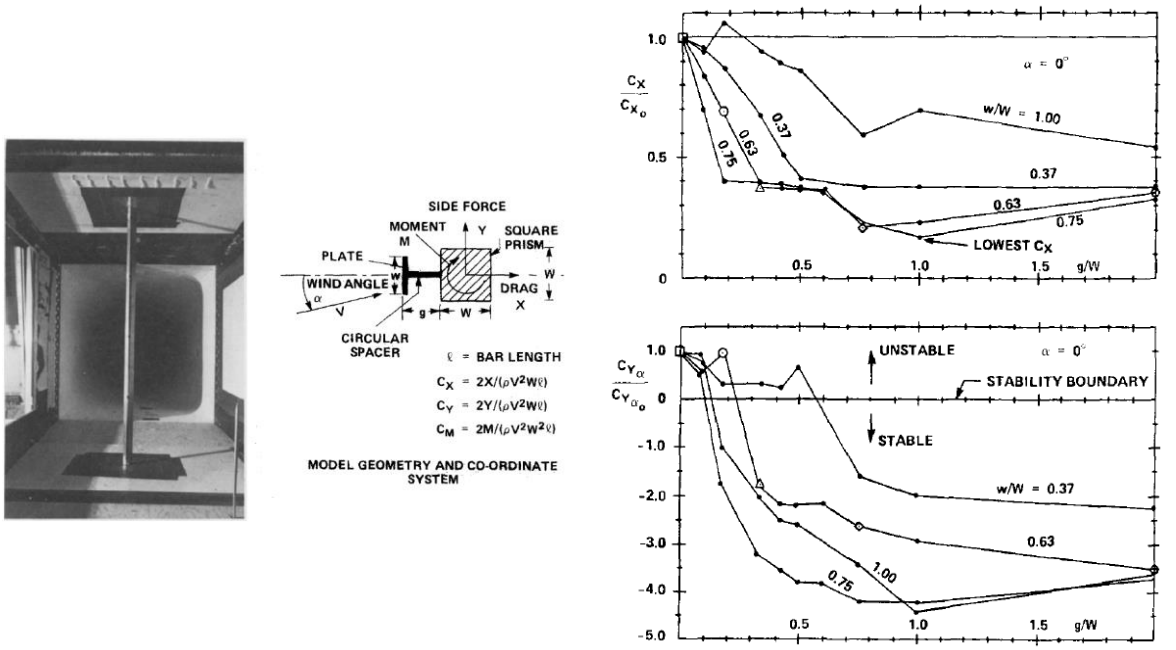

Fig. 2.10 - Set up arrangement and results obtained by Cooper (Cooper, 1988). C_x/C_{x0} is the drag coefficient normalized by one obtained for the square section without screen, $C_{Y\alpha}/C_{Y\alpha0}$ is the lift coefficient slope normalized by one obtained for the square section without screen.

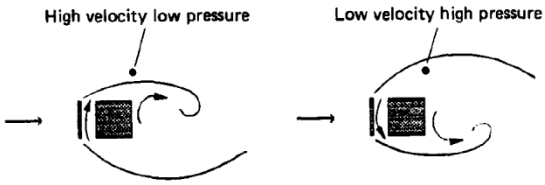

Fig. 2.11 - Movement of the shear layers on separate halves of the vortex cycles (Bentley and Nichols, 1990).

2.4 Oscillating flows

The observations on the flow behavior in presence of a forebody screen, support the necessity of in-deep studies on the flow in the cavity behind the screen. According to the contributions gathered, the internal flow, for wind perpendicular to the screen, may oscillates driven by the vortex shedding. The cavity extremities behind the sharp edge separation points of the body are characterized by an almost sinusoidal pressure gradient due to vortex shedding. The oscillating pressure gradient tends to drive an oscillating flow inside the cavity in turn.

Oscillating flows are considered a branch of the more general research field of pulsating flows. In a pulsating flow instantaneous quantities (*i.e.* pressure, velocity,...) are distinguished in three components: an ensemble-averaged part related to a "long-time average", an additional ensemble-averaged part related to the oscillatory component due to the pulsation (oscillation) and a fluctuating turbulent component (Gundogdu and Carpinlioglu, 1999). The oscillating flow is defined as a pulsating flow with zero-mean. This type of flow is quite unusual in wind engineering, therefore its theoretical basis are briefly recalled.

Governing equations for an incompressible fluid

It seems useful here to firstly introduce non-dimensional numbers that characterize the flow. For a steady incompressible flow, Navier-Stokes (NS) equations can be rewritten in a non-dimensional form only as a function of the Reynolds number. Following the same approach, for

an oscillating incompressible flow the non-dimensional form of the NS equations requires the use of an additional non-dimensional parameter linked to the frequency of oscillation, that is a reduced frequency (k_{RF}).

Starting from the momentum equation (see *e.g.* Fung 1997):

$$\rho\frac{\partial u_i}{\partial t}+\rho\left(u\frac{\partial u_i}{\partial x}+v\frac{\partial u_i}{\partial y}+w\frac{\partial u_i}{\partial z}\right)=X_i-\frac{\partial p}{\partial x_i}+\mu\left(\frac{\partial^2}{\partial x^2}+\frac{\partial^2}{\partial y^2}+\frac{\partial^2}{\partial z^2}\right)u_i \qquad \textit{(eq. 2.3)}$$

where: u_i denotes the velocity vector (with component u, v, w)

X_i is the body force per unit volume

p is the pressure

ρ and μ are the air density and viscosity respectively

Then, a characteristic velocity U_{chr}, frequency ω_{chr} and length L_{chr} are chosen to rewrite the equations in terms of non-dimensional quantities:

$$x'=\frac{x}{L_{chr}},\ y'=\frac{y}{L_{chr}},\ z'=\frac{z}{L_{chr}},\ u'=\frac{u}{U_{chr}},\ v'=\frac{v}{U_{chr}},\ w'=\frac{w}{U_{chr}},\ p'=\frac{p}{\rho U_{chr}{}^2},\ t'=\omega_{chr}t$$

Introducing now the non-dimensional parameters:

- $\mathrm{Re}=\dfrac{U_{chr}L_{chr}\rho}{\mu}=\dfrac{U_{chr}L_{chr}}{\upsilon}$ (Reynolds number)
- $k_{RF}=\dfrac{\omega_{chr}L_{chr}}{U_{chr}}$ (Reduced frequency)

By omitting the body force and dividing by $\rho U_{chr}{}^2/L_{chr}$, the equations, by substituting, can be rewritten, for the u' component, as:

$$\frac{\omega_{chr}L_{chr}}{U_{chr}}\frac{\partial u'}{\partial t'}+u'\frac{\partial u'}{\partial x'}+v'\frac{\partial u'}{\partial y'}+w'\frac{\partial u'}{\partial z'}=-\frac{\partial p'}{\partial x'}+\frac{\mu}{\rho U_{chr}L_{chr}}\left(\frac{\partial^2 u'}{\partial x'^2}+\frac{\partial^2 u'}{\partial y'^2}+\frac{\partial^2 u'}{\partial z'^2}\right) \qquad \textit{(eq. 2.4)}$$

With the same procedure, the continuity equation can also be rewritten as:

$$\frac{\partial u'}{\partial x'}+\frac{\partial v'}{\partial y'}+\frac{\partial w'}{\partial z'}=0 \qquad \textit{(eq. 2.5)}$$

Since the two equations above constitute the complete set of field equations for an incompressible fluid, it is clear that only two physical parameters, namely *Re* and k_{RF}, enter into the field equations of the flow. The momentum equation with the two parameters can be given as:

$$k_{RF}\frac{\partial u'}{\partial t'}+u'\frac{\partial u'}{\partial x'}+v'\frac{\partial u'}{\partial y'}+w'\frac{\partial u'}{\partial z'}=-\frac{\partial p'}{\partial x'}+\frac{1}{\mathrm{Re}}\left(\frac{\partial^2 u'}{\partial x'^2}+\frac{\partial^2 u'}{\partial y'^2}+\frac{\partial^2 u'}{\partial z'^2}\right) \qquad \textit{(eq. 2.6)}$$

From eq. 2.5 it is clear that for $k_{RF}=0$ the flow is steady. It is also expected that for a low k_{RF} value the flow behaves in a quasi-steady manner, while for high k_{RF} values the flow behaves as unsteady, though different from the quasi-steady one. Depending on the field of study, other parameters can be employed instead of k_{RF}, as in the present study the Womersley Number:

$$Wo=L_{chr}\sqrt{\frac{\omega_{chr}}{\upsilon}} \qquad \textit{(eq. 2.7)}$$

Critical Reynolds number for an oscillating flow

Similarly to the steady case, for an oscillating flow too is possible to distinguish three flow regimes: laminar, transitional and turbulent. The definition of the two threshold limits, respectively for the fully turbulent regime and for the laminar regime must consider both the Reynolds number and a frequency parameter. In the literature, the Womersley number is the most widely employed as frequency parameter. The dependence on the frequency parameter is needed as it is well-known that the velocity profile varies its shape depending on the frequency of oscillation. Therefore, the position of the peak velocity and the region where turbulence is generated changes together with these non-dimensional quantities.

When the flow is in the laminar regime, the Womersley number alone can properly describe the velocity profile features, and three sub-regimes are identified, as explained in the next section. When the flow becomes turbulent, the whole velocity profile follows the 1/7 power law shape (Gundogdu and Carpinlioglu, 1999). It remains with this shape for almost the entire oscillating period, except for the initial phase of acceleration and the last part of deceleration.

Ohmi and Iguchi (1982), investigated internal oscillating flow in a circular pipe, defining the limits to distinguish laminar, transitional and turbulent regimes. Based on the Womersley number (Wo) and a local Reynolds number ($\mathrm{Re}_{OSC,C}$, namely, a Reynolds number defined with local quantities of the internal flow) they obtained the following results for a circular pipe:

Critical Reynolds number at which generation region of turbulence is fully built up

For quasi- steady flow behavior

$$\mathrm{Re}_{OSC,C} = 2450 \qquad \textit{when } Wo < 1 \qquad \textit{(eq. 2.8)}$$

For oscillating flow behavior

$$\mathrm{Re}_{OSC,C} = 882 \cdot Wo \qquad \textit{when } Wo > 7 \qquad \textit{(eq. 2.9)}$$

Critical Reynolds number at which generation of turbulence disappears

For quasi- steady flow behavior

$$\mathrm{Re}_{OSC,C} = 1800 \qquad \textit{when } Wo < 5.026 \qquad \textit{(eq. 2.10)}$$

For oscillating flow behavior

$$\mathrm{Re}_{OSC,C} = (211 \cdot Wo)^{8/7} \qquad \textit{when } Wo > 7 \qquad \textit{(eq. 2.11)}$$

The results obtained by Ohmi and Iguchi (1982), summarized also in Fig. 2.12, are valid for internal flows in circular pipes. Hence, for the case of two-parallel plates different values are expected. Nevertheless, to the author's knowledge, the critical Reynolds numbers for an oscillating flow between parallel plates are still missing. Only Loudon and Tordesillas (1998) in their work on oscillating flow between parallel plates reported that the flow is probably laminar for $\mathrm{Re}_{MAX} < 5000$ and $Wo < 20$, referring to a "Re_{MAX}", instead a "$\mathrm{Re}_{OSC,C}$" based on the mean velocity in the section. However, it is not clear whether they were referring to the parallel plates or to the circular pipe channel (or tubes, or vessels) by giving the above mentioned values for Re_{MAX} and Wo.

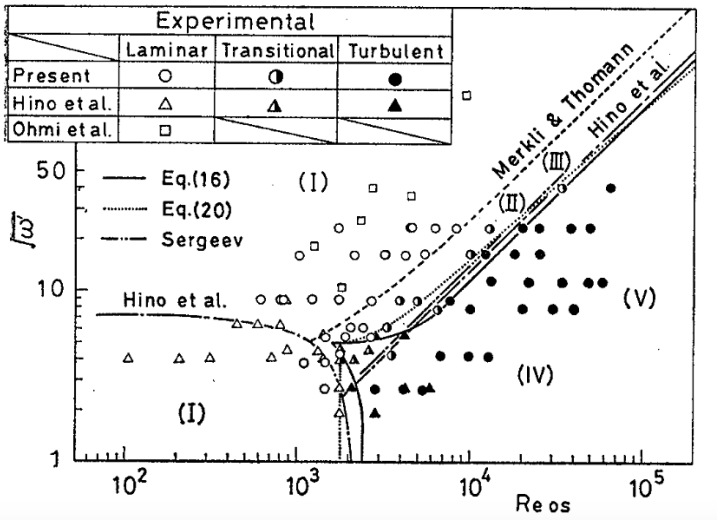

Fig. 2.12 - Laminar, transitional and turbulent regimes for an oscillating flow in a circular pipe. Comparison of estimated and experimental results of $\mathrm{Re}_{OSC,C}$ (Ohmi and Iguchi, 1982). In the figure, the Womersely number is expressed as $\sqrt{\omega'}$, the $\mathrm{Re}_{OSC,C}$ as Re_{OS}.

2.4.1 Womersely Number

The oscillating flow in laminar regime is fully characterized by the Womersley number alone. In particular, it exhibits two distinct behaviors for $Wo<1$ and $Wo>>1$, separated by an intermediate range of mixed conditions. When $Wo<1$, the fluid behaves in a quasi-steady manner. Increasing Wo the velocity profile maintains its parabolic shape but begins to show a phase lag with respect to the pressure gradient. Finally, when $Wo>>1$, the phase lag increases and the velocity profiles changes its shape, with the maximum velocity no longer located in the middle between the two plates (Fig. 2.13). The phase lag phenomenon was first observed and formalized by Womersley (1955).
These considerations can be formalized through the equations presented in the following.

For parallel plates the Womersley number, is defined as:

$$Wo = \frac{L}{2}\sqrt{\frac{2\pi f}{\nu}} \qquad \textit{(eq. 2.12)}$$

where L is the distance between the plates
f is the oscillation frequency
ν is the kinematic viscosity

The governing equation of motion for the oscillating flow in laminar regime is given by:

$$\frac{\partial^2 u(y,t)}{\partial y^2} - \frac{\rho}{\mu}\frac{\partial u(y,t)}{\partial t} = \frac{1}{\mu}\frac{\partial p}{\partial x} \qquad \textit{(eq. 2.13)}$$

where: $u(y,t)$ is the x-component of the velocity
$\frac{\partial p}{\partial x}$ is the pressure gradient

The boundary conditions are: $u\left(-\frac{L}{2},t\right)=0$, $u\left(\frac{L}{2},t\right)=0$ (for any t).

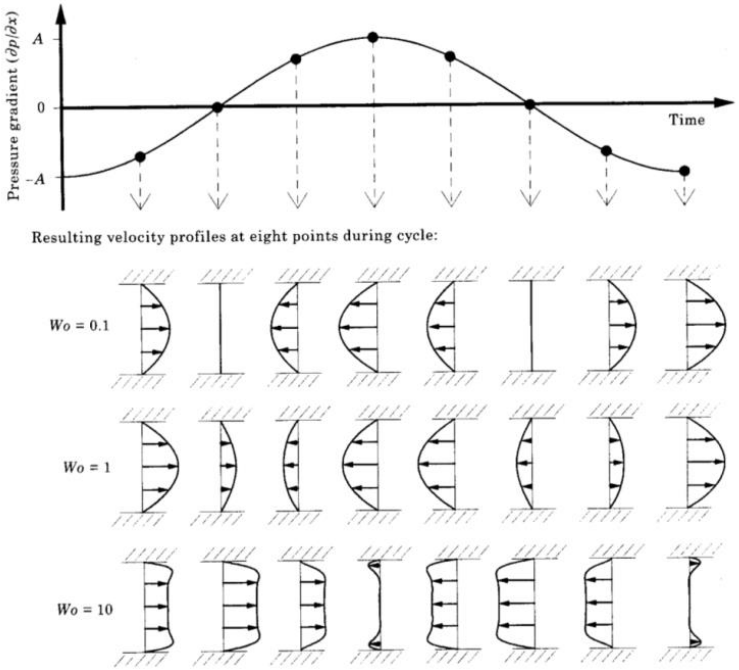

Fig. 2.13 - Velocity profiles between two flat plates at eight points in time during a single cycle of a sinusoidally-varying pressure gradient for three values of the Womersley number (Loudon and Tordesillas, 1998).

Considering a pressure gradient periodic in time as:

$$\frac{\partial p}{\partial x} = \frac{p_2 - p_1}{l} = -Ae^{i\omega t} \qquad \textit{(eq. 2.14)}$$

where: $i = \sqrt{-1}$

$\omega = 2\pi f$

A is a real constant which indicates the amplitude of the oscillating quantity the solution for the velocity in this case may be found as:

$$u(y,t) = \frac{A}{i\omega\rho}\left[1 - \frac{\cosh\left(Wo \cdot i^{1/2} \cdot \frac{y}{L/2}\right)}{\cosh\left(Wo \cdot i^{1/2}\right)}\right] e^{i\omega t} \qquad \textit{(eq. 2.15)}$$

Therefore, the velocity varies along the coordinate normal to the flow (y) and in time. The amplitude depends on the pressure gradient amplitude (A) and on the Womersley number. Then, the attention is focused on the real part of the solution in order to define the velocity profile features:

$$u(y,t)_{real} = \frac{A}{n\rho\gamma}\left\{\begin{array}{l}\left[\sinh\Phi_1(y)\sin\Phi_2(y) + \sinh\Phi_2(y)\sin\Phi_1(y)\right]\cos(nt) + \\ \left[\gamma - \cosh\Phi_1(y)\cos\Phi_2(y) - \cosh\Phi_2(y)\cos\Phi_1(y)\right]\sin(nt)\end{array}\right\} \qquad \textit{(eq. 2.16)}$$

where:

$$\Phi_1(y) = \frac{Wo}{\sqrt{2}}\left(1 + \frac{y}{L/2}\right), \qquad \Phi_2(y) = \frac{Wo}{\sqrt{2}}\left(1 - \frac{y}{L/2}\right), \qquad \gamma = \cosh\left(\sqrt{2}\cdot Wo\right) + \cos\left(\sqrt{2}\cdot Wo\right)$$

The amplitude of this oscillating velocity (maximum velocity) is:

$$u_{MAX} = \frac{A}{n\rho\gamma}\left\{\begin{array}{l}\left[\sinh\Phi_1(y)\sin\Phi_2(y) + \sinh\Phi_2(y)\sin\Phi_1(y)\right]^2 + \\ \left[\gamma - \cosh\Phi_1(y)\cos\Phi_2(y) - \cosh\Phi_2(y)\cos\Phi_1(y)\right]^2\end{array}\right\}^{0.5} \qquad \textit{(eq. 2.17)}$$

Finally, the volume flow rate per unit depth is given by:

$$Q(t) = \int_{-L/2}^{L/2} u(y,t)\,dy \qquad \textit{(eq. 2.18)}$$

Volume flow rate varies with Wo according to the variation of the velocity profile. For instance, if the driving pressure gradient oscillates more rapidly without changing amplitude, the corresponding oscillation in total flow also increases in frequency, but it decreases in amplitude when the frequency is high enough to result $Wo > 1$ (Fig. 2.14).

In Fig. 2.15, the general pattern of the decrease in amplitude for the oscillating volume flow rate in the range $0 < Wo < 10$ is reported. It is to note that, in the case of parallel plates, the flow rate decreases rapidly from $Wo = 1$ (where it is the 92% of the steady case) to $Wo = 2$, where it is almost half of it (Fig. 2.15). According to Loudon and Tordesillas (1998), this drop is even sharper than that one observed for the geometry of flow inside circular cylinder, where the amplitude is not halved until $Wo > 3$. This argument entails some doubts on the applicability of the critical Reynolds values found by Ohmi and Iguchi (1982) for the parallel plates case.

For sake of completeness, it must be mentioned that the variation of velocity profile influences the shear stress at the wall, varying in time, because it is related to the velocity gradient at the wall. The magnitude of the maximum velocity gradient at the wall during oscillatory flow changes dramatically with a change in Wo. However, the maximum values are expected for low Wo numbers.

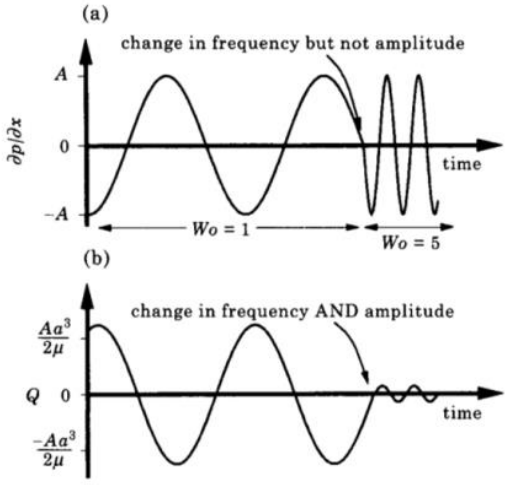

Fig. 2.14 - The oscillating pressure gradient frequency variation effect on the volume flow rate (Loudon and Tordesillas, 1998)

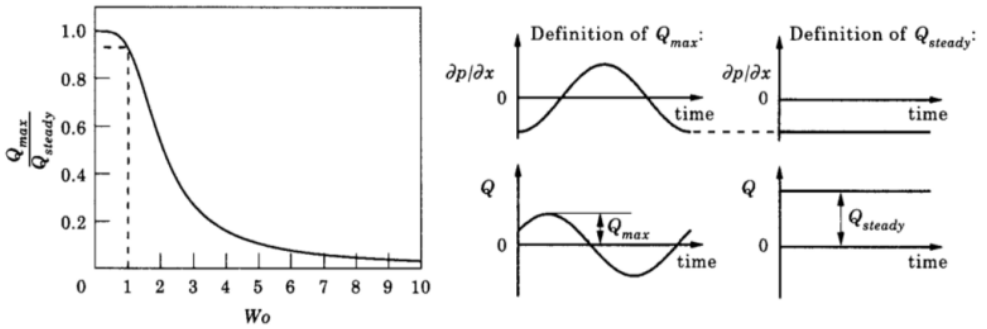

Fig. 2.15 - Volume flow rate normalized by the corresponding steady-state value varying Wo (Loudon and Tordesillas, 1998)

On the use of Womersley number in the present study

In the present work, an interaction between the external flow around the body and the internal flow behind the screen is expected. If the frequency oscillation of the pressure drop at the extremities of the cavity behind the screen, is driven only by the vortex detachment, it is possible to rearrange the expression of the Womersley number (eq. 2.10). The small gap widths considered in the current work (from *D*/40 to *D*/10) allows to hypothesize that the Strouhal frequency is not affected by the presence of the screen (later verified, for the case tested in the experimental campaign, Chapter 3).

Therefore, by combining the bluff body vortex shedding frequency equation:

$$f = St \cdot \frac{U_\infty}{D} \qquad \textit{(eq. 2.19)}$$

where: St is the Strouhal frequency

U_∞ is the free stream mean velocity of the approaching flow

D is the characteristic body dimension

with the Womersley expression (eq. 2.10), it is possible to rewrite:

$$Wo = \frac{L}{D} \cdot \sqrt{St \cdot \mathrm{Re}} \cdot \sqrt{\frac{\pi}{2}} \simeq 1.253 \cdot \frac{L}{D} \cdot \sqrt{St \cdot \mathrm{Re}} \qquad \textit{(eq. 2.20)}$$

where: L is the cavity gap

Re is the Reynolds number

Eq. 2.20 is employed in the next chapters to estimate the *Wo* number for a wind direction of 0°, taking into account the screened bluff body section (*St*), the approaching flow (*Re*) and the cavity geometry (*L/D*) characteristics. However, to exhaustively characterize the oscillating flow it is necessary also a local *Re* number ($\mathrm{Re}_{OSC,C}$). At the end of Chapter 4, results of internal flow velocity obtained from explorative numerical simulations are discussed to estimate an approximate value of $\mathrm{Re}_{OSC,C}$.

2.5 Summary

In this Chapter, the main flow features of a two-dimensional bluff body immersed in an incompressible flow were discussed. The massive separation which characterize the bluff bodies suggests to divide the body in two parts, namely, the forebody and the rearbody. This distinction is marked by the separation point, which, in the general case of a rectangular bluff body is fixed at the body edges.

The flow features around a rectangular cylinder were analyzed in order to relate them with the pressures acting on the body. The main flow topology was described through the shear layers curvature and the wake vortex properties. Especially for the case of smooth flow perpendicular to the body face, the relationship between the flow and the body side ratio (*B/D*) was presented and discussed. The rearbody drag is the most affected by the ratio between the depth (*B*) and the width (*D*) of the body, while the forebody drag results almost constant for different side ratios.

Another aspect concerns the free stream turbulence (FST) effects on the body aerodynamics, which was elucidated by clarifying the mechanisms of interaction with the shear layers and the mean flow, with the subsequent “body elongation” effect.

A selective review on peculiar aspects of the square section was recalled. The main flow features described for a generic rectangular cylinder were reported. The square section exhibits the shear-layer/trailing-edge interaction when the approaching flow is turbulent. This can be observed by a pressure recovery on the side. For high values of turbulence intensity (≥12.5%), also the pressure fluctuating component is affected. The presence of FST affects the wind angle at which the flow reattachment occurs. According to the general behavior of the FST on the rectangular sections, the reattachment results anticipated, *i.e.* it occurs for a smaller angle of attack.

Some works on bluff body cross-section modifications were recalled in order to point out that small adjustments on the geometry can considerably affect the overall aerodynamics. The dissertation was then extended from two- to three-dimensional more realistic case studies related to the civil engineering field. These works confirm the importance of the main flow parameters, such as the shear-layer curvature, together with the relation between the wake and the body side ratio (in terms of loci of vortex formation). Indeed, the modifications proposed are effective only if they affect somehow the above mentioned parameters. Hence, it is not only the relative dimension of the change, but also its location.
Literature dealing with corner modifications, turbulence manipulations, active and passive solutions changing the flow, was briefly presented to motivate the expected effects of the screen fixed in front of the bluff body object of the thesis.

In this Chapter, it has been shown that also the presence of a screen in front of a rectangular cylinder can influence the aerodynamics of the new system formed by the screen and the body itself. Two aspects arose from the papers reviewed. First, with the screen fixed at the same distance, the interference effects are different if the open gap cavity allows the flow moving or if the internal cavity is interrupted by an airtight layer. In particular, some authors observed a relation between the vortex shedding and the moving flow behind the screen. Second, the flow behavior of the system it is not easily predictable, and most of the gap widths investigated in the current work have not been investigated yet.
On the basis of the above mentioned observations, the relation between the vortex shedding around the body and an internal oscillating flow, in the cavity behind the screen, may be of high relevance to understand the behavior of the system composed by the screen and the bluff body. The fundamentals of oscillating flows are briefly recalled. Oscillating flow regimes can be characterized based on two non-dimensional quantities, such as the Reynolds number and the Womersley number. Studies on circular duct showed that there are typical limit values to distinguish the oscillating flow regimes, as it occurs with a steady flow. Unfortunately, there are only qualitative indications for the case of oscillating flow between parallel plates, as the flow expected in the current work. However, under a certain Re limit value, the oscillating flow characteristics can be defined only through the Womersley number.
Finally, the Wo number expression has been rewritten for the internal oscillating flow expected in the present work.

Chapter 3 - Experimental tests

The present chapter deals with the experimental campaign performed in the CRIACIV wind tunnel of the University of Florence. The aim of the experimental tests was to obtain reliable values of wind induced forces and pressures, on models reproducing a two-dimensional system composed by an open-gap airtight screen, attached to different rectangular cylinders.
The laboratory facilities and instruments are described, and the design of a new set-up where the section models are installed vertically is motivated. The need to integrate the work with an additional CFD study is introduced, based on the limitations of the experimental arrangements. Information on the model geometries and the approaching flow conditions are given. Then, the configurations tested are described to explain the way in which the results is presented. Finally, the results are summarized and discussed in two distinct sections: one for flow normal to the screen and the other for flow at different angles of attack.

3.1 Experimental set-up

3.1.1 The C.R.I.A.C.I.V. atmospheric boundary layer wind tunnel

All the experimental tests were carried out in the C.R.I.A.C.I.V. (Inter-University Research Centre on Building Aerodynamics and Wind Engineering) atmospheric boundary layer wind tunnel. The wind engineering laboratory is active since 1993, and it is located in *Polo Universitario "Città di Prato"*, a branch of the University of Florence.

The CRIACIV atmospheric boundary layer wind tunnel (Fig. 3.1) is an open-circuit wind tunnel entirely installed inside the laboratory, therefore inlet and outlets are not connected with the external environment.
The wind tunnel cross-section is rectangular with sides of 2.2m by 1.6m at the inlet section, after the air converging section equipped with a honeycomb. The tunnel is then slightly divergent until the working section which is 2.4m wide and 1.6m high. About 3m behind the test section there is the fan powered by the 156kW electric motor which draws the air from the inlet and ejects it from a T-shaped diffuser. The overall length of the wind tunnel from the inlet to the outlets is about 22m. The main characteristic dimension are sketched in Fig. 3.2.

Fig. 3.1 - The C.R.I.A.C.I.V. Atmospheric Boundary Layer Wind Tunnel. View from the inlet.

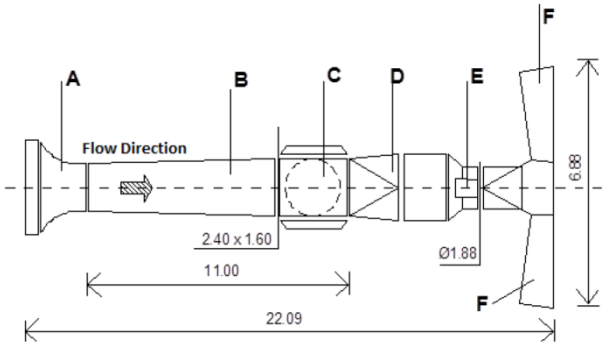

Fig. 3.2 - Geometry of the C.R.I.A.C.I.V. Atmospheric Boundary Layer Wind Tunnel. A) Inlet, B) Zone of development of boundary layer, C) Test Section, D) connection between the test section and the fan, E) motor, F) T-Shape diffuser.

The supporting structure of the wind tunnel is made of steel, closed on the floor and the ceiling with wooden panels, while laterally with glazed panels. In the wind tunnel there are two main working sections: the first, used when the atmospheric boundary layer is reproduced, is equipped with a turning table installed on the floor; the second, used for section models, is about 40cm upstream of the circular working section. The latter is the section employed in the present experimental campaign. Its peculiarity is the presence of an additional steel reinforcement all around the supporting structure in order to fix the section models directly to this, bypassing the deformable wooden floor. The air flow mean speed ranges from 0 to 30 m/s, through a double regulation system: the variation of the fan blades pitch angle and the variation of the fan rotating frequency (r.p.m.) controlled through an inverter.

3.1.2 Model set-up

The set-up was designed in order to measure forces and pressures (on the middle section) acting on the section models tested in a Reynolds number (and Womersley number) range as wide as possible, according to the working ranges of the instruments.

The first goal was to design a set-up where the screen can be fixed as close as possible to the bluff body. Due to the relation between the cross-flow dimension of the rectangular section and the cavity gap, it was necessary to design a bluff body as large as possible according to the blockage constraint. Another issue in the set-up design phase was that an excessively small gap width could influence the flow behind the screen because of the deformability of the screen or the roughness of the model. Moreover, the study of a section model requires the use of a model with high aspect ratio (Berger and Wille, 1972) in order to avoid three-dimensional effects. The solution was to place the section model vertically so to employ the wider side of the wind tunnel. The model obtained was 0.12m wide (which corresponds to 5% of blockage) and 1.24m long for both the square and the rectangular 2:3 sections (Fig. 3.3). The cross-flow section width (D) is the reference dimension to evaluate the Reynolds number, the force coefficients and the geometrical ratios as the gap distance.

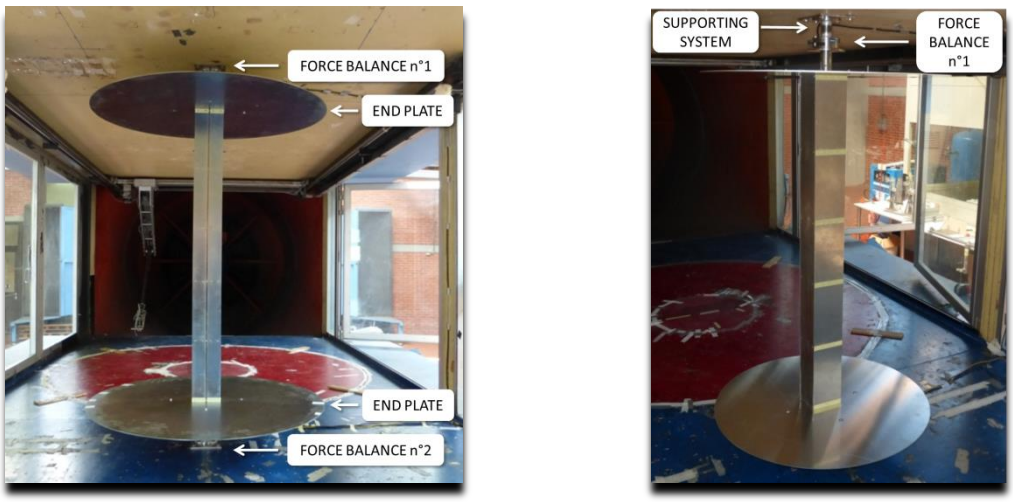

Fig. 3.3 - Views from the wind-tunnel inlet of the two models (2:3 rectangular section on the left, square section on the right) fixed vertically in the wind tunnel.

To test a section model of large dimensions with a high approaching flow speed leads to remarkable wind load. In order to measure forces in the working range of the instruments with such high loads, it has been necessary to share this load fixing two force balances at the model extremities. Moreover, in order to avoid the damage of one of these instruments during the set-up assembly (caused by unintentional loads higher than the full scale values), between the wind tunnel and the model extremities, two flexible couplings were employed, as reported in Fig. 3.4. The force balances were oriented in order to measure the drag force along the X-axis and the lift force along the Y-axis.

The model needed to be equipped with different screens at variable distances, and it was necessary to switch easily from the rectangular 2:3 cross-section to the square geometry. Therefore, it was designed with an internal structure made of aluminum ribs of 16mm thickness fixed to a stainless steel pipe (Fig. 3.5). The internal pipe has a 60.3mm diameter and 2mm thickness. It gives the model high stiffness and allows the passage of the cables from the section equipped with pressure taps to the interface unit for data acquisition. The aluminum ribs have different types of threaded holes on each side: on the front there are holes used to fix the frontal panel and holes to fix the screen across it; on both sides there are holes to fix the lateral panels; finally, on the rear part there are again two types of holes: the first type to fix the rear panel of the cylinder, the second to vary the body cross-section. Indeed, if the model section is switched from the rectangular 2:3 section to the square section, an additional rib is fixed on the rear part to the main one, as shown in Fig. 3.5.

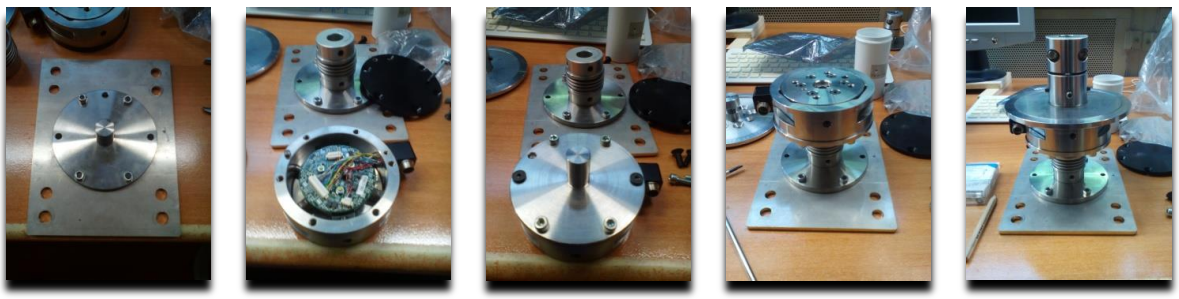

Fig. 3.4 - Assembly steps of the model supporting system on one side. The elastic device of coupling is fixed on the plate, while the force balance is equipped with a special adapter. Finally, a clamp, which can rotate, is connected to the balance.

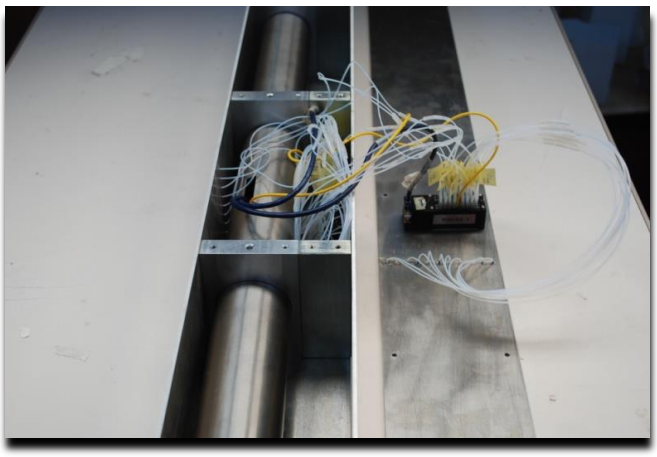

Fig. 3.5 - Picture of the model during the assembly. It is possible to see the internal structure with the pipe and the ribs. In this particular case, additional ribs are installed in order to obtain the square section.

Finally, the two ribs at the extremities were equipped with additional threaded holes in order to fix the end-plates and the model to the balances. Two different end-plates were used depending on the rectangular section studied. For the rectangular 2:3 section, they were two circular stainless steel end-plates of 1m diameter and 2mm thick, while for the square section they were two circular aluminum end-plates of 0.84m diameter and 3mm of thickness.
Both the end plates were designed based on the literature recommendations (*e.g.* Obasaju, 1979, *ESDU80024*, 1998).
Between the model and the balances opportune rotating systems were placed: they left the model free to rotate without rotating the force balances. These were employed to reach the desired angle of attack and fastened during the measurements.

The model was equipped with pressure taps in the middle section (Fig. 3.6). The taps were 1.5cm away from the corners and 1cm spaced apart. In order to have a good frequency resolution the pressure tubing system needs tubes of 50cm length from the tap to the pressure transducer. Previous studies conducted in the laboratory demonstrated that longer tubes tend to filter out the pressure signals down to values lower than those related to the expected significant phenomena (*e.g.* the vortex shedding). Therefore, the model was designed to have enough internal space to allocate the two scanners, which have dimension about 3.5cm × 3.5cm × 7cm.

The tested screens (schematized in Fig. 3.7) were designed in order be very thin compared to the cross-section reference dimension *D*, and less deformable as possible. Moreover, it was fundamental to control the distance between the screen and the body with high accuracy. Therefore, stainless steel foils of 1mm (*D*/120) were employed, fixed on the front face of the model at six levels. Metallic or plastic spacers were placed between the screen and the model (Fig. 3.8).
All the three tested screens were obtained from airtight stainless steel foils. Each screen's depth was equal to *D*, namely, 0.12m. Indeed the screen closed internally, named *screen S2* (Fig. 3.9-left), had the same structure as the one without vertical compartmentation (*screen S1*) with additional PVC components of 1cm width. The screen with the opening on the front, *i.e.* the *screen S3* (Fig. 3.9-right), was made of two stainless steel foils fixed at the spacers, in order to obtain an air intake in the front of 6mm (*D*/20) width.

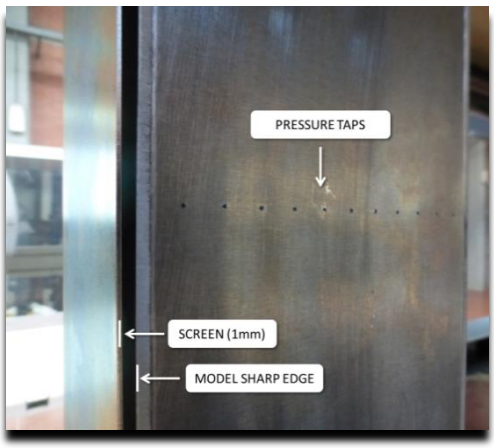

Fig. 3.6 - Detail of the pressure taps on the lateral face of the model. In this configuration the model is equipped with the screen S1. The screens are not equipped with pressure taps.

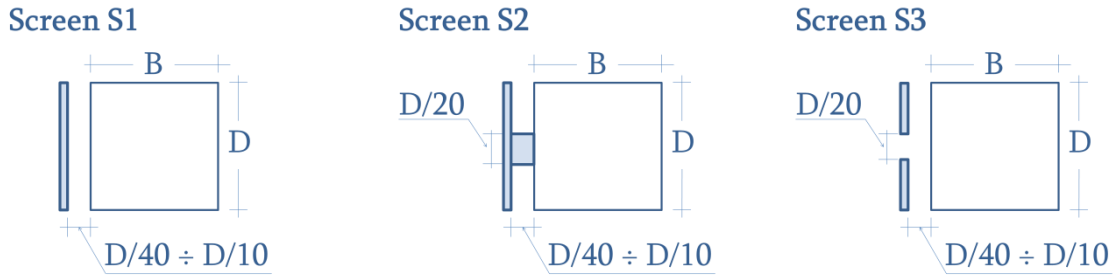

Fig. 3.7 - Schematization of the three screen typologies. Each screen has an airtight surface, it screens the whole face of the rectangular cylinder (depth = *D*) and it has a thickness of *D*/120.

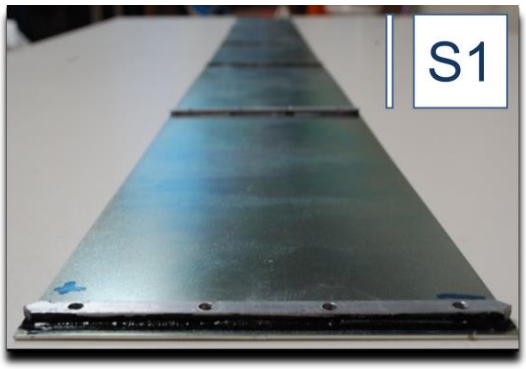

Fig. 3.8 - Picture of the internal layer of the screen S1. The stainless steel plate is equipped with six spacers. Their thickness corresponds to the minimum gap width tested (*D*/40).

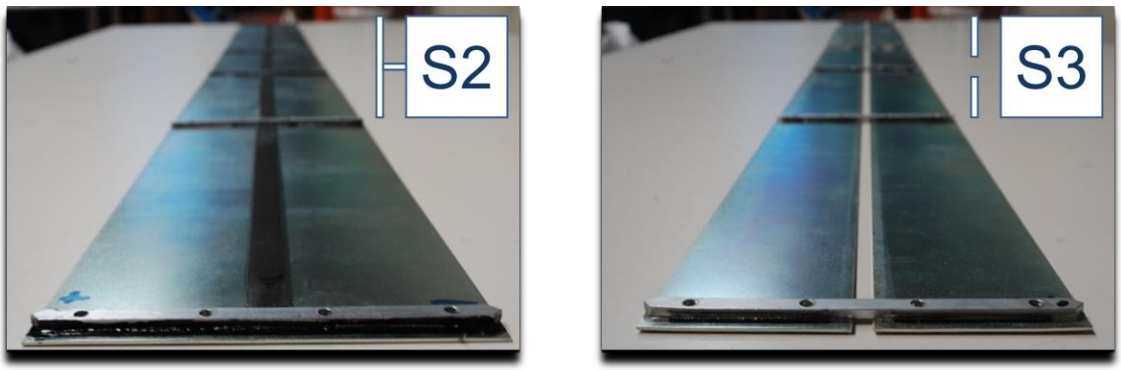

Fig. 3.9 - Pictures of screen S2 and screen S3 internal layers. The screen S2 (on the left) is obtained modifying the screen S1 with additional airtight elements that reproduce the vertical compartmentation. The screen S3 is made of two stainless steel plates fixed through the spacers to create an opening *D*/20 width.

3.1.3 Measuring instruments

Pressure system

The pressure measurement system adopted was the PSI-DTC Initium, in particular two 32-ports ESP pressure scanners were employed (Fig. 3.10). These scanners are miniature electronic differential pressure measurement units consisting of an array of silicon piezo-resistive pressure sensors, one for each pressure port. The sensors are mounted on a common hybrid glass substrate using a proprietary technique which maximizes long term stability. The output of the sensors are electronically multiplexed through a single onboard instrumentation amplifier at rates up to 70kHz using binary addressing. The multiplexed amplified analog output is capable of driving long lengths of cable to a remote A/D converter. The A/D converter is connected to a PC workstation with the DTC Initium software installed. The frequency sampling was 500Hz.

Fig. 3.10 - The DTC Initium Pressure System. The A/D converter and two scanners.

The pressure tubing system was tested and calibrated in order to have a flat transfer function up to 70÷80Hz, therefore all the pressure time histories are filtered at 70Hz through a digital low-pass Butterworth filter. The study of the transfer function and the system calibration was carried out with the help of two PhD students from Slovak University of Technology, Magat M. and Oleksakova I., during their internship. Each tube is made of three parts connected in series: the first one is a Teflon tube of 0.8mm internal diameter of 36cm length, which starts from the tap on the model; the second part is a 0.3mm internal diameter Teflon tube of 1cm length, which acts as a physical damper to avoid resonances in the pressure transferred to the transducer, and connects the first and the third parts of the tubing system; the third part is again a Teflon tube of 0.8mm internal diameter of 13cm length, which ends at the scanner (Fig. 3.11). The three parts are connected through airtight external silicon connections. The configuration adopted is the result of a wide series of tests with a subwoofer, in order to generate specific input signals, and in the wind tunnel with a turbulence generator.

The static accuracy of the pressure transducers is the most important to consider and it depends on the range of use, as summarized in the technical data sheet (Fig. 3.12). In the present work, the pressure measurements were affected by an error of ±2.5Pa.

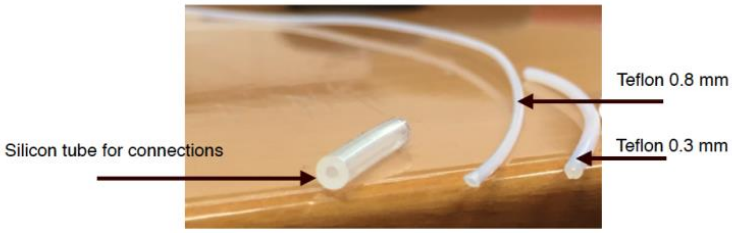

Fig. 3.11 - Typologies of tubes employed.

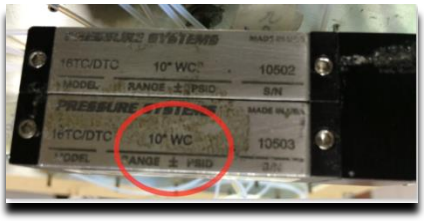

Static Accuracy @ 100% Range	± 0.05 ± 0.10	%FS %FS	After rezero (for ranges >= 5 psid (34kPa)) After rezero (for ranges < 5 psid (34kPa))
@ 33% Range	± 0.10 ± 0.20	%FS %FS	After rezero (for ranges >= 5 psid (34kPa)) After rezero (for ranges < 5 psid (34kPa))
Total Thermal Error @ 100% Range	± 0.002 ± 0.004	%FS/°C %FS/°C	Worst case (for ranges >= 5 psid (34kPa)) Worst case (for ranges < 5 psid (34kPa))
@ 33% Range	± 0.003 ± 0.005	%FS/°C %FS/°C	Worst case (for ranges >= 5 psid (34kPa)) Worst case (for ranges < 5 psid (34kPa))
A/D Resolution	18	bits	
Measurement Resolution	± 0.003	%FS	
Throughput Rate (in engineering units)	625 312	Hz/ch Hz/ch	Using 8 each 32 channel scanners Using 8 each 32 channel scanners

Fig. 3.12 - Range (left) of the DTC Initium pressure scanners, and its accuracy from the data sheet (right).

Force system

The force measuring system adopted consisted of a pair of ATI Industrial Automation FT-Delta SI-165-15 High Frequency Force Balance (HFFB) transducer (Fig. 3.13-left). Each six-components transducer converts force and torque into analog strain gage signals. Therefore, through opportune calibration matrix it is possible to obtain forces and moments with respect to the three axis (x, y and z). The transducers are connected to a power supply box (externally to the wind tunnel), which in turn are connected to the A/D interface. The interface is a multi-channel 24-bit unit by National Instruments, which is connected to a PC workstation and managed with a Labview data acquisition software. The sampling frequency was 2kHz. The accuracy of the force balances is expressed as percentage of the full scale measuring range and it varies depending on the component considered, as summarized in the technical data sheet in Fig. 3.13-right. In the present work, the forces measured along x- and the y- axis were affected by an error of ±0.099N.

Specifications	Values
Range of measurement, F_x, F_y	±165 N
Range of measurement, F_z	±495 N
Range of measurement, M_x, M_y, M_z	±15 Nm
Resolution, F_x, F_y	±1/128 N
Resolution, F_z	±1/64 N
Resolution, M_x, M_y, M_z	±1/2112 Nm
Repeatability	± 0.03 % FS
Full Scale Error, F_x, F_y	± 0.06 % FS
Full Scale Error, F_z	± 0.10 % FS
Full Scale Error, M_x, M_y, M_z	± 0.01 % FS
Resonance frequency	1.700 Hz
Operating temp. range	0 ÷ 70 °C

Fig. 3.13 - Picture of the high frequency force balance ATI FT-Delta SI-165-15 (left) and its accuracy from the data sheet.

Flow-velocity system

The instruments employed to measure the wind speed were the Pitot-Prandtl tube for the flow-velocity mean component and a hot-wire anemometer for the fluctuating component. During the flow characterization in the working section the two instruments were employed together in order to evaluate both the mean wind profile and the turbulence intensity. During the tests on the model, only the Pitot-Prandtl in a fixed position was used. The Prandtl tube allows measuring the mean kinetic pressure of the incoming flow and therefore indirectly the mean wind speed. It is connected to a differential membrane pressure transducer of Setra

Systems, which converts the pressure difference into an electric signal sent to the A/D interface. The hot-wire anemometer is able to measure accurately the wind velocity fluctuations: it works as a sensitive resistor connected to a Weathstone bridge, which varies its resistance depending on the temperature of the probe, and therefore on the wind speed. The system employed was a DANTEC 65C01 instrumented with one mono-component hot-wire probe. The electric signal was amplified and sent to the A/D interface.

3.1.4 Flow characteristics in the test section

The first part of the experimental tests is fundamental in order to know the characteristics of the approaching flow during the tests on the section models. A relatively small blockage ratio of the models (in the present work was around the 5% depending on the model rotation around the longitudinal axis) ensures that the approaching flow is not significantly influenced by the model itself. Therefore, the measurements carried out during the anemometry campaign along the model axis vertical line without the model are considered representative of the approaching flow during the tests.

Smooth and turbulent flow conditions were reproduced during the tests. The smooth flow was obtained without any additional device, so that it is the flow as smooth as possible that can be generated in the C.R.I.A.C.I.V. wind tunnel in that specific section. As shown in Fig. 3.14, the mean velocity and the turbulence index (<1%) of the approaching flow are constant at different velocity in the area confined by the end plates.

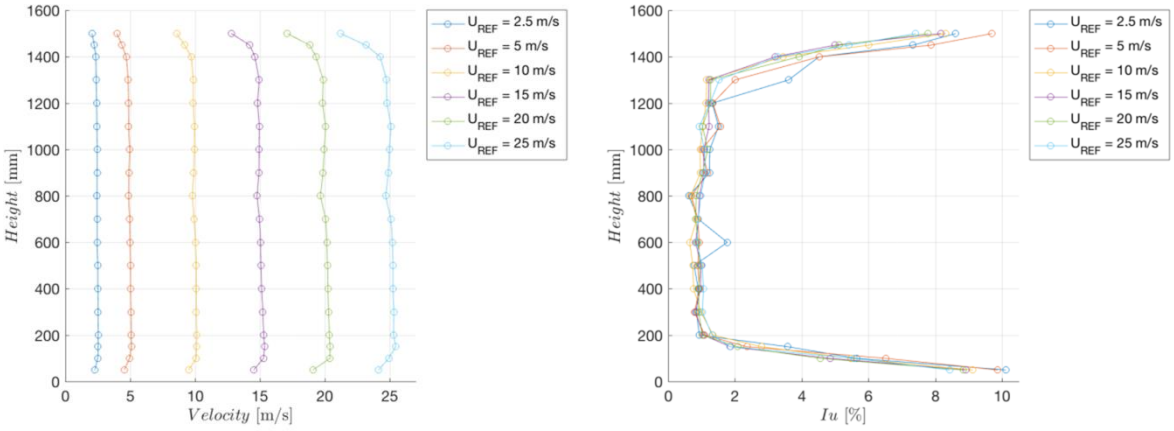

Fig. 3.14 - Mean wind speed (left) and turbulence intensity (right) in smooth flow. U_{ref} denotes the mean flow velocity measured at the central section (height = 800mm).

The turbulent flow was obtained with a wooden grid fixed in the wind tunnel close to the inlet. In this case, the grid characteristics and the distance between the grid and the working section were fixed to obtain a turbulent flow, characterized by a turbulence intensity $I_u \approx$ 13÷15% (depending on the flow velocity) and an integral length scale $Lx/D \approx 2$. As shown in Fig. 3.15, the mean wind profile and the turbulence intensity are not uniform along the vertical axis. This is mainly due to the fact that the turbulence generator was designed to carry out experiments on section models placed horizontally. For this reason, only the pressure measurements on the middle section are considered for the tests carried out in turbulent flow. It is worth noting that warning about this type of issues were given in the literature, for instance by Bearman and Morel (1983).

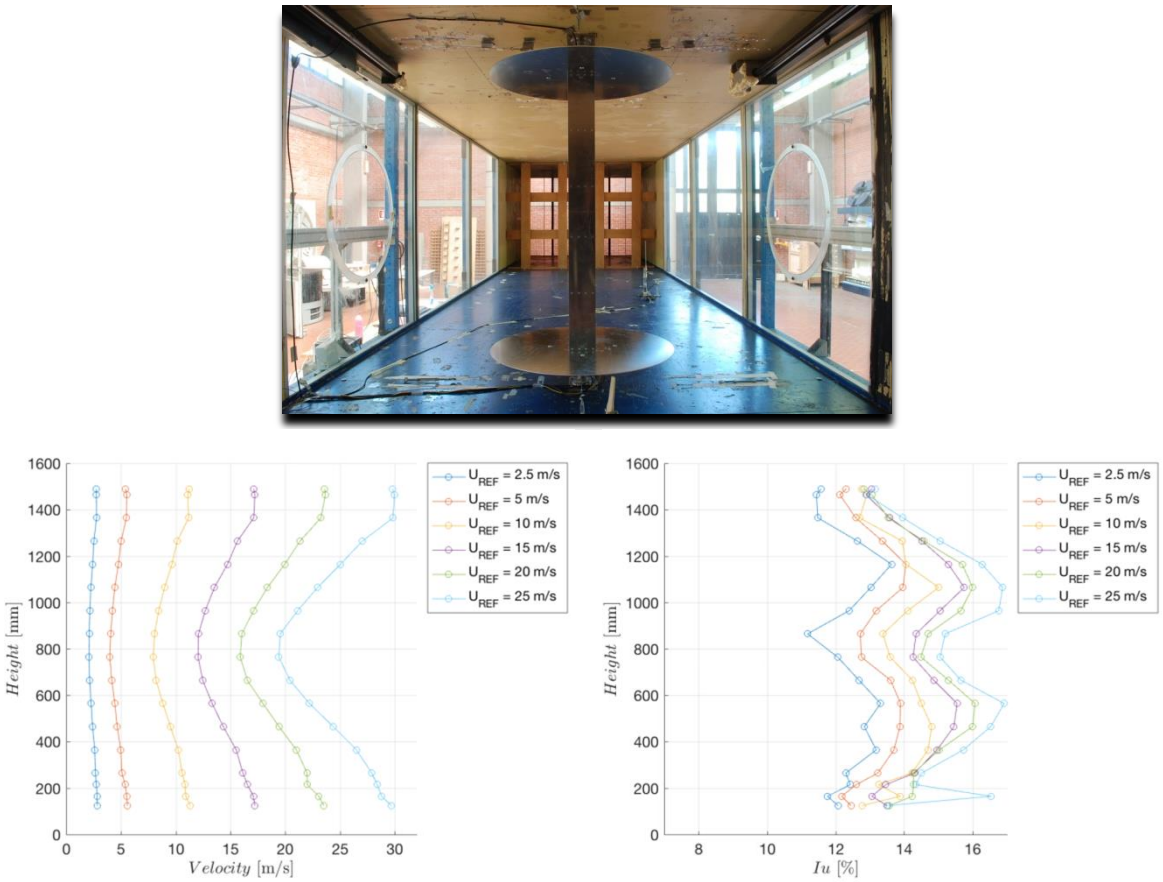

Fig. 3.15 - View from the fan of the square section model with the grid turbulence generator (top). Mean wind speed (bottom-left) and turbulence intensity (bottom-right) in turbulent flow.

3.2 Experimental campaign

3.2.1 Test configurations

Aerodynamic measurements of forces and pressures were performed on section models. The tests were conducted by varying the side ratio of the shielded rectangular cylinders. The effect of three screen typologies (S1, S2 and S3) on the system aerodynamics, was investigated attaching them at several distances. Moreover, wind directions and approaching flow conditions were varied. In Fig. 3.16 all the tested configurations are summarized. A code name was associated with each set of tests as follows:

- *Square – Smooth - S1 – 0°* refers to systems composed by the square section cylinder equipped with the screen S1 (laterally opened without internal vertical compartmentations) fixed at different distances in smooth flow. The tested distances were *D*/40 (3mm), *D*/30 (4mm), *D*/20 (6mm), *D*/13 (9mm) and *D*/10 (12mm). The tests were carried out at three different flow velocities corresponding to Reynolds numbers equal to 7.86×10^4, 1.01×10^5 and 2.26×10^5. The wind direction was normal to the face with the screen ($\alpha = 0°$).
- *Square – Smooth – S2 S3 – 0°* refers to systems composed by the square cross-section in smooth flow equipped with two different screens S2 and S3 at two distances: *D*/40 (3mm) and *D*/20 (6mm). Tests were carried out at three Reynolds numbers, namely $Re = 7.86\times10^4$, 1.01×10^5 and 2.26×10^5. The wind direction was $\alpha = 0°$.
- *Square – Turb - S1 - 0°* is a group of systems geometrically identical to the first set (same geometries and $\alpha = 0°$) but with a turbulent approaching flow. In this case the turbulence

generator grid reduced the Reynolds numbers to the values 7.29×10^4, 8.89×10^4 and 1.58×10^5.

- *2:3 – Smooth - S1 – 0°* refers to systems composed by the rectangular 2:3 cross-section equipped with the screen S1 (laterally opened without vertical compartmentations) fixed at different distances in smooth flow. The tested distances were *D*/40 (3mm) and *D*/20 (6mm). Tests were carried out at four Reynolds numbers, respectively equal to 1.41×10^5, 1.62×10^5, 1.82×10^5 and 2.03×10^5. The wind direction was perpendicular to the screen (α = 0°).
- *2:3 – Smooth – S2 S3 – 0°* refers to systems composed by the rectangular 2:3 section cylinder equipped with the screens S2 and S3 at the distance of *D*/40 (3mm). Tests were carried out at four different velocities corresponding to *Re* = 1.41×10^5, 1.62×10^5, 1.82×10^5 and 2.03×10^5. The wind direction was α = 0°.
- *Square – Smooth – S1 – AllAng* refers to systems composed by the square cross-section and the section with the screen S1 fixed at different distances in smooth flow for several wind direction. The tested distances were *D*/40 (3mm) and *D*/20 (6mm). Tests were carried out at three different Reynolds numbers equal to 7.86×10^4, 1.01×10^5 and 2.26×10^5.
- *Square – Turb – S1 – AllAng* is a group of systems geometrically identical to the previous one (same geometry) but with a turbulent approaching flow. Tests were carried out at *Re* = 7.29×10^4, 8.89×10^4 and 1.58×10^5.
- *2:3 – Smooth – S1 – AllAng* refers to a system composed by the rectangular 2:3 cross-section with and without the screen S1 (laterally opened without vertical compartmentations) fixed at *D*/20 (6mm) in smooth flow for various wind directions. Tests were carried out at *Re* = 1.41×10^5, 1.62×10^5, 1.82×10^5 and 2.03×10^5.

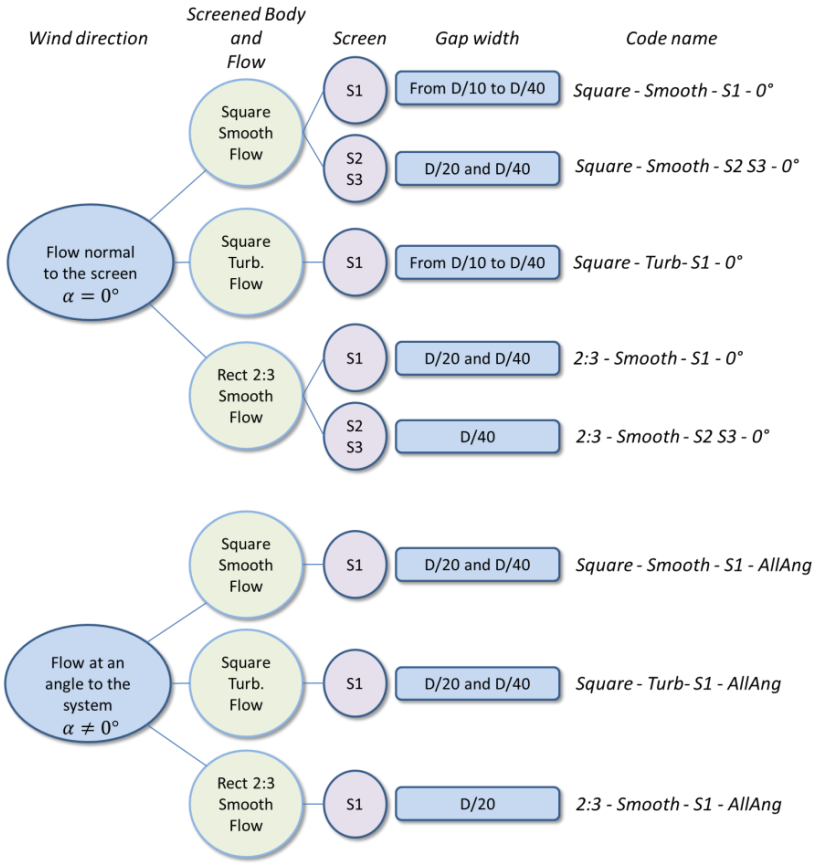

Fig. 3.16 - Scheme of the tested configurations. The results are presented following this scheme.

3.2.2 Limits of the set-up

The experimental tests gave reliable results according to the limits related to the study of a *model*, with *instruments* in a specific *set-up*. In the current section these limits are briefly analyzed for a better interpretation of the results.

First of all, the use of a wind tunnel implies a maximum wind speed limit. The CRIACIV wind tunnel has a ten-blade fun powered by a 156kW electrical motor which allows achieving a maximum wind speed of about 30m/s in smooth flow condition. This determines the maximum Reynolds number reachable during the tests. The range of velocity was also limited on the lower side, because of the accuracy of the instruments. The study of the behavior behind the screen S1 at very low Womersley numbers (reachable reducing the Reynolds number) was prevented by the fact that pressures of a low absolute value are more affected by the instrument tolerance (*i.e.* an unacceptable relative error occurs).

The force balances were connected to the model and the wind tunnel support structure through components that cannot ensure an orientation perfectly parallel to the flow. For this reason, the position of 0° wind direction (approaching flow perpendicular to the model face) was found through the analysis of the mean and standard deviation of the pressures on the sides of the models. In particular, for the case of the rectangular 2:3 cylinder it was necessary to correct the force values, while in the case of the square section the error was negligible (less than 1° of misalignment). This correction was done by the comparison between the forces measured with the balances and the integrated pressure resultants over the cross section.

The flexible constraints at the ends of the models were fundamental in the assembly phase. Nevertheless, at the same time a flexible localized element was introduced in the system, where the model is much stiffer than the constraints. Consequently, this system had a range of flow speeds where the lock-in phenomenon arose. This problem, combined with the vibration of the end-plates, affected the fluctuating components measured with the force balances. The choice of so wide end-plates was due to the bluff-body dimension, according to the literature.

The number of cases tested is another limit of the experimental campaign. In the current work the focus was on the square section equipped with the screen S1; therefore, all the other configurations tested were necessary for the sake of comparison with this reference case.

The model was equipped with pressure taps all around the middle section of the bluff body but it was not possible to mount pressure taps also on the screen. So that, for a null wind angle, it was necessary to assume that the pressure distribution was identical on both internal layers of the cavity gap (the one on the bluff body side is equipped with pressure taps), and that on the face directly hit by the wind, the pressure distribution was not affected by the type of screen or its distance to the model. This last assumption is supported by the results of Da Matha Sant'Anna *et al.* (1988), about the already discussed pressure distribution on the forebody of rectangular cylinders with different aspect ratios.

Finally, the absence of devices to carry out flow visualization, and the physical impossibility to measure the wind velocity behind the screens were other two limitations. In the present work, the complementary role of CFD simulations arises with the aim to overcome these limits.

3.3 Experimental results

The experimental results are reported to show and analyze the system aerodynamics. In order to give the results in a clear way, they are divided into three subsections, according to Fig. 3.16:

- *3.3.1 Models without the screen*. The results are given for the two models without the screen. The case of the square section with turbulent approaching flow is also discussed. This part gives information about the reliability of the results through the comparison with the literature, as well as about the quality of the models employed. It represents the starting point to measure the effect of the screens installed later.
- *3.3.2 Results for flow normal to the screen*. This section contains the main results in terms of global and local aerodynamic quantities for flow perpendicular to the screen. The lift coefficient slope centered in $\alpha = 0°$ is a parameter included in this section.
- *3.3.3 Results for flow at an angle of attack to the system*. The section deals with the results obtained for different angles of attack. The attention is focused on the range of angles in which the screen effects observed at $\alpha = 0°$ are still visible. Moreover, the case of screen fixed behind the bluff body ($\alpha = 180°$) is discussed.

To investigate possible effects of the screen, global and local aerodynamics quantities, related to systems in different configurations, are compared. In the following, these quantities are also indicated as global and local parameters of the system. In the current work, the global parameters employed are:

- the drag coefficient (C_D), evaluated on the overall system, measured with the force balances;
- the rearbody drag coefficient (C_{DRB}), evaluated through the integration of the pressures on the rear face of the model;
- the Strouhal number (St) of the overall system, evaluated through the pressures on the lateral sides, approximating the values obtained at different velocities with the least mean square fitting technique;
- the lift coefficient standard deviation (C_L'), evaluated through the integration of the pressures on the model;
- the difference between the drag coefficient on the overall system and the integration of the pressures all around the shielded body, resulting in the mean drag coefficient on the screen (C_{DS});
- the mean lift coefficient slope $dC_L/d\alpha$ centered around the 0° wind direction, estimated from the measurements with the force balances.

The force coefficients are normalized respect to the cross-flow dimension D, the model length L_m, and the mean flow velocity measured in the middle section of the wind tunnel U_∞. Therefore, the generic force (F) measured on the model is non-dimensionalized as follows:

$$C_F = \frac{F}{1/2 \rho U^2 D L_m} \qquad \textit{(eq. 3.1)}$$

The wind direction is varied following a counterclockwise rotation (as shown in Fig. 3.17) thanks to the supporting system that is able to rotate the model. It is worth noting that the current work, similarly to Cooper's paper (1988), focused only on the drag and lift forces.

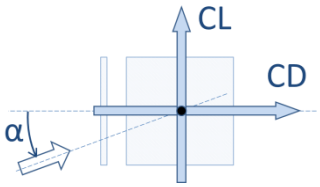

Fig. 3.17 - Scheme of the conventional signs adopted for positive angle of attack, drag and lift coefficients.

The local effects are compared through the pressures measured locally and normalized according to eq.2.1. In particular:

- the mean base pressure coefficient ($\overline{C_{bp}}$), where the term "base" refers to the middle point of the rear face of the bluff body;
- the standard deviation of the base pressure coefficient (C_{bp}');
- the mean pressure coefficient at the separation point ($\overline{C_{sep}}$), measured at the tap closest to the upstream edge of the model (1cm downstream the body edge);
- the standard deviation of the pressure coefficient at the separation point (C_{sep}');
- the mean pressure coefficient behind the screen ($\overline{C_{pScr}}$).

Moreover, the phase difference between signals measured at different locations and the pressure spectra are employed to comprehend the flow behavior.

Values obtained from the pressure taps are reported through body aligned coordinates or by following the numeration shown in Fig. 3.18.
It is worth noting that in the current chapter the measurements for the wind direction $\alpha = 0°$, referred to the first tap on the lateral side of the section models right behind the edge (taps n°11 and 23 for the square section, taps n°7 and 19 for the rectangular section), are called "separation point" even if the presence of a screen anticipates the flow separation point at the screen edge.

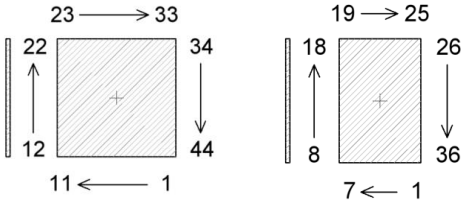

Fig. 3.18 - Pressure taps numeration around the square and the rectangular 2:3 cross-sections.

3.3.1 Models without the screen

To show the reliability of the results, the rectangular section models employed, without any screen, are compared with some previous studies. Results for both the square and the rectangular 2:3 sections, are reported considering only the case of wind normal to the building section. In this way, possible model imperfections and/or limits of the set up can be highlighted.
The effects caused by the presence of the screen are evaluated through the comparison of results obtained in systems with a screen versus the rectangular cross-sections treated in this section. For this reason, in the following of the thesis, the two-dimensional cross-sections reproducing the system without the screen are also named *baseline cases*.

Square cross-section in smooth and turbulent flow

The aerodynamic coefficients obtained for the square cross-section in smooth flow agree with the literature data, as shown in Tab. 3.1. Even if the lift coefficient fluctuations are slightly higher than the values reported from other works, the quality of the model is confirmed by the pressure distributions reported in Fig. 3.19-left. In particular, the characteristic base pressure distribution (described in section 2.2), related to the locus of vortex formation on the centerline, occurs.

Despite the uniformity problems mentioned above, the square cross-section in turbulent flow behaves as expected. While the global aerodynamic coefficients seem to be more in line with the literature data related to a lower turbulence (Tab. 3.2), the comparison based on the mean pressure coefficients distribution (Fig. 3.19-right) clarifies that such disagreement with Lee's results (1975) is probably caused by the effect of the distorted approaching velocity profile in turbulent flow rather than by a lower turbulence intensity. Indeed, the values of $\overline{C_p}$ in the separated regions seem to be shifted compared to the literature data from Lee, obtained for I_u = 12.5%. Such a discrepancy could be due to the velocity non-uniformity caused by the turbulence generator: since the mean velocity is higher in the lateral portions of the model (Fig. 3.15-bottom), it is supposed that the pressure in the wake tends to equalize, lowering the pressure on the lateral and rear side of the mid span equipped cross-section. Moreover, the blockage correction was performed in the literature reported, while it was not in the current work. To conclude, while these studies could give meaningful information about the turbulence effects on the system considered, further tests are necessary with a turbulence generator properly designed for this set-up.

Nevertheless, according to the literature recalled in section 2.2, the mean pressure coefficients on both side walls exhibit a different trend compared to the smooth flow case, because the free-stream turbulence interacts with the shear layers which are deflected by the downstream corners of the body. Therefore, the turbulence acts as a body stretching in the streamwise direction, with a consequent increase of both lateral spacing and base distance of the forming vortices. The mean pressure coefficients reported in Fig. 3.19-right exhibit a pressure recovery on the side walls and an almost uniform base pressure distribution.

The Strouhal frequency in turbulent flow results increased compared to the smooth flow case. This is in accordance with Lander *et al.* (2016) and Lee (1975) for a turbulence intensity of 6.5%, to Vickery (1966) with I_u = 10%, but not with the results obtained by Lee with I_u = 12% and L_x/D = 0.94.

On the other hand, the pressure coefficient standard deviations (C_p'), on the lateral sides of the body approached by a smooth flow, exhibit a bump (Fig. 3.20-left). The peak centered in the second half of the side (≈ ¾ *D*) moves forward (≈ ½ *D*) for an approaching turbulence of 12.5%, as noticed by Lee. However, the peak in smooth flow was higher than in turbulent condition. The opposite trend is observed on the front face, around the stagnation point, where the turbulence increases the fluctuations.

Generally, significant effects by varying the Reynolds number in the tested range were not observed. Since the measuring instruments perform better in the highest workability range, (*i.e.* the relative measurement errors are reduced), in the present work, experimental data are mainly reported for the highest tested *Re*.

	Current	Vickery (1966)	Lee (1975)	Bearman (1982)	Schewe (1984)	Lander *et al.* (2016)
C_D	2.34	-	2.05	2.29	2.15	2.35
C_{DRB}	1.53	≈1.3	≈1.3	≈1.6	-	≈1.6
St	0.125	≈0.118	≈0.122	≈0.129	0.121	≈0.114
C_L'	1.39	≈1.32	≈1.2	≈1.25	-	1.14
$dC_L/d\alpha$	-4.4	-	-	-	-4.35	-

Tab. 3.1 - Global parameters evaluated for the square cross-section at α = 0° in smooth flow. Results for Re = 2.26×10⁵ (data from literature are indicated as approximated when they are extrapolated from figures).

	Current – I_u = 13-15%	Vickery – I_u = 10%	Lee – I_u = 6.5%	Lee – I_u = 12.5%	Lander *et al.* – I_u = 6.5%
C_D	2.03	-	≈1.95	≈1.5	1.86
C_{DRB}	1.22	≈0.7	≈1.2	≈0.8	≈1.4
St	0.135	≈0.12	≈0.125	≈0.120	≈0.120
C_L'	0.89	≈0.67	≈0.95	≈0.6	1.10

Tab. 3.2 - Global parameters evaluated for the square cross-section at α = 0° in turbulent flow. Results for Re = 1.58×10⁵.

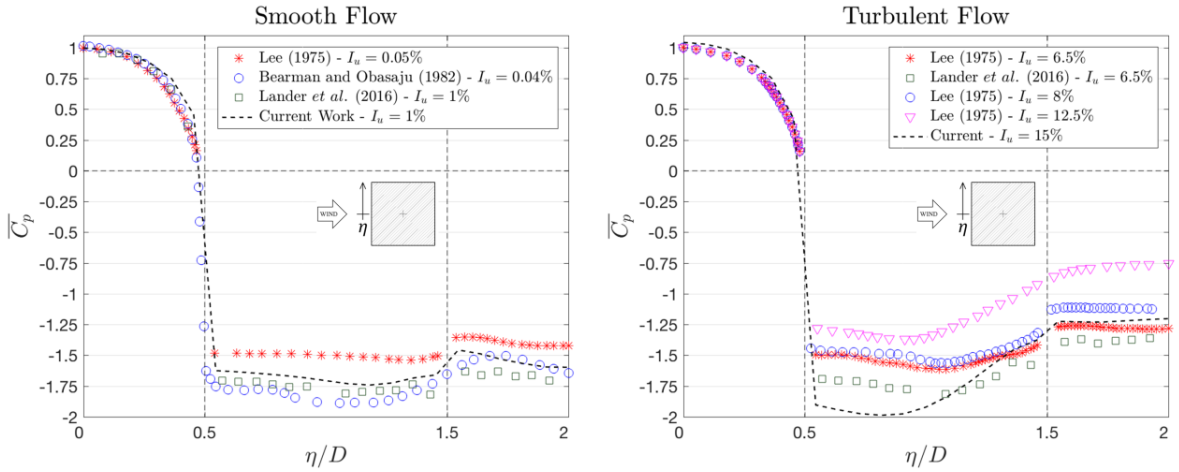

Fig. 3.19 - Mean pressure coefficients around the square cross-section. Comparison with some literature data. On the left, smooth approaching flow data from Lee (1975) with I_u = 0.05%, Bearman and Obasaju (1982) with I_u = 0.04%, Lander *et al.* (2016) with I_u = 1% and the current work with I_u < 1%. On the right, turbulent approaching flow data from Lee (1975) with I_u = 6.5-12.5%, Lander *et al.* (2016) with I_u = 6.5% and the current work with I_u = 15%.

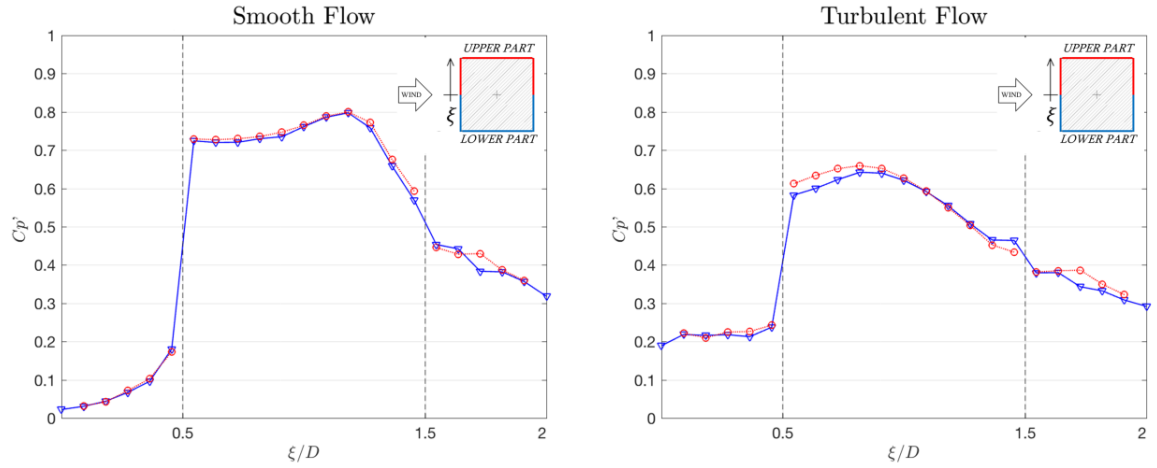

Fig. 3.20 - Square cross-section at α = 0° in smooth flow (left) and turbulent flow (right). Pressure coefficient standard deviations at the highest Reynolds numbers tested (Re = 2.26×10⁵ smooth flow, Re = 1.58×10⁵ turbulent flow). The values obtained on the upper (red-circle) and lower (blue-triangle) parts, in symmetrical locations are overlapped.

Rectangular 2:3 cross-section in smooth flow

The rectangular 2:3 cross-section was tested only in smooth flow, and it exhibits higher drag coefficient and lift fluctuations if compared to the square cross-section case (Tab. 3.3). The drag coefficients reported in Laneville and Yong (1983), corrected for blockage, range between 3 and 2.65 for side ratios respectively between 0.6 and 0.7, so that, the C_D = 2.91 results a value in accordance with the literature.

The $\overline{C_p}$ are in good agreement with the results in the literature, except in the rear corner area where both the lateral and the base pressures exhibit a different trend (Fig. 3.21). It is to note that the values employed in the comparison were corrected for the blockage, which was estimated by the Authors to be about 9.8%. However, the expected pressure distribution at the base occurs. The $\overline{C_{bp}}$ is equal to -2.29, therefore it lies between the corrected values reported by Da Matha Sant'Anna et al. (≈ -2.125) and Laneville and Yong (≈2.375) for rectangular cylinder with a side ratio equal to 0.6.

The distribution of C_p' around the rectangular 2:3 cylinder are reported in Fig. 3.22.

Finally, as noticed for the square cross-section, experimental data concerning the rectangular cylinder are given mainly for the highest tested Reynolds number, since no significant effects were observed by varying this parameter. Nevertheless, due to the possible presence of internal flows (in cavity created by the screen), Reynolds effects were investigated for each system with the screen.

	Current
C_D	2.91
C_{DRB}	2.01
St	0.127
C_L'	1.62
$dC_L/d\alpha$	-3.04

Tab. 3.3 - Global parameters evaluated for the rectangular 2:3 cross-section for α = 0°, in smooth flow, at Re = 2.03×10^5.

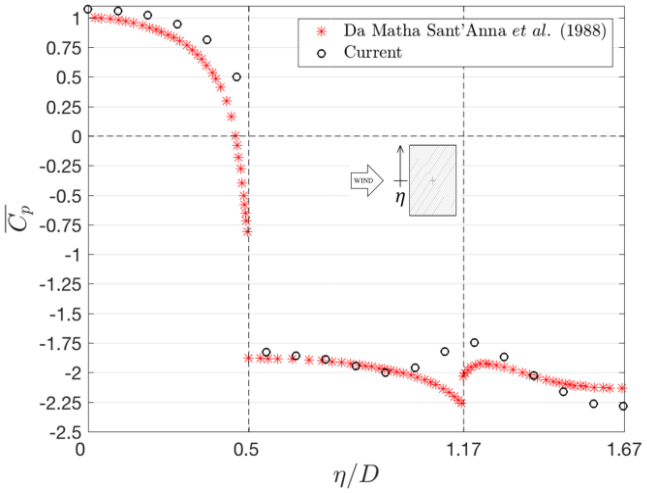

Fig. 3.21 - Mean pressure coefficients around the rectangular 2:3 cross-section for wind normal to the long side, at Re = 2.03×10^5. Comparison with Da Matha Sant'Anna *et al.* (1988) for a side ratio equal to 0.6.

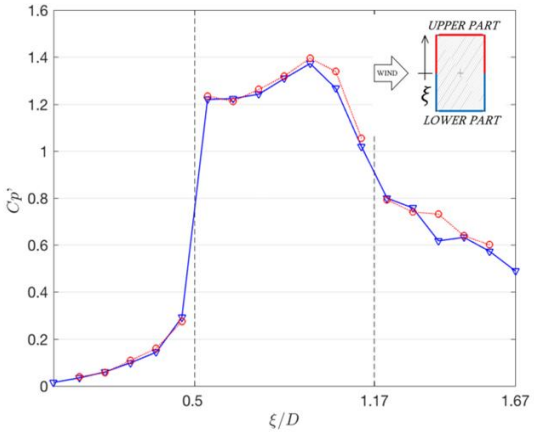

Fig. 3.22 - Pressure coefficient standard deviation around the rectangular 2:3 cylinder at $\alpha = 0°$, in smooth flow at $Re = 2.03\times10^5$. The values obtained in symmetrical locations respect to the axis parallel to U_∞ are overlapped: in red, the upper part, in blue the lower part.

3.3.2 Results for flow normal to the screen

Systems with the square cross-section in smooth flow

The global parameters reported in Tab. 3.4 (and Fig. 3.23) show that the presence of the screen slightly affects the overall behavior of the new system, when the smooth flow is perpendicular to the face equipped with the screen ($\alpha = 0°$). With the exception of the lift coefficient slope, the global aerodynamic quantities evaluated in the baseline case without the screen, exhibit variations at most equal to 10% when the screen is present. On the other hand, the pressure coefficient statistics, also in some selected points (Tab. 3.5 and Fig. 3.23), show the occurrence of an aerodynamic modification when the screen S1 is present, but the screen interaction results more evident in terms of mean ($\overline{C_p}$) and standard deviation (C_p') pressure coefficient distributions, as reported in Fig. 3.24 and Fig. 3.25.

Fig. 3.24 shows that on the lateral sides of the screened section, independently of the gap distance, a pressure reduction at the separation point occurs, while close to the downstream edges the pressure increases, compared to the baseline case without the screen. Despite the fact that this effect on the body sides appears similar to the recovery effect caused by a turbulent approaching flow, the mean pressure coefficients at the base are reduced (Fig. 3.23), with a distribution that indicates that the vortex formation is still on the centerline, so that two possibilities are considered: either the locus of vortex formation is closer to the base (toward the base) with an almost unchanged intensity, or it is moved downstream with an increased energy content. It may also be possible that both the mechanisms act simultaneously.

In general, the pressure distributions do not vary monotonically increasing with the gap width. Therefore, on the basis of the results reported in Fig. 3.24, it seems logical to distinguish two sub-groups of gap widths, which cause different types of aerodynamic effects: the first for the distances *D*/40 and *D*/30, the second for the distances from *D*/20 to *D*/10. Indeed, re-considering Tab. 3.4, the two sub-groups are marked off clearly by the C_L' (Fig. 3.25).

In Fig. 3.26 some results reported in Tab. 3.5 are highlighted, as the pressure coefficient standard deviation at the separation point and at the base, to show that the two-sub groups are distinguished also for all the Reynolds numbers tested.

When the screen S1 is present, also the pressure fluctuations exhibit a different distribution. In particular, a significant increase is observed on the upstream part of the body sides and at the base, close to the rear-side corners. Fig. 3.25 shows that the peak of C_p' results anticipated on the first half of the side. However, it is to note that in the second half, the two sub-groups distinction occurs again: the group related to the smallest gap widths (D/40 and D/30) exhibits higher fluctuations compared to the pressures measured in case without the screen, while for the other group, C_p' are lower than those obtained in the baseline configuration.

For a deeper view at the pressure fluctuations, maximum and minimum pressure coefficients are reported in Fig. 3.27. These values are evaluated for each time history as the mean of the ten percent of respectively the maximum and minimum peak values measured. If compared to the baseline case without screen, maximum peaks differ more in the portion of body side close to the cavity extremities, while the minima in the base region. In particular, the shape of the maximum values ($\hat{C}_p$) seems to be affected by the Reynolds number in proximity of the cavity extremities.

The variation of pressure fluctuations at the base observed in Fig. 3.25 is investigated also through power spectral density analyses. The comparisons between the pressure spectra at the separation point and in some locations at the base reported in Fig. 3.28 show that an increase of fluctuations occurs at the separation point when the screen is present. The energy content of the pressures close to the rear corner is centered around the Strouhal frequency (St). Moreover, the second sub-group of screen distances seems to reduce the process bandwidth.

The presence of the screen can also be appreciated through global parameters by slightly varying the wind angle of attack. For example, for the D/40 and D/20 cases, a lift coefficient slope (in the origin) of -3.2 and -0.6 respectively were obtained. These values are significantly reduced as compared to the square section in smooth flow ($dC_L/d\alpha$ = -4.4). Therefore, the screen fixed at a distance of $0.05D$ makes the section stable with respect to galloping instability (according to the Den Hartog criterion). It is to note that Cooper (1988) for a gap width equal to $0.09D$ obtained an unstable system.

GLOBAL PARAMETERS	No Screen	D/40	D/30	D/20	D/13	D/10
Drag coefficient C_D	2.34	2.33	2.38	2.34	2.35	2.38
Rear body drag coefficient C_{DRB}	1.53	1.58	1.62	1.53	1.56	1.60
Strouhal number St	0.125	0.120	0.122	0.121	0.119	0.120
Lift coefficient standard deviation C_L'	1.39	1.49	1.52	1.39	1.43	1.42
Drag coefficient on the screen C_{DS}	-	2.68	2.80	2.82	2.89	2.90
Lift coefficient slope in 0° $dC_L/d\alpha$	-4.4	-3.2	-	-0.6	-	-

Tab. 3.4 - Global parameters without and with the screen S1 fixed to the square section model, at different distances, in smooth flow. Results for $Re = 2.26\times10^5$.

LOCAL PARAMETERS	No Screen	*D*/40	*D*/30	*D*/20	*D*/13	*D*/10
Mean base pressure coefficient $\overline{C_{bp}}$	-1.60	-1.68	-1.71	-1.59	-1.64	-1.69
Standard deviation base pressure coefficient C_{bp}'	0.32	0.37	0.37	0.30	0.33	0.34
Separation point mean pressure coefficient $\overline{C_{sep}}$	-1.62	-1.68	-1.79	-1.80	-1.80	-1.59
Separation point standard deviation pressure coefficient C_{sep}'	0.72	0.72	0.72	0.66	0.68	0.68
Mean pressure coefficient behind the screen $\overline{C_{pScr}}$	-	-1.92	-2.03	-2.01	-2.09	-2.12

Tab. 3.5 - Local parameters for the system with screen S1 fixed to the square section model, at different distances, in smooth flow. Results for $Re = 2.26\times10^5$.

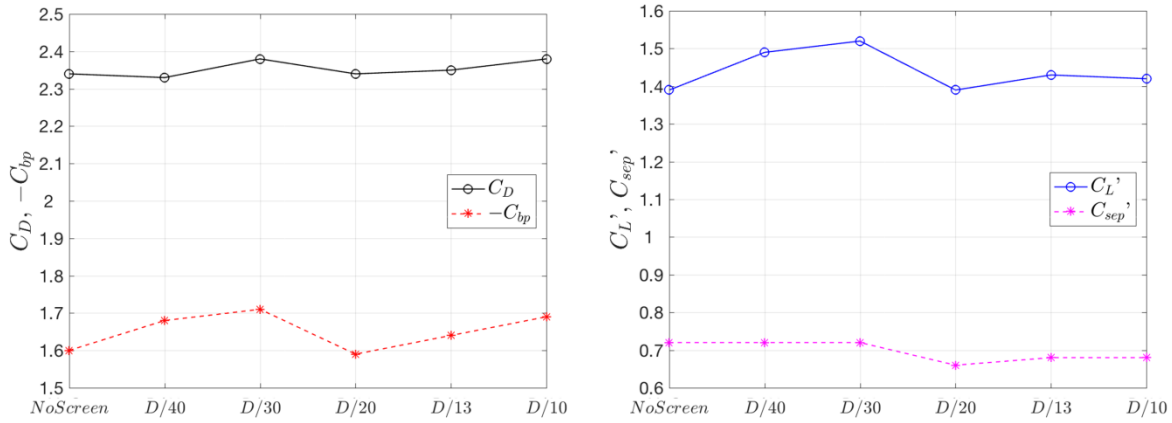

Fig. 3.23 - Main aerodynamic parameters for systems without and with the screen S1 at different distances ($Re = 2.26\times10^5$): on the left, drag coefficient and mean base pressure coefficient; on the right, standard deviations of the lift coefficient and pressure coefficient at the separation point.

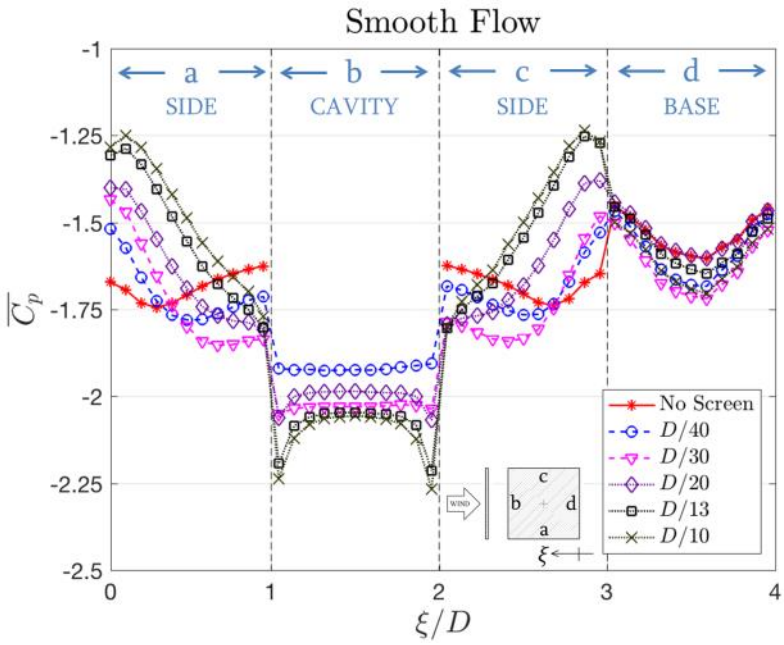

Fig. 3.24 - Mean pressure coefficients around the screened square cross-section in smooth flow, at $Re = 2.26\times10^5$, with wind normal to the screen ($\alpha = 0°$). The screen S1 is fixed at different distances between *D*/40 and *D*/10.

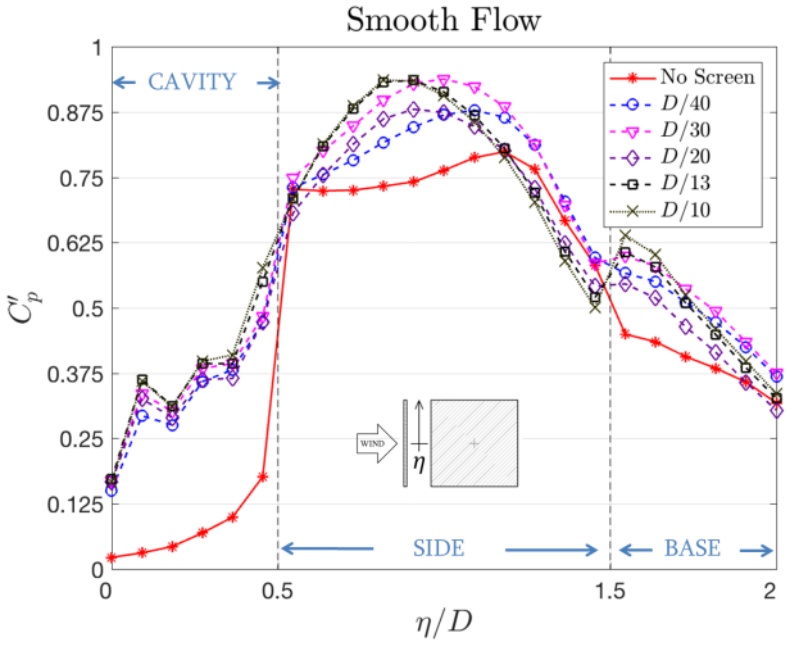

Fig. 3.25 - Pressure coefficient standard deviations around the screened square cross-section in smooth flow, at Re = 2.26×10^5, α = 0°, screen S1 gap widths from D/40 to D/10.

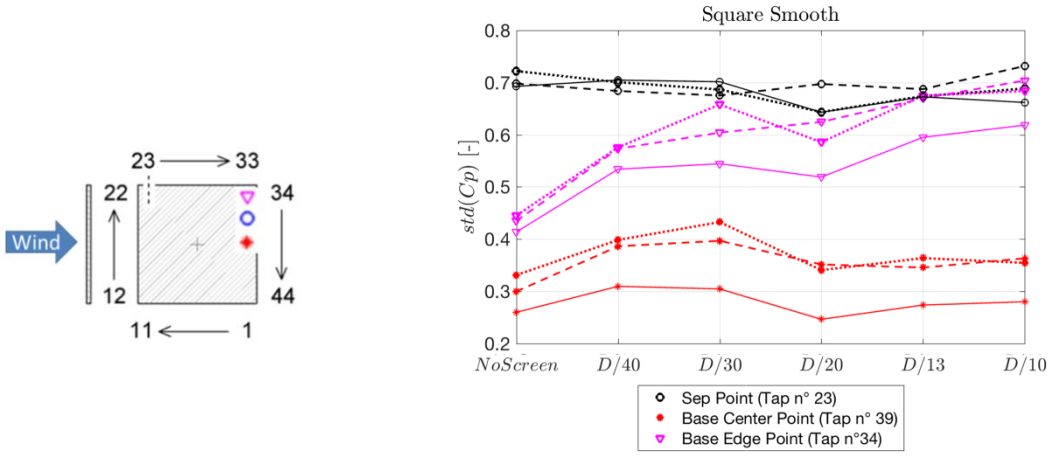

Fig. 3.26 - The screen effects on selected locations for different Reynolds numbers. On the left, the tap numeration and markers employed. On the right, C_p' at the separation point and other two base points for different gap width. Each line type represents the Reynolds number tested: continuous line (Re=2.26×10^5), dashed line (Re=1.01×10^5), dotted line (Re=7.86×10^4).

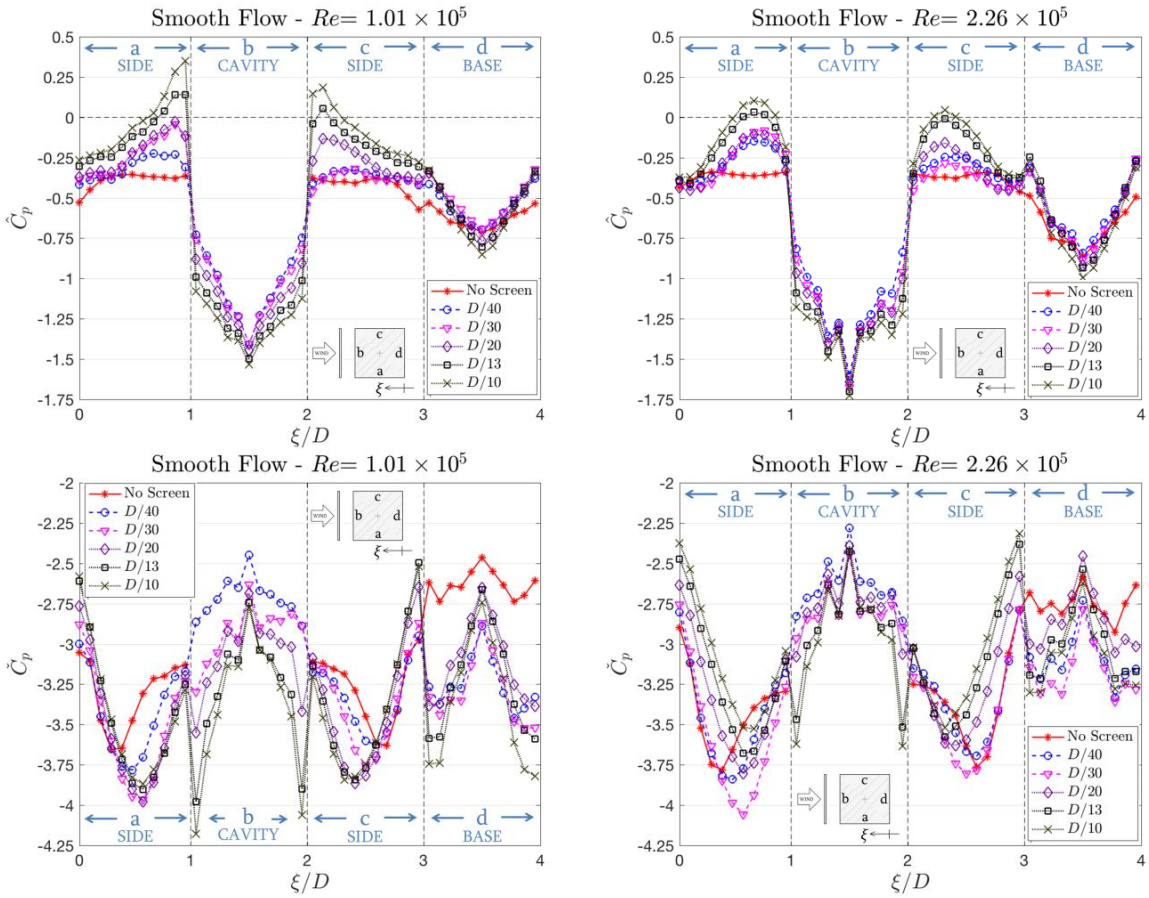

Fig. 3.27 - Maximum (top) and minimum (bottom) pressure coefficients around the square cross-section with the screen S1 at two different Reynolds numbers.

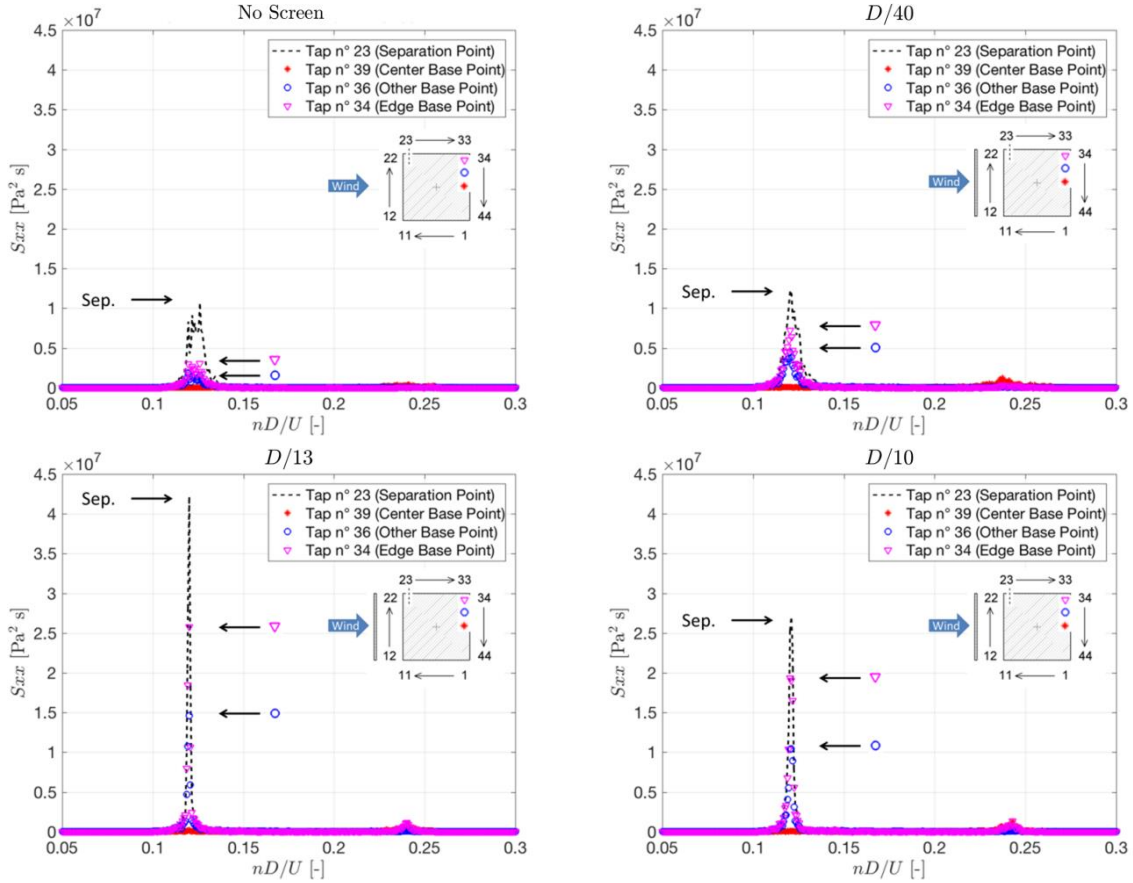

Fig. 3.28 - Pressure spectra at the separation point and in some locations along the base of the square section model in smooth flow. Re=2.26×10^5.

The presence of an open gap cavity, with the extremities close to the separation point of the bluff body system, involves an oscillating flow driven by an oscillating pressure gradient caused, in turn, by the vortex shedding. The oscillating flow occurrence is also confirmed through the CFD simulations reported in Chapter 4.
The non-dimensional frequency of vortex shedding is slightly lower when the screen is present (Tab. 3.4). However, St does not vary much by increasing the gap width. This implies that the use of eq. 2.20 to define the Womersely number (Wo) may be a representative dimensionless number to characterize the oscillating flow in the cavity, at least in the range of screen distances tested.

Behind the screen, the $\overline{C_p}$ distribution in the central portion of the cavity is almost constant, and local effects close to the extremities occur for the second sub-group of gap widths (Fig. 3.24). This is supposed to be caused by the model sharp edge, when the air is drawn in the cavity and, locally, a flow separation occurs. However, the CFD flow visualization discussed in the next chapter clarifies this peculiar effect.
The mean pressure coefficient ($\overline{C_{pScr}}$) in the cavity is always negative, and it ranges from -1.92 to -2.12. Assuming the pressure distribution on the external face of the screen to be similar to those measured on the body face without screen, and the pressures on the internal face similar to those measured on the corresponding locations of the screened body face, the estimated mean value of the screen drag coefficient (C_{DS}) ranges between 2.7 and 2.9.

Fig. 3.25 shows that the pressure fluctuations in the cavity reduce moving toward the center location. In particular, the internal pressure dominant frequencies are related to the vortex shedding, as confirmed by the power spectral density analysis reported in Fig. 3.29 for two tested geometries. Each figure shows two peaks, respectively at St and $2St$. Therefore, the driving pressure gradient at the extremities of the cavity is a periodic signal composed by two dominant frequencies, one twice the other. The phase difference between these components has been studied through FFT (Fast Fourier Transform) analyses, but it does not seem a deterministic quantity. On the other hand, the combination of such components with a random phase, in a narrow band process such as the vortex shedding in this system, may explain the non-null skewness that has been found in most of the cavity pressure signals. However, moving towards the middle of the cavity, the pressures exhibit a higher (tap 16), or at least equal (tap 14), energy content at the first superharmonic frequency. The two peaks seem slightly affected by the screen distance: only when the screen is fixed at D/13 and D/10 they result increased.
Generally, by increasing the Reynolds number, and therefore the Womersley number, the pressure oscillations seem to regularize. This behavior can also be recognized in the pressure spectra, where the difference between the energy content at the two dominant frequencies above discussed, and the other remaining frequencies, results increased.
The values of C_p' measured along half of the cavity, respectively one for each sub-group, are reported in Tab. 3.6 and Tab. 3.7. The values reported for different Re numbers, seem to be more affected by the position along the cavity than by the Re (and subsequently Wo) number variation. Referring to Fig. 2.12, this may indicate that the oscillating flow, in the investigated range of Wo numbers, lies in the same regime. The pressure measured at the central point (tap 17) seems to exhibit the highest variations.

N° Tap	$Re = 7.86\times10^4$ $Wo \approx 3$	$Re = 1.01\times10^5$ $Wo \approx 3.5$	$Re = 2.26\times10^5$ $Wo \approx 5$
17 (central)	0.24	0.22	0.15
16	0.30	0.30	0.29
14	0.38	0.37	0.36
12 (edge)	0.49	0.48	0.47
11 (model separation point)	0.70	0.70	0.72

Tab. 3.6 - System with the square cross-section and screen S1 at $D/40$ in smooth flow. Pressure coefficient standard deviations behind the screen and at the separation point.

N° Tap	$Re = 7.86\times10^4$ $Wo \approx 6$	$Re = 1.01\times10^5$ $Wo \approx 7$	$Re = 2.26\times10^5$ $Wo \approx 10$
17 (central)	0.29	0.27	0.17
16	0.35	0.36	0.32
14	0.39	0.40	0.36
12 (edge)	0.50	0.51	0.47
11 (model separation point)	0.66	0.69	0.66

Tab. 3.7 - System with square cross-section and screen S1 at $D/20$ in smooth flow. Pressure coefficient standard deviations behind the screen and at the separation point.

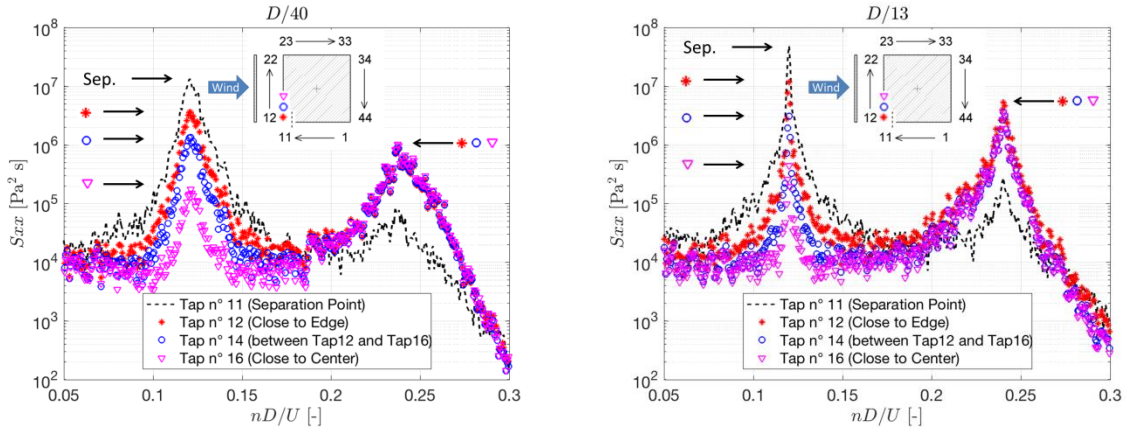

Fig. 3.29 - Pressure spectra behind the screen S1 and at the separation point. Systems with the square cross-section in smooth flow: gap width equal to $D/40$ (left), Re=2.26×10⁵ (Wo=5) and to $D/13$ (right), Re=2.26×10⁵ (Wo=16). It is to note that here the colors and markers indicate taps different than Fig. 3.26.

Tests with different screen configurations

The pressure distribution around the screened model results completely different if the cavity is internally closed (Fig. 3.30), or if the screen has an opening (Fig. 3.32). The global aerodynamic coefficients in these configurations, described in Fig. 3.7 and Fig. 3.9, are summarized in Tab. 3.8.

Screen S2

For a system which employs a screen with closed cavity (screen S2), both $\overline{C_p}$ and C_p' exhibit a trend similar to the baseline case without screen, and basically the flow sees the screen as an elongation of the model in the streamwise direction (given by the screen thickness plus the gap width). In particular, the mean pressure coefficients follow the distribution suggested by the literature, *i.e.* the side wall pressures and base pressures are increased (*e.g.* Laneville and Yong, 1983).

As shown in the left side of Fig. 3.30, the mean pressures behind the screen are similar to the mean pressure measured at the separation point. Moreover, while behind the screen S1 the fluctuations reduce moving toward the central location of the cavity, behind the screen S2 the C_p' are similar to the value measured at the separation point.

Power spectral density analyses reveal that the energy content of pressure fluctuations behind both the screens S1 and S2 is mainly concentrated around the Strouhal frequency (Fig. 3.31). However, the air-tight compartmentation employed in the screen S2 divides the cavity gap into two cavities, each one with an external opening placed behind the separation point. This geometry prevents internal flows and, at the same time, it exhibits pressure oscillations equally distributed all over each cavity. This pressure oscillates according to the pressure at the separation point both in terms of frequency and amplitude.

In this configuration, the use of external pressures around the baseline case without the screen (*i.e.* a model which does not reproduce the screen) to evaluate the internal ones, namely the external and internal pressures decoupling, seems to be allowed.

The oscillating flow features highlighted with the cavity internally closed must be kept in mind for future three-dimensional studies. In this perspective, the results obtained preventing the oscillating flow, suggest to consider possible Helmholtz resonances (*e.g.* Holmes, 1979) and the required volume distorted scales.

GLOBAL	No Screen	S1 – *D*/40	S2 – *D*/40	S3 – *D*/40	S1 – *D*/20	S2 – *D*/20	S3 – *D*/20
C_D	2.34	2.33	2.27	2.46	2.34	2.27	2.51
C_{DRB}	1.53	1.58	1.45	1.63	1.53	1.43	1.65
St	0.125	0.120	0.122	0.116	0.121	0.124	0.119
C_L'	1.39	1.49	1.34	1.45	1.39	1.26	1.38
C_{DS}	-	2.68	2.38	2.03	2.82	2.40	2.35

Tab. 3.8 - Global aerodynamic coefficients for the square section model, in smooth flow, with the screens S1, S2 and S3 at different distances. Results for Re=2.26×10^5.

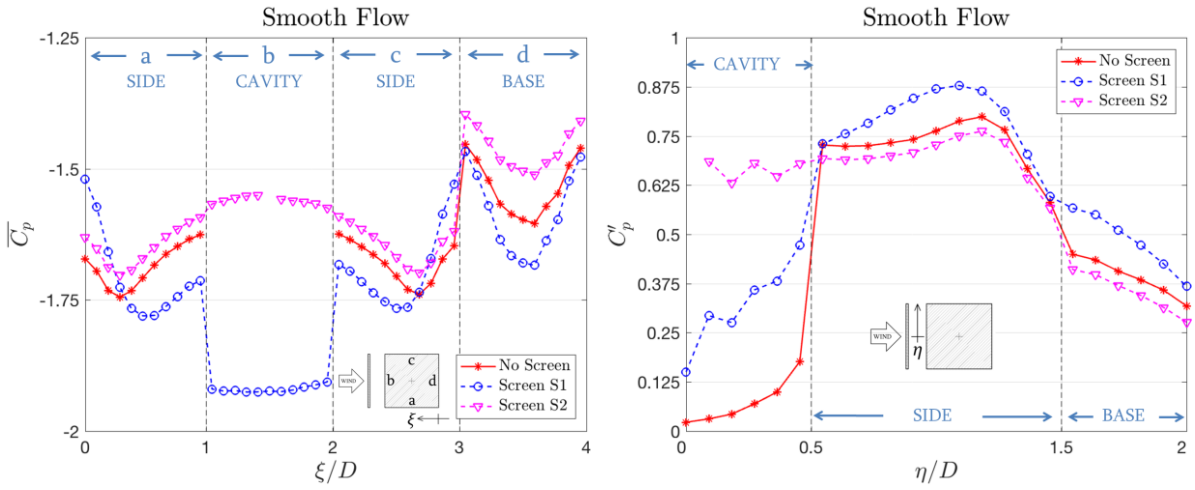

Fig. 3.30 - Mean (left) and standard deviation (right) of the pressure coefficients around the screened square section in smooth flow, at Re = 2.26×10^5, with wind perpendicular to the screen and the two screens (S1 and S2) fixed at the same gap width equal to *D*/40.

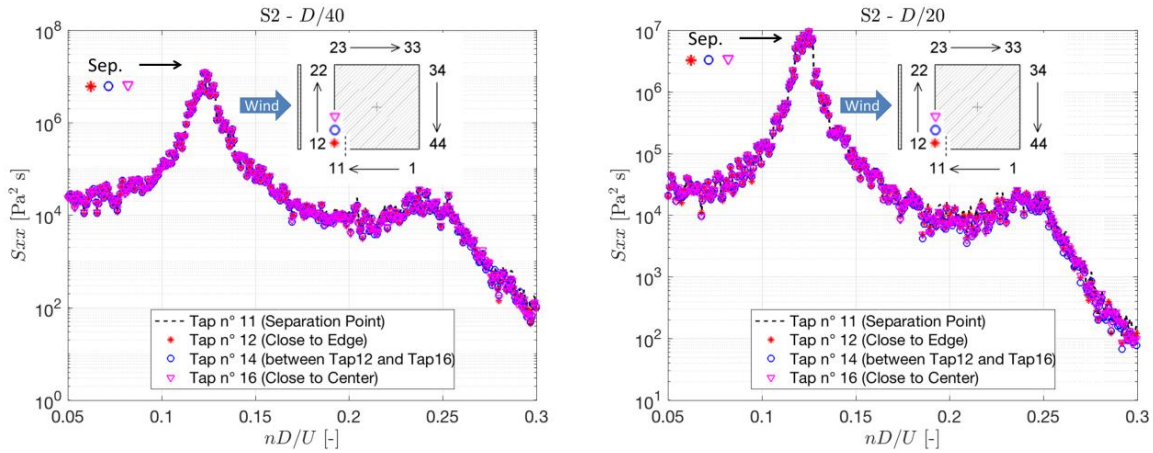

Fig. 3.31 - Square cross-section in smooth flow with screen S2 fixed at $D/40$ (left) and $D/20$ (right), at $Re = 7.86\times10^4$: spectra of the pressures behind the screen and at the separation point.

Screen S3

The behavior of the system with the screen S3 (the screen with a central opening on the front face) appears more complicated compared to the other two examined cases. The aerodynamic coefficients when such a screen is present, especially in terms of C_D and St, exhibit remarkable variations, as reported in Tab. 3.8.

The mean and standard deviations of the pressure coefficients describe a different system as compared to screen configurations analyzed up to now (Fig. 3.32). The pressures on the body sides are always higher than the reference case. In terms of C_p', with the exception of the last two taps at the leeward corner, the pressures fluctuate uniformly along the side length. At the base, a typical U-shaped mean pressure distribution indicates that the formation of vortices still occur in the centerline. Nevertheless, the standard deviation trend in this part is shifted compared to the baseline configuration, and the pressure is significantly lower.

Behind the screen S3, the pressures in the proximity of the extremities are higher than those measured with the screen S1 or S2, while in correspondence of the central opening, a stagnation point occurs. The pressure reduces moving toward the center, up to the two taps close to the opening. These exhibit a $\overline{C_p}$ lower than all the other taps, and a C_p' higher than at any other location around the body surface, even higher than at the separation point. This can be explained supposing that during the vortex shedding, on the side where the maximum instantaneous suction occurs, the air in the gap (behind the whole screen) is forced to move together with the air that is entering through the frontal opening toward this side. The strong mean suction measured in the two taps behind the middle one suggests that the flow close to these points "feels" a constriction that causes an increase in the local velocity (and therefore a reduction of the pressure). The constriction is supposed to be the composed by two effects, namely: a *vena-contracta* effect at the screen opening (as an orifice plate), and the effect caused by the air in stagnation on the central portion of the cylinder's face.
Generally, behind the screen S3 an oscillating flow occurs with different fluid-dynamic characteristics, as compared to the one observed with the screen S1.

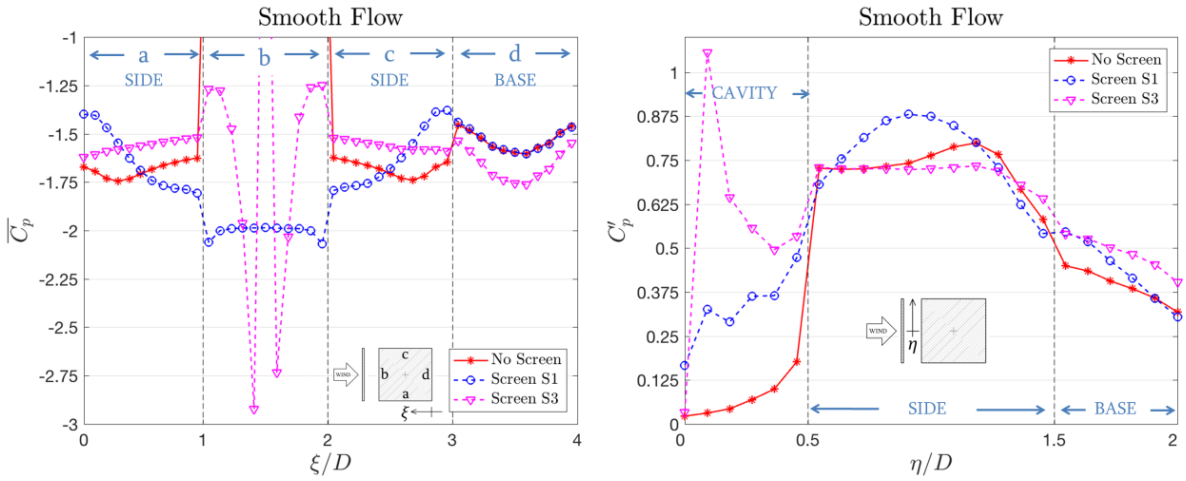

Fig. 3.32 - Mean (left) and standard deviation (right) of the pressure coefficients around the screened square section in smooth flow, at $Re = 2.26\times10^5$, with wind normal to the screen and the two screens (S1 and S3) fixed at the same gap width equal to $D/20$.

Systems with the square cross-section in turbulent flow

The presence of the screen S1 in turbulent flow at null angle of attack provides less variations of pressure and force coefficients compared to the smooth flow case, as shown in Tab. 3.9, Tab. 3.10 and Fig. 3.33. Both St and C_L' exhibit a different value if the screen is present, but the values remain almost unchanged for different gap widths until $D/10$, where a small variation of C_L' occurs. The C_{DRB}, evaluated through the pressures at the base, show that the variation of drag pressure at the rearbody is negligible. On the basis of the C_{DRB} trend and the previously discussed features of the forebody drag in rectangular cylinders, it seems reasonable to consider the C_D a global coefficient almost unaffected by the presence of the screen S1.

It is to note that in this case, all the global aerodynamic coefficients are evaluated through integration of the pressures. Due to the non-uniformity of the approaching flow, the forces measured with the force balances at the extremities of the whole model were not considered usable.

Generally, the pressures on the external faces of the body are less affected by the variations of the gap width as compared to the smooth flow case. The distributions of both $\overline{C_p}$ (Fig. 3.34) and C_p' (Fig. 3.35) of the pressure coefficients seem to vary monotonically with the screen distance, with the exception of some C_p' values obtained with the screen spaced of $D/10$.

The mean pressure coefficients close to the separation point are the most affected by the presence of the screen. In the first half of the side, the pressures are always lower than in the baseline case without the screen, while in the second part they are all higher than those.

The mean pressure distribution at the base is almost the same for all the tested configurations. It seems that the shear layers in turbulent flow are enough stable to result almost unaffected by the presence of the screen. Therefore, the shear layer/trailing-edge interaction remains basically unchanged and the locus of vortex formation is more distant from the base as compared to the smooth flow case.

On the other hand, the pressure coefficient fluctuations are affected by the presence of the screen. Along the lateral sides, the peak results slightly shifted downstream, as it occurs with a lower index of turbulence (Lee, 1975). However, the C_p' laterally (except than close to the front corner) and at the base, result increased if compared to the baseline case without screen. The power spectral density analysis confirms an increase of energy content on the portion of base close to the edge (compared to the smooth flow case), while C_{sep}' remains almost unchanged (Fig. 3.36).

GLOBAL PARAMETERS	No Screen	*D*/40	*D*/30	*D*/20	*D*/13	*D*/10
C_D	2.03	-	-	-	-	-
C_{DRB}	1.22	1.24	1.23	1.23	1.23	1.20
St	0.135	0.130	0.131	0.128	0.132	0.131
C_L'	0.89	0.96	0.96	0.96	0.96	0.92
C_{DS}	-	(2.86)	(2.89)	(2.95)	(2.99)	(2.98)
$\partial C_L/\partial\alpha$ [rad]	-5.5	-	-	-	-	-

Tab. 3.9 - Global parameters of square cross-section without and with the screen S1 at different distances, in turbulent flow. Results for $Re = 1.58\times10^5$.

LOCAL PARAMETERS	No Screen	*D*/40	*D*/30	*D*/20	*D*/13	*D*/10
$\overline{C_{bp}}$	-1.20	-1.23	-1.22	-1.22	-1.20	-1.18
C_{bp}'	0.29	0.34	0.33	0.34	0.34	0.35
$\overline{C_{sep}}$	-1.87	-1.99	-2.02	-2.08	-2.11	-2.11
C_{sep}'	0.58	0.58	0.56	0.55	0.54	0.52
$\overline{C_{pScr}}$	-	-2.06	-2.09	-2.15	-2.19	-2.18

Tab. 3.10 - Local parameters of square cross-section without and with the screen S1 at different distances, in turbulent flow. Results for $Re = 1.58\times10^5$.

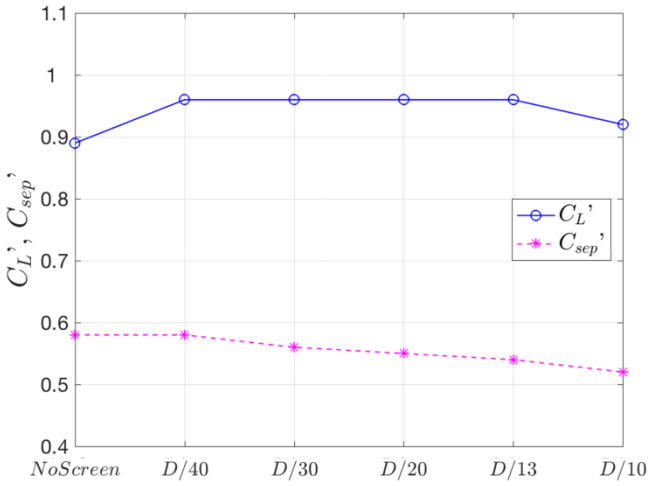

Fig. 3.33 - Standard deviations of the lift coefficient and pressure coefficient at the separation point, for systems without and with the screen S1 at different distances, in turbulent flow with a $Re = 1.58\times10^5$.

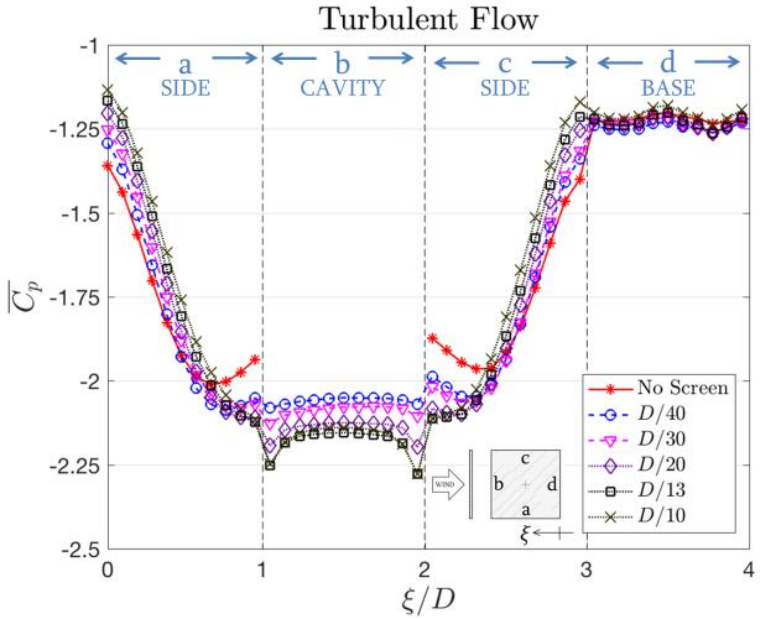

Fig. 3.34 - $\overline{C_p}$ distributions around the square cross-section equipped with the screen S1 at different distances in turbulent flow for $\alpha = 0°$ at $Re = 1.58\times10^5$.

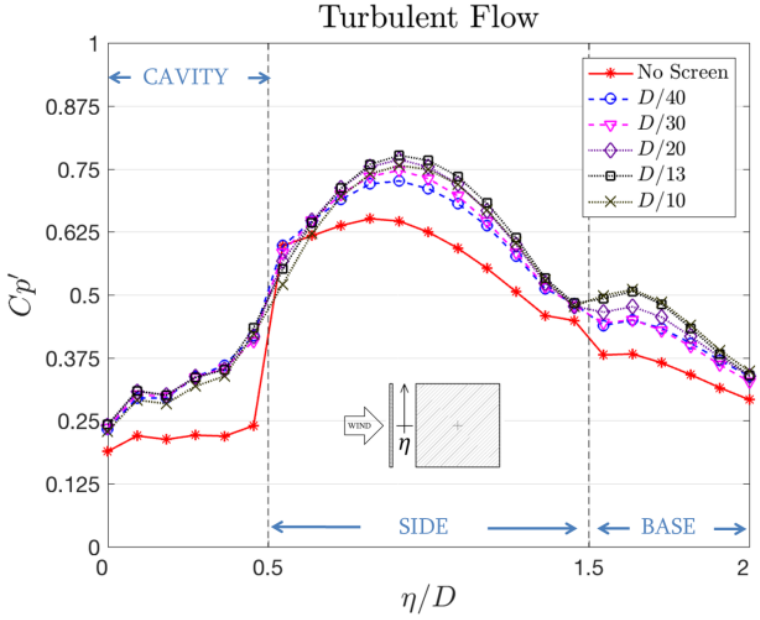

Fig. 3.35 - C_p' distributions around the square cross-section with the screen S1, gap width between $D/40$ and $D/10$, turbulent flow, $\alpha = 0°$ and $Re = 1.58\times10^5$.

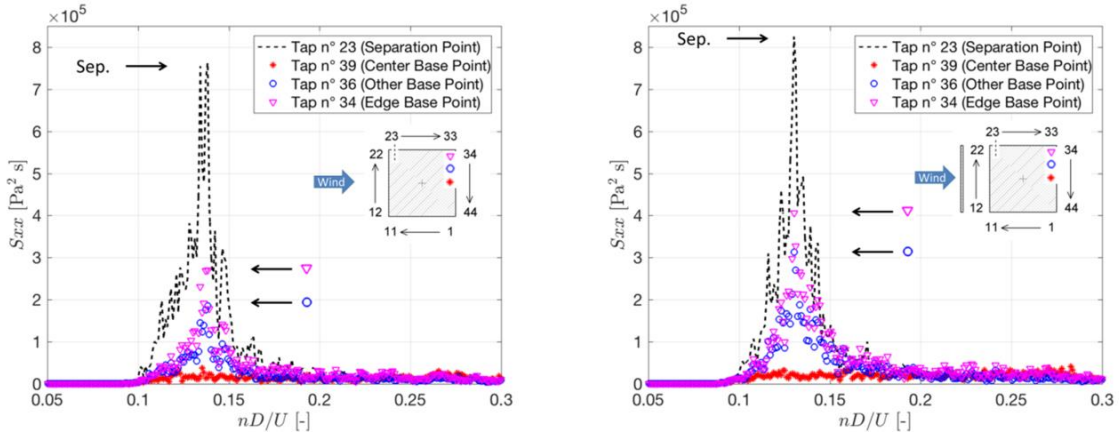

Fig. 3.36 - Pressure spectra at the separation point and the base of the square section model in turbulent flow at $Re = 1.58\times10^5$: case without the screen (left) and with the screen fixed at $D/20$ (right).

Behind the screen, the $\overline{C_p}$ distribution is similar to the one observed in the smooth flow case. The mean pressure coefficient is always negative (values in the range -2.06 to -2.18), and local effects close to the cavity extremities occur for screen distances higher or equal to *D*/20.

In terms of C_p', Fig. 3.35 shows lower values in the cavity as compared to the smooth flow case. However, due to the presence of the screen, these fluctuations are still driven by the vortex shedding process. The time histories and the pressure spectra (filtered around the Strouhal frequency) reported in Fig. 3.37 show that an oscillating flow occurs, although influenced by a widened range of frequencies, as compared the smooth flow case. The time interval reported on the left side of Fig. 3.37 is representative of a signal less regular in amplitude and phase due to a modulation effect. Therefore, in many cases the time signals of symmetric pressure taps alternate an almost perfect phase opposition with a nearly in-phase behavior. The data reported in Fig. 3.37 were filtered around St to clearly show the modulation effect. However, as compared to the smooth flow case, the present case does not exhibits evident peak at $2\,St$.

In Fig. 3.38, the phase lags measured between the pressure taps behind the screen and the first tap on the lateral side close to the separation point are reported. In both cases, respectively with a smooth and a turbulent flow, the phase lag only depends on the gap width. The turbulent case exhibits a phase variation lower than the smooth one, although a dependency on the gap width still remains. It is supposed that, while the "driving force" of oscillations remains almost of the same intensity, the higher volume of fluid to move by increasing the gap width tends to increase the phase lag in turn.

Tests carried out at different Reynolds numbers show that the phase lag is not affected by this parameter in the investigated range. A similar *Re*-independent trend was already observed and discussed referring to C_p' into the cavity with an approaching smooth flow (Tab. 3.6 and Tab. 3.7).

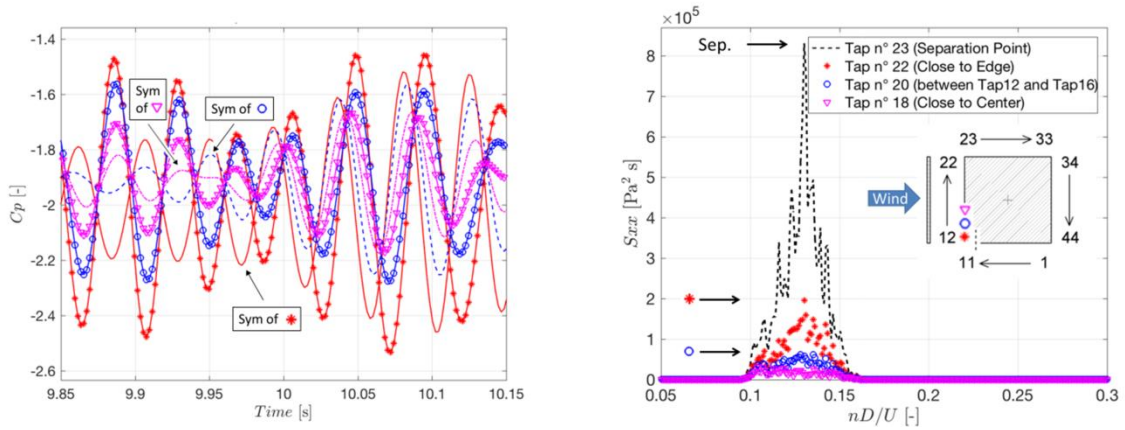

Fig. 3.37 - Pressure time histories (left) and spectra (right) behind the screen S1 at *D*/20. System with the square cross-section, turbulent flow, $Re = 1.58\times10^5$.

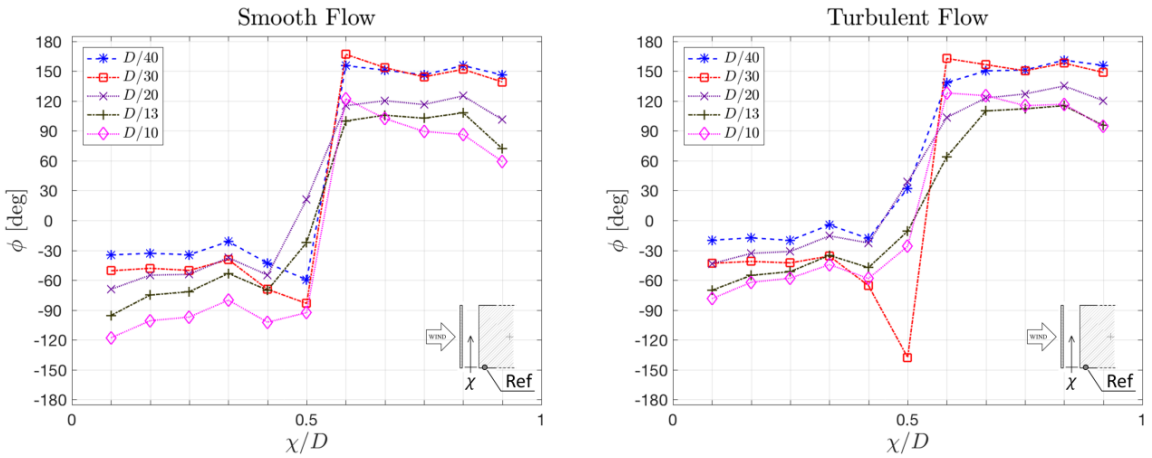

Fig. 3.38 - Phase difference between the pressure measured on the side wall close to the separation point and the pressures measured along the cavity, for a null wind angle of attack, at the highest Reynolds numbers (smooth Re=2.26×10^5, turbulent Re=1.58×10^5). Comparison between smooth (left) and turbulent (right) approaching flow in systems with the square cross-section.

Systems with the rectangular 2:3 cross-section in smooth flow

The system with rectangular 2:3 cross-section, in smooth flow, at null angle of attack, is influenced by the presence of the screen S1, as pointed out by the global (Tab. 3.11) and local (Tab. 3.12) parameters, summarized in Fig. 3.39. Therefore, the system globally seems more influenced than the square cross-section case with the same flow condition and, as discussed in the following, the $\overline{C_p}$ distributions exhibit some differences (Fig. 3.40).

The drag coefficient, along with the mean pressure distribution on the rear side, increases with the gap width (up to 7.5% of growth). This parameter (more affected than in the square section case) indicates that the presence of the screen S1 strengthens the underpressure in the body wake and/or it shifts the forming vortex core closer to the body.

In the current set of measurements only two gap widths were tested, so that it is less clear the presence of discontinuities in the pattern of global and local parameters respect to the gap width.

One of the main differences between the screen S1 effects on the square and the rectangular 2:3 cross-sections lies in the $\overline{C_p}$ distribution on the lateral sides (Fig. 3.40-left). In the current case, the presence of the screen fixed at D/20 increases the pressure on the body sides, which results always higher than those measured without screen. With the attempt to find a common pattern to the square cross-section case, the gap width can be expressed respect to the side length B, so that the screen distance of 0.05D results equal to 0.075B. Nevertheless, the $\overline{C_p}$ distribution has still not a trend like that obtained for square cross-section with the screen S1 at D/13 (=B/13≈0.076B). Moreover, when the screen S1 is present, in the base region the pressures are reduced almost uniformly, while in the square section case the central portion of the base was the most affected. This may be explained recalling the basic flow features of a rectangular cylinder with such a small side ratio (see Section 2.2). The shear layers of the rectangular 2:3 cross-section without screen are not influenced by the trailing edges, and the base pressure indicates that they are still unaffected when the screen S1 is attached on the body face. Therefore it is shown that, locally, the aerodynamic effects produced by the screen depend also on the shielded cross-section side ratio employed in the system.

On the other hand, the C_p' distributions reported in Fig. 3.40 show on the lateral side a modified trend respect to the case without screen, according to the square cross-section case of Fig. 3.24. Also on the base, the pressure fluctuations are influenced with the same patterns observed for the square cross-section in smooth flow. The comparison of power spectral densities reported in Fig. 3.41 confirms the occurrence of a mechanism of interaction similar to the one encountered with the square cylinder in this region.

The case of the screen S1 fixed at *D*/20 was also tested varying the angle of attack. In this case, the lift coefficient slope in the origin is equal to -1.24. The $dC_L/d\alpha$ evaluated on the baseline case without screen results less than halved when the screen is present, so that, the system becomes stable with respect to the galloping instability.

GLOBAL PARAMETERS	No Screen	*D*/40	*D*/20
C_D	2.91	3.00	3.13
C_{DRB}	2.01	2.14	2.22
St	0.127	0.127	0.128
C_L'	1.62	1.72	1.55
C_{DS}	-	3.33	3.45
$dC_L/d\alpha$	-3.04	-	-1.24

Tab. 3.11 - Global parameters for the system with rectangular 2:3 cross-section in smooth flow without and with the screen S1 at different distances. Results for Re=2.02×10^5.

LOCAL PARAMETERS	No Screen	*D*/40	*D*/20
$\overline{C_{bp}}$	-2.29	-2.40	-2.45
C_{bp}'	0.55	0.54	0.50
$\overline{C_{sep}}$	-1.83	-1.95	-1.74
C_{sep}'	1.22	1.28	1.15
$\overline{C_{pScr}}$	-	-2.47	-2.54

Tab. 3.12 - Local parameters for the system with the rectangular 2:3 cross-section without and with the screen S1 at different distances in smooth flow. Results for Re=2.02×10^5.

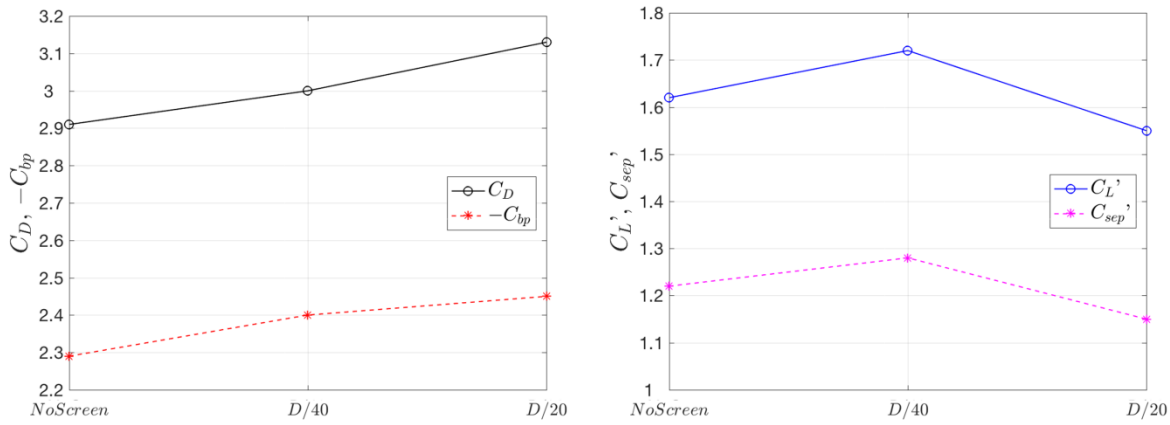

Fig. 3.39 - Main aerodynamic parameters for systems with the rectangular 2:3 cross-section without and with the screen S1 at different distances (smooth flow, Re = 2.02×10^5): on the left, drag coefficient and mean base pressure coefficient; on the right, standard deviations of the lift coefficient and pressure coefficient at the separation point.

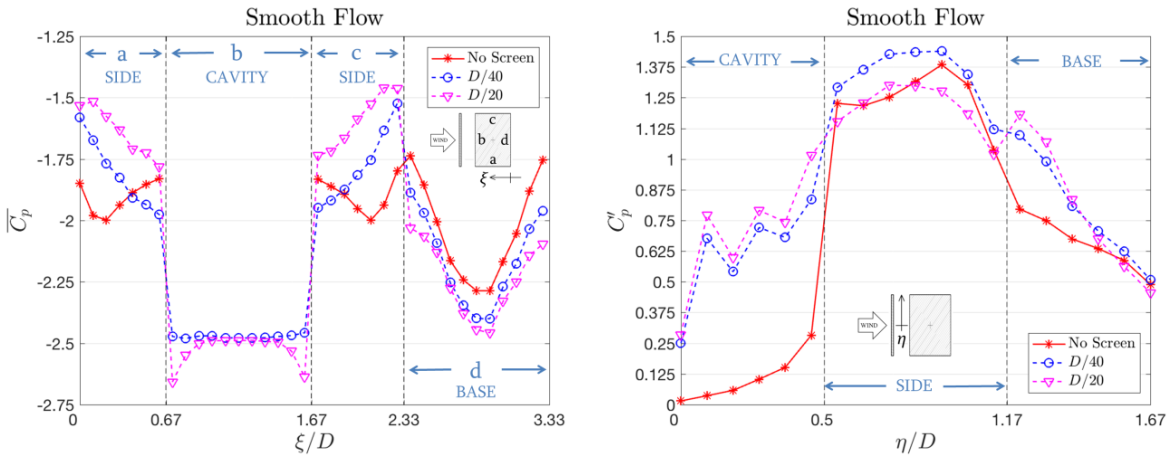

Fig. 3.40 - $\overline{C_p}$ (left) and C_p' (right) distributions around systems with rectangular 2:3 cross-section and screen S1 fixed at different distances at $Re = 2.02\times10^5$, in smooth flow, at null wind angle of attack.

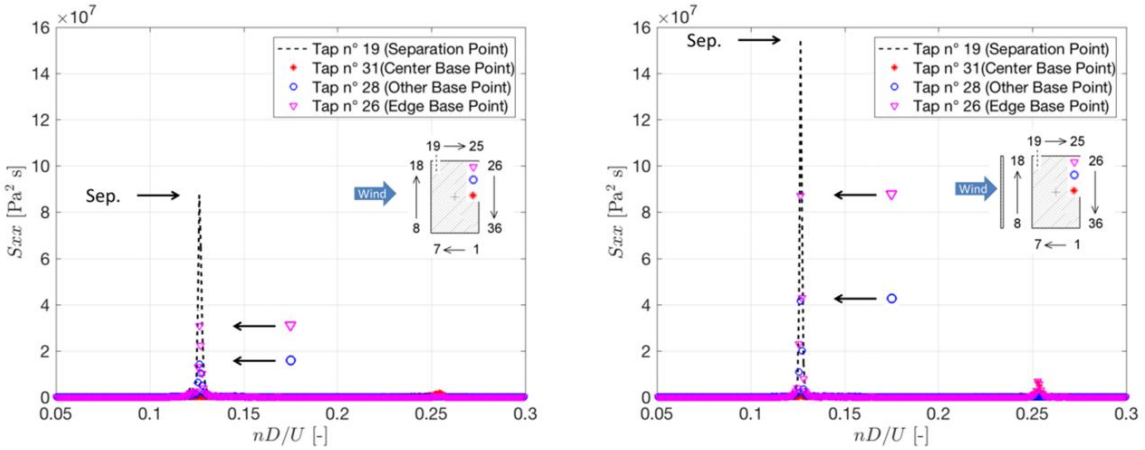

Fig. 3.41 - Pressure spectra at the separation point and the base of the 2:3 rectangular section model in smooth flow at $Re = 2.02\times10^5$: case without screen (left) and case with screen at $D/40$ (right).

According to the two previous cases with the square cross-section in smooth and turbulent flow, a wider gap leads to a local reduction of mean suction behind the screen, close to the extremities (Fig. 3.40). Behind the screen the mean pressure coefficient is lower than in the systems with square cross-section, so that the screen drag coefficients of 3.33 and 3.45 are obtained (Tab. 3.11).

The pressure behind the screen regularly oscillates driven by alternate vortex shedding on the lateral body sides. As it occurs with the square section in smooth flow, an additional component at $2\,St$ was observed.

The phase difference of cavity pressures, with respect to a point close to the separation corner (Fig. 3.42), also exhibits a trend with the gap width similar to the first case discussed (Fig. 3.38). Nevertheless, while for a cavity depth of $D/40$ (Fig. 3.42-left), the phase lag at the Strouhal frequency is closer to the values obtained with the square cross-section, for the $D/20$ case (Fig. 3.42-right), such a phase angle results higher in the system with the rectangular cylinder.

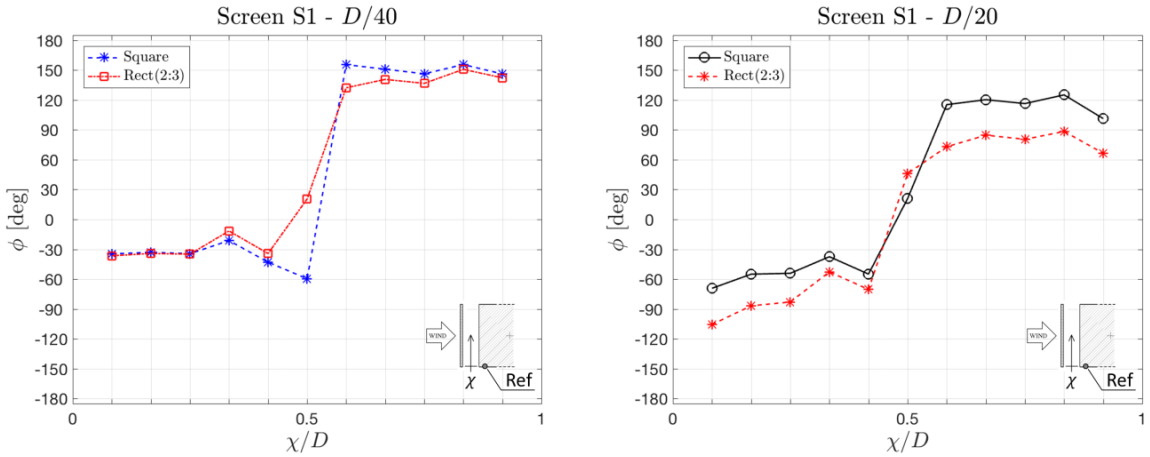

Fig. 3.42 - Phase difference between the pressure measured on the side wall close to the separation point and the pressures measured along the cavity: comparison between the systems with square and rectangular 2:3 cross-sections, with the screen S1 at *D*/40 (left) and at *D*/20 (right). Smooth flow, $Re = 2.26\times10^5$ (case with the square), $Re = 2.02\times10^5$ (case with the rectangle), $\alpha = 0°$.

When the cavity is closed, the system shares a common behavior with the square cross-section case. Global and local parameters, respectively reported in Tab. 3.13 and Tab. 3.14, confirm that the screen S2 reduces the overall drag of the system, once again, simply as if the streamwise length of the body was increased. In particular, with the screen S2 the pressures follow on both lateral sides the patterns observed for the baseline section model without screen, while the pressure distribution at the base is increased.

In this case, as in the analogue with the square cross-section, the external and internal pressures decoupling seems possible. As shown in Fig. 3.43, the values of $\overline{C_p}$ and C_p' measured in the cavity, are similar to the values measured on the rectangular 2:3 cross-section without the screen, in the proximity of the extremity locations, namely at the separation points.

Observing, for instance, the C_p' for a gap width equal to *D*/40 (Fig. 3.43), it is possible to notice that the above mentioned effects of the screen S1 in terms of fluctuations increase (Fig. 3.40) do not occur when the screen S2 is employed.

GLOBAL PARAMETERS	No Screen	S1 – *D*/40	S2 – *D*/40	S3 – *D*/40
C_D	2.91	3.00	2.82	2.83
C_{DRB}	2.01	2.14	1.90	1.86
St	0.127	0.127	0.126	0.123
C_L'	1.62	1.72	1.49	1.31
C_{DS}	-	3.33	2.64	2.15

Tab. 3.13 - Global parameters evaluated for systems with rectangular 2:3 cross-section and screens S1, S2 and S3 at *D*/40, in smooth flow, at $Re = 2.02\times10^5$.

LOCAL PARAMETERS	No Screen	S1 – D/40	S2 – D/40	S3 – D/40
$\overline{C_{bp}}$	-2.29	-2.40	-2.11	-2.09
C_{bp}'	0.55	0.54	0.51	0.60
$\overline{C_{sep}}$	-1.83	-1.95	-1.79	-1.55
C_{sep}'	1.22	1.28	1.13	0.99
$\overline{C_{pScr}}$	-	-2.47	-1.72	-1.18

Tab. 3.14 - Local parameters evaluated for systems with rectangular 2:3 cross-section and screens S1, S2 and S3 at *D*/40, in smooth flow, at $Re = 2.02\times10^5$.

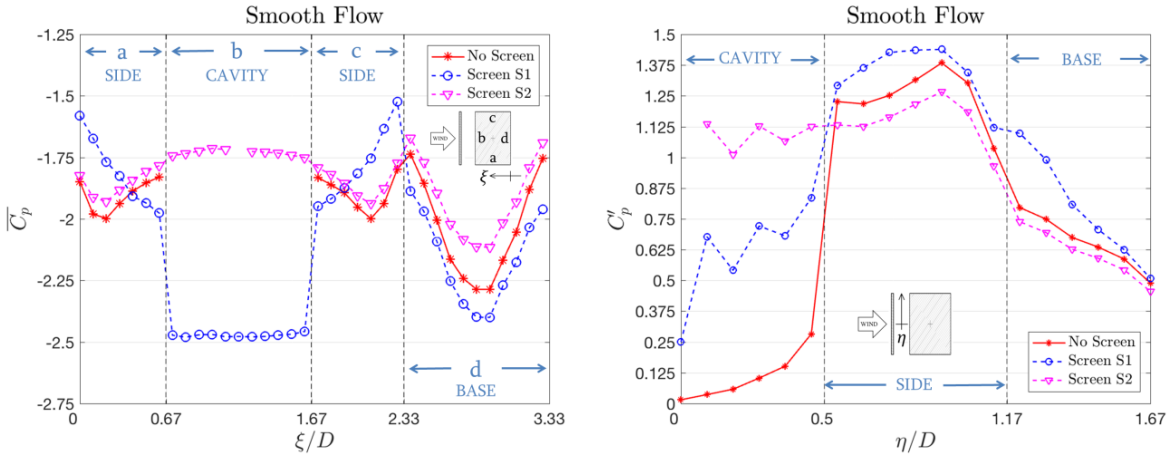

Fig. 3.43 - $\overline{C_p}$ (left) and C_p' (right) distributions around the rectangular 2:3 cross-section at Re = 2.02×10^5 in smooth flow for α = 0° with the screen S1 and S2 at the same distance (D/40).

The screen S3 attached at a distance equal to D/40 from the body face, influences the aerodynamics of the rectangular 2:3 cross-section in a different way compared to what observed for the system with the square cylinder. In particular, the presence of the screen S3 causes the highest parameter variation, as compared to the same system configuration with the square cross section: a reduction of 18.9% is achieved for C_L' (Tab. 3.13). However, the C_D and C_L' of the baseline case (rectangular 2:3 cross-section without the screen) result reduced when the screen S3 is present.

The pressures at the base are higher than those measured on the baseline configuration without the screen, while for the square cross-section, a reduction of pressures in this portion of the body was observed (more evident than with the screen S1).

The different mechanism of interaction can be shown also in the frequency domain. The comparison between the two cross-sections without and with the screen S3 at D/40 is reported in Fig. 3.45. The screen S3 attached to the rectangular 2:3 cross-section reduces the peak at the separation point, and the energy content at the base, close to the rear corner. On the contrary, if the screen is fixed to the square cross-section, these values are increased along with the growth of an additional Strouhal super harmonic peak, measured at the tap in the middle of the base.

On the other hand, the wind induced pressures behind the screen in the two systems behave similarly. The discontinuous distribution of $\overline{C_p}$ in the cavity is influenced by the values in the vicinity of the opening, even if the fluctuation of the pressure coefficients near the central opening are similar to the value measured at the separation point. This result is also evident in the frequency domain. Increased fluctuations are found mainly in correspondence of the Strouhal frequency and its first superharmonic for systems with both cross-sections when the screen is fixed at D/40, while the energy growth seems more pronounced on the whole spectrum when the screen in distanced of D/20 (Fig. 3.46).

It is worth noting that the pressure distribution related to the screen S3 reported in Fig. 3.44, is not symmetrical behind the screen itself. This problem is due to an imperfection of the screen. It is possible that the two stainless steel foils were deformed while fixing them to the spacers. Otherwise it is possible that the whole screen, equipped to the section model through screws, was not opportunely fixed during this measurement (with a gap width of D/20 this problem is less evident).

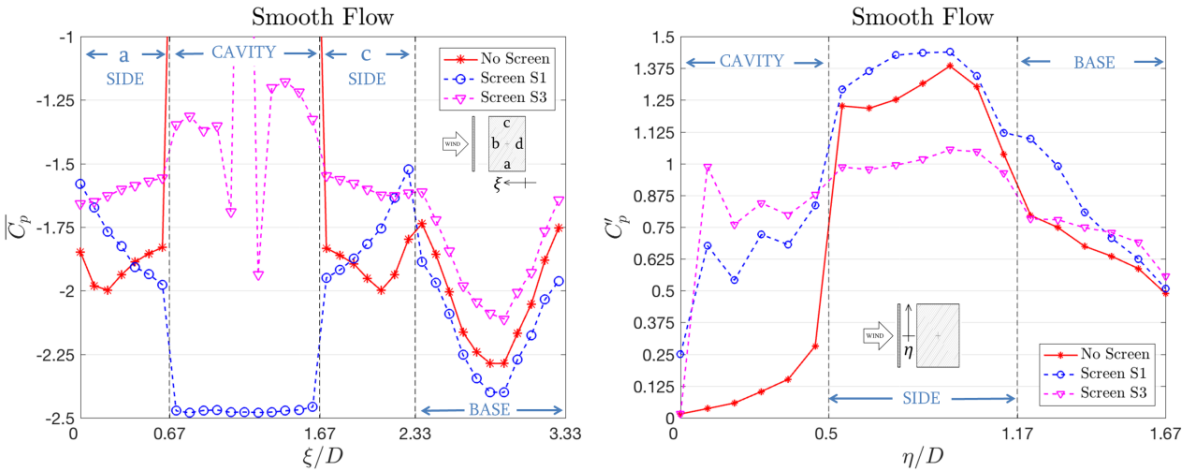

Fig. 3.44 - $\overline{C_p}$ (left) and C_p' (right) distributions around the rectangular 2:3 cross-section with the screen S1 and S3 at the same distance (D/40), at $Re = 2.02\times10^5$, in smooth flow, for $\alpha = 0°$.

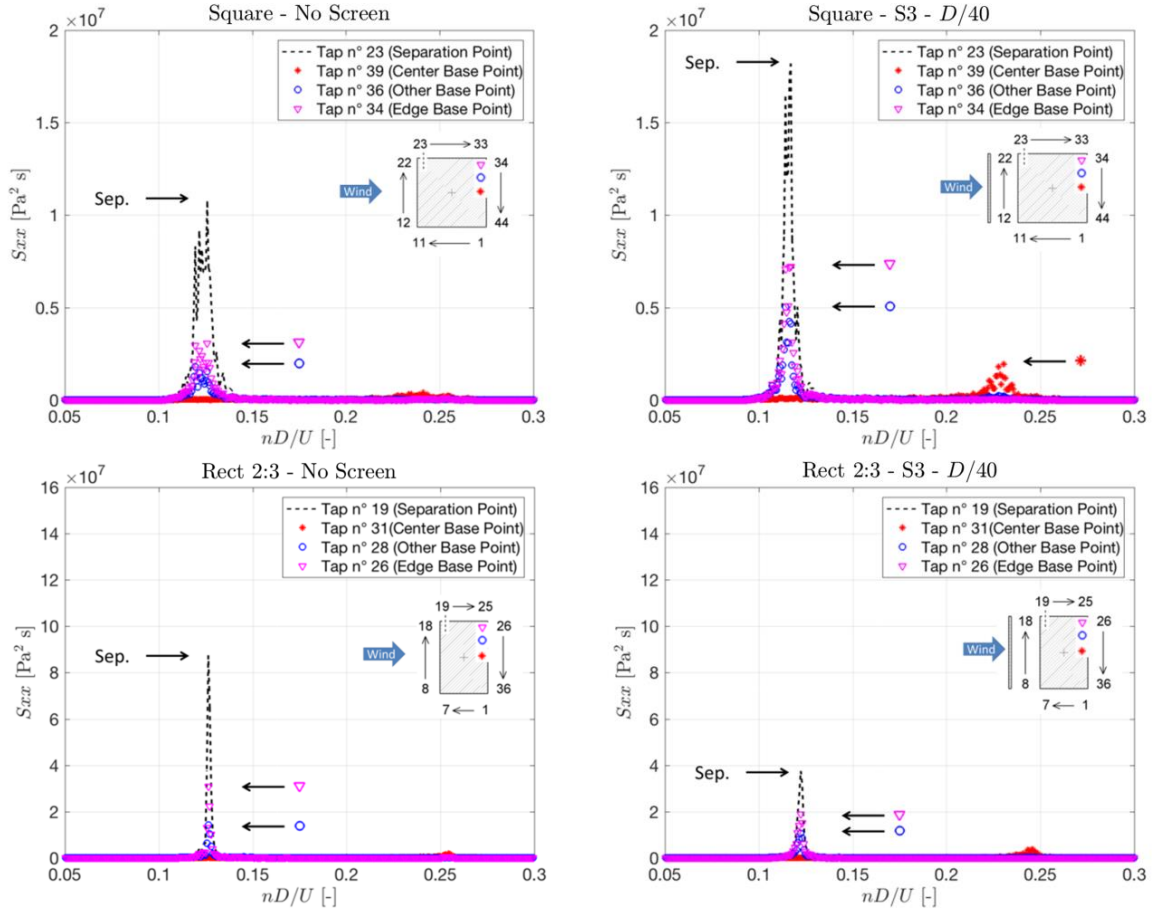

Fig. 3.45 - Pressure spectra at the separation point and at the base of two systems with the screen S3 at the same distance (D/40), in smooth flow. On top, the square cross-section without (left) and with the screen (right) at $Re = 2.26\times10^5$. On bottom, the rectangular 2:3 cross-section without (left) and with the screen (right) at $Re = 2.02\times10^5$.

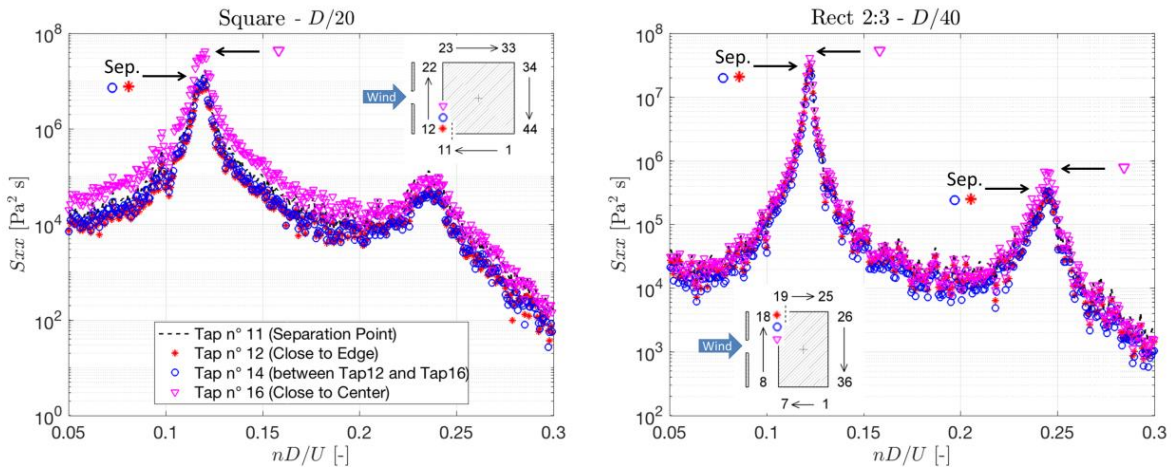

Fig. 3.46 - Pressure spectra behind the screen S3. On the left, the square cross-section in smooth flow with the screen at $D/20$, $Re = 2.26\times10^5$. On the right, the rectangular 2:3 cross-section with the screen at $D/40$, $Re = 2.02\times10^5$.

3.3.3 Results for flow at an angle of attack to the system

Systems with the square cross-section in smooth flow

The results obtained for systems with a square cross-section without and with the screen, fixed respectively at $D/40$ and $D/20$, approached by a smooth flow are presented. In this set of tests, the wind direction ranges between α = -5° and α = +180° considering α = 0° the wind normal to the shielded face of the bluff body. However, for the sake of clarity, the data are reported only up to α = 90°. The experimental tests were carried out varying the Re numbers in the range previously described for flow normal to the screen.

The drag (C_D) and lift (C_L) coefficients obtained for the baseline case without screen are reported in Fig. 3.47. The highest value (in absolute terms) of C_L occurs for α = 13°. According to the literature (*e.g.* Lee, 1975, Rockwell, 1977), around this angle of attack (the angle slightly varies from one work to another), which follows a counter clockwise rotation (according to Fig. 3.17), the flow mean reattachment occurs at the body lower side. Generally, for a rectangular cylinder, the angle for flow reattachment corresponds to a local minimum of the C_D.

In the baseline configuration, the lift coefficient slope centered in 0° is equal to -4.4. Such parameter was evaluated through a linear regression of the values corresponding to the wind angles between -2° and +2° (Tab. 3.4).

When the screen S1 is fixed at the distances of $D/40$ and $D/20$, the lift coefficient slope centered in 0° ($dC_L/d\alpha$) is equal respectively to -3.2 and -0.6, both obtained through a linear regression of the values measured between α = -5° and α = +5°. In these cases, reported respectively in Fig. 3.48 and in Fig. 3.49, it is evident the reduction of $dC_L/d\alpha$ due to the presence of the screen, even if only with a gap width of $D/20$ the section is stable to the galloping phenomenon (according to the Den Hartog criterion).

The maximum C_L (in absolute value) obtained for the system with the screen S1 at $D/20$ results shifted to α = 15°. Therefore, it seems that the presence of such screen slightly delays the flow mean reattachment.

It is to note that the angle for reattachment of a rectangular cylinder in smooth flow tends to increase if the side ratio reduces. For instance, Da Matha Sant'Anna *et al.* (1988), obtained an angle for reattachment α = 13.5-14° for the square section and α = 16° for the rectangular cylinder with side ratio B/D = 0.8. However, the angle at which reattachment occurs, in the system with the screen at $D/40$, remains around α = 13°.

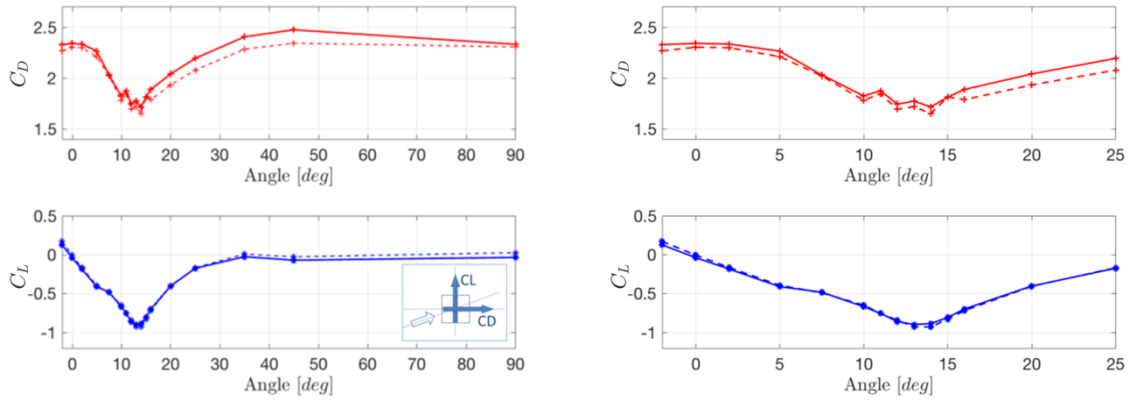

Fig. 3.47 - On the left, C_D and C_L measured on the baseline square cylinder, α = -5° ÷ 90°, smooth flow, Re = 2.26×10⁵. Values measured with the force balances (continuous line) and values obtained through the integration of pressures (dotted line) are reported. On the right, a focus on the range α = 0° ÷ 25°.

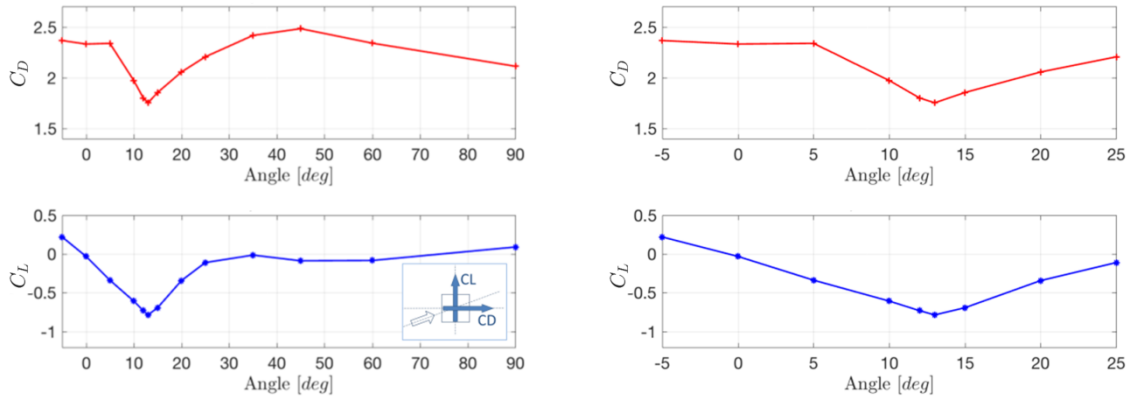

Fig. 3.48 - On the left, C_D and C_L measured on the system composed by the square cross-section and the screen S1 at $D/40$, α = -5° ÷ 90°, smooth flow, Re = 2.26×10⁵. On the right, a focus on the range α = 0° ÷ 25°.

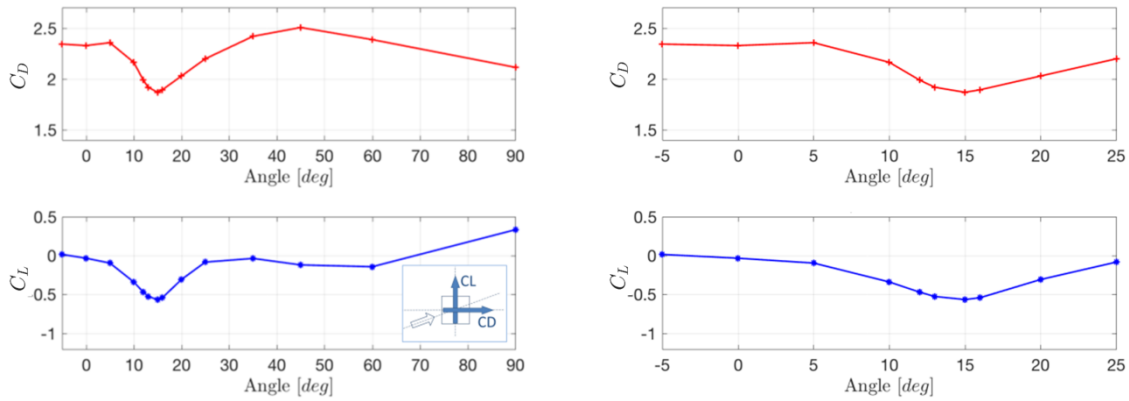

Fig. 3.49 - On the left, C_D and C_L measured on system composed by the square cross-section and screen S1 at $D/20$, α = -5° ÷ 90°, smooth flow, Re = 2.26×10⁵. On the right, a focus on the range α = 0° ÷ 25°.

The $\overline{C_p}$ distributions measured around the middle section of the cylinder, for angles of attack in the range $\alpha = 0° \div 25°$, are shown in Fig. 3.50. The screen effects observed for a wind direction equal to 0°, occur also for a small angle of attack. When the screen S1 is present, for $\alpha = 5°$ and 10°, the pressures on the upper side (the opposite to that where a reattachment is expected) and at the base are almost always lower than in the baseline case, irrespectively to the gap width. Since for such small wind angles of attack a mean pressure difference occurs at the cavity extremities, it is argued that the oscillating flow observed for $\alpha = 0°$, becomes a pulsating flow, namely, a flow composed by a non-zero mean and an fluctuating component.

For a wind direction $\alpha = 15°$, the mean pressure distributions still exhibit a small jump between the external value in the proximity of the upper extremity and into the cavity. The pressures measured at the base of the three systems exhibit the same distribution. This pattern also occurs on the lateral side in the wake region when the angle reaches 20°. In particular, at this angle of attack, the pressure in the cavity is equal to the pressures at both the extremities. With the help of the C_p' reported in Fig. 3.51, it is supposed that such condition represents the end of the oscillating flow behavior driven by the vortex shedding. For α = 20°, also the pressure fluctuations behind the screen, although attenuated, are similar to those at the exterior, in the proximity of the extremities.

Then, at α = 25° the presence of the screen influences only the lateral side directly exposed to the flow. A completely different role of the screen is expected for values between this angle and $\alpha = 90°$. The flow tends to go directly in the cavity (Fig. 3.52), and local effects at the inlet are expected.

Finally, for a wind direction parallel to the screen, an increased lifting behavior by increasing the gap width is shown in Fig. 3.48 and Fig. 3.49.

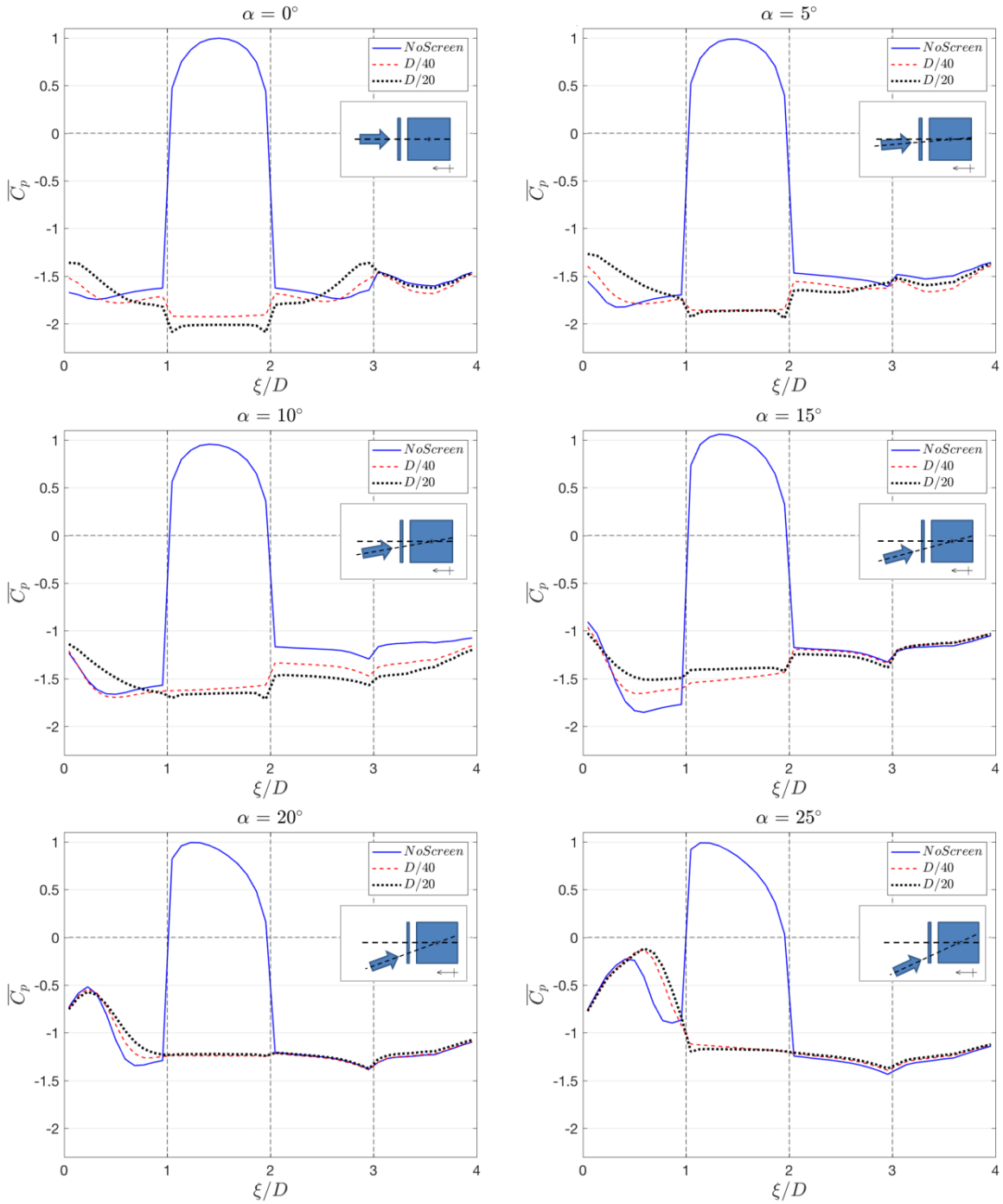

Fig. 3.50 - Mean pressure coefficients at different angles of attack (α = 0°, 5°, 10°, 15°, 20°, 25°). Systems with the square cross-section without screen and with the screen S1 at *D*/40 and *D*/20, smooth flow, $Re = 2.26 \times 10^5$.

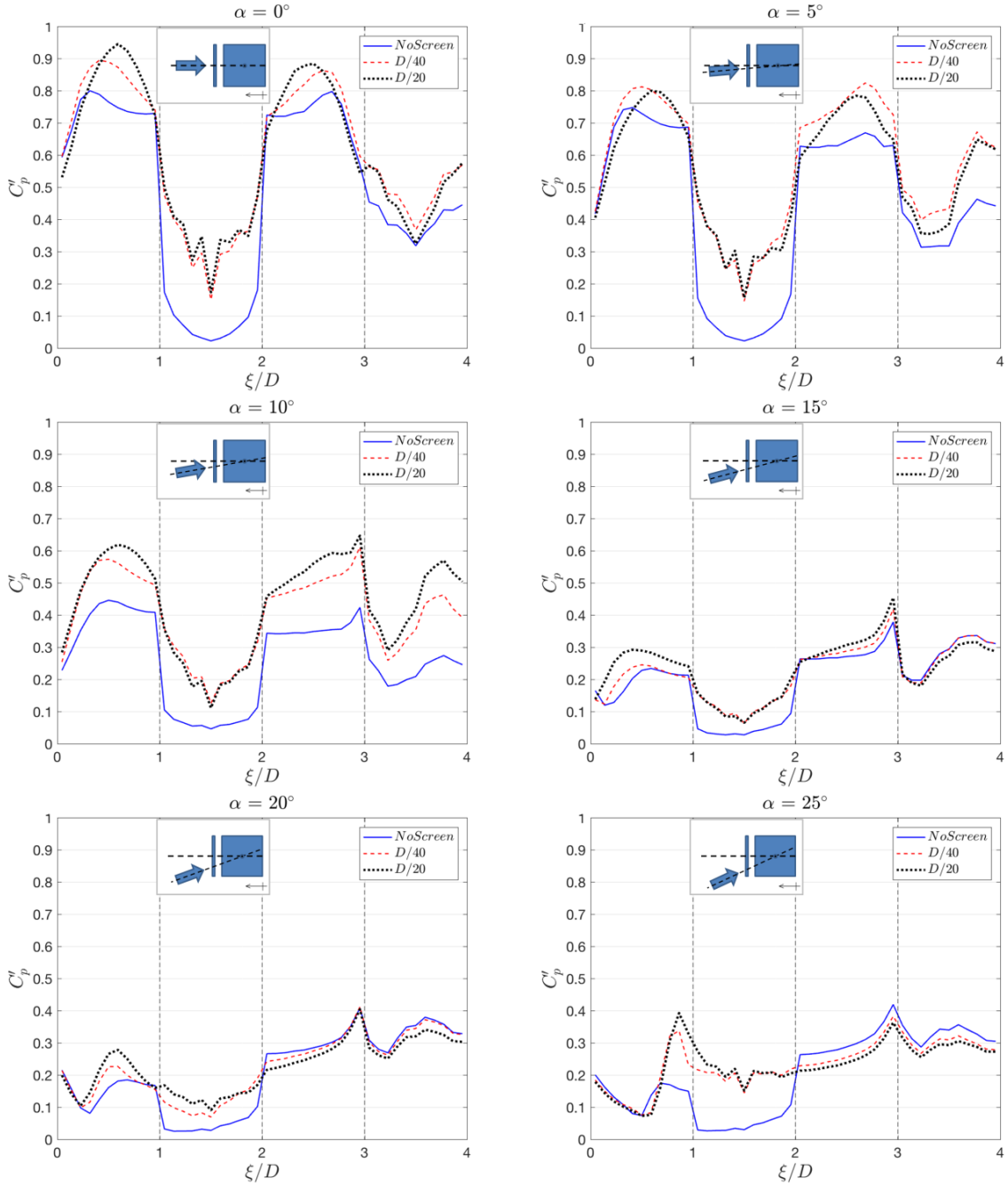

Fig. 3.51 - Pressure coefficient standard deviations at different angles of attack. Systems with the square cross-section without screen and with the screen S1 at $D/40$ and $D/20$, smooth flow, $Re = 2.26\times10^5$.

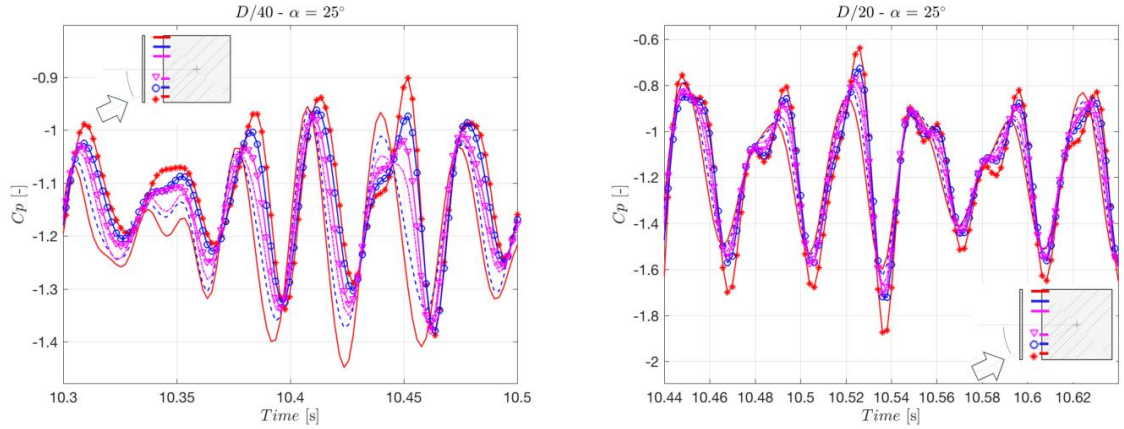

Fig. 3.52 - Some time intervals of pressure time histories measured behind the screen fixed at $D/40$ (left) and $D/20$ (right), for an angle of attack equal to 25°, smooth flow, $Re = 2.26\times10^5$. The same color is used for symmetric taps.

Systems with the square cross-section in turbulent flow

In Fig. 3.53, the mean pressure coefficient distributions around the square cross-section employed in turbulent flow, without and with the screen S1, are reported. The signals measured with the force balances were not employed.

In contrast to the previous case in smooth flow, the mean pressures at the base already coincide for a null angle of attack. By varying the wind direction in the range $\alpha = 0 \div 25°$, the pressures in this portion of the body remain unaffected by the presence of the screen, irrespectively of the gap width. By contrast, the pressures on the upper body side behaves similarly to the previous case in smooth flow. From a small angle of attack ($\alpha = 5°$), up to 15°, the distributions of $\overline{C_p}$ are lower when the screen is present at $D/20$ or $D/40$.

The shear layers stability enhanced by the turbulence, seems to preserve on the rear side the peculiar pressure distributions caused by the screen, up to $\alpha = 15°$. In smooth flow, at this angle of attack, the pressures in this portion of the body were not affected by the presence of the screen anymore.

For a wind direction equal to 20°, the pressure exhibits patterns similar to the distributions observed in smooth flow for $\alpha = 25°$. This seems to be in line with the literature, in which the turbulence effects can be explained as a body elongation, with a corresponding anticipated angle of flow reattachment as compared to the smooth flow case.

Behind the screen, close to the edge directly exposed to the flow, the mean pressures exhibit a local peak. This local effect of flow separation occurs for $\alpha = 20°$ irrespectively of the gap width, but it becomes higher when the screen is fixed at $D/20$, and the angle of attack reaches 25°. The cavity extremity on the upper side (according to Fig. 3.53), connects the interior of the cavity with a separated flow region. Therefore, the internal pressures tend to equalize with the pressures in the wake.

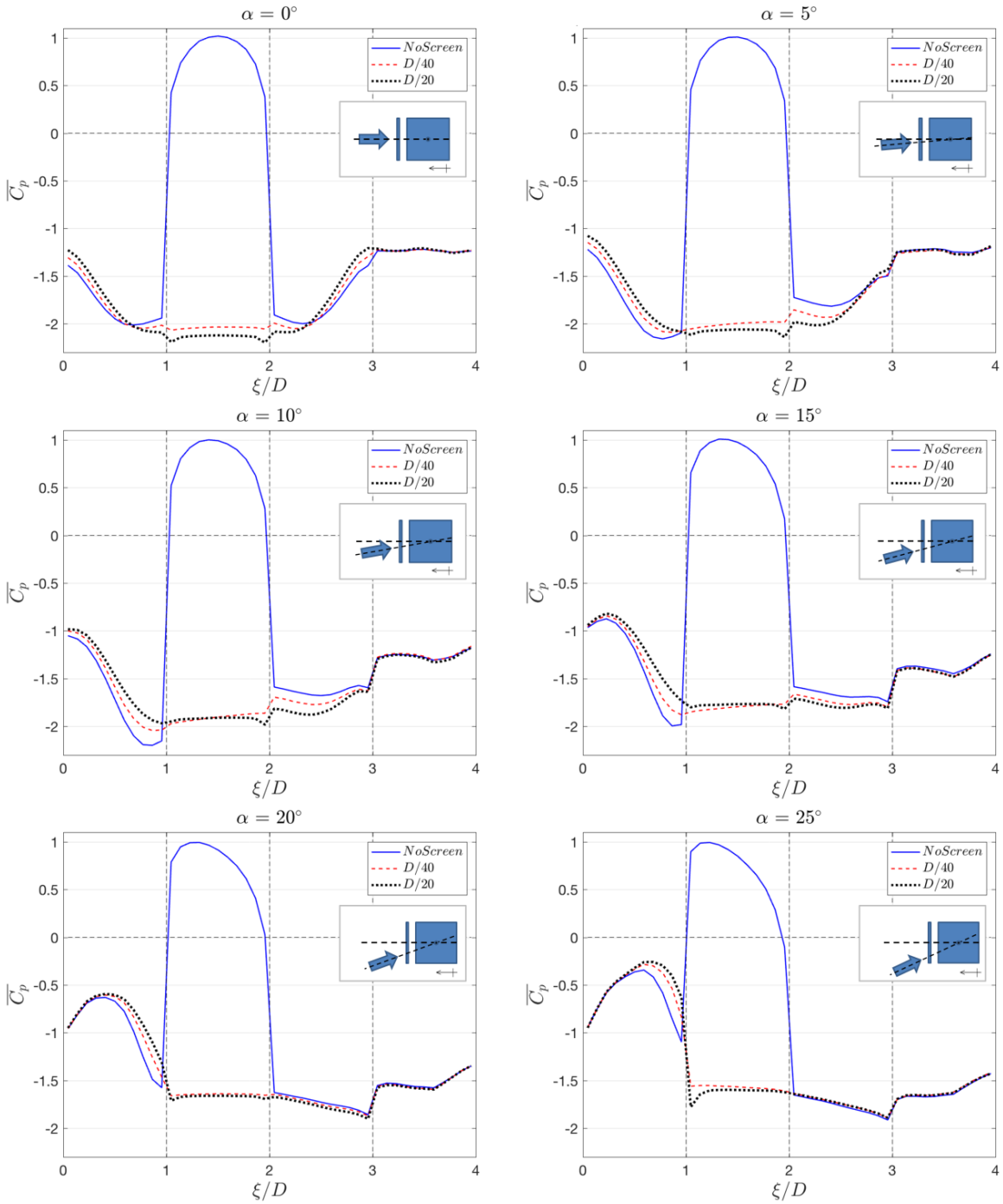

Fig. 3.53 - $\overline{C_p}$ at $\alpha = 0°$, 5°, 10°, 15°, 20°, 25°. Square cross-section without and with the screen S1 fixed respectively at $D/40$ and $D/20$, turbulent flow, $Re = 1.58\times10^5$.

Systems with the rectangular 2:3 cross-section in smooth flow

The C_D and C_L coefficients obtained for systems with the rectangular 2:3 cross-section, without and with the screen S1, are reported respectively in Fig. 3.54 and Fig. 3.55. The model without the screen for α = 90°, is a rectangular 3:2 cylinder with the wind normal to the shortest face. The maximum lift coefficient (in absolute value) occurs around $\alpha = 20°$. Da Matha Sant'Anna *et al.* (1988), reported a flow reattachment for a rectangular cylinder with side ratio equal to 0.6 at $\alpha = 19°$.

Fig. 3.55 shows that the C_L peak-shifting-effect caused by the presence of the screen, and observed also with the square cross-section in smooth flow, still occurs. In this case, less measurements were performed, so it is not possible to indicate exactly the angle of flow reattachment with the screen. However, in the figure it is evident that the peak lies between α = 20 and 25° (Da Matha Sant'Anna *et al.* indicate that for a side ratio of 0.5 the flow reattaches at 23°).

The lift coefficient slope around 0° is equal to -3.04, and it is obtained through a linear regression of the values corresponding to the wind directions between -3° and +3°. When the screen S1 is present, $dC_L/d\alpha$ is equal to -1.24 (linear regression of C_L for 0° ≤ α ≤ +5°). In agreement with the results obtained for the systems with the square cross-section, the reduction of lift coefficient slope introduced by the presence of the screen S1 is evident, and it leads the system to became stable against the galloping phenomenon.

The pressure distributions reported in Fig. 3.56 confirm the results observed at null angle of attack, in the previous section. Locally, the rectangular 2:3 and the square cross-sections are affected by the screen S1 in different ways.
For a small angle of attack, such as 5°, the pressure distributions without and with the screen are similar. This behavior can be due to the strong mechanism of vortices formation related to the rectangular 2:3 cross-section. The lateral side in the region of separated flow has all the pressures lower than the baseline case without screen only when the angle of attack reaches 15°. With the square cross-section this condition was reached for α = 5°.
The angle for reattachment is shifted by the presence of the screen. In case with square cross-section, the angle for reattachment (with the screen) was at 15°, and from α = 20° the pressure in the cavity was equalized with the wake pressure. In a similar way, with rectangular 2:3 cross-section, the system with the screen experiences flow reattachment between 20° and 25°, and the cavity pressure equalization is achieved for α = 25°. It is argued that, when the flow completely reattaches on the body side, the recirculating bubble "trapped" by the shear layer and the wake portion on the opposite side, are connected by the cavity, so the pressure equalizes.

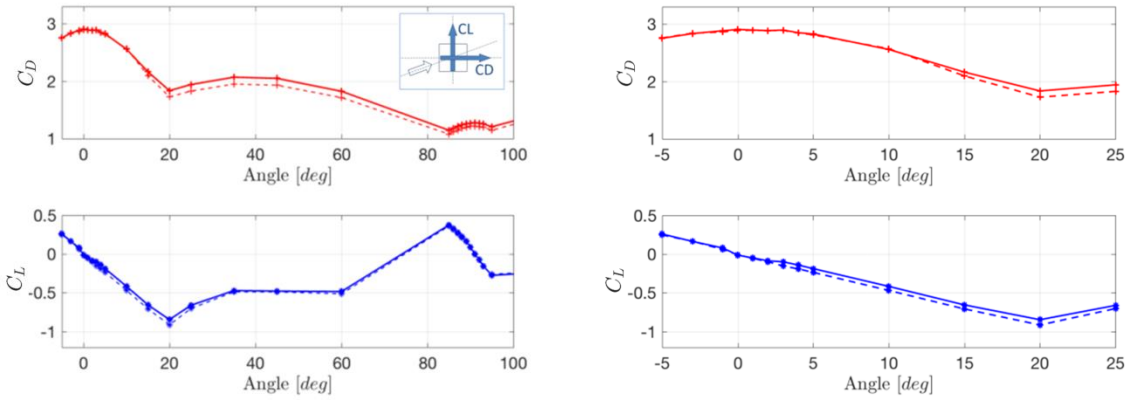

Fig. 3.54 - On the left, C_D and C_L measured on the rectangular 2:3 cross-section without screen, α = -5° ÷ 100°, smooth flow, Re = 2.03×10⁵. Values measured with the force balances (continuous line) and values obtained through the integration of pressures (dotted line) are reported. On the right, a focus on the range α = 0° ÷ 25°.

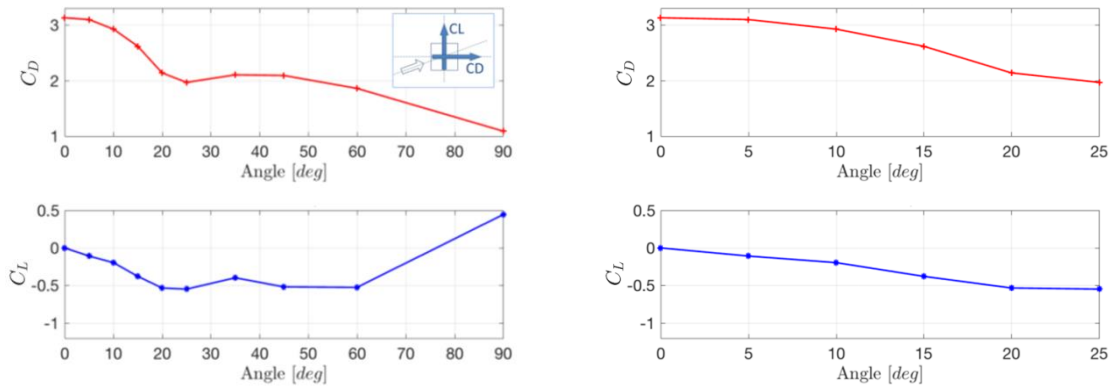

Fig. 3.55 - On the left, C_D and C_L measured on the rectangular 2:3 cross-section with screen S1 at $D/20$, α = -5° ÷ 90°, smooth flow, $Re = 2.03\times10^5$. On the right, a focus on the range α = 0° ÷ 25°.

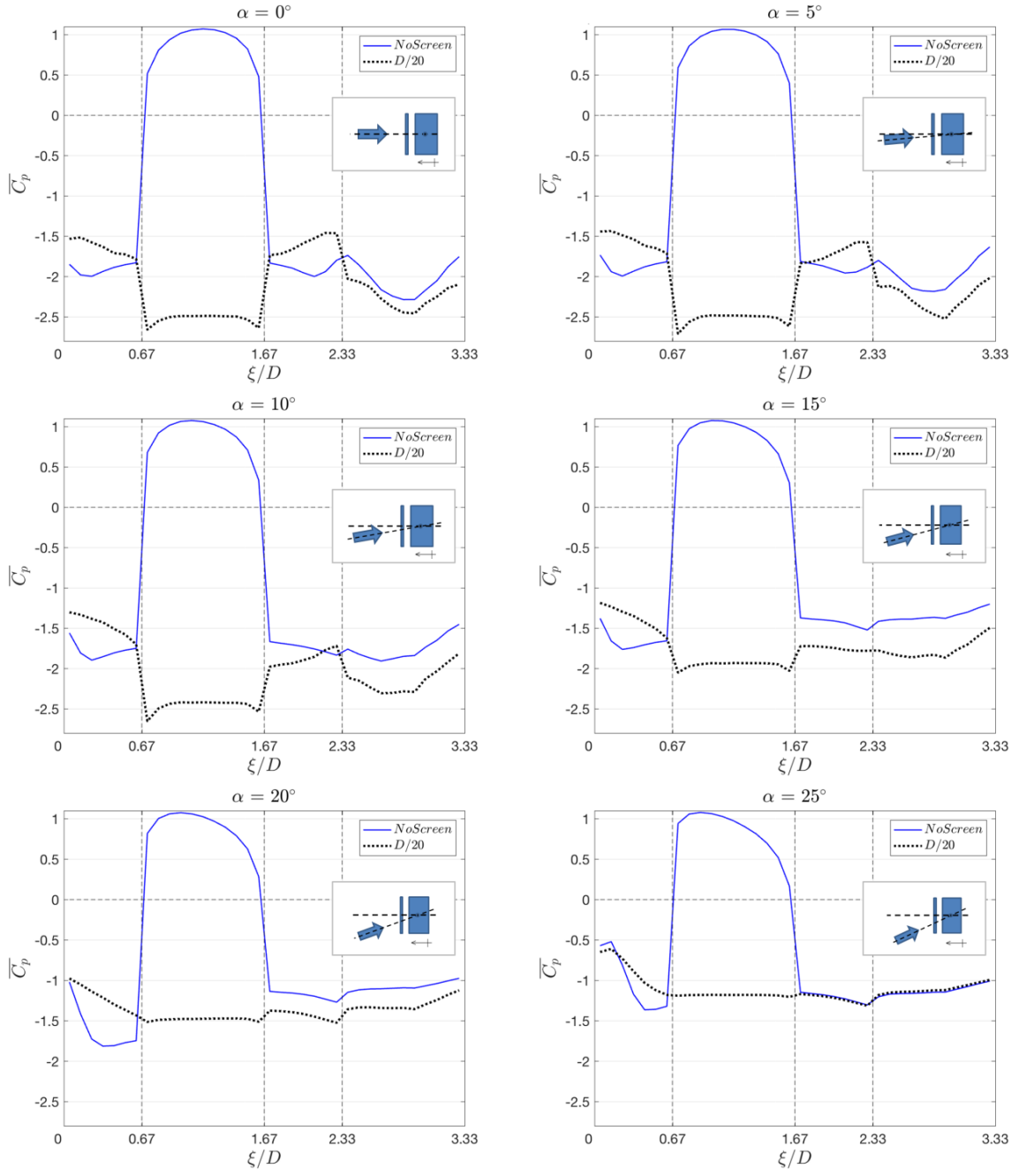

Fig. 3.56 - $\overline{C_p}$ for $\alpha = 0° \div 25°$. Rectangular 2:3 cross-section without and with the screen S1 at $D/20$, smooth flow, $Re = 2.03\times10^5$.

The case of screen S1 fixed at the base (α = 180°)

The tests carried out by varying the angles of attack were focused on the wind directions around the configuration of flow normal to the screen S1. The range of wind directions for which the oscillating flow (observed for α = 0°) persists was investigated. However, the experimental campaign was conceived in order to measure the screen effects also when the flow comes from the opposite direction, namely, for the configuration of screen attached at the base of the bluff body.

The global aerodynamic coefficients reported in Tab. 3.15 show that, generally, the screen fixed at the base influences the system aerodynamics much less than when it is placed on the front. Depending on the side ratio of the screened bluff body, some parameters result almost unaffected, as C_D and C_L' for the square cross-section, while parameters as the C_L' for the rectangular 2:3 cross-section varies. In particular, the lift coefficient fluctuations are always reduced. Based on the side ratio, the screen may result slightly pushed toward the body (case with the square cross-section) or pulled away from the body (with the rectangular 2:3 cross-section).

The two cases in smooth flow, reported respectively in Fig. 3.57 and Fig. 3.59, exhibit higher mean pressures along the body sides when the screen is fixed at the base. In the case of square cross-section with a turbulent flow they are much less affected (Fig. 3.58).
When the square cross-section is employed in smooth and turbulent flow, the distribution of $\overline{C_p}$ inside the cavity is lower than the one measured at the base of the bluff body without the screen. The assumption of a distribution on the external layer of the screen similar to the base distribution for the baseline case, may explain the results reported in Tab. 3.15, for which the screen results attracted to the body. With the same approach, the pressure distributions measured in the cavity of the rectangular 2:3 cross-section case may explain the positive value of C_{DS} (the screen tends to be distanced from the body).
The presence of the screen tends to reduce the pressure fluctuations in any configuration tested. In particular, when it is fixed behind the rectangular 2:3 cross-section, the C_p' are reduced along the body sides and at the base equipped with the screen. On the other hand, with the square section in smooth and turbulent flow a reduction of C_p' is observed behind the screen and, laterally, in the proximity of the leading edge.

Generally, when the screen S1 is fixed in front of the body, the oscillating flow is driven by the opposite pressure variation, namely an oscillating pressure gradient. By contrast, when the screen is attached behind the body, the flow moves inside the cavity following the air movement of the wake, which is characterized by a transversal component even without the screen. The presence of such a component was explained in Chapter 2 while describing the entrainment interaction between two opposite vortices (see Fig. 2.4).

GLOBAL PARAMETERS	Square Smooth Flow			Square Turbulent Flow			Rect 2:3 Smooth Flow	
	No Screen	*D*/40	*D*/20	No Screen	*D*/40	*D*/20	No Screen	*D*/20
C_D	2.36	2.36	2.36	(2.02)	-	-	2.91	2.85
St	0.123	0.120	0.122	0.133	0.136	0.124*	0.127	0.128
C_L'	1.43	1.38	1.39	0.89	0.82	0.82	1.59	1.26
C_{DS}	-	-0.1	-0.04	-	(-0.1)	(-0.08)	-	+0.09

Tab. 3.15 - Global parameters for the square and the rectangular 2:3 cross-sections without and with the screen S1 at different distances. Results for α = 180°, Reynolds numbers respectively equal to 2.26×10^5 , 1.58×10^5 , 2.02×10^5.
(*) from the power spectral density analysis, the lift coefficient and the pressures close to the separation point exhibited two dominant peaks, one at 0.138, lower, and one at 0.124, higher.

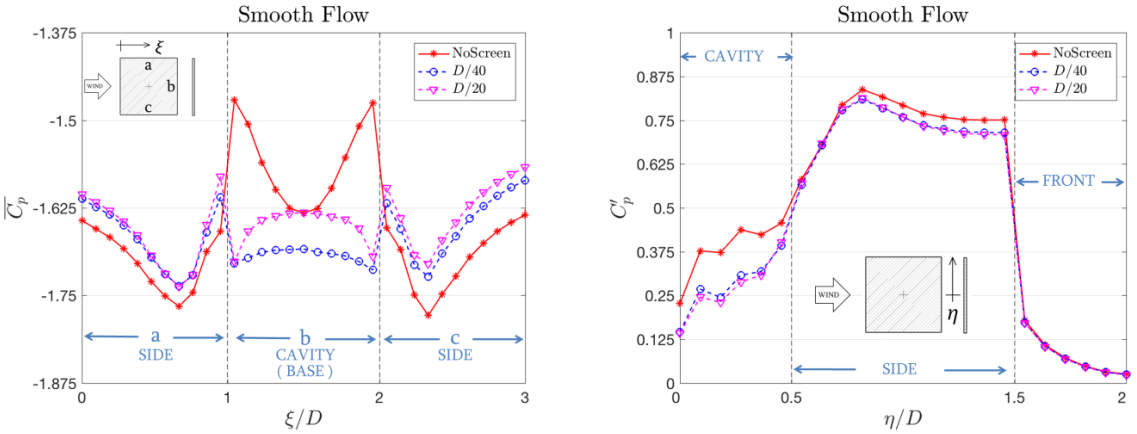

Fig. 3.57 - $\overline{C_p}$ (left) and C_p' (right) for the square cross-section with screen S1 at *D*/40 and *D*/20. Smooth flow. α = 180°, *Re* = 2.26×10^5.

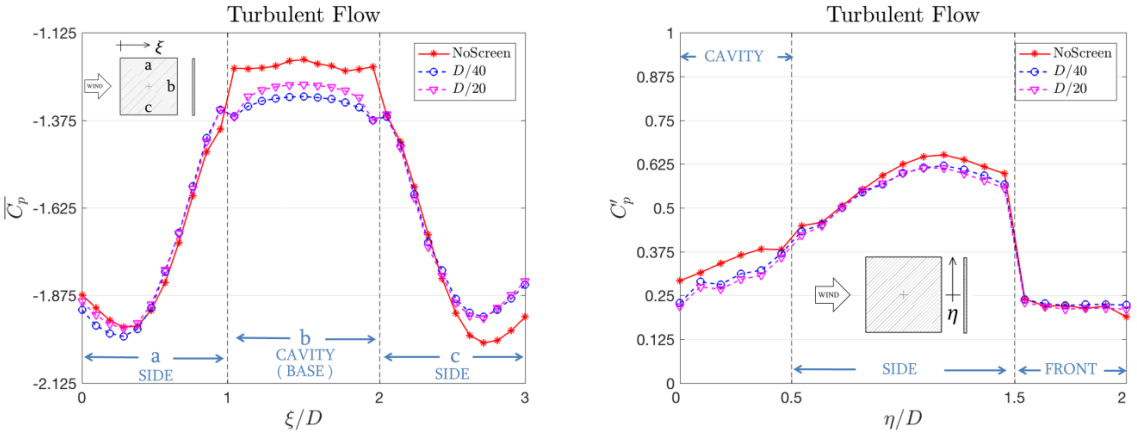

Fig. 3.58 - $\overline{C_p}$ (left) and C_p' (right) for the square cross-section with screen S1 at *D*/40 and *D*/20. Turbulent flow (Iu=15%). α = 180°, *Re* = 1.58×10^5.

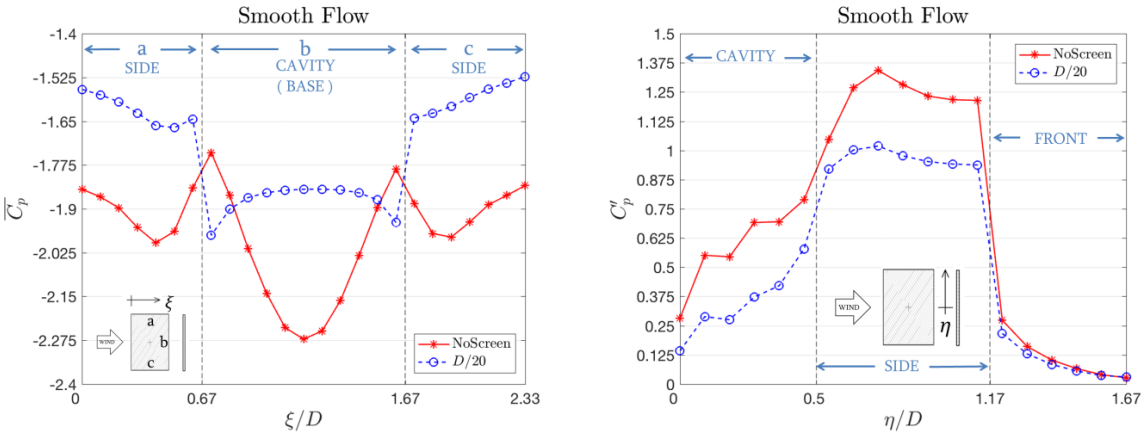

Fig. 3.59 - $\overline{C_p}$ (left) and C_p' (right) for the rectangular 2:3 cross-section with screen S1 at *D*/20. Smooth flow. α = 180°, *Re* = 2.02×10^5.

3.4 Summary

Wind tunnel tests were performed on systems composed by a rectangular cylinder equipped with an airtight screen. The tests aimed to investigate the effects of the screen on the system aerodynamics. The screen had the same depth of the face of the two rectangular cylinders over which it was attached on. The cylinders were characterized by a square and a rectangular 2:3 cross-section. In order to better understand the role of the through cavity created between the screen and the model face, different screens were employed. The tests were carried out at different Reynolds numbers in smooth and turbulent flow, for different wind angles of attack, by varying the gap width between the screen and the body. In particular, gap widths between 1/40 and 1/10 of the characteristic body cross-section dimension were tested.

In the preliminary part of the experimental campaign, the wind tunnel set-up was described, and its inherent limitations discussed. Then, possible model imperfections were checked through the comparison with some literature data. While the physical models appeared of good quality and the smooth flow had the characteristics expected, the turbulent flow generated by the grid was non-uniform. Nevertheless, the results obtained in turbulent flow seem to be representative in terms of turbulence interaction with the system aerodynamics.

Generally, for flow normal to the shielded face, the presence of the screen with open gap cavity (screen S1) affects the system aerodynamics, resulting in a new fluid-dynamic system.
Despite the gap width dimensions are an order of magnitude smaller respect to the two-dimensional body dimensions, the influence of the airtight screen with through cavity plays a crucial role: an oscillating flow occurs in the cavity irrespectively of the shielded cross-section and approaching flow features. The oscillating flow is driven by the oscillating pressure gradient at the cavity extremities, caused by the alternate shedding of vortices, occurring almost at the same frequency, with or without the screen.
The presence of an oscillating flow, which draws and expels air from the extremities, modifies the pressure distributions along the lateral body sides and at the base (*i.e.* the separated flow region around the body). In smooth flow, the screen S1 tends to increase the drag coefficient of the system, even if the modified pressure distributions do not vary monotonically by increasing the gap width. On the other hand, regardless of the approaching flow features, the mean pressures on the downstream portion of the lateral body sides are always higher than in the baseline case without screen. In addition, pressure fluctuations are enhanced in the part of the body close to the trailing edge, laterally and at the base. However, the screen effects are more evident in smooth than in turbulent flow, and the systems with the rectangular 2:3 cross-section result the most affected cases.
Tests performed with the cavity closed by an airtight vertical compartmentation demonstrated that the oscillating flow is fundamental to obtain such peculiar aerodynamic effects. In fact, if the cavity flow was prevented, the system would feel the presence of the screen just as a body elongation in the streamwise direction. Other investigations concerning small modifications of the system geometry were performed. They showed that also an opening on the screen with depth comparable to the gap width may lead the system to a different aerodynamic behavior, as compared to configurations with an airtight screen.

The mean pressure coefficients in the cavity for a flow normal to the screen are always negative, in particular, they result much lower than the pressures on the lateral body side, behind the separation point. Despite the many performed tests, it was not possible to explain the flow mechanism that causes this "pressure jump". An empty space with flow able to move behind the separation point represents undoubtedly a different boundary condition close to the shear layer origin, as compared to that imposed when the flow separates from the edge of a rectangular cylinder without screen (*i.e.* the velocity at the wall is null). It is supposed that this different boundary condition affects a very sensitive region for the system aerodynamics which could also explain the mean underpressure measured in the cavity. However, further studies are needed to profoundly understand the flow mechanism that occurs in this portion of the flow field.
When the square cross-section is employed in the system, the cavity pressures are lower than those at the base. On the contrary, for systems with the rectangular 2:3 cross-section, the suction behind the screen and at the base are comparable.
An additional observation concerning the internal pressures is that, for certain gap widths, regardless the cross-section side ratio, local effects further reduce the mean pressures in the proximity of the extremities. It was argued that these effects are related to a local flow separation when the air is drawn in the cavity.
Between the oscillating pressures along the cavity and the pressure measured laterally, close to the separation point, it was observed a phase lag which increases by increasing the gap width.
An attempt to characterize the oscillating flow through the Reynolds and the Womersley numbers was carried out. However, it was not observed any remarkable variation in the range of Re (and Wo) numbers tested.

Significant global effects are measured for different wind angles of attack. In terms of lift coefficient slope, impressive variations were measured compared to the case without a screen. Indeed, the presence of the screen in some cases prevents the galloping instability of the system.
The mean pressure distributions around the section show an angle for flow reattachment increased when the screen is present. The oscillating cavity flow observed for wind normal to the screen, becomes a pulsatile flow (with a non-zero mean) increasing the angle of attack, which continues to oscillate and to interfere with the external flow. This behavior persists up to the angle in which two regions characterized by an almost constant pressure are formed: the recirculation bubble on the body side which experiences the flow reattachment, and the separated region on the opposite side. Through the cavity that connects the two regions, the pressure tends to equalize. Therefore, the oscillating flow disappears and the internal pressures result almost constant, with values similar to the external pressures in the proximity of the cavity openings.

The complex flow-interaction observed suggests to integrate the experimental results with the CFD simulation ones, reported in Chapter 4, prior to attempting an interpretation of the effects caused by the presence of the open-gap screen.

Chapter 4 - Computational fluid dynamics simulations

The experimental tests performed on the two-dimensional systems, composed by a screen and a rectangular cylinder, produced a large amount of data in terms of global and local aerodynamic parameters. Through these results, it was possible to describe the effects of different screen configurations, aiming at a better comprehension of the fluid dynamic behavior of the systems. Nevertheless, the experimental campaign was affected by some limits, as described in Chapter 3, such as the lack of flow visualization, the impossibility to equip the screen with pressure taps and the limited range of Reynolds numbers (*Re*) tested. The Computational Fluid Dynamics (CFD) simulations here performed aim to overtake some of the limitations encountered in the experimental tests, playing them a complementary role.
In the present work, two-dimensional Unsteady Reynolds Averaged Navier-Stokes (URANS) simulations were carried out with the Spalart-Allmaras and the Menter's kω-SST turbulence models, by using the open source software package OpenFOAM®. In the following, the numerical set-up of the simulations is described in terms of computational mesh, turbulence models and numerical schemes. Then, after the discussion of the results obtained for the square cross-section without screen (characterized by a cross-flow dimension *D*), the attention is focused on the system composed by the square section with the screen S1 fixed at a distance of *D*/20. This specific case has the screen at an intermediate distance, it is stable with respect to galloping instability and it exhibits remarkable local effects at the cavity extremities. A deeper insight, through a flow visualization, may improve the comprehension of the aerodynamic behavior of such a system.

4.1 Simulation set-up

The CFD is a wide field of study in which numerical methods and algorithms are employed to solve fluid flow problems over a discrete domain. Among the many available discretization methods, the use of finite volumes is the most employed to study computationally the wind effect on civil structures (this field is called Computational Wind Engineering, CWE): to assess wind loads (*e.g.* Dagnew and Bitsuamlak, 2013, Tominaga, 2015), to understand pedestrian comfort (*e.g.* Stathopoulos and Wu, 1995, Blocken, 2014) and to evaluate diffusion of pollutants (*e.g.* Li *et al.*, 2008, Ramponi *et al.*, 2015). CFD studies with the finite volume method are also widely employed in the field of bluff body aerodynamics (*e.g.* Rodi, 1997, Shur *et al.*, 2005, Raisee *et al.*, 2010, Mannini, 2015).

In the current work, the governing equations are the incompressible Navier-Stokes equations, that is the system of equations composed by:

the momentum equations $$\rho\frac{\partial u_i}{\partial t}+\rho u_j\frac{\partial u_i}{\partial x_j}=-\frac{\partial p}{\partial x_i}+\frac{\partial t_{ij}}{\partial x_j} \qquad \textit{(eq. 4.1)}$$

and the continuity equation $$\frac{\partial u_i}{\partial x_i}=0 \qquad \textit{(eq. 4.2)}$$

expressed for a flow velocity component u_i. ρ is the fluid density, p indicates the pressure and t_{ij} the viscous stress tensor expressed as:

$$t_{ij} = 2\mu s_{ij} \qquad \textit{(eq. 4.3)}$$

where μ is the molecular dynamic viscosity and s_{ij} is the strain-rate tensor:

$$s_{ij} = \frac{1}{2}\left(\frac{\partial u_i}{\partial x_j} + \frac{\partial u_j}{\partial x_i} \right) \qquad \textit{(eq. 4.4)}$$

There are mainly three ways to solve the Navier-Stokes equations over a fluid domain discretized through finite volumes, depending on the approach employed to consider the turbulence:

(i). Direct Numerical Simulation (DNS), where the equations are completely solved. In this case the domain and time discretization must be fine enough to computationally solve the motion flow field down to the smaller turbulence length scales in the turbulence spectra. Usually, this type of simulation requires a huge amount of computational resources since the number of grid cells must be proportional to Re^3.

(ii). Large Eddy Simulations (LES), where filtered equations are solved. In this case a new set of equations is obtained after the filtering. The domain discretization must reach a certain level of fineness proportional to the filter itself. All the length scales smaller than this threshold are modeled, while the larger scales are solved. This type of simulation requires a lower number of grid cells as compared to DNS. Nevertheless, it needs a significant use of computational resources.

(iii). Steady or Unsteady Reynolds-Averaged Navier-Stokes equations (RANS or URANS), where the whole turbulence spectrum energy content is modeled into a new set of equations arisen after the averaging process. This type of simulations is one of the cheapest from a computational resource point of view. In contrast to the two previous cases, it allows to solve two-dimensional problems, which means an additional saving in computational demand. Despite their many limits, RANS and URANS are approaches able to give reliable results for many aerodynamic problems.

Unsteady RANS Simulations

First of all, a brief description of the concept of Unsteady RANS (URANS) is carried out. According to Wilcox (1993), the three forms of Reynolds averaging most employed in turbulence-model research are: the time average, the spatial average and the ensemble average. The current case refers to the ensemble average.

To explain the URANS approach, it may be helpful to consider an instantaneous velocity component $u_i(\mathbf{x},t)$, related to a position $\mathbf{x}$ at time t, as the sum of a mean and a fluctuating part:

$$u_i(\mathbf{x},t) = U_i(\mathbf{x}) + u_i'(\mathbf{x},t) \qquad \textit{(eq. 4.5)}$$

where the velocity component $U_i(\mathbf{x})$, time-averaged over a finite time interval T, can be expressed as:

$$U_i(\mathbf{x}) = \lim_{T\to\infty} \frac{1}{T} \int_t^{t+T} u_i(\mathbf{x},t)\,dt \qquad \textit{(eq. 4.6)}$$

Since it is impossible to measure an infinite T in a physical flow, it is sufficient to consider a very long time T (as compared to the maximum period of the velocity fluctuations T_1), but, for flows in which the mean velocity component contains very slow variations, also the period of these variations T_2 must be considered. In this manner it is possible to re-write the average as:

$$U_i(\mathbf{x},t) = \lim_{T\to\infty} \frac{1}{T} \int_t^{t+T} u_i(\mathbf{x},t)\,dt \qquad T_1 \ll T \ll T_2 \qquad \textit{(eq. 4.7)}$$

In the current work, this interpretation (sketched in Fig. 4.1) can be applied assuming the hypothesis that the time scales T_2 (related, for instance, to the period of vortex shedding) and T_1 are separated by a spectral gap (i.e. the two time scales differ by several order of magnitude).

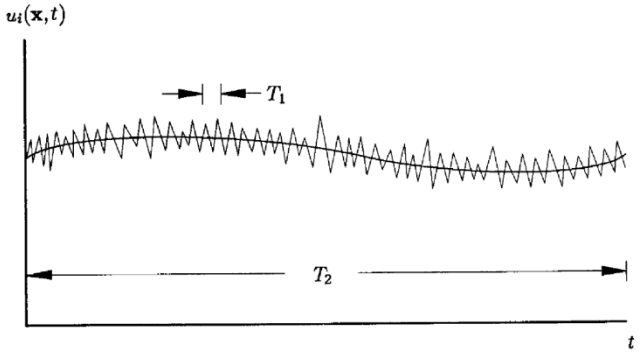

Fig. 4.1 - Time averaging for nonstationary turbulence (Wilcox, 1993).

It is worth pointing out that URANS cannot be considered as "Very Large Eddy Simulations" (V-LES), even if in some cases it could be more evocative (Speziale, 1998). Indeed, according to Shur *et al.* (2005), in URANS, grid refinement will not extend the range of resolved eddies as it occurs in LES. This is because in LES the differential equations are tied to the grid spacing, while in URANS they are not. In URANS, grid refinement leads to a solution closer to the exact solution of a system of equations. Nevertheless, it has been proven that the use of URANS to study the aerodynamics of a square cylinder gives better results than steady RANS (*e.g.* Iaccarino *et al.*, 2003, Raisee *et al.*, 2010).

4.1.1 Turbulence models tested

When the Navier-Stokes equations are Reynolds averaged, additional unknown quantities are introduced in the momentum equation, therefore, additional equations are required. The turbulence models provide these additional equations, modeling the effects of the turbulence on the mean, or slowly varying, flow. In particular, the Reynolds-averaged Navier-Stokes equations for an incompressible, Newtonian fluid, are expressed in the following form:

$$\frac{\partial U_i}{\partial x_i} = 0 \qquad \textit{(eq. 4.8)}$$

$$\rho \frac{\partial U_i}{\partial t} + \rho U_j \frac{\partial U_i}{\partial x_j} = -\frac{\partial P}{\partial x_i} + \frac{\partial}{\partial x_j}\left(2\mu S_{ij} - \rho\overline{u'_j u'_i}\right) \qquad \textit{(eq. 4.9)}$$

where the capital letter means an averaged variable.

The Reynolds-stress tensor $\rho\overline{u'_j u'_i}$ introduces six additional unknown quantities (it is symmetrical). Usually it is denoted as:

$$\tau_{ij} = -\rho\overline{u'_j u'_i} \qquad \textit{(eq. 4.10)}$$

The problem, after the average operation, has now ten unknown quantities (three mean-flow velocities + pressure + six Reynolds stress components) and only four equations (three momentum equations + continuity equation).

In this research, two turbulence models were alternatively tested to close the problem: the Spalart-Allmaras (SA) model, which introduces one additional equation, and the kω-SST

model, which introduces two additional equations. Both the models are based on the Boussinesq hypothesis, which states that the momentum transfer caused by turbulent eddies can be modeled as an eddy viscosity. Therefore, a linear relation is found between the Reynolds-stress tensor and the mean velocity gradients, expressed as:

$$\tau_{ij} = 2\mu_T S_{ij} + \delta_{ij}\sqrt{2}\nu_T \sqrt{S_{ij}S_{ij}} \Big/ \left(3a_1\right) \quad \textit{(for the Spalart Allmaras model)} \qquad \textit{(eq. 4.11)}$$

$$\tau_{ij} = 2\mu_T S_{ij} - \frac{2}{3}\rho k \delta_{ij} \qquad \textit{(for the kω-SST model)} \qquad \textit{(eq. 4.12)}$$

where μ_T is the eddy viscosity, S_{ij} is the mean strain-rate tensor and $k = 1/2\overline{u'_i u'_i}$ is the kinetic energy of the turbulent fluctuations. The term a_1 is called the "structure parameter", $\nu_T = \mu_T/\rho$ is the kinematic eddy viscosity.

Since a turbulence model provides the missing equation(s) to close the problem, aiming to reproduce the turbulence effects, different fluid dynamic problems require different turbulence models, *i.e.* it does not exists a "universal" turbulence model which could give accurate results for any flow condition.

When the system composed by the square cross-section and the screen with a through cavity is considered, the fluid dynamic problem is complicated by the simultaneous presence of confined (in the cavity) and unconfined (around the body) flows. Moreover, the experimental tests pointed out that, for a wind flow normal to the shielded face, an oscillating flow takes place into the cavity. According to Scotti and Piomelli (2002) such a flow condition represents a challenging test case for URANS models.

Both the SA and the kω-SST models were previously employed for two-dimensional simulations in bluff body aerodynamics. For instance, a modified version of the SA model was employed to study the wind action on two-dimensional square section by Soda *et al.* (2011), obtaining reliable results as compared to experimental tests. The kω–SST model was employed on the same geometry by Xu *et al.* (2011) who observed that, compared to other turbulence models (standard kε, RNG-kε, Realizable-kε, standard kω), the kω–SST model showed the best agreement with the experimental results.

Scotti and Piomelli (2002) investigated turbulence models for pulsating flow, concluding that the SA and an earlier version of the kω (the kω² model of Saffman and Wilcox, 1974) both give reasonably accurate results in terms of velocity profile. According to the Authors, these models might, however, be inaccurate to investigate quantities such as the Reynolds shear stress.

In the following, the turbulence models employed are described starting from their first versions in order to explain their theoretical basis. In particular, in this research the two turbulence models are employed as "Low-Reynolds" models, *i.e.* the equations are integrated through the viscous sub-layer down to the wall. This means that the equations are solved without the use of wall functions. This should allow a better modeling of the flow features, especially behind the screen. OpenFOAM® implements different versions of both the SA and the kω-SST turbulence models, depending on the software version. In the present work the version 2.3.1 was employed.

The Spalart-Allmaras turbulence model

The work carried out by Spalart and Allmaras (1992) minutely describes the development of the one-equation turbulence model "from scratch", based on the use of a modified eddy viscosity additional equation. In the current work the meaning of each term in the additional equation is synthetically explained. For a complete description of the model, the original paper is suggested.

The modified eddy viscosity transport equation is:

$$\frac{D\tilde{\nu}}{Dt} = c_{b1}\left[1 - f_{t2}\right]\tilde{S}\tilde{\nu} + \frac{1}{\sigma}\left[\nabla\cdot\left(\left(\nu+\tilde{\nu}\right)\nabla\tilde{\nu}\right) + c_{b2}\left(\nabla\tilde{\nu}\right)^2\right] - \left[c_{w1}f_w - \frac{c_{b1}}{\kappa^2}f_{t2}\right]\left[\frac{\tilde{\nu}}{d}\right]^2 + f_{t1}\Delta U^2 \qquad \textit{(eq.4.13)}$$

The transported quantity is the modified eddy viscosity $\tilde{\nu}$, as highlighted by the total derivative on the left-hand side of the equation, and it is necessary in eq. 4.11 to close the problem. Symbols and letters employed are:

- the "~" cap over the letters, which indicates a modified quantity;
- c, σ and κ, which are constants. In particular the last two are the Prandtl and the Von Karman numbers;
- f followed by the subscript indicates a blending function.

The concept of modified eddy viscosity arises to solve the equation in the near-wall viscous region. Indeed, the relation $\nu_T = \tilde{\nu} f_{v1}$ shows that, thanks to the use of the blending function f_{v1}, the eddy viscosity ν_T differs from $\tilde{\nu}$ only in the viscous region.

The first term on the right-hand side of eq. 4.13 is the production term. The basic idea is that, in the flows of interest, turbulence is found only where vorticity is, both emanating from the solid boundaries. The calibration constant c_{b1} is set equal to 0.1355.

The second term on the right-hand side is the diffusion term. It depends on the spatial derivatives of $\tilde{\nu}$, on the Prandtl number ($=2/3$) and the constant c_{b2} ($=0.622$).

The third term was introduced by explaining that in a boundary layer the blocking effect of a wall is felt at a distance through the pressure term, which acts as the main destruction term for the Reynolds shear stresses. This suggested the Author to introduce a destruction term in the transport equation for the eddy viscosity, inversely proportional to the wall distance d. This term tends to zero in free shear flows when d becomes large, and the non-dimensional functions f_w helps the destruction term for a better decay in the outer region of the boundary layer.

Finally, the last term (called "the trip term") is useful to obtain transition where desired. This term is neglected in the Spalart-Allmaras model implemented in the OpenFOAM® version employed in this work.

The kω-SST turbulence model

The kω-SST two-equation turbulence model by Menter (1992, 1993, 1994) is a mix of two other models: the kε model in its standard form (Jones and Launder, 1972, Launder and Sharma, 1974) and the kω model by Wilcox (1988), together with an additional feature to improve its behavior in adverse pressure gradient flows.

According to Menter, the kε model has demonstrated good performance in a large variety of flow conditions, but it is less accurate when adverse pressure gradients are involved. Moreover, the standard kε model needs the use of wall functions or damping functions when applied in low-Reynolds form. This is because the turbulence dissipation rate ε does not go to zero at a no-slip surface.

On the other hand, the kω model performs better than the kε models under adverse pressure gradient conditions, it has a simple formulation in the viscous sublayer, but it exhibited a strong dependence on the freestream value of ω (turbulence frequency).

The kω-SST blends these two models in order to take advantage of the strong points of both of them. Indeed, the model is identical to the kω model of Wilcox for the inner region of a boundary layer (up to approximately $\delta/2$, where δ is the boundary layer thickness) and gradually changes to the high Reynolds number version of the kε model of Jones and Launder (1972) in the outer region. Therefore, in order to perform the computations with just one set of equations, the Jonas-Launder kε model is re-written in a kω formulation, while the blending between the two regions is performed by a blending function.

Moreover, on the basis of the good results obtained with the Johnson and King model (1988), which accounts for the effect of the transport of the principal turbulent shear-stress, the model has a further feature: the SST (Shear-Stress Transport). Menter (1991), referring to the kε and kω models, re-wrote the equation of the turbulent shear-stress for a boundary layer, outside the viscous sublayer. Therefore the equation:

$$-\overline{u'v'} = c_\mu \frac{k^2}{\varepsilon}\frac{\partial u}{\partial y} = \frac{k}{\omega}\frac{\partial u}{\partial y} \qquad \textit{(Menter's notation)} \qquad \textit{(eq. 4.14)}$$

was re-written to obtain:

$$-\overline{u'v'} = \sqrt{\frac{Production_k}{Dissipation_k}}\, a_1 k \qquad \textit{(Bradshaw's assumption in Menter's notation)} \qquad \textit{(eq. 4.15)}$$

Menter noticed that for an equilibrium boundary layer, the ratio of production to dissipation is close to one in the outer part of the layer, so to obtain $-\overline{u'v'} = a_1 k$. Differently, for an adverse pressure gradient flow this ratio can be larger than one. Therefore, on the basis of experimental results (Driver, 1991), Menter underlined the necessity to limit the turbulent shear-stress to the maximum values measured in adverse pressure-gradient flow. These considerations to overtake the problem of the high shear-stress levels produced in adverse pressure-gradient flows (in the standard kω model by Wilcox) were implemented through a modification of the eddy viscosity term (as shown in the following eq. 4.25).

Hereafter the main equations to describe the kω-SST model (Menter, 1992) are summarized, starting from the original kω and the transformed kε models.

The original kω model reads:

Turbulent kinetic energy

$$\frac{\partial \rho k}{\partial t} + \frac{\partial \rho u_j k}{\partial x_j} = P_k - \beta^* \rho \omega k + \frac{\partial}{\partial x_j}\left[\left(\mu + \sigma_{k1}\mu_T\right)\frac{\partial k}{\partial x_j}\right] \qquad \textit{(eq. 4.16)}$$

Specific turbulent dissipation rate

$$\frac{\partial \rho \omega}{\partial t} + \frac{\partial \rho u_j \omega}{\partial x_j} = \gamma_1 P_\omega - \beta_1 \rho \omega^2 + \frac{\partial}{\partial x_j}\left[\left(\mu + \sigma_{\omega 1}\mu_T\right)\frac{\partial \omega}{\partial x_j}\right] \qquad \textit{(eq. 4.17)}$$

The transformed kε model reads:

Turbulent kinetic energy

$$\frac{\partial \rho k}{\partial t}+\frac{\partial \rho u_j k}{\partial x_j}=P_k-\beta^*\rho\omega k+\frac{\partial}{\partial x_j}\left[\left(\mu+\sigma_{k2}\mu_T\right)\frac{\partial k}{\partial x_j}\right] \qquad \textit{(eq. 4.18)}$$

Specific turbulent dissipation rate

$$\frac{\partial \rho \omega}{\partial t}+\frac{\partial \rho u_j \omega}{\partial x_j}=\gamma_2 P_\omega-\beta_2\rho\omega^2+2\rho\sigma_{\omega2}\frac{1}{\omega}\frac{\partial k}{\partial x_j}\frac{\partial \omega}{\partial x_j}+\frac{\partial}{\partial x_j}\left[\left(\mu+\sigma_{\omega2}\mu_T\right)\frac{\partial \omega}{\partial x_j}\right] \qquad \textit{(eq. 4.19)}$$

where:

$$P_k=\mu_T\frac{\partial u_i}{\partial x_j}\left(\frac{\partial u_i}{\partial x_j}+\frac{\partial u_j}{\partial x_i}\right)-\frac{2}{3}\rho k\delta_{ij}\frac{\partial u_i}{\partial x_j}$$

$$P_\omega=\rho\frac{\partial u_i}{\partial x_j}\left(\frac{\partial u_i}{\partial x_j}+\frac{\partial u_j}{\partial x_i}\right)-\frac{2}{3}\rho\omega\delta_{ij}\frac{\partial u_i}{\partial x_j}$$

with the following constants (for the two sets):

$\sigma_{k1}=0.5$; $\sigma_{\omega1}=0.5$; $\beta_1=0.0750$; $\beta^*=0.09$; $\kappa=0.41$; $\gamma_1=\beta_1/\beta^*-\sigma_{\omega1}\kappa^2/\sqrt{\beta^*}$

$\sigma_{k2}=1.0$; $\sigma_{\omega2}=0.856$; $\beta_2=0.0828$; $\beta^*=0.09$; $\kappa=0.41$; $\gamma_2=\beta_2/\beta^*-\sigma_{\omega2}\kappa^2/\sqrt{\beta^*}$

The equations of the original kω model are multiplied by the blending function F_1, while those of the transformed kε model are multiplied by $(1-F_1)$; then they are added together to give the kω-SST model:

$$\frac{\partial \rho k}{\partial t}+\frac{\partial \rho u_j k}{\partial x_j}=P_k-\beta^*\rho\omega k+\frac{\partial}{\partial x_j}\left[\left(\mu+\sigma_k\mu_T\right)\frac{\partial k}{\partial x_j}\right] \qquad \textit{(eq. 4.20)}$$

$$\frac{\partial \rho \omega}{\partial t}+\frac{\partial \rho u_j \omega}{\partial x_j}=\gamma P_\omega-\beta\rho\omega^2+2\rho\left(1-F_1\right)\sigma_{\omega2}\frac{1}{\omega}\frac{\partial k}{\partial x_j}\frac{\partial \omega}{\partial x_j}+\frac{\partial}{\partial x_j}\left[\left(\mu+\sigma_\omega\mu_T\right)\frac{\partial \omega}{\partial x_j}\right] \qquad \textit{(eq. 4.21)}$$

In the kω-SST, each constant φ_1 from the original kω model (σ_{k1},…) and the respective constant φ_2 from the transformed kε model (σ_{k2},…) are related to the constant of the new model (σ_k,…) through the following relation:

$$\varphi=F_1\varphi_1+\left(1-F_1\right)\varphi_2 \qquad \textit{(eq. 4.22)}$$

The blending function is expressed as:

$$F_1=\tanh\left(\arg_1^4\right) \qquad \textit{(eq. 4.23)}$$

$$\arg_1=\max\left(\min\left(\frac{\sqrt{k}}{0.09\omega y};0.45\frac{\omega}{\Omega}\right);\frac{400\nu}{y^2\omega}\right) \qquad \textit{(eq. 4.24)}$$

Where :

- Ω is the absolute value of the vorticity;
- The first argument $\frac{\sqrt{k}}{0.09\omega y}$ indicates the turbulent length scale $\frac{\sqrt{k}}{0.09\omega}\left(=\frac{k^{3/2}}{\varepsilon}\right)$ divided by the distance to the closest surface y;

- The second argument $0.45\frac{\omega}{\Omega}$ is needed to limit the spurious solution of the original kω model with small freestream values;
- The third argument $\frac{400\nu}{y^2\omega}$ ensures that the function F_1 does not go to zero in the viscous sublayer.

The eddy viscosity (which includes the SST modification) assumes the form:

$$\nu_T = \frac{a_1 k}{\max\left(a_1\omega; \Omega F_2\right)} \qquad \textit{(eq. 4.25)}$$

where the blending function F_2 is defined in a similar way to F_1, and limits ν_T, as expressed below:

$$\arg_2 = \max\left(2\frac{\sqrt{k}}{0.09\omega y}; \frac{400\nu}{y^2\omega}\right) \qquad \textit{(eq. 4.26)}$$

$$F_2 = \tanh\left(\arg_2^2\right) \qquad \textit{(eq. 4.27)}$$

This form of the eddy viscosity leads to a lower eddy viscosity estimation, and it requires the modification of the constants in the first set of equations as follows:

$\sigma_{k1} = 0.85$; $\sigma_{\omega 1} = 0.65$; $\beta_1 = 0.0750$; $\beta^* = 0.09$; $\kappa = 0.41$; $\gamma_1 = \beta_1/\beta^* - \sigma_{\omega 1}\kappa^2/\sqrt{\beta^*}$

Finally, once the k and ω are evaluated, through eq. 4.12, the problem can be closed and numerically solved. In particular, the term $\mu_T = \rho\nu_T$ of such equation takes into account for the eddy viscosity reported in eq. 4.25, which, in turn, may assume the $k\omega$ standard form $\left(\nu_T = \frac{k}{\omega}\right)$ or the SST modified form $\left(\nu_T = \frac{a_1}{\Omega F_2}\right)$.

4.1.2 Domain discretization

The computational domain was discretized through the BlockMesh mesh generator. It is included in the open source package of OpenFOAM® and it is a powerful mesh generator in case of simple geometries with sharp edges because it allows the generation of cartesian grids. The BlockMesh mesh generator allows a geometrically isotropic grid refinement all over the computational domain. Moreover, thanks to the cartesian grid, the mesh skewness was null and the mesh non-orthogonality problem completely avoided.

Other mesh generators were tested: from the open source SnappyHexMesh, Salome, Gmsh to the commercial software Ansa from BetaCAE Systems. This exploratory part of the work showed that each of the aforementioned mesh generators has pro and cons, proving that the choice of the tool to use depends on the case study features. For instance, if there was the necessity to rotate the studied two-dimensional section (in order to change the angle of attack), a mesh generator different from BlockMesh would have been needed.

The domain employed in all the simulations is sketched in Fig. 4.2. Its overall dimensions were fixed in order both to ensure a low blockage ratio and to avoid problems due to boundaries too close to the studied object. The number of cells slightly varies depending on the case study. According to Spalart's recommendation (2000, 2001), the growth ratio of the cells size away from the wall (measured in the direction normal to the wall surface) was maintained around to 1.2, as detailed in section 4.2. The mesh designed for the reference case study with the screen ($Re = 7.56\times10^4$) was also employed for the cases with lower Re values.

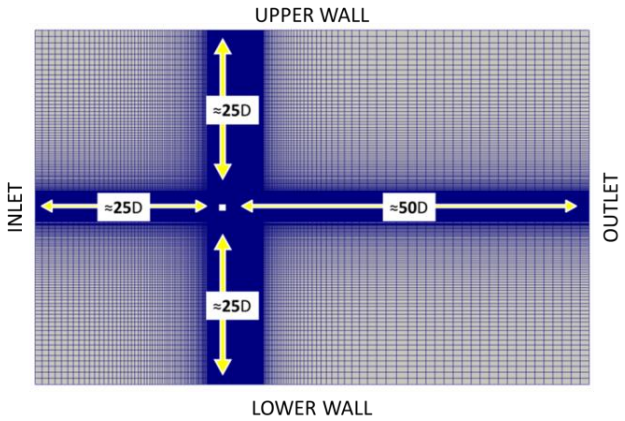

Fig. 4.2 - Computational domain defined in terms of the characteristic body dimension.

4.1.3 Boundary and Initial Conditions

The boundary and initial conditions are fundamental to properly define, and then to solve, the case study. The studied marching problem is governed by parabolic equations, so that initial conditions are needed in the entire domain, and conditions on all the boundaries are required for all the simulation time.

The physical boundaries that delimit the computational domain are: the *Inlet* and *Outlet*, the lateral sides (*UpperWall* and *LowerWall*), the faces of the object (*StlSurface*) and finally the *Front* and *Back* sides of the domain (OpenFOAM® deals only with three-dimensional domains). An example is given in Tab. 4.1, where the boundary and initial conditions are described for the simulations carried out with the SA model. It is worth noting that the *StlSurface* boundary includes all the object faces even if they are disconnected, as in the case of the square with the screen.

In Tab. 4.1, *U* and *p* are velocity and pressure, while *nut* and *nuTilda* (according to the OpenFOAM® file names) are respectively the eddy viscosity (ν_T) and the modified eddy viscosity $(\tilde{\nu}_T)$. The boundary condition typologies are explained through the names employed in the program files (*i.e. zeroGradient* means that the specific quantity respects a Neumann condition which imposes a null gradient across that boundary). It is worth noting that the boundary condition at the Outlet is a particular Neumann condition with an additional feature to avoid reflection. Moreover, the *empty* condition (at the Front and Back) is employed in two-dimensional simulations to speed up the solution.

To complete the description, at the instant t=0 also the internal field must have a starting value (namely, an initial condition), as reported in Tab. 4.2.

The values employed in Tab. 4.1 and Tab. 4.2 refers to the case $Re = 7.56\times10^4$, that corresponds to a Womersley number *(Wo)* equal to 6 when the body section is equipped with the screen. The boundary and initial values of eddy viscosity are set according to the prescriptions of Spalart and Allmaras (1992).

	U	p	nut	nuTilda
Inlet	type fixedValue; value uniform (0.189 0 0)	type zeroGradient;	type calculated; value uniform 1.05e-07	type fixedValue; value uniform 1.5e-06
Outlet	type inletOutlet; inletValue uniform (0.189 0 0) value uniform (0 0 0)	type fixedValue; value uniform 0	type zeroGradient;	type zeroGradient;
UpperWall	type symmetryPlane;	type symmetryPlane;	type symmetryPlane;	type symmetryPlane;
LowerWall	type symmetryPlane;	type symmetryPlane;	type symmetryPlane;	type symmetryPlane;
FrontAndBack	type empty;	type empty;	type empty;	type empty;
StlSurface (*e.g.* The Square Section)	type fixedValue; value uniform (0 0 0)	type zeroGradient;	type fixedValue; value uniform 1e-20	type fixedValue; value uniform 1e-20

Tab. 4.1 - Boundary and initial conditions with the SA model.

	U	p	nut	nuTilda
Internal Field	uniform (0.189 0 0)	uniform 0;	uniform 1.05e-07	uniform 1.5e-06

Tab. 4.2 - Internal field initial conditions.

4.1.4 Adopted numerical schemes

OpenFOAM® employs a cell-centered finite volume method, and it gives the user the possibility to set the whole numerical procedure. The main information about the numerical set up are reported in the following.

The backward differencing method was employed for time discretization. It is an implicit second-order method, provided that the spatial discretization is also second-order accurate. The convection term was discretized through the application of the Gauss theorem, where the interpolation scheme to obtain the face values of the variables was a central differencing scheme blended with an upwind scheme. The same blended scheme was employed for the transport of $\tilde{\nu}$. The diffusion term was discretized in a similar way to the convection terms, but the interpolation scheme employed was a central differencing. A similar set-up was adopted with the kω–SST model, where, for the transport equations of k and ω, the same scheme employed for the transport of $\tilde{\nu}$ was used. It is worth noting that the use of a cartesian grid ensures the absence of non-orthogonality and skewness errors.

The PIMPLE algorithm, a combination of the PISO and the SIMPLE algorithms, was employed for pressure-velocity coupling. Regarding the time step, the use of implicit time schemes allows overtaking the Courant-Friedrichs-Lewy (CFL) stability condition. This condition, usually indicated through the Courant number (Co), relates the time step (Δt) of the time-marching simulation with the local value of velocity (u) and the dimension (Δx) of each cell all over the domain. The condition is usually expressed as:

$$Co = \Delta t \cdot \frac{u}{\Delta x} < 1 \qquad \textit{(eq. 4.28)}$$

Generally, in CFD the goal is to accurately solve the equations also when the maximum Courant number $(\max Co)$ is higher than 1, in order to speed up the simulations. The PIMPLE

algorithm used, namely *pimpleFoam*, allows fixing a $\max Co$ all over the domain, instead of adopting a constant time step. When the simulation reaches a steady regime, the time step does not vary much, and therefore it is possible to associate a characteristic time step (Δt_{ch}) with each $\max Co$ fixed. Moreover, Δt_{ch} can be expressed in a non-dimensional form as:

$$\Delta t^* = \Delta t_{ch} \cdot \frac{U_\infty}{D} \qquad \textit{(eq. 4.29)}$$

Physically, this parameter may represents the ratio of the free-stream flow velocity and unit convection velocity of the body (Soda *et al.* 2011).

The GAMG (Geometric Agglomerated algebraic Multi-Grid) solver, was employed to solve the discretized system of equations. The GAMG uses a coarser grid with fast solutions to smooth out high frequency errors and to generate a starting solution for the finer grid. The solver was employed together with smoothers as the DIC / Gauss-Seidel, in which the simplified diagonal-based incomplete Cholesky smoother for symmetrical matrices is followed by the Gauss-Seidel smoother to ensure that any possible spikes created by the DIC are smoothed out (Behrens, 2009).

4.1.5 Data processing

Since a variable time step was used, the data were first resampled with a constant frequency of about 100÷200 points per period of vortex shedding (depending on the time-step and grid employed). The first part of each simulation exhibits a transient prior to reaching a stable condition of vortex shedding. Evaluating a moving average on the force coefficients and through a visual check, it was possible to consider only the simulation in a developed vortex shedding conditions, neglecting the first part. An example for the square section is reported in Fig. 4.3. It is to note that in many cases, this first part of the computations was obtained with first-order schemes or with coarser meshes.

The force coefficient signals were first analyzed to determine the opportune duration of the simulation. The solution was considered converging when the relative error between the mean value at a certain time and its value two periodicity before, was less than 0.0001. The simulation convergence was also checked by a visual control. The transient part of the solution was also excluded in the analysis of pressures and flow velocities.

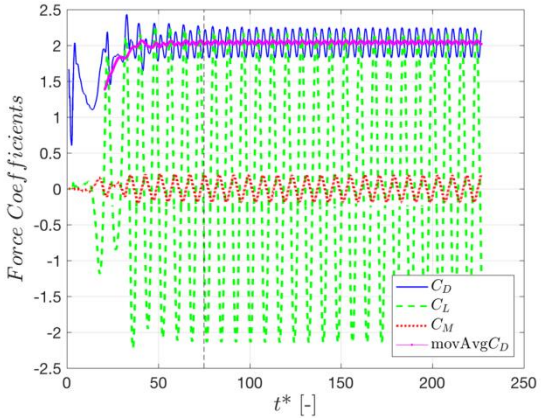

Fig. 4.3 - Computed time histories of the force coefficients with the initial transient part. Medium grid with *maxCo*=4 case study. In this case, the statistics are calculated over the signals after the black dotted line (t^*= 75). The moving average of the drag coefficient signal improved the visual check on the simulation convergence.

4.2 The square cross-section case

Preliminary investigations were carried out on the square cross-section with approaching smooth flow perpendicular to a body face. The simulations were carried out at $Re = 7.56 \times 10^4$, in order to evaluate the best numerical set-up in terms of domain discretization and time step. This Reynolds number was chosen because it was the smallest value that allowed a direct comparison with the experimental tests. With this aim, a grid convergence study was carried out with three grids and the SA turbulence model. The main characteristics of the computational meshes (Fig. 4.4) are summarized in Tab. 4.3. In particular, the *stretching factor* indicates the growth ratio between two consecutive cells, measured in the proximity of the body wall, in direction normal to the wall surface. The *cell dimension in wake* represents the mean cell size around the body, in the portion of the domain external to the near wall region, where the formation of vortices is expected to occur. Similarly, the *normalized cell size closest to the wall* (n_W/D) indicates the level of refinement in the near wall region for each tested grid.
As in the experimental campaign, the results of the numerical simulations are reported in terms of global and local aerodynamic parameters. Aerodynamic coefficients and mean recirculation length of the wake (normalized respect to the body cross-section D) are considered as global parameters. The pressure coefficients, at the separation point and at the base, represent the local parameters. The dimensionless wall distance y^+ is used as an indicator of the wall refinement accuracy. Given the dimension of a cell at the wall surface n_w, for a fluid characterized by a viscosity υ, the y^+ is defined as:

$$y^+ = \frac{u_* n_w}{\upsilon} \qquad \textit{(eq. 4.30)}$$

where u_* is a characteristic non-dimensional velocity at the wall (the friction velocity), evaluated as the square root of the ratio of the wall shear stress to the fluid density. It is to note that, for every studied case, the maximum y^+ value reported in the following (*e.g.* Tab. 4.5) was limited to very few cells close to the edges, in the proximity of the separation point.
Finally, it is to note that, due to its relation with the grid dimension, to fix the same $\max Co$ for different meshes does not correspond to employ the same time step. In this work, $\max Co$ numbers equal to 4, 2 or 1 were used, so that, in Tab. 4.4, a representative value of the normalized time-steps (Δt^*) (evaluated in a regime of regular vortex shedding) related to the tested grids are reported. In the following, considerations about the time step will be carried out referring to the $\max Co$.

	N° of cells	n_W/D	Stretching Factor	Cell dimension in wake
Coarse	59365	6e-4	1.28	*D*/40
Medium	118888	4.95e-4	1.19	*D*/60
Fine	240839	3.5e-4	1.13	*D*/85

Tab. 4.3 - Characteristics of the grids employed in the grid convergence study.

	Coarse Grid			Medium Grid			Fine Grid		
$\max Co$	1	2	4	1	2	4	1	2	4
Δt^*	0.0004	0.0008	0.0016	0.0002	0.0005	0.001	0.0002	0.0004	0.0008

Tab. 4.4 - Maximum Courant number and relative non-dimensional time step.

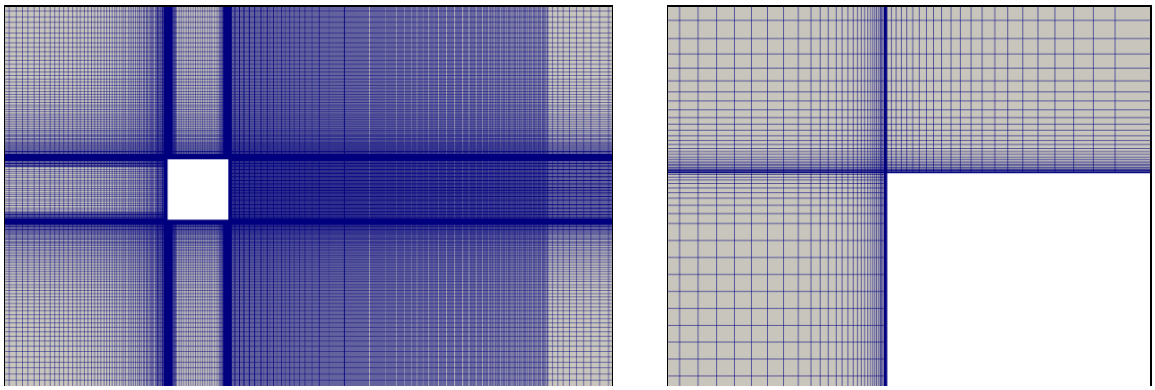

Fig. 4.4 - Two views of the fine mesh: the refinement in the wake region (left); close-up view of the sharp edge refinement (right). The overall domain coincides with the one shown in Fig. 4.2.

Firstly, the grid convergence study was carried out with a $\max Co = 4$. Even if the results showed good agreement with the experiments reported in the previous chapter, in terms of both global (Tab. 4.5) and local (Tab. 4.6) parameters, with $\max Co = 4$ it was not possible to appreciate the effects of the grid refinement.

As reported in Tab. 4.7 and Tab. 4.8, the study was repeated on the same meshes with a smaller time step ($\max Co = 2$) in order to investigate the convergence of the numerical solution. By comparing the results to those obtained in the previous simulations, it is apparent that, while refining the mesh, the solution of the equations does not tend to the experimental results (see Chap. 3). Moreover, as shown in Tab. 4.7, the medium grid exhibits a different solution as compared to the coarse or fine one, so that, in order to clarify this point, a time convergence study was also carried out employing the medium grid.

With the results summarized in Tab. 4.9 and Tab. 4.10, it is possible to interpret those previously obtained in the following way: after the time step reduction from $\max Co = 4$ to $\max Co = 2$, the coarse and the fine grids tend to converge to the numerical solution of the system of equations. It seems that, respectively, the $\max Co = 2$ time step was fine enough for the coarse grid, while the fine grid was intrinsically accurate enough to work with such a "large" time step (Tab. 4.7 and Tab. 4.8). By contrast, the medium grid represented an intermediate condition, which seemed to be in better agreement with the experimental results, but that was "affected" by the time step corresponding to $\max Co = 2$. The further reduction of the time step down to $\max Co = 1$ with the medium grid confirmed that the numerical solution of the governing equations tends to the unphysical one, with $St \simeq 0.1$, as in the case of the fine grid reported in Tab. 4.7 and Tab. 4.8.

GLOBAL PARAMETERS	Drag coefficient (C_D)	Lift coefficient standard deviation (C_L')	Drag coefficient standard deviation (C_D')	Strouhal number (St)	Mean recircul. length (L_C/D)	$\max\left(y^+\right)$
Coarse	2.07	1.57	0.17	0.128	0.5	4÷5
Medium	2.04	1.54	0.15	0.125	0.6	3÷4
Fine	2.02	1.52	0.13	0.126	0.5	2÷3

Tab. 4.5 - Grid convergence results in terms of global parameters with $\max Co$=4.

LOCAL PARAMETERS	Mean base pressure coefficient ($\overline{C_{bp}}$)	Standard deviation base pressure coefficient (C_{bp}')	Separation point mean pressure coefficient ($\overline{C_{sep}}$)	Separation point pressure coeff. standard deviation (C_{sep}')
Coarse	-1.39	0.24	-1.70	0.89
Medium	-1.37	0.22	-1.71	0.87
Fine	-1.32	0.20	-1.69	0.84

Tab. 4.6 - Grid convergence results in terms of local parameters with maxCo=4.

GLOBAL PARAMETERS	C_D	C_L'	C_D'	St	L_C/D	$\max(y^+)$
Coarse	1.91	1.48	0.12	0.116	0.7	4÷5
Medium	2.03	1.52	0.15	0.126	0.5	3÷4
Fine	1.98	1.30	0.36	0.104	0.9	2÷3

Tab. 4.7 - Grid convergence results in terms of global parameters with maxCo=2.

LOCAL PARAMETERS	$\overline{C_{bp}}$	C_{bp}'	$\overline{C_{sep}}$	C_{sep}'
Coarse	-1.15	0.15	-1.57	0.69
Medium	-1.34	0.21	-1.67	0.86
Fine	-1.21	0.47	-1.57	0.64

Tab. 4.8 - Grid convergence results in terms of local parameters with maxCo=2.

GLOBAL PARAMETERS	C_D	C_L'	C_D'	St
$\max Co = 1$	2.00	1.40	0.24	0.116
$\max Co = 2$	2.03	1.52	0.15	0.126
$\max Co = 4$	2.04	1.54	0.15	0.125

Tab. 4.9 - Global results of the time-step convergence study with the medium grid.

LOCAL PARAMETERS	$\overline{C_{bp}}$	C_{bp}'	$\overline{C_{sep}}$	C_{sep}'
$\max Co = 1$	-1.23	0.31	-1.68	0.74
$\max Co = 2$	-1.35	0.22	-1.71	0.86
$\max Co = 4$	-1.37	0.22	-1.71	0.87

Tab. 4.10 - Local results of the time-step convergence study with the medium grid.

The preliminary tests seem to show that the simulations carried out with the SA model tend to the experimental results when additional (numerical) viscosity is introduced either increasing the time step or coarsening the mesh.

In Tab. 4.11, the results obtained in three representative configurations of these preliminary studies are compared to some works (CFD and experimental), with a focus on URANS simulations performed on the two-dimensional square section. The main aerodynamic coefficients obtained with the medium grid and a $\max Co = 2$ ($\Delta t^* = 0.0005$), exhibit differences around 10-15% as compared to the experimental results (uncorrected for blockage effects) obtained in the present work. Moreover, despite the simplicity of the SA model, the results (except the mean recirculating wake length) are comparable to other URANS studies performed with more sophisticated turbulence models, such as the two-equation Linearized Explicit Algebraic kω model (LEA), used by Soda *et al.* (2011).

On the other hand, the comparison with the literature, especially with more reliable studies on square cylinders (such as those performed by means of DNS and experimental tests), is quite tricky to interpret, since the case *Medium* ($\max Co = 2$) exhibits similar values of aerodynamic

coefficient but not of L_c / D, while the case *Fine* $(maxCo = 2)$ seems to predict this parameter but not the frequency of vortex shedding.

However, the CFD results reported in Tab. 4.11, are considered also to complete the observations discussed above on the effects encountered by reducing the time step (case *Medium* $(maxCo = 1)$) or the mesh size (case *Fine* $(maxCo = 2)$).

The only literature reference, among those reported in Tab. 4.11, which used OpenFOAM® is the work by Tian *et al.*, (2012). The Authors investigated the time-step convergence in a range $0.004 < \Delta t^* < 0.006$, and near-wall refinement in the range $0.0015 < n_W / D < 0.004$, obtaining variations of a few percentage. Both the parameters were an order of magnitude higher than in the present work. In their final set-up, the maximum y^+ value, namely $\max\left(y^+\right)$, was equal to 8.4. Given the different parameters range, and the different turbulence model used, a direct comparison with the results by Tian *et al.* (2012) is not possible.

It remains an open question if the unexpected solution trend encountered in the present work (by refining the mesh or the time step) concerns the turbulence model accuracy, or other issues such as its numerical implementation, so that, further investigations are needed.

Nevertheless, aware that the square section is a challenging case for numerical simulations (Rodi *et al.*, 1997), the simulations seem to be still suitable for the qualitative results aimed to integrate the experimental campaign of the square section with the screen.

	Turb. model	C_D	C_L'	C_D'	St	L_c / D
Medium $(\max Co = 2)$	SA	2.03	1.52	0.15	0.126	0.5
Medium $(\max Co = 1)$	SA	2.00	1.40	0.24	0.116	0.7
Fine $(\max Co = 2)$	SA	1.98	1.30	0.36	0.104	0.9
Lübcke *et al.*, 2001	EASM	2.21	0.95	-	0.15	1.64
Iaccarino *et al.*, 2003	$\upsilon^2 - f$	2.22	1.83	0.06	0.141	1.45
Soda *et al.*, 2011	LEA	1.99	1.41	0.17	0.126	1.31
Xu *et al.*, 2011	Std kε	1.59	0.17	-	0.121	2.30
=	RNG - kε	1.94	1.11	-	0.136	0.87
=	Realizable - kε	2.02	1.15	-	0.139	0.83
=	Std kω	2.14	1.50	-	0.131	0.53
=	kω - SST	2.09	1.39	-	0.121	0.91
Tian *et al.*, 2012	kω - SST	2.06	1.49	-	0.136	-
Rodi, 1997 *	RANS	1.64-2.43	0.31-1.49	0-0.27	0.134-0.159	0.98-2.80
Rodi, 1997 *	LES	2.02-2.77	1.15-1.79	0.14-0.27	0.09-0.15	0.94-1.68
Trias *et al.*, 2015	DNS	2.18	1.71	0.205	0.132	1.04
Lyn *et al.*, 1995	Experimental	-	-	-	0.132	0.87
Lander *et al.,* 2016	Experimental	2.35	1.14	-	0.114(**)	0.83(**)
Present work	Experimental	2.34	1.39	-	0.125	-

Tab. 4.11 - Comparison of the results obtained on the square cross-section with some literature data ("Std" means standard version of the turbulence model).

(*) results presented in the ERCOFTAC workshop (Rodi *et al.*, 1997).

(**) values reported from Fig. 5 and Fig. 10 of the original paper.

4.3 The system with square cross-section and screen S1 at *D*/20

The two-dimensional system composed by the square section and the screen S1 fixed at *D*/20, with an approaching smooth flow perpendicular to the shielded face, was modeled building a mesh with the same characteristics of the fine grid (Tab. 4.3). This choice was suggested by both the grid-convergence study and the geometry details, such as the screen thickness (*D*/120) and/or the gap width (*D*/20). Simulations were carried out with two turbulence models (SA and kω-SST), and a time step corresponding to $\max Co = 2$. Theoretically, the presence of an additional part (the screen) modifies the problem geometry, thus requiring an additional grid-convergence study. This was not done, but the cavity was finely discretized, with 30 cells in the direction normal to the cavity walls, gradually refined moving toward the surface, in order to reach a maximum y^+ similar to that obtained without the screen (Fig. 4.5).

The results of the simulations were firstly compared to the experimental results, in order to assess their reliability. As with the previous studies, once the convergence was reached (Fig. 4.6), the comparison was based on the analysis of global (Tab. 4.12) and local (Tab. 4.13) parameters.

The mean aerodynamic coefficients evaluated with the SA model agree well with the experimental results, as reported in Tab. 4.12 and Tab. 4.13. The lift coefficient standard deviation obtained with the SA model, is around 15% higher than the experimental value, while the remaining global coefficient are closer to the wind-tunnel test results. However, such a discrepancy is considered acceptable for the purposes of the present work. The global parameters are in good agreement also with the results obtained with the two-equations kω-SST model, with the exception of C_D, which is slightly smaller than the experimental value.

The mean pressure coefficients are comparable to the experimental results (Fig. 4.7-left), even if, behind the screen, the SA model gives a mean pressure 10% lower than the experimental results.

The main differences observed (the discrepancies are of the order of 10-20%) are related to the fluctuating components of pressure coefficients. In particular, with both the turbulence model, the reference pressure coefficient standard deviation at the separation point is overestimated as compared to the experimental results, and a difference around the 20% was observed. However, quite surprisingly, with the SA model, the pressure coefficient standard deviations in the trailing edge region (on the lateral body side and at the base) agree with the experimental results better than with the kω-SST model (Fig. 4.7-right). It is worth noting that the pressure coefficients corresponding to symmetrical points are averaged to speed up the convergence of the results.

Generally, the results obtained are satisfactory for the sake of complementing the experimental study.

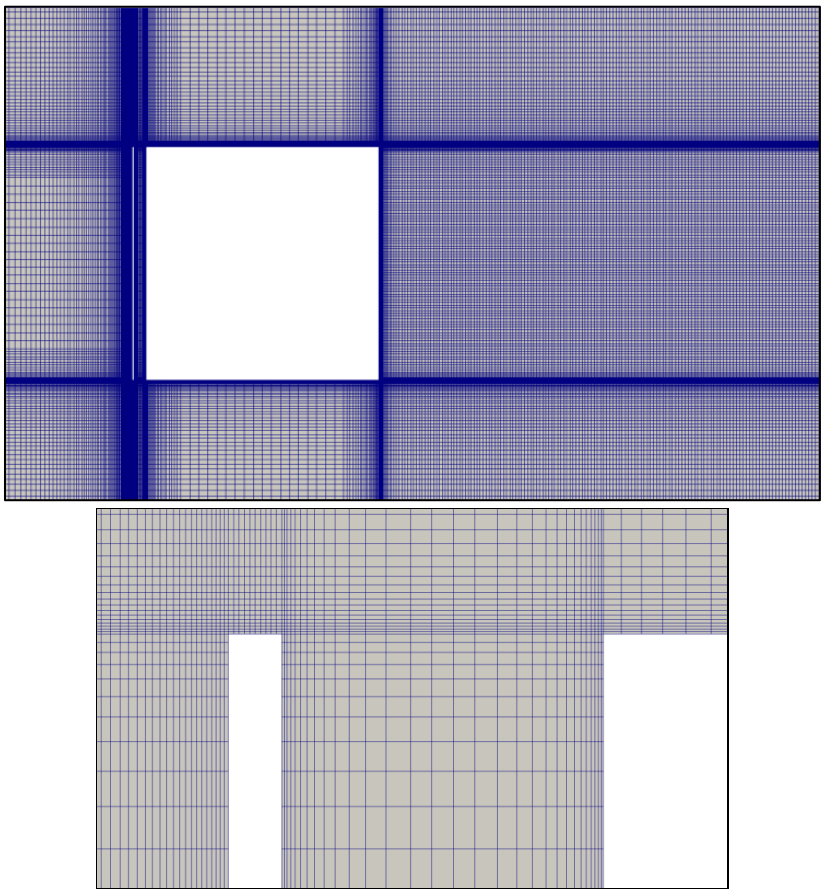

Fig. 4.5 - Mesh domain of the square cross-section with the screen S1 fixed at *D*/20: refinement in the wake region (top) and detail of the discretization at the upper cavity extremity (bottom).

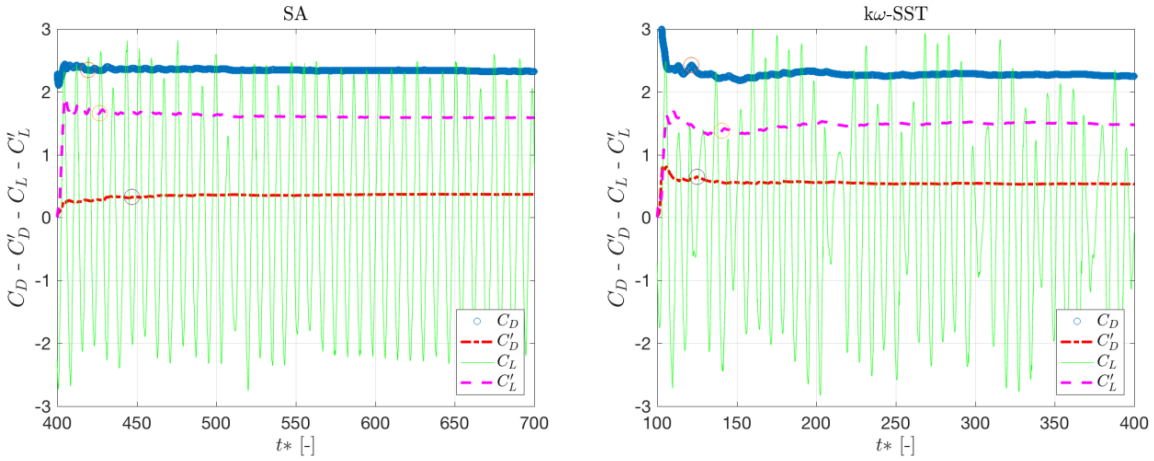

Fig. 4.6 - Convergence in mean of the simulations: results with the SA model (left) and with the kω-SST model (right). In both cases, the mean convergence trend of mean drag coefficient (C_D), drag standard deviation (C_D') and lift coefficient standard deviation (C_L') are shown with the lift coefficient time history. The circular markers indicate when the convergence criterion was satisfied for C_D, C_D' and C_L'. However the visual check suggested to further extend the simulations.

GLOBAL PARAMETERS	No Screen SA (Fine)	No Screen Experimental	Screen S1 *D*/20 SA	Screen S1 *D*/20 kω-SST	S1 – *D*/20 Experimental
Drag coefficient C_D	1.99	2.34	2.32	2.25	2.34
Rear body drag coefficient C_{DRB}	1.22	1.53	1.59	1.51	1.53
Strouhal number St	0.104	0.125	0.126	0.131	0.121
Lift coefficient standard deviation C_L'	1.30	1.40	1.60	1.45	1.35
Drag coefficient on the screen C_{DS}	-	-	2.91	2.77	2.82

Tab. 4.12 - Global parameters without and with the screen S1 at *D*/20. Comparison of the experimental results with the SA and kω-SST models.

LOCAL PARAMETERS	No Screen SA (Fine)	No Screen Experimental	Screen S1 *D*/20 SA	Screen S1 *D*/20 kω-SST	S1 – *D*/20 Experimental
Mean base pressure coefficient $\overline{C_{bp}}$	-1.21	-1.55	-1.68	-1.54	-1.57
Standard deviation base pressure coefficient C_{bp}'	0.47	0.35	0.46	0.71	0.37
Separation point mean pressure coefficient $\overline{C_{sep}}$	-1.57	-1.61	-1.81	-1.68	-1.77
Separation point standard deviation pressure coefficient C_{sep}'	0.64	0.72	0.87	0.85	0.69
Mean pressure coefficient behind the screen $\overline{C_{pScr}}$	+0.83	+0.79	-2.19	-2.03	-2.01

Tab. 4.13 - Local parameters without and with the screen S1 at *D*/20. Comparison of the experimental results with the SA and kω-SST models.

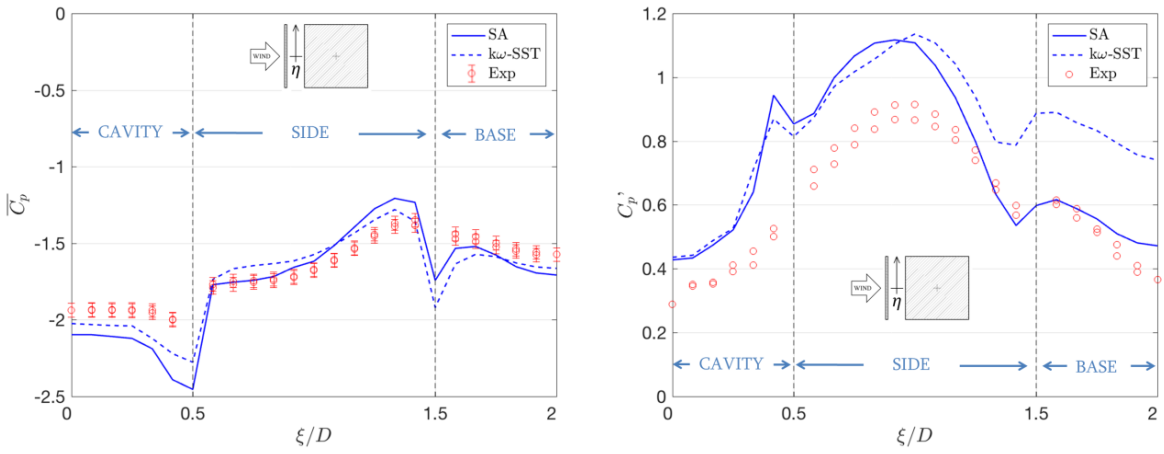

Fig. 4.7 - Comparison of mean (left) and standard deviation (right) of the pressure coefficients around the screened body.

The flow visualization of time-averaged flow improved the comprehension of the mean pressure coefficient distributions. In particular, the pressure recovery on the lateral sides pointed out in Fig. 4.7–left, also observed in experimental results, is shown by the time-averaged flow velocity obtained with the SA model (Fig. 4.8, 4.9 and 4.10). Fig. 4.8 compares the magnitude of the normalized mean velocity without and with the screen S1 at $D/20$. While the shear layers curvature at the separation point does not seem modified, the maximum velocity values are slightly higher when the screen is present. This could suggest that the mean velocity of the shear layers at the origin may be increased by the different boundary condition at the wall, represented by the through cavity. The streamlines reported in Fig. 4.9 are analyzed in detail focusing on the upper side and increased in number in Fig. 4.10. In agreement with Fig. 4.8, the streamlines in the region close to the front corner seem to preserve the same curvature. However, an increased streamline curvature in the downstream corner region, reveals a trailing edge/mean flow interaction, with a behavior apparently similar to that described in the literature for a turbulent approaching flow (*e.g.* Bearman and Morel, 1983).

Fig. 4.9-right and 4.10-right show that the mean flow reattaches when the screen is present. The mean recirculation region is shifted upward along the body side, in agreement with the interpretation of the experimental results discussed in the previous chapter. The anticipated location of this region, and an increased flow velocity around it, may explain the reduction of pressures in the first half of the body side, as previously observed in the $\overline{C_p}$ distribution reported in Fig. 3.24. Moreover, effect on the lateral regions may explain the increased and anticipated C_p' distribution. On the other hand, the discrepancies of C_p' in the first half of the body side reported in Fig. 4.7-right, may indicate that the interference mechanisms in this portion of the flow are not fully captured by the URANS simulations.

In URANS simulations, L_c / D is one of most complicated parameter to match with experimental results, as can also be deduced from Tab. 4.11. However, through the comparison between the case without and with the screen, the wake region behind the base does not seem stretched in the streamwise dimension (as in the case of free-stream turbulence interaction with the shear layers). Despite the mean flow reattachment at the rear corner, the mean recirculating wake length seems only slightly reduced in the direction transversal to the flow. On the other hand, the increased number of streamlines in the wake region close to the body base, as shown in Fig. 4.9, seems to indicate an increase in the energy of the forming vortex.

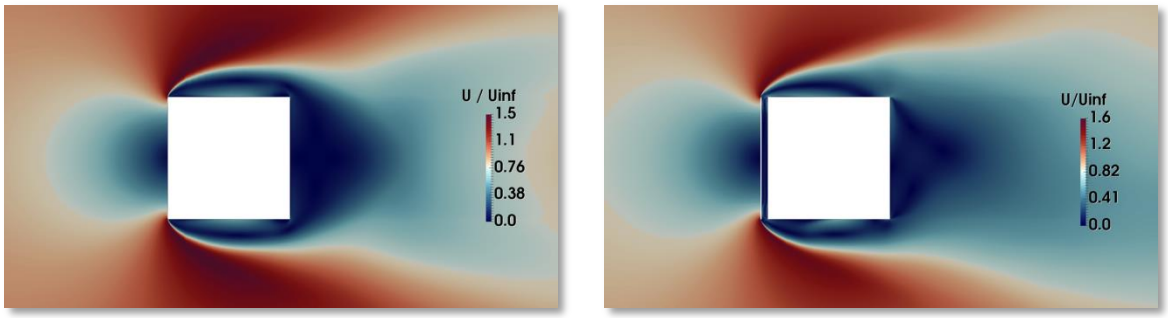

Fig. 4.8 - Mean velocity magnitude (U) normalized respect to the undisturbed velocity flow (U_{inf}). On the left, the square cross-section case; on the right, the system composed by the square cross-section with screen S1 at $D/20$.

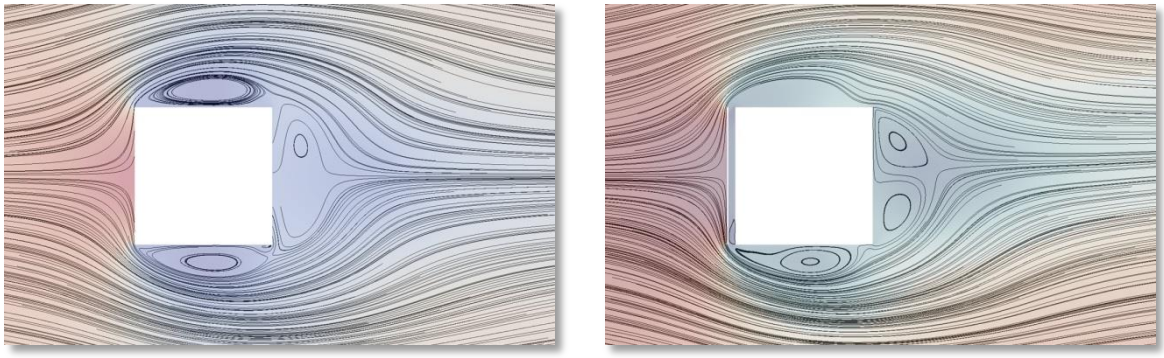

Fig. 4.9 - Streamlines of the mean flow: case of the square cross-section (left) and system with screen S1 at *D*/20 (right).

Fig. 4.10 - Detailed pictures of mean flow streamlines: case of the square cross-section (left) and system with screen S1 at *D*/20 (right). To enhance the differences, the number of streamlines is increased respect to Fig. 4.9.

In Chapter 3, the description of the experimental set-up clarified the impossibility to equip the screen with pressure taps. In CFD this problem is overtaken, therefore the pressure distribution was measured all around the screen. The measurements were carried out with both the SA and the kω-SST turbulence models, as shown in Fig. 4.11, where the pressure values are averaged on symmetrical points. The results are plotted with a distorted scale at the abscissa, because the four pressure taps on the upper and lower sides of the screen are placed on a side which is 1/120 of the front side.

The pressure coefficients on the internal face of the screen exhibit a slightly reduced mean value (reduction of about 5%) in the taps located close to the end of the cavity, as compared to the corresponding pressures measured on the shielded face. It is supposed that in this portion of the cavity, the pressure distribution on the screen internal face and the square front face is affected by the presence of a mean vortex, as shown in Fig. 4.10-right in the proximity of the cavity extremity. However, all over the remaining part of the internal face of the screen, the mean pressure coefficients are almost equals to those on the screened face of the square section.

Generally, the pressures behind the screen behave similarly to those obtained by means of wind tunnel tests reported in Fig. 3.29. In particular, the power spectral densities obtained with the SA model (Fig. 4.12-left) exhibit two peaks, respectively at the Strouhal frequency (St) and at its first superharmonic. While at the extremity of the cavity (*e.g.* tap 12) the peak is centered in St, by moving towards the center of the cavity (*e.g.* tap 16), the peak occurs at $2\times St$. The analysis of pressure spectra obtained from the simulations carried out with the kω-SST model are less clear (Fig. 4.12-right), probably because the analysis was performed on a lower number of cycles (the simulated time was shorter than with the SA model).

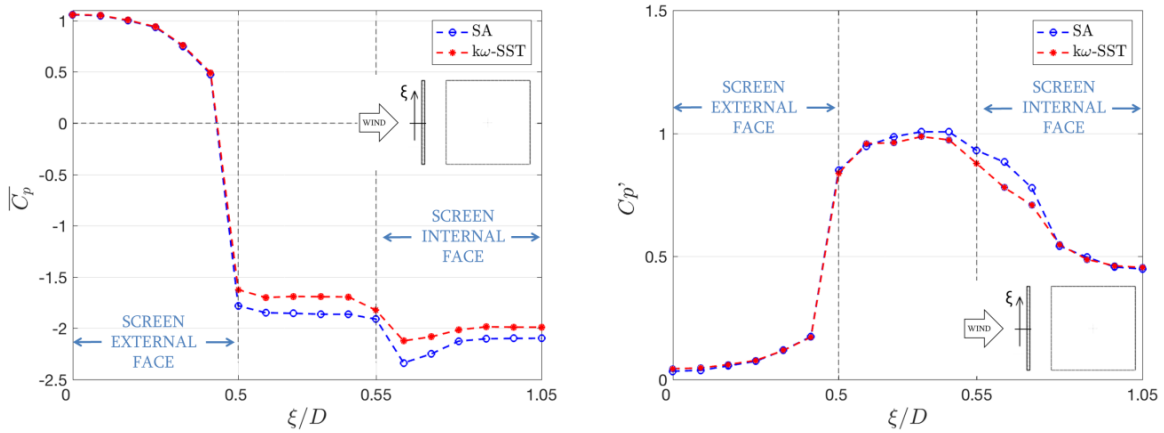

Fig. 4.11 - Mean (left) and standard deviations (right) of the pressure coefficients around the screen.

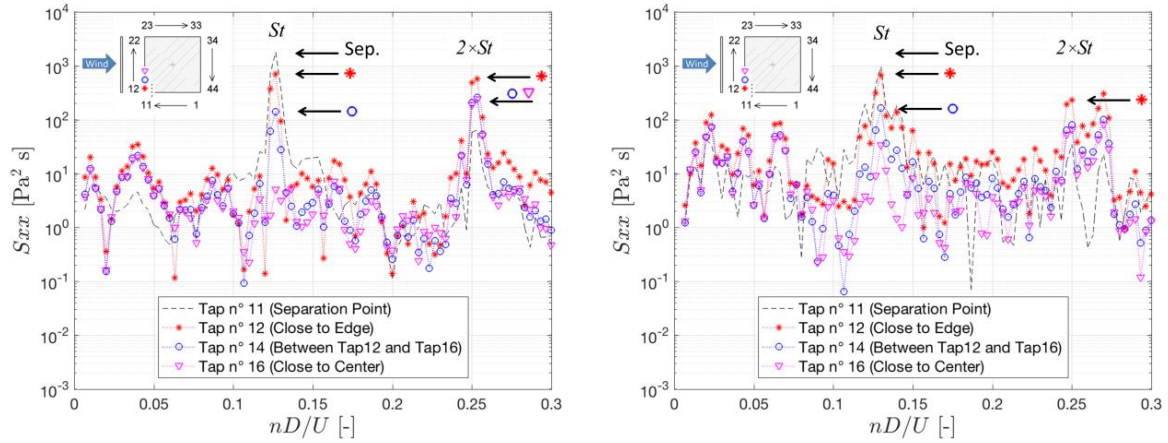

Fig. 4.12 - Pressure spectra at the separation point and in some selected points behind the screen: on the left, results with the SA model; on the right, results with the kω-SST model.

The aerodynamic effects caused by the presence of the screen were investigated by means of the comparison between two cases at the same Reynolds number, namely, the square section without (Fig. 4.13) and with the screen S1 at *D*/20 (Fig. 4.14). Such a comparison was based on flow visualization, by dividing the vortex shedding cycle in eight equal parts. Both the simulations were carried out with the SA turbulence model. The numerical set-up used for the square cross-section has been described in detail in 4.2. In particular, for the geometry without screen, data are reported for the medium grid and a time-step corresponding to *max*Co = 2. On the other hand, the numerical set-up adopted for the system with the screen is explained in the first part of the current section. The figures are plotted overlapping colors, representing the instantaneous pressures, and streamlines.

Fig. 4.13-a shows the instant of maximum suction on the upper side. Later, the recirculating region behind the separation occurred at the upstream corner moves toward the downstream corner (Fig. 4.13-b), down to its "breakage" (Fig. 4.13-c). Simultaneously, the wake vortex moves away from the base. While the upper recirculating region spreads out, on the lower side the opposite area of vorticity grows in intensity (Fig. 4.13-d), and a little recirculating bubble seems to appear on the downstream edge of the upper side (Fig. 4.13-e). Meanwhile, at the base, a recirculating zone similar to that seen in Fig. 4.13-a grows up. The recirculating region on the lower side moves toward the downstream corner, as seen in (Fig. 4.13-b) for the upper side. Then it enlarges together with the shear layer movement (Fig. 4.13-g). Meanwhile a little

recirculating area localized at the lower downstream corner (Fig. 4.13-h) occurs, similarly to Fig. 4.13-e, and the vortex shedding cycle ends.

On the other hand, the presence of the screen complicates the flow topology during the vortex shedding. In analogy with Fig. 4.13-a, the description here starts with the instant of maximum suction on the upper side (Fig. 4.14-a). However, in this case, an additional internal airflow occurs, due to the air drawn in the cavity from the lower side. While the upper recirculating region extends downstream (together with the vortex at the base), on the lower side of the screen, in the proximity of the cavity extremity a small vortex forms (Fig. 4.14-b). In this vortex shedding phase, the driving pressure gradient at the cavity extremities is reduced, so it seems that the external flow tends to drag the air out of the cavity (from the lower extremity). The presence of the small vortex modifies the formation of the lower recirculating region (Fig. 4.14-c), as compared to Fig. 4.13-c. The little vortex grows and enlarges downstream (Fig. 4.14-d), and at the base, close to the lower corner, the wake recirculating area appears. This area enlarges together with the recirculating region on the lower side, which is close to the instant of maximum suction (Fig. 4.14-e). Later, Fig. 4.14-f and –g show the little opposite vortex, located on the upper body side, originated in proximity of the cavity extremity. It deflects the streamlines too, down to the body wall in the rear corner region of the lateral side, thus influencing the formation of the recirculating region on it, as observed in Fig. 4.14-c and -d. Finally, in Fig. 4.14-h the instant before the end of the vortex shedding cycle is reported.
Therefore, the presence of the screen influences the vortex shedding process. In particular, the formation of alternate vortices at the cavity extremities tends to promote an intermittent flow reattachment in the proximity of the trailing edge (visible also in the time-averaged flow field and pressure coefficients), which, in turn, influences also the portion of the base behind that corner.

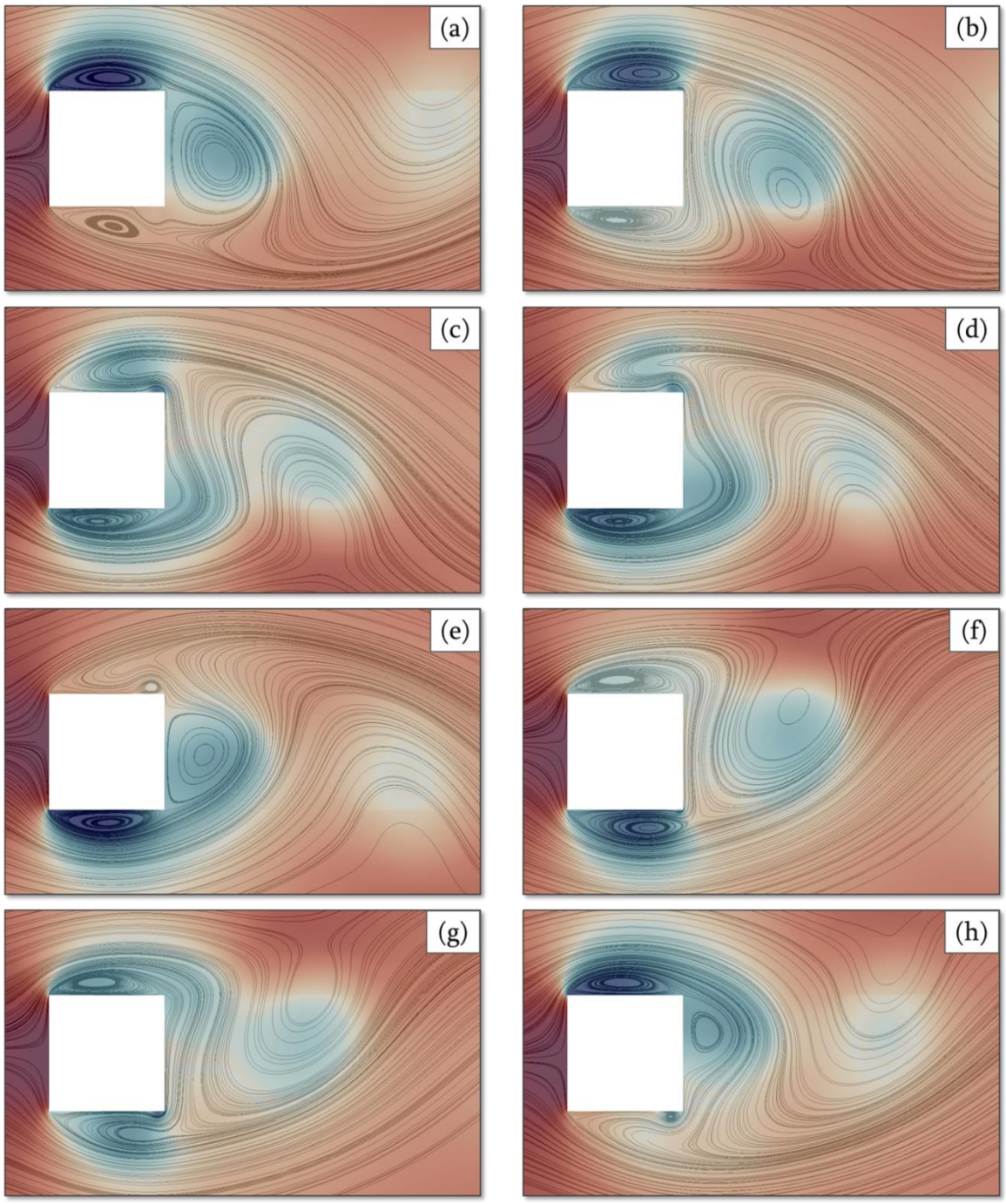

Fig. 4.13 - Streamlines of the square cross-section simulations at Re=7.56×10⁴ with a time step corresponding to maxCo=2 and the medium grid. Colors indicates the pressure field (blue, low pressure - red, high pressure).

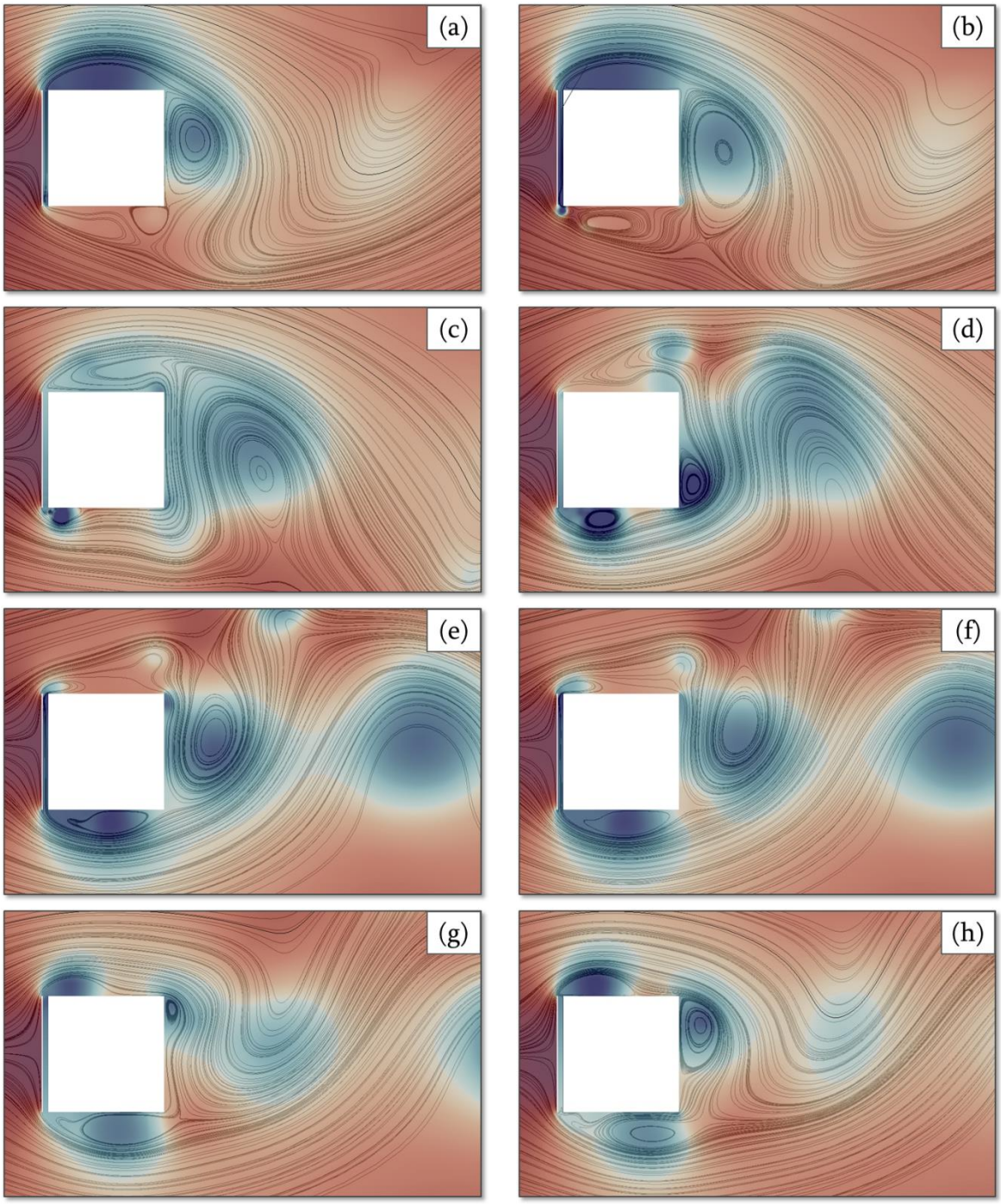

Fig. 4.14 – Pressure field (see Fig. 4.13 for colors) and streamlines of the system with square cross-section and screen S1 fixed at *D*/20 during a vortex shedding cycle. $Re = 7.56 \times 10^4$ and the estimated *Wo* number is around 6.

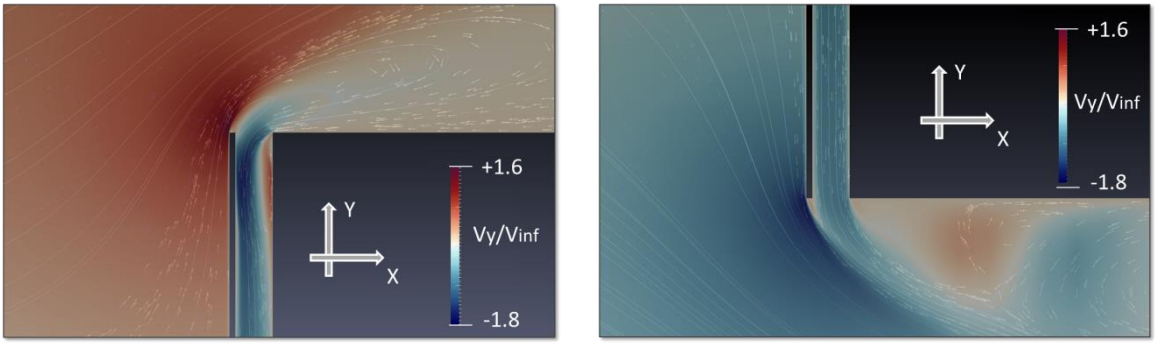

Fig. 4.15 - Cavity flow of the velocity y-component (Vy) normalized to the approaching flow velocity (Vinf). Detail of the two extremities at the same instant.

The flow drawn and ejected from the cavity is reported in Fig. 4.15. In Fig. 4.15-left, it is possible to visualize the behavior hypothesized from the analysis of the experimental results and to confirm that the cavity airflow is driven by the pressure gradient caused by the vortex shedding. As a matter of fact, the air drawn in the cavity comes from the area below the shear layer, in a recirculating zone close to the body lateral side, where the flow has a low velocity. This means that the flow does not enter into the cavity with a straight path, but with a sharp-edged elbow (according to the hydraulic nomenclature). Then, the incoming air exhibits a section reduction due to the separation at the edge. Therefore, locally, a flow acceleration together with a pressure reduction occur. By contrast, when the flow exits from the cavity extremity, the local effects are negligible (Fig. 4.15-right). Hence, also averaging in time the pressure time history at this point, the local effects observed when the air is entering are still visible.

Flow features in the cavity

The difficulty to measure the flow velocity in the cavity during the experimental tests is evident. Indeed, the gap widths tested in wind tunnel range from $D/40$ to $D/10$, which at model scale correspond to 3mm to 12mm respectively. Considering that a hot-wire anemometer support usually employed in the wind tunnel has a diameter of about 2 mm, it is clear that the measurement of the flow velocity in the cavity would be affected by the presence of the instrument. Moreover, due to the accuracy of the employed pressure transducers, the lower limit of the Reynolds-number range tested with the square section was $Re = 7.56\times10^4$. This value, when the screen is fixed at $D/20$, corresponds approximately to $Wo = 6$ for the oscillating flow behind the screen (based on eq. 2.20).

These limitations suggested to investigate through CFD simulations the characteristics of the velocity profile in the cavity (in terms of shape, amplitude and phase respect to the driving pressure gradient), also reducing the velocity of the approaching flow, in order to reach a Womersley number in the cavity equal to 1. This additional simulation was carried out at $Re = 2.1\times10^3$ ($Wo = 1$), with the same numerical set-up adopted in the previous case study with the SA turbulence model.

The comparison carried out between the case at $Re = 7.56\times10^4$ and that at $Re = 2.1\times10^3$, based on global aerodynamic parameters is summarized in Tab. 4.14. It shows that the second case converges to a solution with Strouhal number lower than the expected one, by analogy with the square section when a fine grid or very small time step are employed. During the experimental campaign such a low Reynolds number was not achieved, so that, there are not data to compare with. However, it is supposed that the employed grid (tuned with $Re = 7.56\times10^4$, and therefore acting as a "very fine" mesh for a Reynolds number 36 times smaller), could give the same problems discussed in section 4.2 on the square cross-section.

It is worth noting that this study investigated only a part of the whole Reynolds-number range of interest, but to investigate Reynolds numbers close to full scale values ($Re > 10^6$) was too demanding for the computational resources employed during this study. Indeed, in order to perform a simulation with the same characteristics of those used in the present study (referring, in particular, to the y^+ parameter) required an additional grid- and time-convergence study on a much finer mesh. However, further studies are needed to fill this gap.

GLOBAL PARAMETERS	Screen S1 $D/20$ SA $Re=7.56\times10^4$ - $Wo=6$	Screen S1 $D/20$ SA $Re=2.1\times10^3$ - $Wo=1$
C_D	2.32	2.42
C_{DRB}	1.60	1.67
St	0.126	0.098
C_L'	1.60	1.65
C_{DS}	2.92	2.29

Tab. 4.14 - Global aerodynamic parameters of the system with the screen S1 at $D/20$ employing the SA model. Comparison between Re=7.56×10⁴ (Wo=6) and Re=2.1×10³ (Wo=1).

The velocity profiles in the central section of the cavity (Fig. 4.16a), for different instants, are plotted in the following. These instants were chosen considering five oscillation phases of the time-varying pressure difference at the cavity extremities. As shown in Fig. 4.17, they corresponds to: the positive and negative peaks of the pressure difference (respectively ΔPmax and ΔPmin), the instant when the pressure difference is null (ΔP0), and two intermediate points (ΔP_P and ΔP_N). The pressure difference was calculated as the difference between two pressure time histories, evaluated close to the extremities, after a check of the pressure distribution along the cavity transversal section in different positions. Referring to Fig. 4.16-b the pressure difference was evaluated as $p(A)-p(B)$, so that, for a quasi-steady behavior, a positive value corresponds to a downward airflow that in the following is represented as a negative velocity. By contrast, a negative pressure gradient drives an upward airflow, corresponding to a positive velocity. The pressure time histories in A and B were evaluated averaging the pressure at a point on the screen (A1) and the corresponding point on the square section (A2), as illustrated in Fig. 4.16-c.

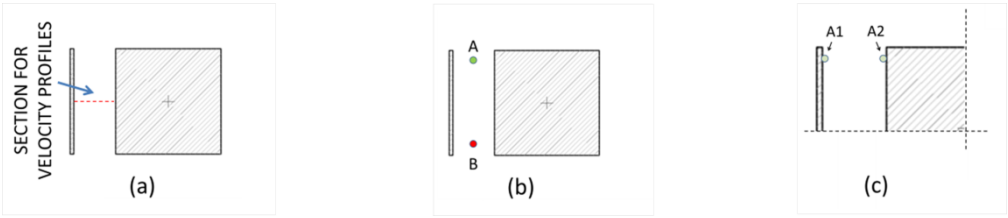

Fig. 4.16 - Sketches to explain the data analyzed.

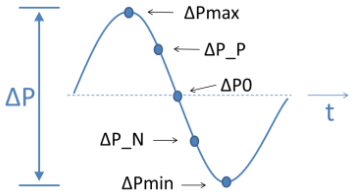

Fig. 4.17 - Pressure gradient at the instants employed to evaluate the velocity profiles.

Fig. 4.18 shows the phase lag between the pressure gradient and the y-component of the velocity (parallel to the screen) along the cavity section, evaluated at the Strouhal frequency. Both the SA and kω-SST turbulence models seem to be able to simulate a ξ-dependent phase difference (where ξ is a coordinate transversal to the cavity flow), as expected for a $Wo >> 1$. By contrast, the simulation carried out at $Wo = 1$ exhibits a quasi-steady flow behavior, because the oscillating flow velocity is slightly out-of-phase with the driving pressure gradient at the extremities. It is worth noting that with the kω-SST model at $Wo = 6$ the phase lag varies between -150° (at the wall) and -75° (at the center), while the values are slightly different at

the walls for the SA model (-135°). The case with $Wo = 1$ exhibits almost constant values along the whole section (around 25°).

Fig. 4.19 shows the velocity profiles expected for the out-of-phase behavior in case of large values of Womersley number. Indeed, when the positive pressure gradient peak occurs, the velocity profile shows that the flow is moving in the opposite direction, as compared to the one expected for a quasi-steady behavior at that specific instant. Moreover, the flow profile shape assumes different forms, as previously discussed in Section 2.4.
The amplitude of the maximum velocity reached in the cavity is of the same order of magnitude of the mean approaching flow. This consideration allows characterizing, in first approximation, the oscillating flow, if combined with the Wo number estimated following eq. 2.20. Therefore, considering the gap width (L) expressed as a fraction of the cross-flow body characteristic dimension (D), a local maximum value of Reynolds ($\mathrm{Re}_{loc,\max}$) can be estimated as a fraction of the Reynolds number (Re) based on the undisturbed flow velocity and D, as follows:

$$\mathrm{Re}_{loc,\max} \approx \mathrm{Re}\frac{L}{D} \qquad \textit{(eq. 4.31)}$$

Despite the global results do not agree with the expected values, the case study at $Wo = 1$ may be representative of the different oscillating flow behavior in the cavity. Indeed, the results reported in Fig. 4.20 seem to confirm that for low Wo number the flow behind the screen nearly behaves in a quasi-steady manner. In this case, the flow is slightly out-of-phase, as clarified by the velocity profile corresponding to the instant of null pressure gradient. Nevertheless, this phase lag is much smaller than in the previous case. In addition, at any instant, the shape of the velocity profile is parabolic, as expected for a quasi-steady laminar flow. The amplitude of velocity fluctuations is smaller than in the previous case.
It is necessary to remind that the pressure gradient is not perfectly sinusoidal as sketched in Fig. 4.17, because of its additional frequency components (especially at $2\times St$), as shown in Fig. 4.12. This is, however, supposed to have a limited impact on the results here presented.

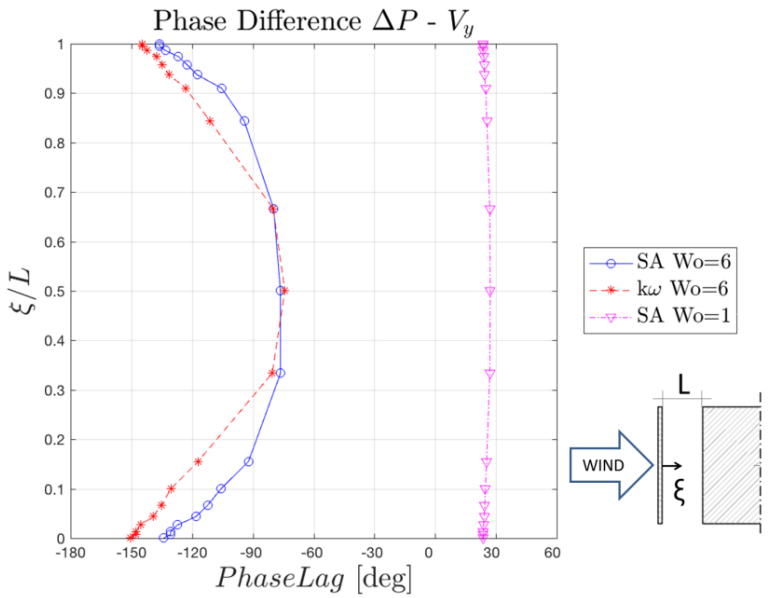

Fig. 4.18 - Phase lag between the pressure gradient and the velocity y-component in correspondence of the Strouhal frequency: case of Wo=6 solved with SA model (blue), Wo=6 with kω-SST model (red), Wo=1 with SA model.

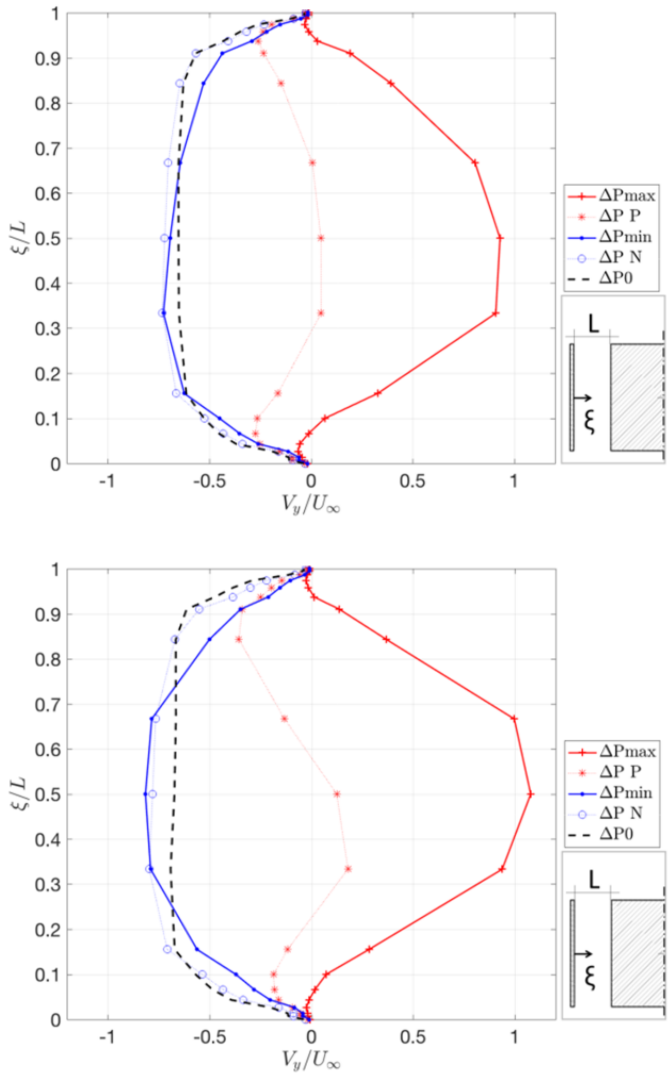

Fig. 4.19 - Velocity profiles in the cavity central section for Re=7.56×10⁴ (Wo=6): results with the SA model (top); results with the kω-SST model (bottom).

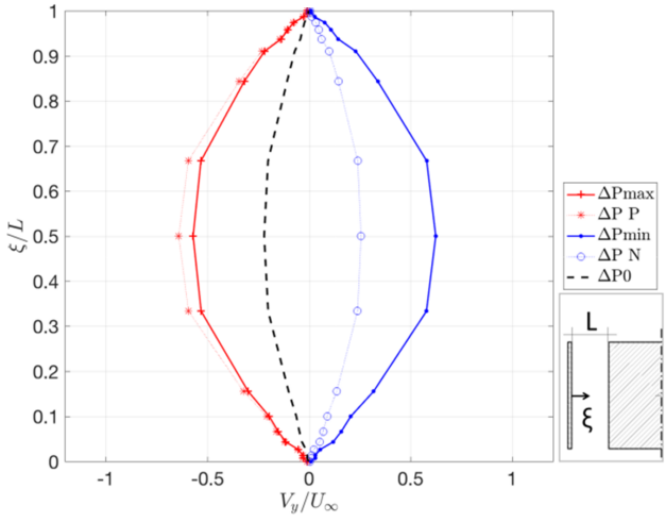

Fig. 4.20 - Velocity profiles in the cavity central section for Re=2.1×10³ (Wo=1), obtained with the SA model.

4.4 Summary

The experimental tests discussed in the previous chapter stressed the necessity of complementary studies for an improved comprehension of the aerodynamic effects caused by the presence of the screen. The potential of URANS CFD simulation has been analyzed through a challenging benchmark: the aerodynamics of a square cross-section with flow perpendicular to a face. This preliminary step revealed that, despite the limitations related to this simplified approach, qualitatively good results are expected to integrate the experimental study.

The simulations concerning the system composed by the square cross-section and the screen fixed at $D/20$ with open gap cavity has been validated through global and local aerodynamic parameters obtained in the experimental campaign.
Time-averaged flow visualizations showed that the mean pressure coefficient distributions observed in the experimental tests on the lateral body sides are caused by a shear layers interference in the rear corners region. In proximity of the trailing edges, the mean streamline patterns exhibit a flow reattachment. This, in turn, anticipates the center of the recirculating region on the lateral body side. Moreover, the area of vortex formation behind the base seems reduced when the screen is present.

The mean pressure distribution around the screen showed that, in the proximity of the cavity extremities, the local effects (already observed in the experiments) causes a relatively small difference between the pressures measured on the internal face of the screen and the corresponding shielded face of the body.

The analysis of streamlines and pressure around the two-dimensional system has been plotted for selected instants of a vortex shedding cycle. The mechanisms of interference, related to the air-flows drawn and ejected from the cavity and the streamlines deflection, supposed in the previous chapter, are confirmed. The focus on the cavity extremities showed that such air movement generates a local separation of flow when the air is drawn.

The simulations performed were able to show that, qualitatively, the velocity profile in the cavity behaves as expected for an oscillating flow. Moreover, a maximum velocity in the cavity of the same order of magnitude as the external undisturbed approaching-flow velocity, allows estimating a local maximum Reynolds number into the cavity, useful to estimate, in first approximation, the internal oscillating flow regime.
Since the discrepancies between the results obtained at $Wo = 1$ and the experimental results, it has not been possible to investigate in details the screen effect on the system when the internal flow behaves as quasi-steady.

Chapter 5 – Conclusions and outlooks

In the present dissertation, the aerodynamics of a two-dimensional system, composed by an airtight screen attached to a rectangular cylinder creating a through cavity was studied. The role of potential influencing factors, such as the gap width, the approaching flow features, the side ratio of the shielded rectangular cross-section, the wind direction and the Reynolds number was investigated. The study was carried out by performing experimental tests and numerical simulations as complementary tools.

5.1 - Main contributions of the present work

The main original contributions achieved in the present work are summarized in the following.

Aerodynamic interference. The presence of the open-gap airtight screen influences the aerodynamics of the original bluff body producing a new fluid dynamic system. In particular, the screen effects on the square and rectangular 2:3 sections were investigated. The interaction occurs even though the gap width is more than an order of magnitude smaller than the characteristic cross-flow body dimension.

The screen affects the system aerodynamics for all the tested screen distances, irrespectively of the approaching flow features and the shielded cross-section side ratio. Anyway, the screen effects are more pronounced in smooth rather than in turbulent flow.

For a wind flow normal to the screen, the vortex shedding process drives an oscillating internal flow in the cavity behind the screen, which may reach a maximum velocity comparable to the mean one of the approaching undisturbed flow. It is argued that the location of the cavity extremities behind the separation point may play a crucial role for the interaction between the internal flow, periodically drawn and ejected, and the outer flow around the body. Based on the results obtained, the cavity oscillating flow can be characterized, as a first approximation, through estimated local values of Womersley (eq. 2.20) and Reynolds (eq. 4.30) numbers, once the system geometry and the oncoming flow Re number are defined.

Global aerodynamic coefficients appear slightly affected by the presence of the screen for a null angle of attack. Nevertheless, the measurements performed by varying the angle of attack showed a reduced slope of the lift coefficient as a function of the angle of attack, implying a reduced proneness of the system respect to the galloping instability.

The pressures around the shielded body exhibit different features depending mainly on the approaching flow turbulence and the cross-section side ratio. Nevertheless, in case of flow normal to the screen, the cavity mean pressure coefficients are always negative, with values between -1.9 and -2.5. Moreover, in the proximity of the extremities, the mean pressure further decreases by increasing the gap width.

The presence of the screen produces a pressure recovery in the rear corner portion of the lateral body sides. In particular, flow visualization pointed out a mean flow reattachment when the screen is distanced from the square section by 1/20 of its characteristic cross flow-dimension.

Generally, pressure distributions along the lateral body sides and the rear face are influenced, in terms of mean and fluctuating components, also for non-zero angles of attack, where investigations revealed that the presence of the screen tends to increase the angle at which the flow reattaches.

External and internal pressure decoupling. The presence of a through cavity is a crucial feature, since, if the transversal flow behind the screen is prevented, the previously mentioned interaction does not occur, and the influence of the screen is reduced to a mere body elongation. The internal airtight compartmentation used to avoid the internal flow splits up the cavity into two regions independently connected to the external flow. In such a configuration and for a flow normal to the screen, it is reasonable to evaluate the internal pressures from the external ones measured in the proximity of the cavity openings. On the contrary, when the cavity is not partitioned and the air passage is allowed, simplified models to determine internal pressures hardly lead to reliable values, given the results sensitivity observed by varying the main influencing factors.

Contributions to the research literature (i). The tested systems provide an experimental data set about two-dimensional geometries not considered yet, to the author's knowledge. Pressure and force measurements on a system with the airtight-screen depth equals to the body cross-flow dimension (D) and gap widths in the range between $D/40$ and $D/10$ were motivated as a preparatory work on permeable building envelopes, but they might be useful for other alike case studies.

Contributions to the research literature (ii). The present thesis' Appendix is useful for planning future studies on more realistic "building + permeable envelope" systems. Therefore, a classification of possible case studies based on the system aerodynamics was proposed. Such classification emerged from the state of art on wind effects on permeable building envelopes. To the author's knowledge, such a collection of literature contributions has not been provided yet.

5.2 – Implications and perspectives

The main fluid-dynamic findings pointed out in the thesis suggest to concentrate future investigations on three-dimensional case studies concerning buildings with permeable envelopes. Therefore, some considerations are reported in the following, especially referring to façades with an external airtight layer and a through cavity.

- *Wind loads on permeable building envelopes*. The present study has pointed out that the interference between internal and external flows may occur when a building with a permeable envelope is considered. In particular, wind loads on the envelope may be strongly affected by the occurrence of peculiar flow features, such as the oscillating flows observed in the present work. Therefore, in order to obtain reliable design values, to perform investigations on models which correctly reproduce the permeable envelope seems a key requirement.
- *A possible structural improvement.* Experimental results has shown a reduced proneness to galloping instability of the two-dimensional section considered. It is suggested to take into account this results for possible studies aiming to improve the stability of slender structures, such as very tall buildings.
- *Natural ventilation.* Results obtained in two-dimensional studies showed that an oscillating internal flow may occur for a limited range of wind directions around the null angle of attack. For all the remaining wind directions either the flow tends to enter directly in the cavity or it gets through the cavity driven by the wake movement (*e.g.* for $\alpha = 180°$). Therefore, it seems possible working towards the design of a wind-driven ventilation for such envelopes, since also for wind normal to the façade an internal ventilation may occur.

- *Energy harvesting.* The wind effects on the system, in terms of both external and internal flows, could represent a potential source for wind energy harvesting devices. Recently, many funding initiatives are paying attention to energy saving and generation from renewable power sources, *e.g.* part of the research and innovation program "Horizon 2020" of the European Community. Nowadays, the use of double-skin façade internal flows for energy harvesting is being discussed among the wind engineering community: for instance, Hassanli *et al.* (2017) proposed a façade configuration designed accordingly. Therefore, a deeper understanding into the flow field around such complex three-dimensional systems may open new possibilities to integrate renewable energy into the building of future smart cities.

5.3 - Future work

The obtained results and implications suggest mainly two possible research paths. At first, the two-dimensional bluff body aerodynamics study needs further in-deep investigations. On the other hand, it is necessary to extend the present study to more realistic three-dimensional case studies.

Bluff body aerodynamics. CFD simulations provided useful qualitative results, but future work should be devoted to obtain quantitative results. The interference observed between the confined (internal) and the unconfined (external) flows, and the related phase difference between the driving pressure gradient and the flow in the cavity, point out that a deeper knowledge of the flow mechanism is required. Moreover, an effort is needed to increase the investigated Reynolds (and Womersley) number range. For these reasons, it is supposed that LES may represent the most suitable tool (instead of RANS and URANS) for further developments of the work. It is supposed that accurate simulations will also be able to overcome the impossibility to measure net peak pressures on the screen encountered in wind tunnel tests.

A further branch of research in this field will be the study of different system configurations, for example by attaching the screen on two opposite body faces, or by using permeable screen instead the airtight one.

Three-dimensional case studies. Although the study of three-dimensional geometries representing building immersed in the atmospheric boundary layer increases the number of potential influencing parameters to investigate, studies oriented towards the definition of wind effects on more realistic case studies are needed. In particular, the case of a permeable envelope characterized by an airtight panel, opened along the lateral sides, with internal horizontal compartmentations (according to present classification proposed in A1.4) seems the most suitable geometry over which planning future works. Numerical and/or experimental studies should be performed aiming to elucidate also the following additional aspects:

- the screen effects depending on the ratio between the building cross-flow dimension and its height, namely the *building aspect ratio*;
- *the role of atmospheric boundary layer* on the wind effect that the permeable envelope may create on the three-dimensional case study;
- *the role of horizontal compartmentations* on the system aerodynamics. Hence the comparison between model with different configurations of horizontal compartmentations (*e.g.* cavity partitioned at each storey, every few storeys and without compartmentations);
- the possible effects caused by the presence of a permeable envelope *on more than one face*.

Such a study represents a challenging task, owing to the scaling issues involved in such a multi-scale problem, combined with the importance of obtaining reliable net wind pressures on the building envelope.

An additional step will be the characterization of such building envelope energy performance, in order to put into relation wind effects and energy efficiency of the façade. It is expected that the definition of the driving parameters will lead to a system optimization, taking into account wind resistance and energetic behavior of the naturally ventilated façade.

Appendix 1 – On the wind effects on permeable double-skin building envelopes

The present work deals with two-dimensional studies on bluff body aerodynamics, preparatory for more complex three-dimensional geometries. Further works will be oriented towards the definition of wind effects on more realistic case studies, such as systems composed by a building with a permeable envelope. The aim of the current appendix is to simplify the extension of the results obtained in this work. For this purpose, a review of the research concerning wind effects on permeable envelopes and a classification of possible case studies, useful to plan future research activities, are carried out.

In the present appendix, firstly, an overview of permeable double-skin building envelope typologies is carried out (A1.1). Three different typologies are considered: *rainscreen walls*, *double skin façades* and *porous screens*. In particular, the first two are examined in depth, trying to clarify the role of each façade component and how these envelopes are usually designed in practice. Then, after a short introduction on porous screen, some selected fundamentals of fluid dynamics are recalled to discuss the use of simplified models to evaluate internal pressures.
Wind effects may be used to define the envelope performance in terms of natural ventilation and/or wind loads. Since the use of wind induced pressures to design internal flows of ventilation, requires the same level of comprehension of the system aerodynamics that it is necessary for the definition of wind loads, the state of art on wind loads on such building envelopes is analyzed (A1.2). Through the review, it is shown that the definition of wind effects on certain building envelope typologies is still an open problem in the wind engineering field.
Finally, an attempt to re-organize the literature through a classification merely based on system components is performed (A1.3).

It should be noted that, the author considers necessary to underline that:

- The present work is focused on the behavior of the permeable building envelopes under the wind action, *i.e.* on the fluid dynamics of the system composed by the building and the façade in case of wind storm. Other issues, such as for instance the "stack effect" due to thermal effects, are neglected.
- The current study treats only envelopes with one additional "skin". In order to have an approach as general as possible, three conceptual layers are considered: the outer layer (also called external skin), the cavity between the two skins and the inner layer (also called air barrier).
- The review deals only with cases in which the cavity is connected to the exterior. The link may be represented by openings or porous screens on the outer layer or at the edges, on the lateral sides, or on the top/bottom sides.

A1.1 An overview of permeable double-skin building envelope typologies

The field of permeable building envelopes merges many different topics. The energetic and acoustic performance, the materials employed and the aesthetic details are only some of the factors influencing the design of the same building component. The aim of this section is to

describe how these envelopes are conceived, in order to understand their fluid-dynamic working principle under the wind action. In this manner, elements with different names and/or appearance could share a common aerodynamic behavior.

A1.1.1 Rainscreen walls

Usually, rainscreen walls have an external skin composed by the assembly of many elements (*e.g.* metal or ceramic panels), each one characterized by a small dimension as compared to the height of a storey. These elements are spaced enough to ensure a ventilation between the external environment and the internal cavity (Fig. A1.1). Rainscreen walls are mainly divided in Pressure Equalized Rainscreen (PER) and Back Vented Rainscreen (BVR):

- PER aims to eliminate the water penetration through the pressure-equalization across the rainscreen;
- BVR allows water to penetrate into a ventilated cavity where it is subsequently drained.

The PER walls are made of three components (Fig. A1.2): the external rainscreen, the internal air barrier and the cavity obtained through the compartmentations. The compartmentations often coincide with the supporting systems of the rainscreen. They also fix the distance between the two skins, *i.e.* the cavity depth, once the thickness of the insulation usually placed in front of the air barrier is known. The openings are often placed along the panel sides. In practical cases the gap width ranges from tenths to few centimeters.

From the early works carried out to describe the operating principle (*e.g.* Johansson, 1946, Garden, 1963) to the most recent guidelines (Baskaran, 1992), the design approach proposed for a good rainwater penetration control is mainly based on:

- the relationship between the air leakage of the air barrier and the size of the openings on the rainscreen (also called venting holes);
- the relationship between the cavity volume and the total area of the venting holes;
- the flexibility of the outer skin;
- the position of the single element on the façade (*e.g.* near the corner, central area, etc.) and the related compartmentation.

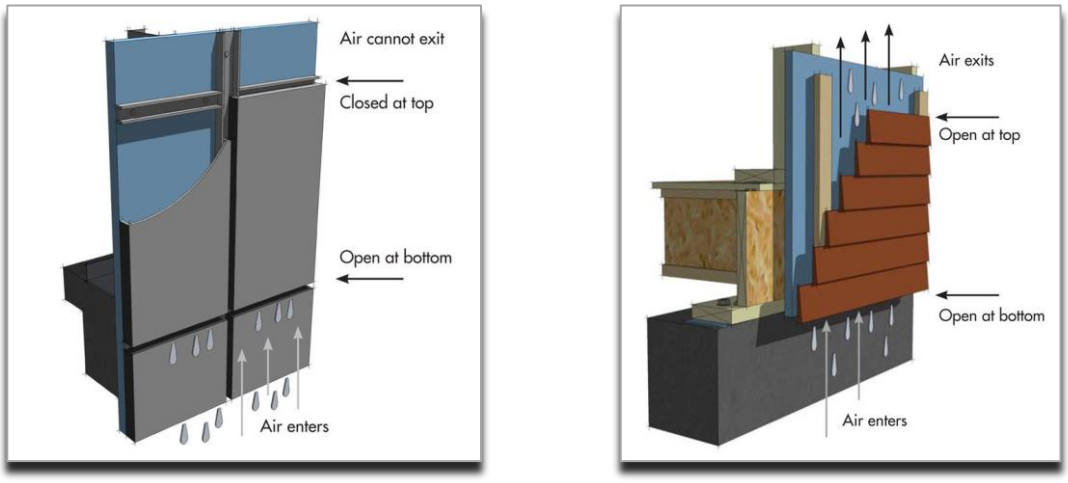

Fig. A1.1 - Working principle sketches of PER and BVR. Illustration of Steve Baczek (http://www2.buildinggreen.com/article/how-rainscreens-work).

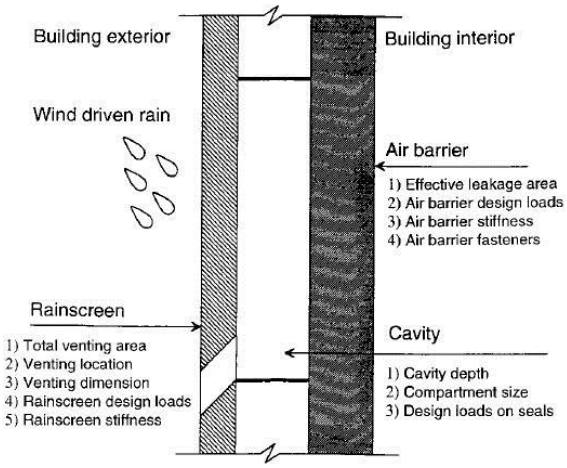

Fig. A1.2 - Principal components and design features of a PER (Baskaran and Brown, 1992).

Based on the above considerations, the PER geometry (cavity width, opening size, etc.) is defined in first approach to ensure a good pressure equalization aiming for a rain water penetration reduction. However, each rainscreen wall geometry corresponds to a pattern of wind induced pressures. Moreover, other issues, such as the effective air-tightness of the inner layer or the spatial pressure variations (Fig. A1.3), that are indicated as a problem in the process of pressure equalization, should be considered in the evaluation of the wind effects on this envelope typology. For example, if the same compartmentalized cavity is connected to two external points at different pressure, this difference acts as a driving force for internal flows. In addition, the pressure on the two points could vary in time influencing both, the rainwater penetration and the wind loads. The concepts related to the pressure equalization of PER were also considered in the first studies on BVR by Gerhardt and Kramer (1983), in which the tests were conducted varying the building aerodynamics (spatial variations) and the wind profile characteristics (temporal variations).

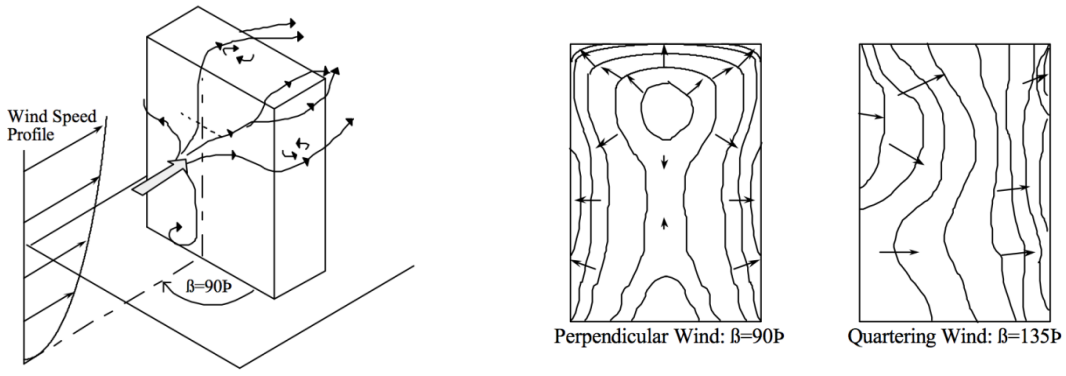

Fig. A1.3 - Sketches of wind streamlines (left) and average spatial pressure gradients (right) on a building face for different wind directions (Straube, 2001).

A1.1.2 Double-skin façades

Historically, the idea of a ventilated façade first appeared in the second half of the nineteenth century, even if the first applications are found in the early 1900s. At the beginning, the priority was to maximize day lighting, as shown in the Post Office Savings Bank in Vienna, designed by Otto Wagner in 1903. Later, other pioneering architects like Ginzburg and Le Corbusier since the 30's have used ventilated double-skin façades with an approach more similar to that used nowadays.

Double-skin façades are employed for their energetic, acoustic and/or aesthetic role. Usually, such permeable envelopes are placed externally on the building framework through apposite supporting systems. The building could be equipped with a ventilated double-skin façade by the direct installation of its components, such as glass panes, or by pre-assembled panes also called "unitized system".

Following the sketches in Fig. A1.4, a double-skin façade system consists of:

- Exterior and interior skins. The two physical layers, the external and the internal one, are commonly called "skins". The choice of the material is almost always oriented to glass. The glass type for the interior and exterior panels depends on the typology of the façade. In case of a façade ventilated with outdoor air, an insulating pane (sealed double-glazed unit) is usually placed as a thermal break at the interior side and a single pane at the exterior side. Both the skins could be equipped with openings, respectively for the ventilation of the cavity and of the building's interior.
- An air cavity between the exterior and interior layers. The ventilation of the cavity may be totally natural, fan supported (hybrid) or totally mechanical. The case of totally mechanical ventilation does not requires the presence of external openings. The depth of the cavity can vary between tenths to few meters. The depth influences the physical properties of the façade and also the way that the façade is maintained.

The openings on the skins of this typology of façade are needed for the ventilation of the internal cavity or, in some cases, to intake air inside the building. For this reason these façades are also called ventilated double-skin façades (VDSF). These façades could be classified according to the Belgian Building Research Institute (BBRI), based on three criteria (Loncour *et al.*, 2004):

- the type of ventilation: natural, mechanical, hybrid;
- the partitioning of the façade: horizontally and vertically per storey, only horizontally per storey, only vertically;
- the modes of ventilation of the cavity: referring to Fig. A1.5, respectively from left to right, outdoor air curtain, indoor air curtain, air supply, air exhaust, buffer zone.

Nevertheless, a specific classification oriented to the wind load, or somehow to the aerodynamic behavior of such building envelopes, has not been provided yet.

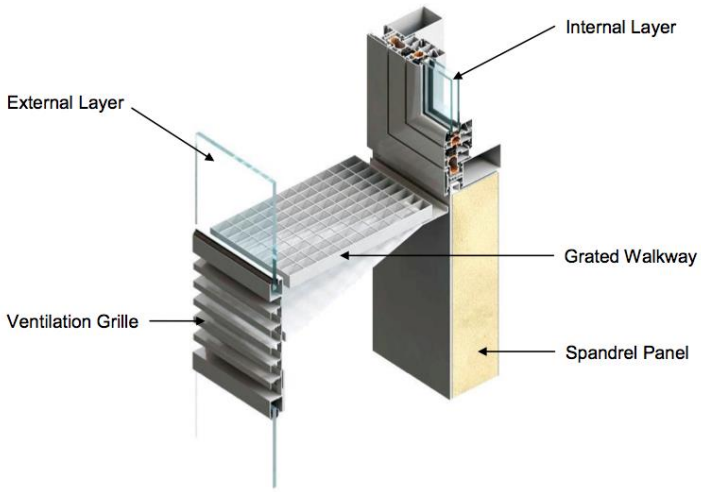

Fig. A1.4 - Principal components of a double-skin façade (ArchiExpo, 2003).

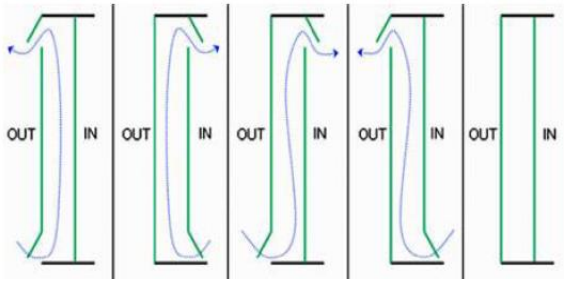

Fig. A1.5 - Ventilation modes for double-skin façades (BESTFACADE, 2007).

Generally, the thermal performance is the first goal in the design of a VDSF. The two most common indexes to evaluate the thermal performance are: the SHGC (Solar Heat Gain Coefficient) and the U–Factor. The former is defined as the fraction of incident solar radiation admitted through a window, both directly transmitted and absorbed and subsequently released inward (SHGC is expressed as a number between 0 and 1). The U-Factor (or U–Value) is the measure of the rate of heat loss through a material. Other important factors in designing a VDSF are the internal glazing temperature and parameters to define the behavior of the fluid in the cavity, like cavity airflow speed and temperature (Doebber and McClintock, 2006).
Performance standards related to acoustic insulation, impact protection, fire resistance, seismic survivability and, of course, wind loads resistance may pose additional requirements for the VDSF design.
From this brief description of the main design parameters it is possible to understand that the design of a VDSF is an iterative process. In common practice analysis, specific software are used to take into account of all the energetic and structural requirements. The wind effects on ventilated double-skin façades in businesslike applications are considered after the geometry definition driven by the comfort and energetic objectives. However, the wind load still remains the main structural design load.
Aiming at a comprehension of the fluid-dynamic behavior of the VDSF, a first distinction can be made, based on the cavity connection typology with the exterior field. Based on Poirazi's review (2004), it is possible to distinguish at least three types of opening configurations, and consequently other three groups of VDSF walls:

- Walls with uniformly distributed openings (Fig. A1.6-a). In this case, the presence of regularly-spaced and similarly-shaped openings connects the cavity to the external field. The so-called *box double-skin façades*, *storey-high double-skin façades* or *corridor façades,* distinguished by the internal compartmentations, are included in this group.
- Walls with openings at the top and the bottom (Fig. A1.6-b). Usually façades with this openings typology are called *multi storey double-skin façade*. In this case, the façade has a sealed external skin, while the cavity is connected to the external field through openings on the top and the bottom of the whole façade.
- Walls with openings on the lateral side (Fig. A1.6-c). This typology is presently less employed in practical application. In this case, the façade has a sealed external skin and the cavity is connected to the external field through the lateral edges of the whole façade. Horizontal partitioning may be required for acoustical, fire safety or ventilation reasons.

It is worth noting that in practical applications a combination of these three basic typologies can be found. Moreover, a fourth case can be considered when a "dominant opening" is formed

on the external skin. This case, only mentioned, could represent a configuration of post debris impact (Minor, 2005).

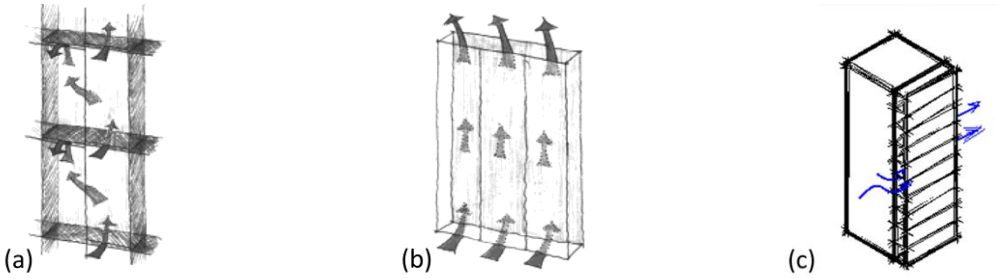

Fig. A1.6 - Sketches of VDSF opening typologies: (a) uniformly distributed openings on the outer layer (Lou *et al.*, 2012); (b) openings at the top and bottom (Lou *et al.*, 2012); (c) with openings on lateral side, sketched by the author.

As aforementioned, the fluid dynamic behavior of a double-skin façade relies on the same parameters of a rainscreen wall (two layers and a cavity connected to the exterior field which can be partitioned). Nevertheless, some parameters have different characteristics, *e.g.*:

- openings and cavity size (expected interaction with the building aerodynamic): the dimension of both the openings and the cavity are usually different. As mentioned above the depth of a VDSF cavity is of an higher order of magnitude as compared to the rainscreen case;
- compartmentations (internal flow paths): the internal partitioning of a VDSF is fundamental for its energetic and thermal performance. Therefore, a VDSF could be designed with a cavity that connects far apart external points of the façade to facilitate the internal flows development. On the contrary, the PER working principle suggest that vertical and horizontal compartmentation must create short paths between the openings to achieve a good pressure equalization;
- materials (typology of information required): in VDSF are often used time sensitivity material, as glass. This could lead the researcher (or the designer) to focus the attention on additional aspects of the wind load compared to the rainscreen case.

Finally, a note on the openings. Adjectives as “uniformly distributed” and “dominant” are similar to the well-known keywords used in the Eurocode 1.4 for the building internal pressures. While the Eurocode on this regards refers to openings on the building wall which directly link the whole internal building volume with the exterior, in the present work, the openings considered are on the external skin of a two layers wall. The internal layer is considered always airtight, and "internal pressures" are referred to the cavity pressures.

A1.1.3 Porous screens

A *porous screens* generally denotes a permeable façade with the external skin made of panels (usually metal panels) with diffuse openings, uniformly distributed and with a similar shape. They are employed mainly to protect the building from the direct sunlight, with the external skin that act as louver.

It seems that the energetic design phase does not involve fluid-dynamic operating principles, in fact, the literature concerning wind effects on this façade typology is quite poor. However, wind effects could affect the performance of porous screens, for example, by causing damages or generating noise. Therefore, in order to understand the aerodynamic behavior of the system building + porous screen, the state of art presented in section A1.2 has been enriched with

works performed on clad scaffolding: temporary structures which share a common fluid-dynamic behavior with such permeable building envelopes if subjected to the wind action.

A1.1.4 On the use of simplified models to evaluate internal pressures

Simplified methods are used in defining the natural ventilation performance of a permeable façade, relating the wind induced pressure distributions with the air ventilation. Such methods use the external pressures in the proximity of the cavity openings as boundary conditions to evaluate internal pressures (since the latter are often not directly measurable). If this approach was applied to the evaluation of wind loads, it could lead to unsafe design values. On this regard, two issues are pointed out: first, the presence of a permeable envelope could influence the external pressure distribution obtained on the system without it, and the values employed as boundary conditions could not be representative. Second, if the influence of the external pressures (due to the presence of the permeable envelope) on the internal ones is negligible, the method to estimate the internal pressures still must still take into account additional factors to give reliable values. In order to show some of the complexities that such method should consider, some basic fluid-dynamic topics are recalled.

Basis I - The flow between fixed parallel plates (the Couette flow)

This elementary topic is briefly recalled because in many situations the flow in the cavity is schematized as a two-dimensional channel (*e.g.* Chino *et al.*, 1991). Therefore, an unidirectional ($u_x \neq 0, u_y = 0, u_z = 0$) incompressible flow between two fixed parallel plates at a distance h is considered (Fig. A1.7).

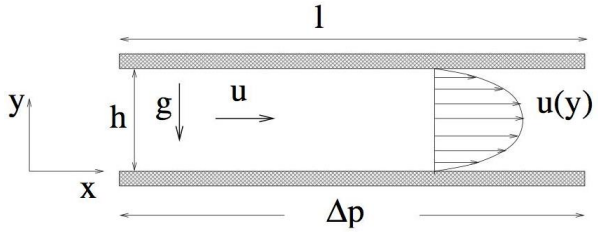

Fig. A1.7 - Parallel plates flow sketch.

In this case, the mass conservation law can be simplified. The endless plates extend on x and z directions, while the velocity u_x depends only on the y direction. Therefore, if the flow is stationary, the Navier-Stokes momentum equations can also be simplified. Integrating the equations and applying the boundary conditions, the velocity equation is obtained:

$$u_x(y) = \frac{1}{2\mu}\frac{\partial p}{\partial x}\left(y^2 - yh\right) \qquad \textit{(eq. A1.1)}$$

where μ is the dynamic viscosity of the fluid and p is the pressure.

Therefore, the maximum velocity is at the center of the gap between the two plates:

$$u_{x,MAX} = u_x\left(\frac{h}{2}\right) = -\frac{1}{2\mu}\frac{\partial p}{\partial x}\frac{h^2}{4} \qquad \textit{(eq. A1.2)}$$

While the mean velocity is:

$$\overline{u_x} = \frac{2}{3}u_{xMAX} = -\frac{1}{3\mu}\frac{\partial p}{\partial x}\frac{h^2}{4} \qquad \textit{(eq. A1.3)}$$

Finally, the mean flow rate is evaluated as:

$$\overline{Q} = \overline{u_x} \cdot h = -\frac{1}{3\mu}\frac{\partial p}{\partial x}\frac{h^3}{4} \qquad \textit{(eq. A1.4)}$$

If l_c is the length of a channel section, and Δp is the pressure difference at its extremities, it is possible to write $\frac{\partial p}{\partial x} = \frac{\Delta p}{l_c}$, in order to show that velocity and flow rate are directly proportional to the pressure difference applied and inversely proportional to the channel section length. The theory briefly presented above is only valid if the flow is laminar, *i.e.* for $\mathrm{Re} < \mathrm{Re}_{\mathrm{lim}}$, where the threshold limit $\mathrm{Re}_{\mathrm{lim}}$ is given by:

$$\mathrm{Re}_{\mathrm{lim}} = \frac{\rho \overline{u}_x h}{\mu} \simeq 1400 \qquad \textit{(eq. A1.5)}$$

where ρ is the density of the fluid.

Basis II - The friction losses

The Darcy-Weisbach equation is a basic equation of the fluid dynamics, which relates the pressure loss (also called the head loss), due to friction along a given length of pipe to the average velocity of the fluid flow.

The head loss can be calculated as:

$$h_f = f_D \frac{l_p}{R_h}\frac{\overline{u}^2}{2g} \qquad \textit{(eq. A1.6)}$$

where: h_f is the head loss due to friction

l_p is the length of the pipe considered

R_h is the hydraulic diameter of the pipe (the ratio of the cross section area over the perimeter)

$\overline{u}$ is the average velocity of the fluid flow

g is the local acceleration to gravity

f_D is a dimensionless coefficient called “Darcy friction factor”

The head loss h_f expresses the pressure loss Δp as the height of a column of fluid:

$$\Delta p = \rho g h_f \qquad \textit{(eq. A1.7)}$$

where ρ is the density of the fluid.

The Darcy–Weisbach equation can also be written in terms of pressure loss:

$$\Delta p = f_D \frac{l_p}{R_h}\frac{\rho \overline{u}^2}{2} \qquad \textit{(eq. A1.8)}$$

The Darcy friction factor f_D (also named Fanning coefficient), depends on the parameters of the pipe and the velocity of the fluid flow, but it is known with high accuracy within certain flow regimes. It may be evaluated for given conditions by using various empirical or theoretical relations, or it may be obtained from published charts.

For laminar flows, it is a consequence of Poiseuille's law that:

$$f_D = \frac{64}{\mathrm{Re}} \qquad \textit{(eq. A1.9)}$$

where *Re* is the Reynolds number calculated substituting for the characteristic length the hydraulic diameter of the pipe, which is equal to the inner diameter for circular pipe geometries.

For turbulent flows, the friction factor f_D is evaluated in different ways, *e.g.* using a diagram such as the Moody chart (Fig. A1.8), solving the Colebrook–White equation, or the Swamee–Jain equation. While the Moody chart and Colebrook–White equation are iterative methods, the Swamee–Jain equation (an approximation of the implicit Colebrook-White equation) allows to directly find f_D for a developed flow in a circular pipe. For smooth walls and for *Re* numbers below 10^5, the turbulent friction factor is well described by the Blasius equation:

$$f_D = \frac{0.3164}{\mathrm{Re}^{0.25}} \qquad \textit{(eq. A1.10)}$$

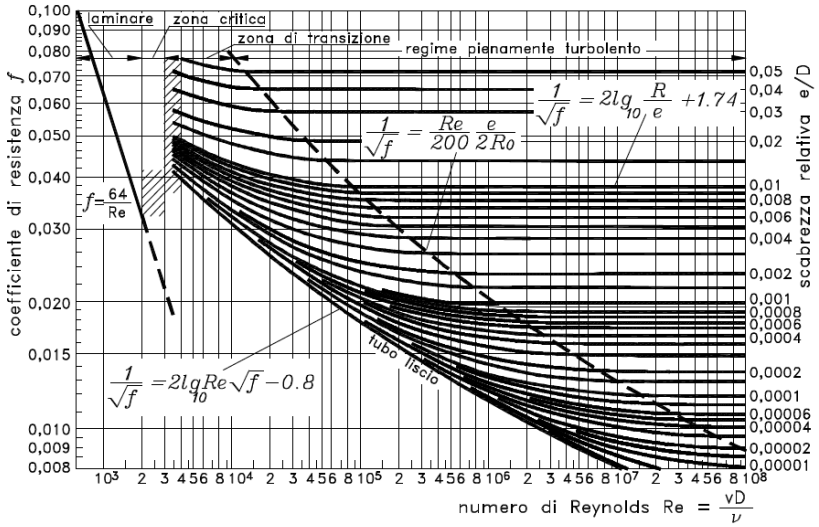

Fig. A1.8 - The Moody's diagram for friction losses (adapted from Longo and Tanda, 2009).

It is worth noting that the internal cavity of a façade could have a rectangular cross-section, while the above equations refer to very simple geometries such as the circular pipe or the endless parallel plates. This problem has been faced in hydraulics applications, where results obtained with circular sections were extended to common non-circular sections.

In case of laminar flow, the corrected friction coefficient f_{corr} can be expressed as:

$$f_{corr} = \frac{C}{R_h} \qquad \textit{(eq. A1.11)}$$

where C is an empirical coefficient that depends on the cross-section shape and R_h is the Reynolds number based on the hydraulic radius (or diameter). In case of fully developed turbulent flow, Moody's diagram for circular sections is used. In this case the diameter D is substituted by the hydraulic diameter, also considering the Reynolds number. In most practical cases, the accuracy of this method is found to be around 15% (White and Corfield, 2006).

Basis III - The local losses

The inlet of a duct can be considered as a cross section reduction (Fig. A1.9). Here, a flow separation with secondary recirculation and a local energy dissipation occur, where the local energy loss is expressed in analogy to the friction losses as:

$$h_L = \frac{\Delta P}{\rho \cdot g} = K_L \frac{U^2}{2g} \qquad \textit{(eq. A1.12)}$$

where K_L is an empirical coefficient that depends on the inlet (or outlet) geometry.

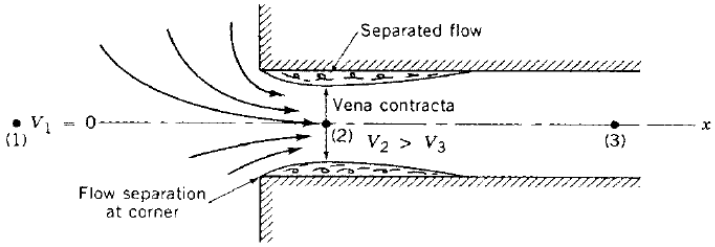

Fig. A1.9 - Local losses at the inlet of a duct (adapted from Sadri and Floryan, 2002).

Depending on the inlet and outlet geometrical characteristics, the disturbances in the duct flow are more or less evident. This concept must be considered as a characteristic that affects every model in which the inlet / outlet are not accurately reproduced. In fact, the local effects shift the fully developed flow profile at a certain distance from the extremities. Two empirical relationships to qualitatively evaluate the distance L_i, after the inlet, needed to reach the fully developed flow conditions are:

$L_i \simeq 0.05\,\mathrm{Re} \cdot D$ *for the laminar case* *(eq. A1.13)*

$L_i \simeq 4.4\,\mathrm{Re}^{1/6} \cdot D$ *for the turbulent case* *(eq. A1.14)*

Nore *et al.* (2010), studying the possibility to decouple external and internal pressures on a narrow ventilated façade, highlighted the inlet problem described above as one of the modeling limitations in this task. Differences between coupled and decoupled simulations are shown in Fig. A1.10. The figure shows the velocity profiles along the cavity for the coupled case (Case A) at two different Reynolds numbers, and the velocity profiles along the decoupled cavity (Case C1).

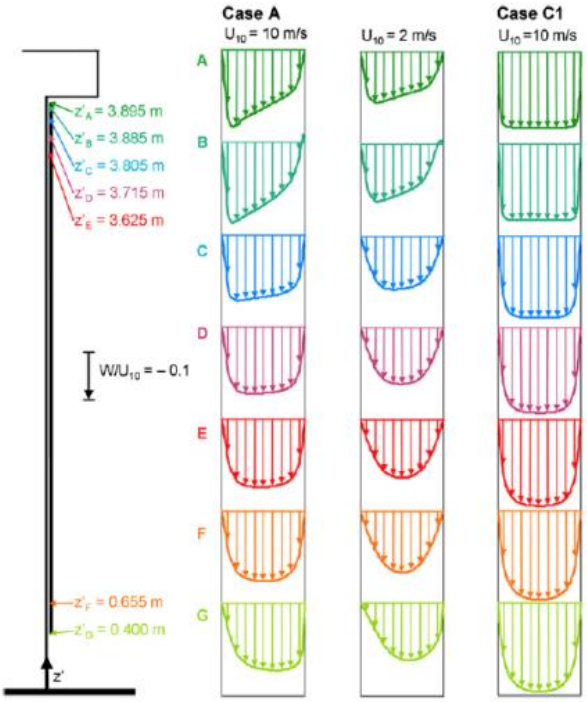

Fig. A1.10 - Profiles of normalized wind velocity across the cavity depth for coupled (Case A) and decoupled (Case C1) simulations (Nore, Blocken, & Thue, 2010)

Basis IV - The flow through an orifice without and with cross-flow

Let's consider a laminar flow through an opening. The flow rate through an opening is determined from the knowledge of its still-air discharge coefficient k_d (dimensionless), which is defined by:

$$k_d = \frac{\bar{Q}}{A}\sqrt{\frac{\rho}{2\Delta p}} = \bar{u}\sqrt{\frac{\rho}{2\Delta p}} \qquad \textit{(eq. A1.15)}$$

where: $\bar{Q}$ denotes the flow rate

A is the area of the opening

ρ is the air density

Δp is the pressure difference across the opening

This coefficient in laminar flow is fixed purely by the shape of the opening and the Reynolds number Re_O, defined by:

$$\mathrm{Re}_O = \frac{\rho \bar{u} d}{\mu} \qquad \textit{(eq. A1.16)}$$

where $\bar{u} = \frac{\bar{Q}}{A}$ and d is the opening characteristic dimension.

The eq.A1.15 can be employed to evaluate the pressure loss across an opening on the envelope external layer considering and approaching smooth flow. For turbulent flow, empirical values of discharge coefficient are adopted. Nevertheless, attention must be paid in case of grazing flows. According to Chiu and Etheridge (2007), the presence of a cross-flow reduces the discharge coefficient k_d up to 50% depending on the ratio between the flow perpendicular component $\bar{u}$ and the parallel component V (Fig. A1.11).

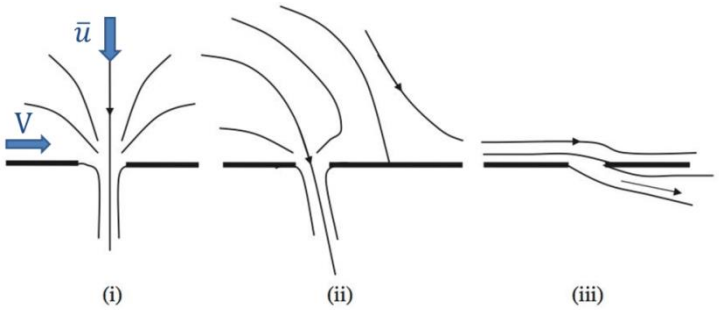

Fig. A1.11 - Streamline patterns in two-dimensional flow for: (i) $V/\bar{u} = 0$, (ii) $V/\bar{u} \ll 1$, (iii) $V/\bar{u} \gg 1$ (Chiu and Etheridge, 2007).

Simplified method - Zonal modeling approach

The simplified method usually called "zonal approach" is presented referring to Lou *et al.* (2012). Here the method is used on a façade with horizontal compartmentations, laterally closed, with diffuse openings (Fig. A1.12). In this method external pressure coefficient are considered known, obtained from experimental tests or from a wind loading code values for a single skin building. With opportune consideration on pressure losses and mass conservation it is possible to evaluate the internal pressures.

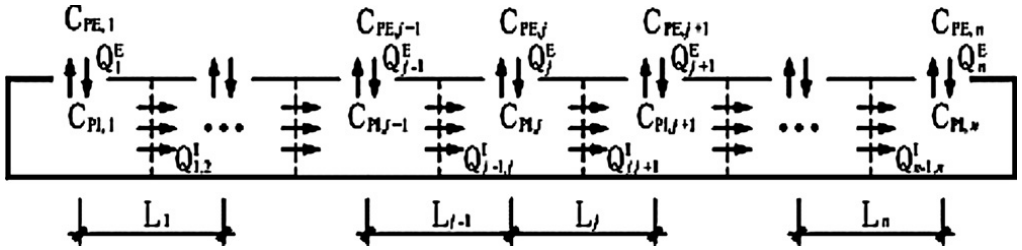

Fig. A1.12 - Schematic top view of the cavity (Lou *et al.*, 2012).

The cavity (corridor) is divided into a number of cells equal to the number of openings. Air flow rate $\bar{Q}$ through openings due to wind pressure difference (Δp) can be determined by the well-known orifice equation, in the following rewritten as:

$$\bar{Q} = k_d A (\Delta p)^t \qquad \textit{(eq. A1.17)}$$

where the flow exponent t could range between 0.5 and 0.8, while k_d is a discharge coefficient.

Starting from this equation Lou *et al.* (2012) define the air flow rate through the *j-th* opening as:

$$Q_j^E = k_d A_E \left(\frac{\rho \bar{u}^2}{2} \right)^t \left(C_{PE,j} - C_{PI,j} \right) \left(\left| C_{PE,j} - C_{PI,j} \right| \right)^{(t-1)} \qquad \textit{(eq. A1.18)}$$

where: $C_{PE,j}$ is the external pressure coefficient at *j-th* cell

$C_{PI,j}$ is the internal pressure coefficient at *j-th* cell

The pressure loss due to friction along cavity of the corridor VDSF can be calculated by the Darcy-Weisbach equation. Therefore the air flow rate inside the VDSF cavity from the *(j+1)-th* cell to the *j-th* cell is expressed as:

$$Q_{j+1,j}^I = \frac{A_I \bar{u}}{\sqrt{\left(f_D \, l_{p,i} / R_h \right)}} \left(C_{PI,j+1} - C_{PI,j} \right) \left(\left| C_{PI,j+1} - C_{PI,j} \right| \right)^{(0.5)} \qquad \textit{(eq. A1.19)}$$

where: A_I is the cross section area of the cavity

$C_{PI,j+1}$ is the internal pressure coefficient at *(j+1)-th* cell

The mass conservation equation of the air flow for the *j-th* cell can be written as:

$$\sum Q_j = Q_j^E + Q_{i-1,j}^I + Q_{j+1,j}^I = 0 \qquad \textit{(eq. A1.20)}$$

finally, with opportune substitutions, and applying the boundary conditions to the first and last cell (j=1 or j=n), the above system of *n* coupled equations can be solved numerically for *n* unknowns of internal pressure coefficients.

As pointed out, simplified models based on the fluid dynamic concepts here recalled are unavoidably affected by limitations. Even if the use of such models could give quite good qualitative results with very simple geometries (Lou *et al.*, 2012), it seems not possible to employ such qualitative results as wind load design values.

A1.2 A literature review on wind effects on building envelopes

The definition of wind effects on building envelopes is a relatively new field of research. Historically, studies regarding the wind effects on buildings considered it as a bluff body with single-layer airtight walls. First studies on the wind action on low-rise buildings were carried

out at the end of the XIX century with very rudimentary wind tunnel facilities (Holmes, 2007). The earliest investigations were fundamental to introduce poorly understood concepts, such as the roof suction. Subsequently, after about 30 years of isolated studies in the few existing aeronautical wind tunnels, two important works were carried-out: Irminger and Nökkentved (1930), tested models with porous walls, measuring both external and internal pressures; Bailey and Vincent (1943) introduced the boundary layer wind tunnel concepts, later explored by Jensen (1958). Since then, many researchers contributed to the development of the wind engineering.

This work deals with wind action on building envelopes that the Eurocode EC 1.4 (EN1991-1-4:2005) defines as "Walls with more than one skin". In such a multi-disciplinary field, it is clear that the actual knowledge level is the result of a wide and complex development of the research on many different topics. Trying to cover chronologically this heterogeneous development, the current review is divided into four subsections as:

- A1.2.1 The first studies
- A1.2.2 Two basic studies
- A1.2.3 Towards the ventilated double skin façades
- A1.2.4 Porous screens

A1.2.1 The first studies

The first pioneering work on the field of building envelopes were carried out by Kramer *et al.* (1979). In this work, the Authors introduced some basic concepts in order to study wind loads on roofing elements, like tiles or paving blocks, that will be later employed for permeable façades. Considering the roofing elements as fixed to an airtight layer, they studied the wind loads acting on the external permeable layer (Fig. A1.13). They asserted that the net wind load is determined by the building flow field, the wind gustiness and the element flow field. In their work, the Authors decoupled external and internal (*i.e.* in the cavity) pressures: a concept still discussed nowadays. Moreover, the many tests done were useful to understand the internal pressure behaviour varying the two main parameters of the external screen: its permeability and the distance from the inner wall. Finally, attention was focused on the supporting systems and how the compartmentations could influence the inner flow and consequently the internal pressure. The reliability of this first study was confirmed by Cheung and Melbourne (1986) and recently by Oh and Kopp (2014, 2015).

In 1983, Gerhardt and Kramer advanced their studies, with a focus on permeable façades. Recalling the previous work, they proposed a wind load mechanism where the internal pressures are influenced by the resistance of the flow through the external layer, and the flow resistance into the internal gap (Fig. A1.14). Internal flows are driven by external pressure differences on the building wall. In that work, the Authors tested many configurations varying the building parameters, permeability of the façade, wind profile and direction, investigating also the effect of vertical compartmentations and lateral side edges.

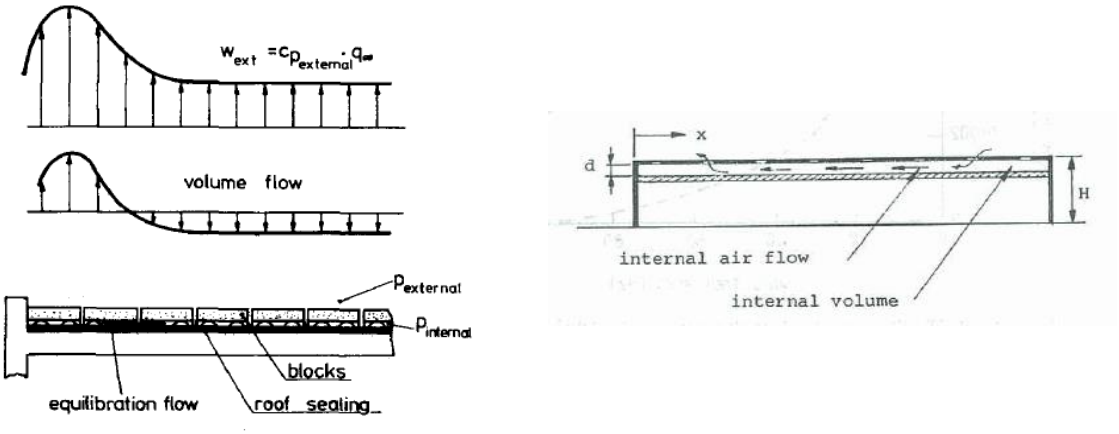

Fig. A1.13 - Sketches from early works on the flow mechanism on permeable roofs: on the left from Kramer *et al.* (1979); on the right from Cheung and Melbourne (1986).

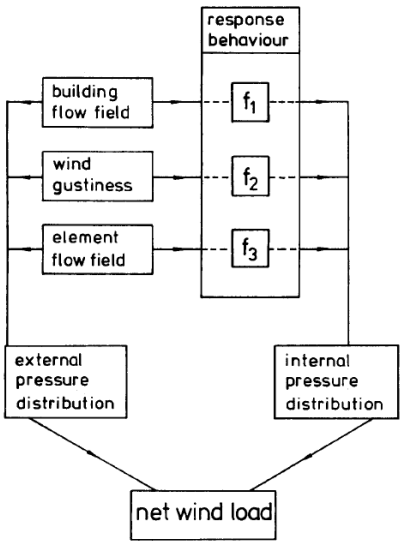

Fig. A1.14 - Schematic of wind loading mechanism of permeable building walls (Gerhardt and Kramer, 1983).

The main conclusions are here summarized:

- concerning the permeability of the exterior wall: increasing the permeability of the cladding a decrease of net wind pressures occurs, while for small permeability the internal pressure is almost constant;
- concerning the flow resistance in the cavity: for a given façade permeability, if the internal flow resistance is increased, the net wind pressure across the external layer decrease. However, the influence of the gap width is negligible for façades with small permeability;
- considering time averaged pressures: the lowest external pressures and the largest net pressures occur if the flow separates at the leading edges and reattaches on the side walls;
- considering both time-averaged and peak pressures: the highest net pressures occur with a smooth approaching flow;
- internal pressures equilibration of two adjacent building walls should be avoided because it increases the net pressures on the external layer.

After this important study, field measurements on rainscreen walls were carried-out by Ganguli and Dalgliesh (1988), and then summarized by Rousseau (1990). Meanwhile, other fundamental studies, on the cavity pressure (Fazio and Kontopidis, 1988), or on permeable

roofs (Amano *et al.*, 1988, Sun and Bienkiewicz, 1993), were carried out. Concerning the topic of internal ventilation, interesting studies with comparisons between experimental and numerical results were carried out by Kato *et al.* (1992).

In 1991 Chino *et al.* developed an analytical approach, in which the Bernoulli equation for multi-room buildings was applied to double skin walls with many openings on the external layer. In the model, for the internal flow between the skins, the equation of flow between parallel plates was employed (Chino *et al.*, 1991). Then, they validated the model with experimental tests. The instrumented wall was placed on a side of the building, *i.e.* in an area of flow separation (Fig. A1.15). They concluded that the results of the analytical model agreed well with the experimental results if proper values for flow resistance between the double walls were used.

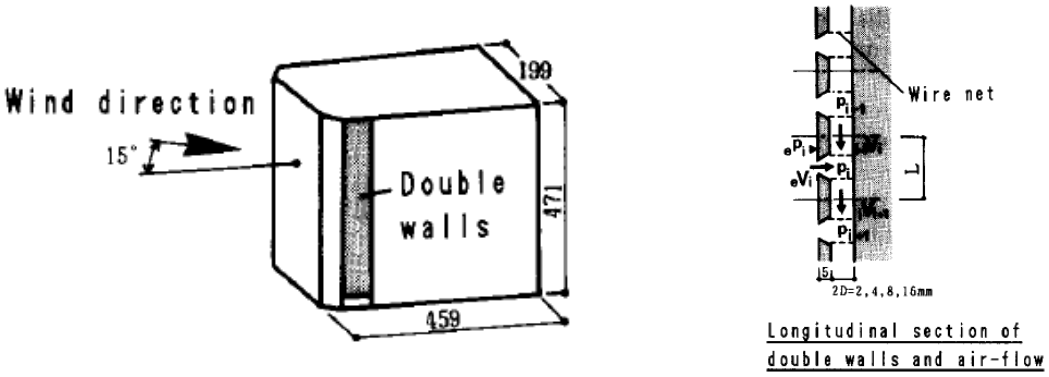

Fig. A1.15 - Sketches of the double wall wind tunnel model (Chino *et al.*, 1991).

A1.2.2 Two basic studies

In 1994, two important researches in the field of rainscreen walls / permeable façades were published: the first deals with a BVR geometry, and it is the conclusion of the work started fifteen years before by Gerhardt, the second concerns PER, and it is the study in the frequency domain by Inculet and Davenport. In the following work these will be discussed in deep.

"Wind loads on wind permeable façades" (Gerhardt and Janser, 1994) represents one of the most important experimental work on permeable façades carried out up to date. Based on the principles of flow resistance through the external layer and in the cavity introduced in the previous section (Fig. A1.16), a huge amount of configurations were tested varying the following parameters:

- The boundary layer: three boundary layers were used for the tests, with profile exponents α_P= 0.1, 0.2 and 0.3.
- The model dimensions: models with relative dimensions h/a = 0.5, 1, 1.5, and 4 and b/a = 1, 2 and 4 with a constant width a = 100mm were tested. The building model was a rectangular prism where h is the height, b and a are the other side dimensions.
- The wind direction: the flow direction was varied in steps of $\Delta\alpha$ =10°.
- The permeability of the external skin: permeabilities of ε = 0.5%, 0.75% and 1% were investigated.
- The gap flow resistance: this parameter was varied by changing the gap width s between the impermeable building, and the porous façade. The tested cases were: s/a= 0.0025, 0.005 and 0.01.

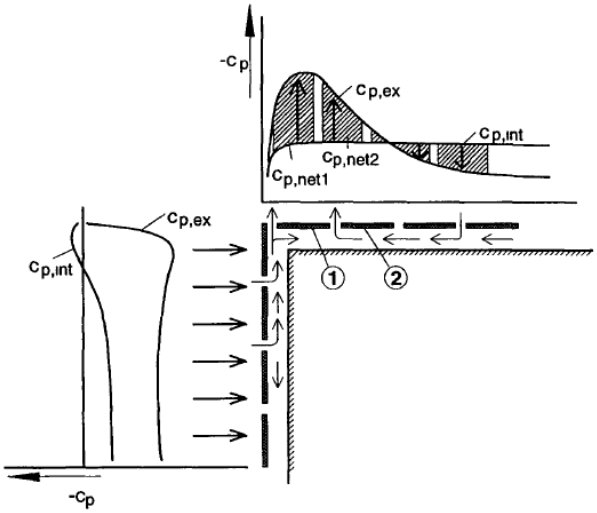

Fig. A1.16 - Flow mechanism (Gerhardt and Janser, 1994).

Two important similarity consideration were done by the Authors:

(i). The first one was on the scaling method for the external screen. To ensure the similarity of the net pressures between the full scale and the model scale, they proposed that the relation between pressure loss (Δp) and volume flow $\left(\dot{V}\right)$ must be conserved. This relation was expressed as:

$$\Delta p = C\dot{V}^n \qquad \textit{(eq. A1.21)}$$

The range of the characteristic values of C and n to ensure this similarity was checked in Gerhardt's thesis (Gerhardt and Kramer, 1983).

(ii). The second one was on the scaling method used for the cavity gap. They considered the gap flow as the flow in the inlet section of a two-dimensional channel (Fig. A1.17). Then, through considerations on the pressure loss at the channel entrance, they proposed a distorted scale criterion for the cavity gap, instead of a geometric one.

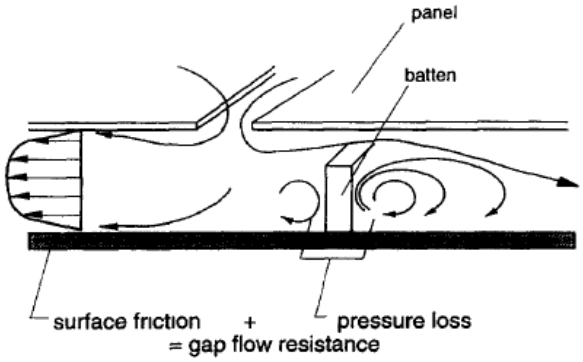

Fig. A1.17 - Representation of the cavity gap flow (Gerhardt and Janser, 1994).

Results were given for the constant wind direction $\alpha = 10°$, because with that value the largest suctions occurred at the edges. Overall, Gerhardt and Janser drawn the following conclusions:

- For a building with rectangular cross-section and a fixed distance between the screen and the building model, the external suctions increase by increasing the building height, while the cavity pressures result less affected (only slightly increasing when reducing the wall permeability). Therefore, the gap pressures are not remarkably affected by the through-flow resistance (Fig. A1.18-a).

- In Fig. A1.18-b, the external and internal pressure coefficients versus the relative building height are plotted. A smaller gap width corresponds to a larger gap flow resistance. Subsequently, it is easier for the gap pressures to follow the external pressures.
- Fig. A1.18-c shows the maximum net pressure coefficient ($\hat{C}_{p,net}$) for relatively large porosity and relatively small gap width. The $\hat{C}_{p,net}$ for each configuration is plotted versus the relative building height. The smallest net pressures occur when the building lie in completely flow-separated regions.
- For typical full scale values of gap widths, the gap flow slightly contributes to the pressure equilibration, since is dominated by the through flow (Fig. A1.18-d). The use of the peak factor approach to evaluate the wind loads, seems reliable to the Authors. Indeed, the pressure equilibration across the permeable cladding occurs at the speed of sound, *i.e.* it is shorter than the typical gust duration time.
- Based on the peak pressures, the influence of the oncoming flow on the wind loads is defined. The internal pressures vary little by varying the approaching flow conditions. External and internal peak pressure were not measured simultaneously. Thus, Fig. A1.18-d shows an envelope of averaged internal peak pressure coefficients. For relatively smooth flow exposure, the smallest net peak pressure coefficient is obtained. However, the external pressure fluctuations are higher, as compared to the internal pressure fluctuations, attenuated by the through-flow and the gap-flow resistances. Nevertheless, the Authors conclude that net pressure coefficients are almost independent on the approaching flow and the most critical condition occurs in open country exposure flow, where for a certain height, the stagnation pressure is higher than for urban flow conditions.

Finally comparisons between full scale studies and model studies were carried out. In the full scale tests also the air tightness of the edges was considered. As an example, Fig. A1.19 shows the effects on the net pressures on the façade. The importance of the vertical closures at the edges pointed out in the previous work dated 1983 was confirmed.

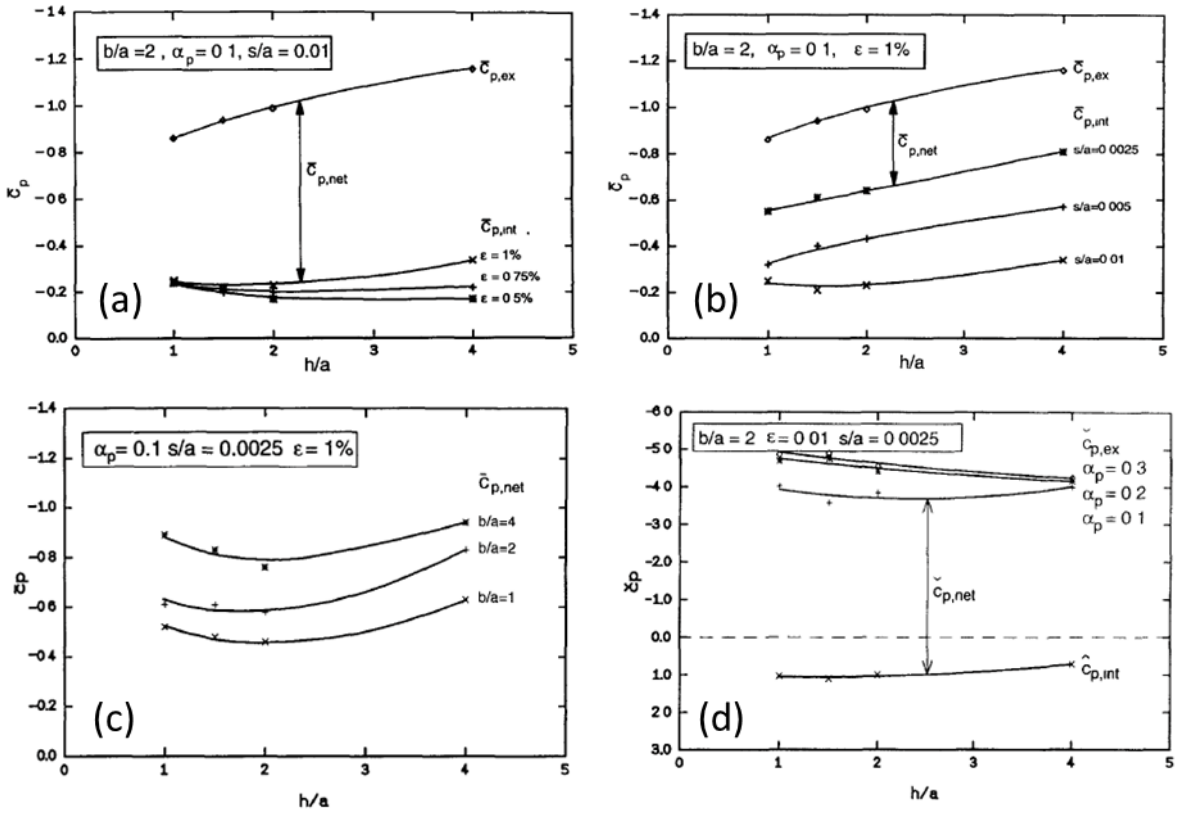

Fig. A1.18 - Results obtained varying different parameters (Gerhardt and Janser, 1994).

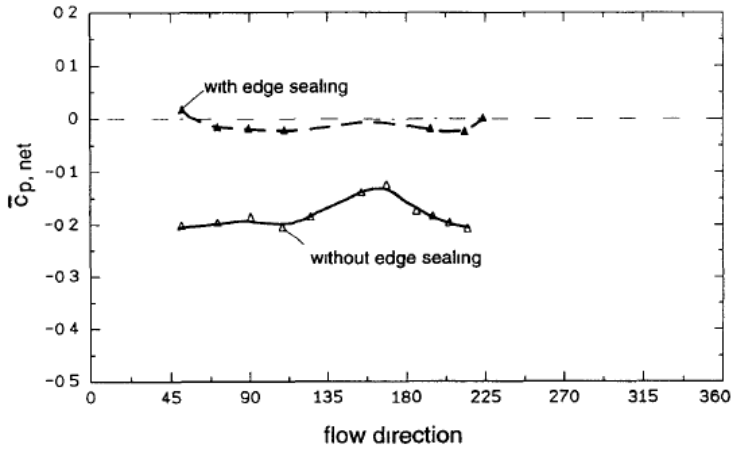

Fig. A1.19 - Effect of the side openings (Gerhardt and Janser, 1994).

This work was followed by another important case study (Gerhardt and Kruger, 1997) in which the principles learnt from the previous studies were applied to the double skin façades of the office building Stadttor Düsseldorf. With this practical case, Gerhardt and Krüger highlighted that a reduction of wind load on a permeable façade respect to an impermeable one is possible in the design phase; moreover, they found that the sum of wind loads on the permeable external and impermeable internal skin is higher than the load on a single skin façade. Nevertheless, very little information on the model and the set up, and few detailed results were provided.

Few remarks can be done on the work by Gerhardt and Janser (1994) before continuing the history of wind load on walls with more than one skin. Surely, the contribution to this field from Gerhardt's research group is precious. They firstly faced the two main problems of this

topic: the high number of parameters involved and the multi-scale nature of the problem. Regarding the first aspect, many configurations were planned and tested. From this point of view, the goal was to find the worst condition for a specific parameter, *i.e.* the wind direction, and then to study the remaining parameters with the first one fixed. Unfortunately the cavity compartmentation was not considered as one of the main parameters. In any case, this work can be considered fundamental for researchers dealing with parametrical experimental studies.
Concerning the second aspect, the adopted scaling criterions are not fully supported by the theory. The scaling problem of a whole building is a relatively easy issue. Usually building models used in wind tunnel tests are equipped with pressure and force transducers. In standard experimental tests on buildings, the Reynolds similarity is not fully satisfied but, especially for practical cases involving sharp edged buildings, Reynolds effects can be neglected. The problem raises up when details of the building need to be scaled. The word "details" refers to parts of the building of a lower scale order, and in this case it refers to small openings or small cavities. The local flow around (or in) a detail could be strongly influenced from the mismatch of the Reynolds similarity. Many researchers tried to study this delicate topic, which strongly influences the accuracy of the results from laboratory tests. For instance, there are many experimental (*e.g.* Stathopoulos and Zhu, 1988, Chand *et al.*, 1998, Maruta *et al.*, 1998) or numerical (*e.g.* Montazeri *et al.*, 2013) investigations carried out on pressure field on buildings with appurtenances or balconies. The problem of the permeable/porous screen and the cavity is more complicated since the "flow behaviour" through these elements must be scaled. In the following, some specific scaling difficulties are pointed out:

- *The rainscreen has small venting openings*. In most of the practical cases, these openings are small. It is easy to understand that if the geometric scale usually employed in wind tunnel range between 1:200 / 1:500, an opening in real scale of around 20mm must be represented in the model as an opening of 0.1 / 0.04mm. Thus, a direct geometric scaling is not possible. Allori *et al.* (2013) proposed a scaling criterion for porous panels based on maintaining the similarities of porosity, ratio of thickness (of the screen) to hydraulic diameter and Reynolds number. Their work referred to the case of a porous screen without a wall behind it. It was not proven whether this criterion can be applied to the external panel of a rainscreen (which has the building wall behind it). The criterion adopted by Gerhardt *et al.* seems very similar to the one proposed by Allori *et al.* thirty years later. To the knowledge of the author, this problem is still open.
- *Usually the cavity in real scale is small*. For a rainscreen, the cavity dimensions are in the order of few centimetres. Therefore, the considerations previously pointed out on the direct geometric scaling are valid also for the cavity. To solve this problem, Gerhardt *et al.* developed another scaling criterion. Their idea was to consider both the gap flow and the outflow through the porous cladding. Therefore, they considered the gap flow as the flow in the inlet section of a two-dimensional channel and its pressure losses. Since it was not possible to apply a direct geometry scaling to the cavity, the proposed method was based on ensuring the same amount of losses. Considering a laminar flow in the gap, the Authors used a relation between the losses at the entrance of a two-dimensional channel and the laminar flow to increase the cavity depth and reach the same amount of losses.
  The reliability of the proposed method was not assessed. In particular, the results could be affected by the assumed hypothesis and the measurements accuracy in such a small cavity. In their work, Gerhardt *et al.* adopted a constant width of the model equal to a = 100mm.

The gap width tested are: s/a = 0.0025, 0.005 and 0.01. This means that the absolute value of the cavity is respectively s = 0.25 mm, 0.5mm and 1mm. With these values, also the roughness of the model material and imperceptible deformations due to the wind action could affect the results.

Despite the aforementioned limitations, the huge work done by Gerhardt *et al.* is the basis of the general principles of a permeable façade without compartmentations. Most of the works in the field of rainscreens are based on their intuitions, later extended to ventilated double-skin façades.

In the same year, 1994, another fundamental work on pressure equalized rainscreens was published by Inculet and Davenport. The study discusses the primary factors that control the pressure-equalization via the results of theoretical models, wind tunnel experiments, and full scale experiments on two separate rainscreen typologies. The primary factors considered in their work are:

- the leakage of the air barrier;
- the aerodynamic damping introduced by venting in the rainscreen;
- the spatial non-uniformity of mean exterior pressures and of fluctuating exterior pressures due to building aerodynamics and turbulence.

Inculet and Davenport carried out a parametric study varying the leakage of the air barrier, the compartment size (volume and exterior dimensions), venting configurations and wind characteristics. The different approach adopted makes the study complementary to that by Gerhardt and Janser (1994). In the latter, the cavity between the two layers of the whole façade was considered as a single volume (treated as a two-dimensional channel), while the internal supporting structures were considered as obstacles for the flow than airtight layers of compartmentations. Therefore, from a fluid-dynamic point of view, the case is different from that of Inculet and Davenport (1994). The attention on a smaller "elementary unit", as the compartmentalized unit (Fig. A1.20), led the two researchers to focus the study on different parameters, as the air barrier leakage and the venting configurations.

In Inculet and Davenport (1994), a relationship between mean pressure differences across rainscreen and air barrier was developed at first. The relation obtained from simple orifice equations was based on the assumptions that the flow was incompressible, steady, and that the two layers had different flow exponent. Therefore, in this case, also the air barrier was considered permeable. The Authors recognised the complexity of the problem due to the many parameters involved, even for the simplest studied primary factor. In particular, they underlined that the discharge and flow coefficients, employed in the proposed relation, require clarification. These remarks can be read now as suggestions for further studies on the discharge coefficients, which were later provided, for instance by Carey (2001), Karava *et al.* (2005), Chiu and Etheridge (2007).

Fluctuating external pressures tend to drive fluctuating flows through the venting holes of a rainscreen. These small holes provide a resistance to the flow which tends, in turn, to suppress the fluctuations: Inculet and Davenport referred to this phenomenon as a damping effect. Therefore, the Authors concluded that an high damping of the flow through the venting holes corresponds to high differential pressures on the rainscreen. In their work, they re-arranged the Helmholtz theory for the pressure equalization problem. Therefore, a theoretical model

developed based on a sinusoidal pressure fluctuations applied, obtaining an equation similar to that proposed by Holmes (1979). The equation was further extended to random fluctuations and validated with experimental and full scale tests. The obtained results suggest to design a rainscreen wall with a small cavity volume and a large venting area in order to increase the natural frequency of the cavity and minimize the damping. In particular, comparing theoretical and experimental results, three aspects were highlighted:

(i). The theory is valid, aside from a minor discrepancy in phase lag.

(ii). Leakage in the air barrier reduces the transfer function value for all exterior pressure frequencies and amplitudes. This anticipates the results obtained with a more specific work on pressure fluctuations in a low-rise building by Guha *et al.* (2010).

(iii). The superimposition of a mean pressure drop on the unsteady pressures has different effects depending on the amplitude fluctuations: small fluctuations may be significantly reduced while higher amplitudes are less susceptible to this effect.

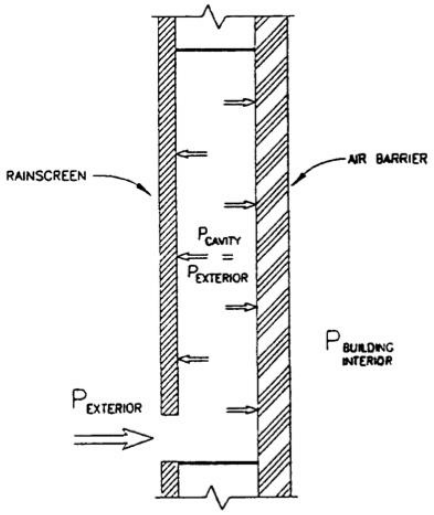

Fig. A1.20 - Principle of pressure-equalized rainscreen (Inculet and Davenport, 1994).

In the compartmentation of the cavity, employed to reduce the exterior pressure-gradient spatial effects, the size and the venting configuration are the only parameters that a designer can use in the design phase. Therefore, another aim of the work by Incluet and Davenpoert (1994), was to determine a panel size over which the average peak pressure across the rainscreen (spatial average) was acceptably reduced as compared to the average exterior peak pressure at any point of the panel. This goal was achieved comparing the joint acceptance function related to three configurations of rainscreen walls. The "Case A" of venting configuration in Fig. A1.21, resulted the most effective.

Even if its contents appear hardly applicable, in this paper it is possible to find all the basics to study each single element on a wall with more than one skin with internal vertical and horizontal compartmentations.

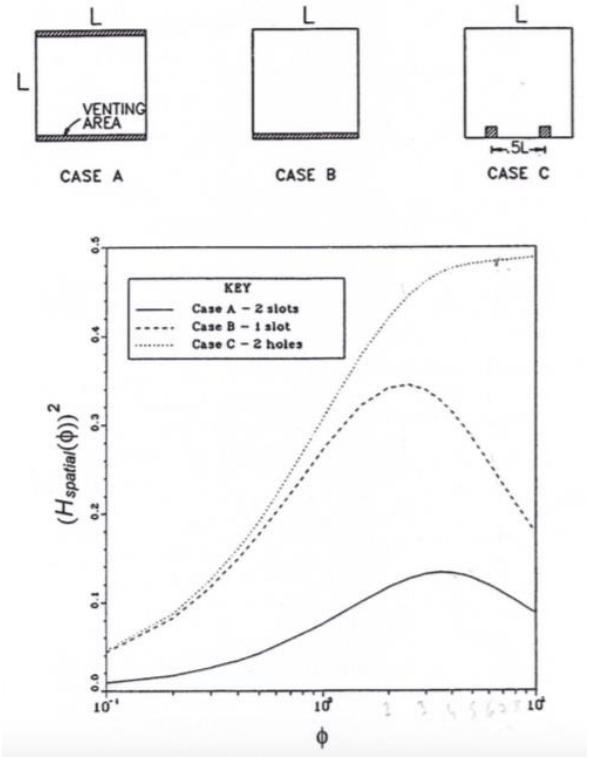

Fig. A1.21 - Effect of spatial averaging of pressures on rainscreen loading for three venting configurations (Inculet and Davenport, 1994).

A1.2.3 Towards the ventilated double-skin façades

The strong similarity between "Permeable Façades", "Pressure Equalized Rainscreens (PER)" and "Double-Skin Façades (DSF)" has been recognized from the first studies carried out in this field. However, even ignoring in a first approach the difference between the materials usually employed in PER or DSF, the idea of a DSF as a "bigger PER" is not always directly applicable.
Gerhardt and Krüger in 1997 extended their studies to the façade of the "Stadttor Dusseldorf" building but the façade was not instrumented in order to make a comparison between theory and real case. Inculet and Davenport (1994), reported two full-scale studies, which revealed some discrepancies compared to the theory. Generally the differences could be:

- between the theoretical model and the real case, therefore a lack of details in the model leads to discrepancies;
- between the prototype and the model studied in the wind tunnel. Therefore, different geometric scale effects in fluid dynamics may affect, for instance, the possible flow regime in the cavity.

Regarding the role of gap width, Wellershoff and Hortmanns (1999) published the results of experimental tests in wind tunnel on gaps greater than 15cm (Fig. A1.22). Three building were tested with their relatives façades with gap width in the range of ≈ 0,4m-1,4m. They showed that the reduction of wind load on the external skin suggested in the Eurocode version of that time was not reliable for those building systems. The Authors, therefore, rose the attention on the importance of the gap width parameter.

In 1992 Baskaran and Brown carried out a study on the performance of a PER wall under cyclic loading with numerical simulations and experimental tests. The Pressure Equalization Index was proposed. A venting area greater than 1% was suggested to equalize the cavity pressure.

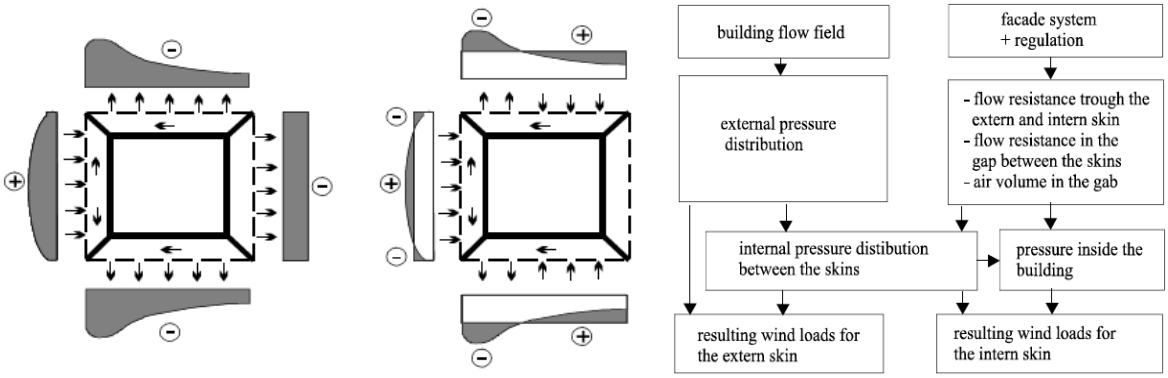

Fig. A1.22 - Wellershoff and Hortmanns' approach. On the left, external pressure and principle pressure induced flow in the gap; on the right, relation between the parameters influencing the resulting wind loads on both skins (Wellershoff and Hortmanns, 1999).

In 1998, Van Schijndel and Schols proposed a first-order one-zone model for the cavity unit of a DSF, validated with experimental studies. The model was based on the Helmholtz equation and one isothermal equation. The agreement between the model and the experimental results was frequency dependent.

Later, in 2003 Ishida carried out similar tests of dynamic loads on a double skin façade unit (Fig. A1.23). The Authors considered four openings conditions (on the outer or inner layer). The case having openings only on the external skin shows that the increase of the opening area ratio leads to an increase of the inner load. For an opening area ratio of 20cm^2/m^3 Ishida measured an inner skin load about the 100% of the wind pressure. Ishida did not find any differences varying the gap depth from 30cm to 60cm.

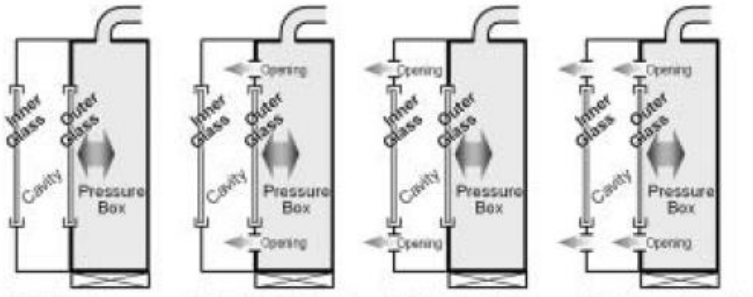

Fig. A1.23 - Four test cases with different types of openings (Ishida, 2003).

Few years later, Kawai (2006) presented a simplified method to estimate the pressure in a cavity of a building-high double-skin façade opened at the edges. Despite the lack of information (not even the cavity depth is provided) regarding the experimental tests, the numerical method was based on an extended Bernoulli's theory, using the external pressures as boundaries. Therefore, in this study it was implicitly assumed that the presence of the gap flow does not affect the external pressure distribution. The Authors found comparable results between the model and the experimental tests.

In the same period Da Silva and Gomez (2008) published a wide study on the gap inner pressures in multi-storey double-skin façades. The study deals with façades opened at the edges, without openings on the external panel and without internal compartmentations. Different configurations of internal connection between façades and building faces were considered. The gap width was varied, testing three values related to the longer side of the building model (Lx): Lx/16.25, Lx/10.83 and Lx/8.125. Moreover, different configurations of the

lateral openings were considered. The study showed that the inner wall pressure distribution is highly influenced by the above mentioned parameters. However, the pressure coefficients within the gap were always negative, regardless the wind direction. Results were given as recommendations instead of applicable values. Also Wellershoff and Hortmanns (1999) concluded with a recommendation addressed to the Eurocode. Both these recommendations can now be found in the Eurocode 1: "*The National Annex may give rules for cases where the extremities of the layer between the skins are air tight and where the free distance between the skins is less than 100mm*" (EN1991-1-4:2005).

In 2009 Kawai *et al.* conducted field measurement of wind pressure on a DSF with a ventilator, the year after, Bettenhausen *et al.* (2010) carried out a simple two-dimensional Computational Fluid Dynamics (CFD) simulation in order to investigate the effect of the opening position on the upper side of double-skin façades. Meanwhile, many works were published on the field of internal pressures: on the effects related to the internal pressure fluctuations (Ginger *et al.*, 2008, Holmes and Ginger, 2009, Guha *et al.*, 2010), on buildings with large façade openings (Karava and Stathopoulos, 2011), on the discharge coefficients (Karava *et al.*, 2005, Chu and Wang, 2009, Lo and Novoselac, 2012).

In the field of CFD simulations for ventilated façades, a remarkable study was carried out by Nore *et al.* (2010). In that study, three-dimensional steady RANS (Reynolds-Averaged Navier Stokes) simulations were performed. Interesting considerations are expressed about the possibility to decouple the problem of the system building plus façade. Moreover, for the first time it is clearly expressed that difficulties due to the multi-scale properties of the problem arise also in CFD simulations. The limitations encountered by Nore *et al.* were also found by Montazeri *et al.*, (2013) in their CFD study to evaluate wind comfort behind a DSF.

In recent years, other studies were carried out, mainly experimental tests. Lou *et al.*, (2012) reported on a wide series of tests related to pressures on corridor DSF of a tall rectangular building (Fig. A1.24). The cavities were horizontally compartmentalized, closed at the edges and the openings were diffuse in the upper and lower part of each storey. Different cavity depths were tested. In particular, referring to the longer side of the building (Lx) cavity gaps were: Lx/34, Lx/17 and Lx/8.5. Different layouts of connection between façades and building sides were considered. They found that both the gap inner pressure and net pressures on the external skin depend on the varied parameters. A maximum net mean pressure coefficient of 1.6 was observed at the external skin of the L-shaped DSF (a DSF on two building sides internally connected). Moreover, a numerical methods was proposed and compared to the experimental results with a relatively good agreement. It considers the external pressure coefficients as boundary conditions, therefore it assumes that internal flows do not affect the external pressure distribution.

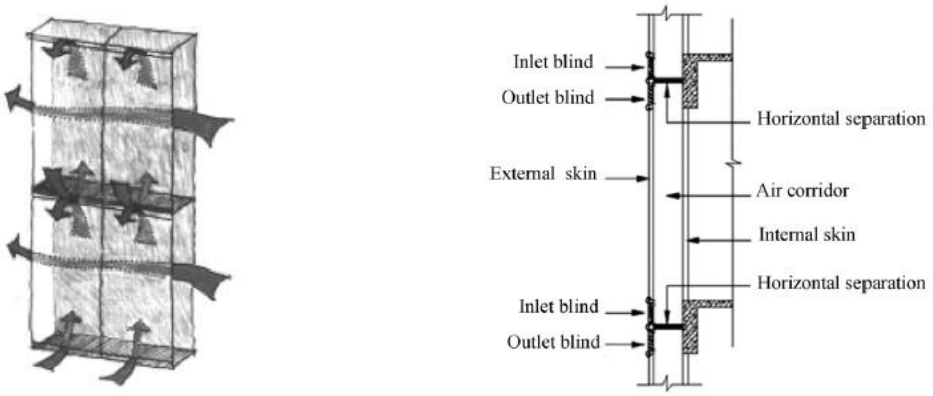

Fig. A1.24 - Schemes of a corridor DSF with external openings (Lou *et al.*, 2012).

Most of the studies based on numerical modelling were schematically summarized by Oh and Kopp (2014), referring to a double-layer roof system, as reported in Fig. A1.25. The common feature of all these studies is that external pressures are a given input. In fact, these numerical models are used to determine internal pressure distributions considering a connection with the external field (local losses) which can cause possible internal flows (friction losses), and/or resonance of internal pressures (amplification or reduction effects) given a known external pressure. This could have two possible interpretations. The first is that when these models are applicable, the knowledge of the external pressures does not depend on the internal one, therefore, the case could be studied in a wind tunnel as a building with a standard façade (or roof). The second is that if the external pressures are influenced by the internal ones, these numerical methods are not applicable. At the moment, there are a few comparison of these methods with corresponding case studies, and there are not parametric studies aimed to investigate the limits of their applicability.

Reference	Dimensions in space	Dimensions in time	Model	Application
Killip and Cheetham [23]	Uniform pressure	Steady	Power law equation	Rainscreen walls
Fazio and Kontopidis [16]			(i.e., discharge equation)	
Baskaran and Brown [3]		One-dimensional		
Xie et al. [45]		(fluctuating)		
Burgess [8,9]			Power law equation + ideal gas law	
Van Schijndel and Schols [43]				
Inculet and Davenport [21]			Helmholtz resonator	
Choi and Wang [13]			(i.e., unsteady discharge equation)	
Kumar and Van Schijndel [28]				
Holmes [20]				Building internal pressure
Vickery [44]				
Sharma and Richards [37]				
Oh et al. [33]				
Ginger et al. [19]				
Lou et al. [30]	One-dimensional			Double-skin facades
Amano et al. [1]	Two-dimensional			Roof pavers
Trung et al. [42]				Porous roof cover sheets
Sun and Bienkiewicz [41]		Steady	Darcy's law (friction losses)	Roof pavers
Current study (2014)	One-dimensional	One-dimensional	Unsteady discharge equation +	Double-layer roof
		(fluctuating)	Couette flow (friction losses)	

Fig. A1.25 - Summary of numerical models for internal pressures by Oh and Kopp (2014).

Recently, Geurts *et al.* (2015) carried out a series of wind tunnel studies on a floating cube equipped with a permeable outer layer (Fig. A1.26). The aim of the study was to show the effects of opening size and cavity width. Internal compartmentations were not considered, while different typologies of lateral connections between the external layers were part of the study. They found that above a certain gap width (≥10mm) the internal pressures are almost constant over the whole cavity: the pressure coefficient is approximately equal to -0.6, except close to the openings, where there are local effects. When the size of the cavity decreases (down to 2 mm), the distribution of the pressures inside the cavity differs considerably. Little

variations were measured varying the ratio between the gap width and the opening size in the range between 0.2 and 0.8. These studies are also supported by ongoing full scale experiments, as reported in Van Bentum and Geurts (2015).

The most recent work on this topic was presented at the 8th International Colloquium on Bluff Body Aerodynamics and Applications (BBAA) conference in 2016 by Hu *et al.* (Fig. A1.27). In the work, the effects of a double-skin porous façade system on the wind-induced response of the CAARC Standard Tall Building were investigated through wind tunnel aeroelastic study. Four different laterally opened screen configurations were tested, starting from the sealed one, progressively increasing the number of openings on the front. All the screens were fixed at a distance of *B*/22.5, where *B* denotes the characteristic cross-flow dimension. The different behaviour of the system with a sealed screen as compared to the cases with openings was discussed. In particular, in the case without openings, the across-wind response is amplified. The study was also supported by CFD simulations.

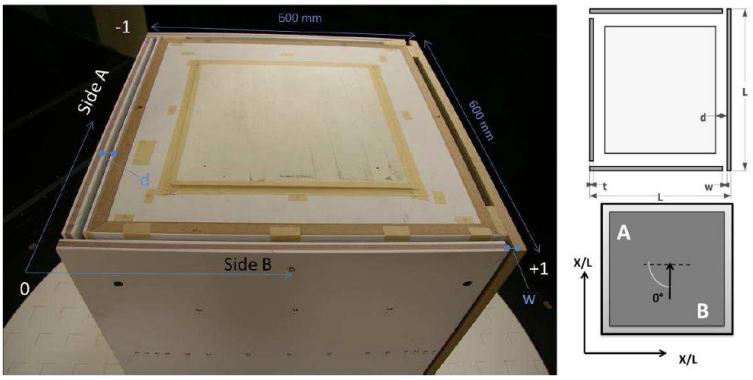

Fig. A1.26 - Picture and sketches of the model used by Geurts *et al.* (2015).

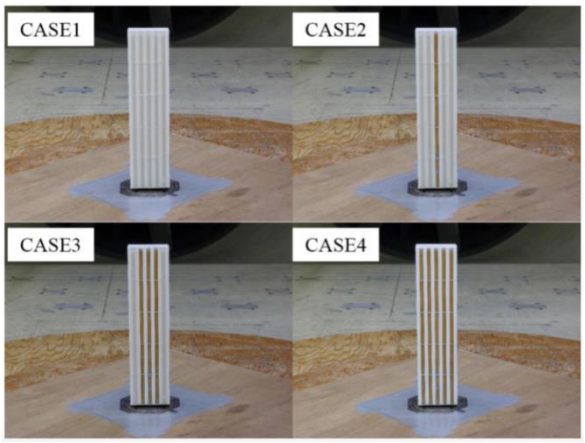

Fig. A1.27 - Test building model with a double skin façade. The four screen tested (Hu *et al.*, 2016).

A1.2.4 Porous screens

The early applications of porous screens refers to panels used as wind barriers in agriculture (*e.g.* Richards and Robinson, 1999, Robertson *et al.*, 2002). Nevertheless, in the last decades, they have been employed for many civil engineering applications (Briassoulis *et al.*, 2010, Giannoulis *et al.*, 2012). For instance, the name "porous screen" for civil engineering applications have been used to describe a permeable façade (or roof) (Trung *et al.*, 2011), or to describe an apparatus specifically applied which can interact with the aerodynamic of the main object on which is mounted on (Belloli *et al.*, 2014) (Fig. A1.28). In some circumstances, also a sun shading screen could be considered a porous screen.

Fig. A1.28 - Render (left) and pictures of the wind tunnel set-up (centre and right) from Belloli *et al.* (2014).

A porous screen is a permeable layer. Therefore it is important to point out the distinction between a porous/permeable façade and a façade with diffuse openings. To the author, this is based on the relationship between the openings and the gap fluid dynamic of the façade. For instance, when the façade is a pressure equalized rainscreen wall (with vertical and horizontal compartmentations), its design against wind loads can be approached referring to many single independent components. Here, the single component on which the designer is focused considers the corresponding external opening as "the main" opening, even if the façade itself has many of these openings and their absolute dimensions are small. In this case the name *diffuse openings*, is more evocative. Conversely, if the same façade does not have internal compartmentations the relationship between the openings and the cavity is different: in this case the whole façade is affected from all the many openings, therefore from the overall permeability of the *permeable/porous façade*.

A particular typology of porous façade is represented by the clad scaffoldings. These temporary structures are typically covered with nets or plastic sheets to prevent construction equipment from falling. From a wind load point of view a clad scaffolding presents the same geometry of a permeable façade. Moreover, the many applications (and studies) of scaffoldings with airtight cladding broaden the possibility to compare their fluid-dynamic behaviour also with the double-skin façades.
In 2005, Yue *et al.* carried out a series of wind tunnel tests for integral lift scaffolds for a regular tall buildings. This type of scaffolding is temporarily fixed all around the building for a certain height, then it is uplifted while the construction grows. In their tests both the blocking ratio of the scaffolds and the opening ratio of the building (which represented the different construction phases) were varied. The atmospheric boundary layer was not reproduced. The drag coefficient on the screen was measured through a force balance, but the model was not equipped with pressure taps. They found that the load acting on the scaffold reached a maximum for wind perpendicular to the building face. The shape value increased almost linearly with the blocking ratio of the screen.
Later, in 2007, Charuvisit *et al.* performed a series of experimental tests with a solid sheet clad scaffolding in uniform flow. They tested different configurations, as reported in Fig. A1.29. The scaffold screen was reproduced as an airtight layer 7mm thick, fixed at a distance of 2mm from the building face, in any configuration. Considering that the smallest building model side was 132mm, the screen, without internal compartmentations and laterally-opened (also on top),

was fixed at the relative distance of 1/66 of the building side. They found that the mean net wind pressure becomes the positive maximum when the screen is directly exposed to the wind action, with a direction perpendicular to the scaffold. This value was higher for shorter building walls and shorter scaffolds. Therefore, the width of both, the building wall and the scaffolds, are important parameters on the resulting wind load.

Irtaza *et al.* (2012) conducted wind tunnel tests on the well-known Silsoe Cube surrounded by an impermeable sheeting. Tests were carried out with the scaffold model fixed on the ground and, later, slightly elevated. The screen thickness was 1/100 of the building dimension, but it was fixed at a distance equal to 1/4 of the cube side. Tests were carried out reproducing the atmospheric boundary layer in accordance with the literature on the Silsoe experiments. The Eurocode provisions for sheet-clad scaffoldings and experimental results were compared. Except on the leeward side, where a pressure coefficient of 0.25 was suggested, they found an agreement with the code values.

Finally, in 2013 Wang *et al.* investigated the wind loads on nonporous scaffoldings through a wide experimental campaign. Many scaffolding configurations were tested varying the building opening ratio and wind angle of attack (Fig. A1.30). The screen model was 5mm thick, so, almost 1/40 of the shorter building model dimension. The scaffold models was slightly higher than the building model, and it was equipped with a huge number of pressure taps. The largest local peak net pressure coefficients were found in the upper region or side edge of the scaffoldings. The interference between scaffolding placed on more building sides tended to reduce the magnitude of both positive and negative peak pressures. Moreover, they concluded that European (BS EN 12811, 2003), Chinese (JGJ 128, 2000) and Japanese (SCEA, 1999) recommendations underestimate the mean force coefficients for certain scaffolding geometries. In particular, the SCEA (Scaffolding and Construction Equipment Association of Japan) recommendations underestimates the negative area-averaged wind force coefficients for some geometries. The results were then integrated with the study of the interference caused by surrounding buildings (Wang *et al.*, 2014).

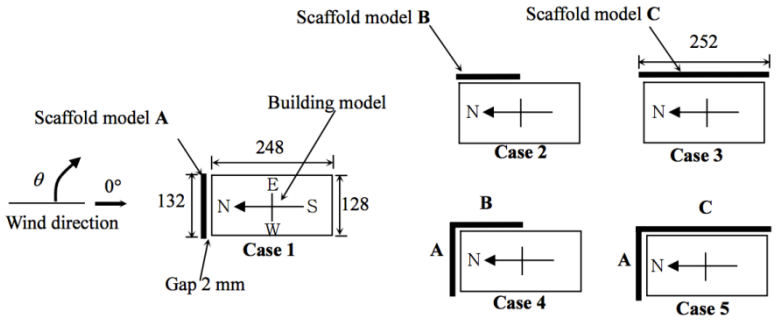

Fig. A1.29 - Experimental configurations (unit: mm) tested by Charuvisit *et al.* (2007).

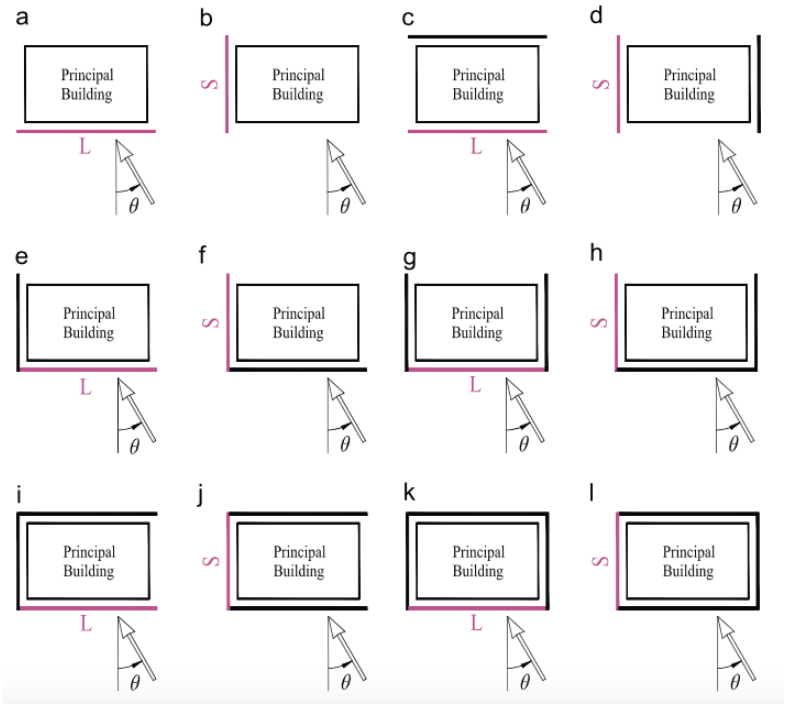

Fig. A1.30 - Experimental configurations tested by Wang *et al.* (2013).

As a permeable layer, the porous screen complicates both the experimental and the computational study. In experimental tests there are scaling problems which need further in-deep studies. Recently Allori *et al.* (2013), found a scaling procedure for porous screens. Unfortunately it is not possible to extend it for the cases in which a wall is placed behind the screen. There might also be difficulties when adopting a computational approach. Even if it is possible to deal with models at full scale, there is the necessity to simplify the problem. For instance, CFD simulations were carried out on porous screens to investigate the possibility to consider a porous equivalent element instead modelling the complete real screen (*e.g.* Teitel, 2010, Chen *et al.*, 2012). The same approach was employed by Irtaza *et al.* (2010), in the above mentioned parametric numerical study, but a validation of the results obtained modelling such porous scaffoldings was missing.

To conclude, it is to note that as much the porosity of the external skin attached on a building wall increases, as much the façade and its supporting systems became a series of appurtenances of the wall. If the façade elements become appurtenances, to consider them as surface roughness could be more opportune. In this field many researchers as Kramer *et al.* (1979), Stathopoulos and Zhu (1988), Maruta *et al.* (1998) carried out significant studies. Nevertheless, up to now, there is not a porosity threshold which distinguishes the case of a porous screen from a façade with appurtenances. This could represent an additional difficulty to codify the already complex field of building envelopes with external openings.

A1.2.5 Wind loading Codes

The lack of answers that, presently, a Code could give to the façade designer is evident. It is argued that this may be related to the huge number of possible case studies. The scientific literature also reveals how, despite many years of research in this field, design rules for such construction types are lacking *(Geurts et al.*, 2015). In the following, a brief overview of international wind loading Codes is discussed. The attention is focused firstly to the Eurocode 1.4 (EN1991-1-4:2005), then other national Codes and standards are considered.

The European code

The Eurocode ENV 1991-1-4:2005 provides a section dedicated to *Pressure on walls and roof with more than one skin*. It gives rules for cases where extremities of the cavity between the skins are airtight and the cavity depth is less than 100mm. First, the permeability μ of a skin is defined as the ratio between the total area of the opening and the total area of the skin (a skin is defined as impermeable if μ is lower than 0,1%). Then, on the basis of the permeability of both the skins it is possible to evaluate the net pressures on the external and internal layers, using pressure coefficients given by the code. It is also suggested to consult the National Annexes. For instance, following the British National Annex the rules provided in the Eurocode are not applicable for "*small format overlapping roofing elements*", and for "*cavity walls when one or both leaves are constructed of small masonry units*" (BS-NA-EN1991-1-4:2010, 2010).

Other codes and standards

The Australian wind loading code, the AS-NZS 1170-2:2011, contains a section dedicated to *Permeable cladding reduction factor K_p for roof and side walls* (Fig. A1.31), which can be used for façades with a ratio of solid area to the total area of the surface out of the range 0.99-0.999. The reduction factor decreases the external pressure coefficient in function of the horizontal distance from the windward edges (AS-NZS1170-2:2011, 2011) in order to give design values.
On the other hand, the American ASCE 7-10 recommends the designer to reduce wind loads on *Air Permeable Cladding* without giving explicit values (ASCE-7-10, 2010).

PERMEABLE CLADDING REDUCTION FACTOR (K_p)

Horizontal distance from windward edge (see Note)	K_p
0 to $0.2d_a$	0.9
$0.2d_a$ to $0.4d_a$	0.8
$0.4d_a$ to $0.8d_a$	0.7
$0.8d_a$ to $1.0d_a$	0.8

NOTE: d_a is the along-wind depth of the surface, in metres.

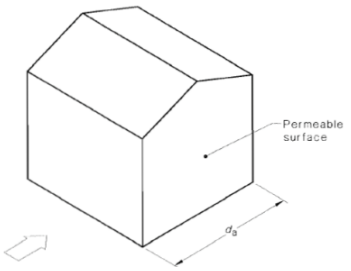

Fig. A1.31 - Australian-New Zeland wind loading code reduction factor (AS-NZS1170-2:2011, 2011).

The main European Standards on this field are: UNI EN 13116 *Curtain walling - Resistance to wind load - Performance requirements* and UNI EN 12179 *Curtain walling - Resistance to wind load - Test method*. The UNI EN 13116 standard specifies the structural performance requirements of curtain walling under wind load under positive and negative (suction) static air pressure (UNI-EN13116:2002, 2002). The main performance requirement given concerns limits of deflection under positive or negative permissible loads. The standard indicates that these permissible wind loads must be calculated in accordance with the procedure laid down in the Eurocode. On the other hand, the UNI EN 12179 standard defines the method for determining the resistance to wind load of curtain walling under positive and negative (suction) static air pressure (UNI-EN12179:2002, 2002) but, as in the UNI 13116, the permissible wind loads must be calculated in accordance with the procedure laid down in the Eurocode.
The American ASTM Standards follows a similar approach to the European Standards regarding the use of wind load values. They treat also the problem of the impact by windborne debris (ASTM E1996, ASTM E1886). However they always refer to "the latest edition of ASCE 7" to evaluate the wind load values.

A1.3 A classification of permeable double-skin building envelopes

The state of art performed aims to include a very wide group of façades, namely every façade that is not a common single-skin façade, with an internal cavity connected to the exterior field. The review of literature contributions (A1.2) underlines the lack of a classification based on the system aerodynamics. Therefore, a classification based on the main components of the façade is here proposed, in an attempt to include as many cases as possible.

The definition of the wind effects on the system (composed by the building and the permeable envelope) is also influenced by the approaching wind characteristics, the building shape, and the configuration of the façade fixed to the building. Therefore, the current classification, focused on the building envelope, must be considered as a part of a procedure for evaluating wind effects, as sketched in Fig. A1.32. Referring to the figure, the façade characteristics are divided in *macro-parameters* and *additional information*. Both the entries are necessary to properly define the system aerodynamics but, for the sake of simplicity, the classification deals only with a part of them.

The use of this classification may become part of a procedure, helpful to the façade designer that is looking for useful values, recommendations and other case studies to compare with.

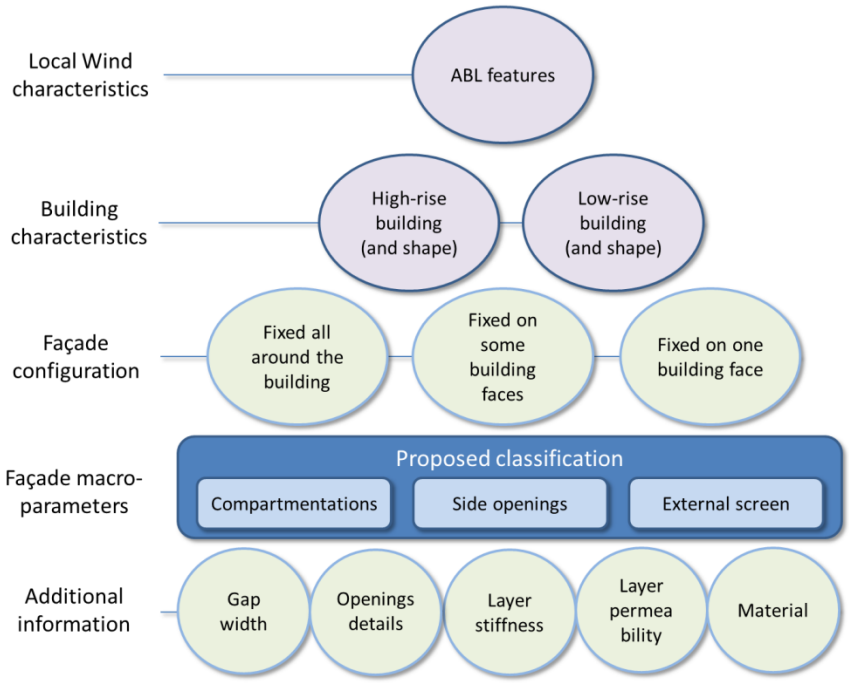

Fig. A1.32 - The parameters involved in the proposed classification into a hypothetical workflow to define the wind effects on permeable double-skin building envelopes.

A1.3.1 An attempt of classification for permeable double-skin building envelopes

The wide number of parameters involved in the study of a permeable double-skin building envelope requires a first classification based on the main façade components, here defined *façade macro-parameters* (Fig. A1.32 and Fig. A1.33). They are: *the compartmentations* of the gap between the two skins, *the side openings* at the lateral edges or at the top/bottom and the *external layer* configuration.

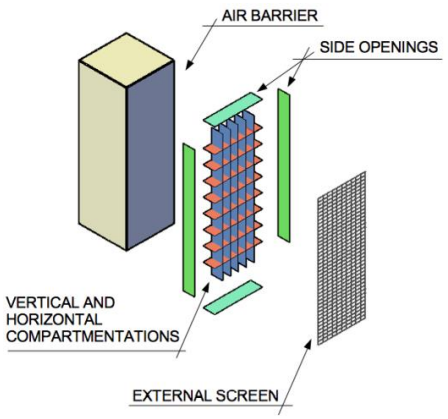

Fig. A1.33 - Scheme of the macro-parameters employed in the classification.

Each one of the above mentioned façade components act as flow constraint, or boundary. In the proposed classification, the smallest flow domain behind the screen is denoted as an "elementary unit" of the façade. The elementary unit geometry is defined through the macro-parameters used in the classification. For instance, the case of a building envelope without compartmentations has a unique elementary unit, while the case with vertical and horizontal compartmentations has multiple elementary units. This concept could be helpful for the façade designer to visualize and to understand the role of each part of the system building + façade, for both the evaluation of the internal pressures and the natural ventilation of the envelope.

Considering a permeable double-skin building envelope fixed only on a single face of the building, the proposed classification is based on the following hypotheses:

a. *The internal layer (air barrier) is airtight.* Even if the air barrier could be equipped with openings and/or has its permeability (*e.g.* Tamura and Shaw, 1976, Inculet and Davenport, 1994), these characteristics are not considered in the proposed classification. However, it is to note that to consider openings and/or porosity on the internal layer, also of the pressure inside the building has to be known.
b. *The compartmentations and the closure at the edges can have only two levels of permeability: 0% (airtight) or 100% (open).* It is well known that the internal compartmentations could be made with permeable layers (*e.g.* metal grids), in order to ensure a certain level of ventilation driven by thermal effects, and leaving also the possibility of an easy maintenance of the façade itself, but also this aspect is left for future improvements. It is implied that, in first approach, a layer conceived to ensure a good ventilation is closer to an open layer than to a closed one.
c. *All the elements of the façade are considered as rigid bodies (flexibility is neglected).* Studies related to the resonance of internal pressure fluctuations based on the Helmholtz resonator model consider the influence of the wall flexibility. According to the literature, this parameter tends to reduce the resonance effects, therefore neglecting it should be conservative.
d. *The gap width is not considered.* As aforementioned, this parameter could be fundamental to completely define the governing equations of the fluid dynamics of the elementary unit, and it could also determine if the façade interacts with the building aerodynamics. In the literature, there are some works which describe the effect of varying this parameter (*e.g.* Gerhardt and Janser, 1994). Nevertheless, to preserve the classification approach, the author prefers not to consider the gap width as a classification parameter. Further

investigations and upgrades focused on the gap width may improve the classification, so to include the screen distance among the main façade parameters.

Before a schematic view of the proposed classification, an explanation of the macro-parameters chosen is given, in order to understand their role in the working principles of the façade. Moreover, the code assigned to each configuration is introduced.

Compartmentations (C): this parameter is fundamental to understand if the studied façade can be divided into further elementary units. Net pressures require the knowledge of the internal pressure distribution. Hence, defining the flow domain behind the screen is of primary importance. For instance, in terms of internal pressures, a building envelope without any compartmentation must be studied entirely, because its flow domain is the whole cavity. The same façade with horizontal and vertical compartmentations could be studied isolating each single elementary unit if opportune conditions of non-interference were satisfied.

The compartmentations are considered as rigid elements, with no permeability. As sketched in Fig. A1.34, four types of configurations are considered:

- Without compartmentations (C0)
- Horizontal compartmentations (C1)
- Vertical compartmentations (C2)
- Vertical and horizontal compartmentations (C3)

In Fig. A1.35, an existing case study with horizontal compartmentations is presented.

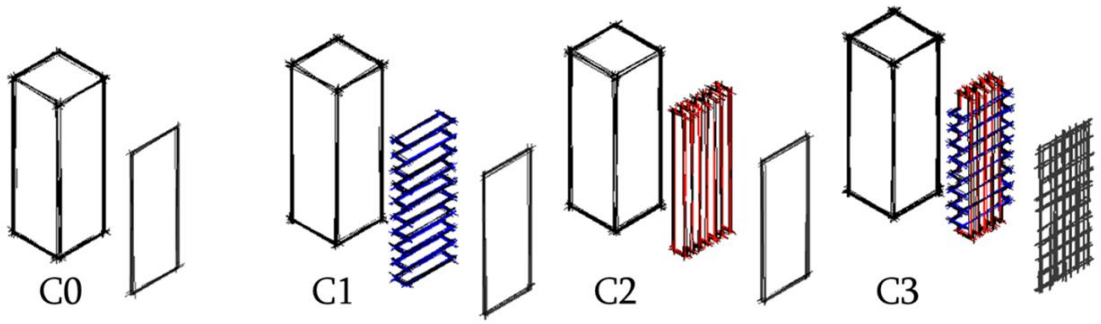

Fig. A1.34 - Sketches of the four cavity compartmentations considered (from left to right C0, C1, C2, C3).

Fig. A1.35 - Practical example of building envelope with horizontal compartmentation: the Unipol Tower (Bologna, Italy). In this case the building is equipped with a permeable envelope on two building sides. View of the two double-skin façades during the construction (left), and at the end of construction (center). On the right, a horizontal section with the two façades is highlighted. Courtesy of Permasteelisa Group.

Side openings (B): a façade with more than one skin can be opened or closed at the lateral sides or at the top and bottom sides. This parameter is strictly linked to the compartmentation of the cavity gap in order to define the geometry and the boundary condition of the elementary unit behind the screen. It is an important parameter since the edges of a building (a three-dimensional bluff body) immersed in a flow are sensitive points. There, the flow usually separates, determining the aerodynamics of the building, and pressure peaks are usually encountered. If a side of the façade is open, this point could become the main "inlet" or "outlet" of the identified elementary unit. For this reason, in this case the cavity could influence the overall building aerodynamics.
Also for the side openings, intermediate values of permeability are not considered. This leads to four conditions of side openings, as shown in Fig. A1.36:

- All sides opened (B0)
- Lateral side opened (B1)
- Top and bottom opened (B2)
- Without side openings (B3)

In Fig. A1.37, an example of building envelope with opened lateral side is reported.

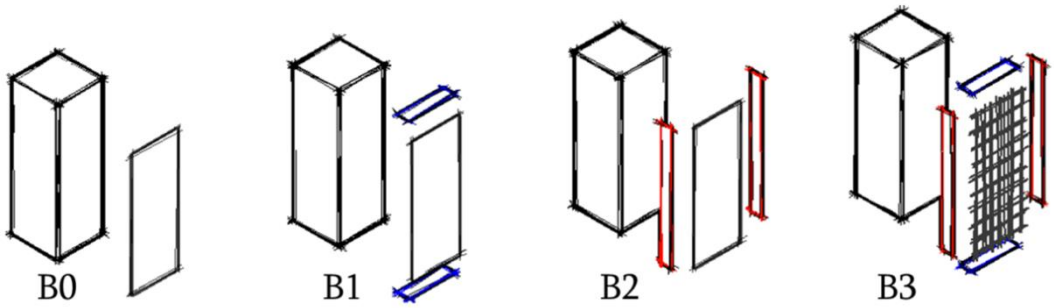

Fig. A1.36 - Sketch of the four side opening considered (from left to right B0, B1, B2, B3).

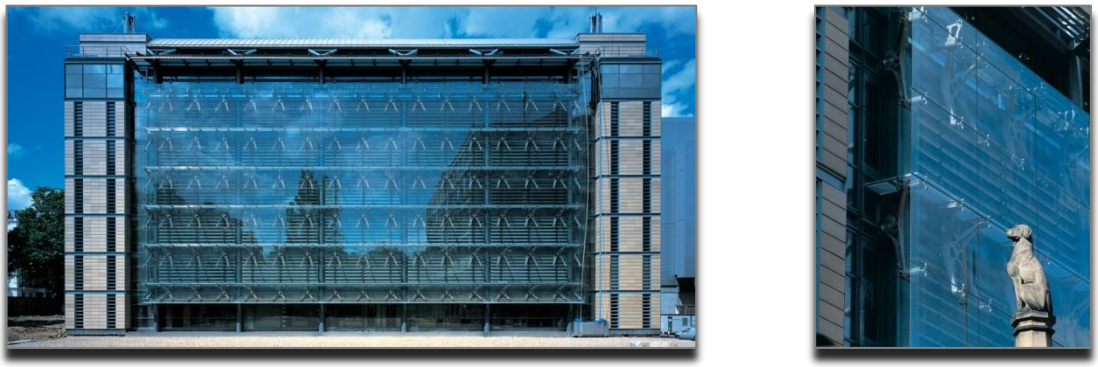

Fig. A1.37 - Example of lateral side opened building envelope: the Darwin Center Phase One, National History Museum (London, UK). Font: www.hok.com.

External Panel (A): when the geometry of the elementary unit is defined, the type of external panel together with the side openings complete the façade characteristics. The external panel could have different opening configurations regarding the position, size and their effect on the internal cavity.
In particular, three different typologies of external panels, as sketched in Fig. A1.38, are considered in the classification:

- Airtight panel (A1)
- Skin with diffuse openings (A2)
- Porous screen (A3)

As explained in section A1.2.4, the main difference between a skin with diffuse openings and a porous screen lies in their relationship with the elementary unit. When the external panel has diffuse openings, a detailed study is required. The size, position, shape, thickness of the openings are necessary to characterize the fluid dynamic behavior of the elementary unit. On the other hand, a porous screen has uniform characteristics (*e.g.* Fig. A1.39); the connection with the external field is not limited to the exact position of the openings but it is diffused on the whole area occupied by the panel.

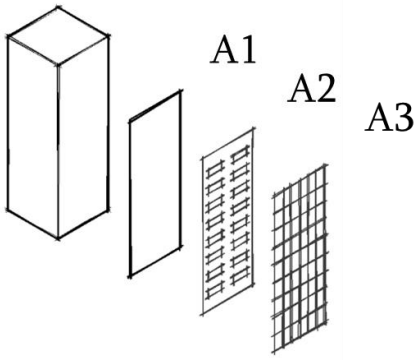

Fig. A1.38 - Sketches of three panel typologies considered (from left to right A1, A2, A3).

Fig. A1.39 - An application of building envelope with porous screen: the GreenPix zero-energy media wall designed by Simone Giostra and partners (Beijing, China). Font: www.archdaily.com.

The matrix of possible cases derives from three external panel typologies (A1, A2, A3), four side openings conditions (B0, B1, B2, B3) and four types of compartmentations (C0, C1, C2, C3), resulting in 48 cases. The number of possible cases could increase if the situation after a debris impact failure is considered, as suggested by Minor *et al.* (2005). In the present section this topic will not be treated, but it remains an interesting field of study which needs to be further explored to be included in such classification.

Among all the possible cases mentioned above, twenty-three meaningful cases were identified. They are presented in Tab. A1.1 where useful entries, for instance concerning practical applications and the literature references, are linked to each façade typology defined through a *Code*, and a *Classification Name*.

A first comment is required on the *"Practical Use / Keywords"* adopted in the classification. The approach is as general as possible, especially referring to possible practical applications. These entries aim to help the designer classifying his case study. For instance, either a *nonporous clad scaffolding* of a tall building, or a *glazed screen* fixed in front of an *existing building* for aesthetical and protective reasons, can be classified as a façade with an *airtight panel, all sides opened, without compartmentations (Code: A1,B0,C0* - Tab. A1.1*).*

In Tab. A1.1, *"Approx"* is the abbreviation of *Approximation*. This entry must be read from the point of view of a schematic macro-classification. It could help the façade designer, especially for the investigation of possible external and internal pressures decoupling. The abbreviation "3D" means that a study of the whole façade must be carried out to preserve the three-dimensionality of the problem. In the table, the absence of internal compartmentations advises against the resort to simplified studies. A further simplification could be to consider the façade very large, so that, for symmetry, in the middle vertical plan, it is possible to approximate the problem as a "2D" problem. In some cases this simplification is adopted, as shown in the literature (*e.g.* Chino *et al.*, 1991, Bettenhausen *et al.*, 2010, *Nore et al.*, 2010). Therefore, the abbreviation "2D" used in the table means that, under specific conditions, the designer could study two-dimensional elementary units of the façade as a very first approximation of the problem. In particular, the classification distinguishes whether the two-dimensional section considered is vertical (2DV), or it is horizontal (2DH). Obviously with the awareness that the whole system building + façade under the wind action is a three-dimensional problem. Finally, the "1D" cases are referred to the presence of both horizontal and vertical compartmentations. Usually in these cases the compartmentations are closed (and small) enough to prevent significant internal flows. For this kind of problems, the fluctuating component of the wind load plays a fundamental role (*e.g.* Helmholtz resonances).

The cited *"Existing studies"* could give the reader/designer information about existing studies, sometimes directly usable for design (Tab. A1.1). These are the main contributions in the literature collected by the author, but the hope is to see a continuous update of this table.

The *"EC"* entry indicates if information on the specific case can be found in the Eurocode EC 1.4.

Code			Classification Name	Practical Use / Keywords	Approx	Existing Studies	EC
A 1	B 0	C 0	Airtight panel, all sides opened, without compartmentations	Glazed screen for existing building Photovoltaic wall Screen for advertising billboard, Clad scaffoldings	3D	Kawai H., (2006), Charuvisit *et al.* (2007), Wang *et al.* (2013), Geurts *et al.*, (2015)	no
A 1	B 1	C 0	Airtight panel, lateral side opened, without compartmentations	Glazed screen for existing building Screen for advertising billboard	3D	-	no
A 1	B 1	C 1	Airtight panel, lateral side opened, with horizontal compartmentations	Ventilated façade with transversal ventilation Corridor double skin façade (opened laterally)	2DH	-	no
A 1	B 2	C 0	Airtight panel, top and bottom opened, without compartmentations	Multi storey ventilated double skin façade	3D	Da Silva and Gomez (2008)	no
A 1	B 2	C 2	Airtight panel, top and bottom opened, with vertical comp.	Multi storey ventilated double skin façade (with compartm.)	2DV	Nore *et al.* (2010), Dan Bettenhausen *et al.* (2010)	no
A 2	B 0	C 0	Skin with diffuse openings, all sides opened, without compartmentations	Cantilevered glazed screen for existing building Screen for advertising billboard Permeable façade	3D	-	no
A 2	B 1	C 0	Skin with diffuse openings, lateral side opened, without compartmentations	Cantilevered glazed screen for existing building Screen for advertising billboard Permeable façade	3D	-	no
A 2	B 1	C 1	Skin with diffuse openings, lateral side opened, horizontal comp.	Corridor double skin façade (opened laterally)	2DH	Wellershoff and Hortmann (1999)	no
A 2	B 2	C 0	Skin with diffuse openings, top and bottom opened, without compartmentations	Back Vented Rainscreens / Permeable façade	3D	Gerhardt and Kramer (1983), Gerhardt and Janser (1994)	no
A 2	B 2	C 2	Skin with diffuse openings, top and bottom opened, vertical comp.	Ventilated façade Screen for banner and advertising	2DV	-	no
A 2	B 3	C 0	Skin with diffuse openings, without side openings, without comp.	Back Vented Rainscreens / Permeable façade	3D	-	yes
A 2	B 3	C 1	Skin with diffuse openings, without side openings, horizontal comp.	Corridor double skin façade (laterally closed)	2DH	Wellershoff and Hortmann (1999), Lou *et al.* (2012)	yes
A 2	B 3	C 2	Skin with diffuse openings, without side openings, vertical comp.	Shaft box façade Ventilated façade	2DV	Chino *et al.* (1991), Wellershoff and Hortmann (1999)	yes
A 2	B 3	C 3	Skin with diffuse openings, without side openings, vertical and horizontal compartmentations	Pressure Equalized Rainscreen Cellular facade / Box double skin façade Photovoltaic wall	1D	Ganguli and Dalgliesh (1988), Baskaran and Brown (1992), Incluet and Davenport (1994), Van Schijndel and Schols (1998), Wellershoff and Hortmann (1999), Ishida (2003), Kawai *et al.* (2009)	yes

Code			Classification Name	Practical Use / Keywords	Approx	Existing Studies	EC
A	B	C	Porous screen, all sides opened, without comp.	Permeable façade Photovoltaic wall	3D	Gerhardt and Kramer (1983)	no
3	0	0					
A	B	C	Porous screen, lateral side opened, without compartmentations	Back Vented Rainscreens / Permeable façade (closed on top and bottom)	3D	-	no
3	1	0					
A	B	C	Porous screen, lateral side opened, horizontal comp.	Louver façade / Porous façade (compartmentalized)	2DH	-	no
3	1	1					
A	B	C	Porous screen, without side openings, without compartmentations	Back Vented Rainscreens / Permeable façade / Louver façade	3D	-	no
3	2	0					
A	B	C	Porous screen, top and bottom opened, vertical compartmentations	Louver façade / Porous façade (compartmentalized)	3D (2DV)		
3	2	2					
A	B	C	Porous screen, top and bottom opened, without compartmentations	Back Vented Rainscreens / Permeable façade / Louver façade (open on top and bottom)	3D	Gerhardt and Janser (1994)	yes
3	3	0					
A	B	C	Porous screen, without side openings, horizontal compartmentations	Back Vented Rainscreens / Permeable façade / Louver façade	2DH	-	yes
3	3	1					
A	B	C	Porous screen, without side openings, vertical comp.	Back Vented Rainscreens / Permeable façade	2DV	-	yes
3	3	2					
A	B	C	Porous screen, without side openings, vertical and horizontal comp.	Porous façade / Cellular façade	1D	Montazeri *et al.* (2013)	yes
3	3	3					

Tab. A1.1- The proposed classification.

A1.4 Summary and concluding remarks

Permeable double-skin building envelope geometries are defined to achieve high aesthetic, acoustic and energetic standards, or, in some cases, simply to protect the walls from rainwater penetration. From an aerodynamic point of view, the flow around a building immersed in the atmospheric boundary layer (ABL), with the internal cavity of the envelope connected through opening and/or porosity to the exterior, results in a complex system. In the following, the main points highlighted in the current section are summarized:

- The wind effects on permeable double-skin building envelopes depend on many factors, namely: the approaching wind characteristics, the building shape, the façade configuration (*i.e.* how many building faces the permeable envelope is fixed on) and the façade characteristics. Moreover, different load mechanisms act on the façade depending on the wind direction (*e.g.* the permeable envelope exhibits a different behavior if located on the windward or on the leeward building side).
- The use of scaled models reproducing the building envelope geometry is a quite difficult task. The problem involves a wide range of geometric scales, from the ABL down to the façade details. In most of the cases, the envelope features are not directly reproducible. Scaling rules must be employed to overcame the problem, *i.e.* reproducing the smallest geometric scale effects, but further investigations are needed in this topic.

  In certain cases the smallest scales are neglected, under the hypothesis that they do not affect the fluid-dynamic system behavior. The cavity pressures are evaluated given the external pressures in proximity of the openings location, but this approach seems to be reliable only under specific conditions. Generally, it is not clear in which cases the use of such a simplified approach might lead to reliable results.

An alternative approach to the problem is the in-deep study of an overall simplified model, but with the envelope characteristics reproduced. In this case, the largest scales are neglected or somehow modeled, while the attention is focused on the façade details.
In the current work, explorative studies were carried out on a simplified system following this approach (Chapter 3 and Chapter 4). The study of such a reduced fluid-dynamic system leads only to approximated results, but it could be helpful to understand the importance and the role of façade parameters of a lower order of size, as pointed out in Chapter 2. Moreover, in the thesis the comparison between the configuration *without* and *with* the façade is carried out, with the aim to point out the approximations introduced by decoupling the external and internal pressures.

- Some building envelopes with a different name (given in practice) could share a common behavior under the wind action. The lack of a classification based on the aerodynamics of permeable envelopes raises from the literature review. This can also explain the inadequacy of wind loading codes in this topic, where the given design values are usable only in very few cases.
- In the current appendix a classification was proposed. The smallest flow domain behind the screen is denoted as an "elementary unit" of the façade. The façade components employed in the classification define, in first approach, the cavity geometry, *i.e.* the elementary unit typical of each building envelope. The chosen macro-parameters are at the same time easy to employ (in the classification) and fundamental in the definition of the wind load. Twenty-three cases were identified through the selective combination of four *compartmentations* typologies, four conditions of *side openings* and three *external screen* configurations. Moreover, to further simplify the classification, the following hypotheses are adopted:
  a. The internal layer is airtight.
  b. The compartmentations and the closure at the edges could have only two levels of permeability: 0% or 100%.
  c. All the elements of the façade are considered as rigid bodies (flexibility is neglected).

  Finally, to enhance the classification, each entry is linked to: a code, a name, a series of keywords that evokes the practical use, a suggestion on the possibility to perform simplified studies, the related scientific literature and if the Eurocode EC1.4 consider the façade typology in question.

To conclude, based on the classification proposed, the thesis work may be considered as exploratory for a building envelope with "*Airtight panel, lateral side open, with horizontal compartmentations*" (Tab. A1.1 - *Code: A1,B1,C1*). *Approximate* (*2DH*) two-dimensional investigations on representative horizontal sections of the system building + façade pointed out useful results preparatory for a deeper and more realistic aerodynamic study. Based on the literature review, there are not *Existing studies* on such a façade typology, which results not covered by the Eurocode recommendations (*EC1.4*) yet.

Bibliography

Allori, D., Bartoli, G., and Mannini, C. (2013). Wind tunnel tests on macro-porous structural elements: A scaling procedure. *Journal of Wind Engineering and Industrial Aerodynamics*, 123, 291–299.

CISBE (2005). Natural ventilation in non-domestic buildings. CISBE Application Manual, AM10.

Amano, T., Fujii, K., and Tazaki, S. (1988). Wind loads on permeable roof-blocks in roof insulation systems. *Journal of Wind Engineering and Industrial Aerodynamics*, 29(1–3), 39–48.

AS-NZS1170-2:2011, (2011). Structural design actions - Part 2: Wind actions, *Standards Australia*.

ASCE-7-10, (2010). Minimum Design Loads for Buildings and Other Structures, *American Society of Civil Engineers*.

Bailey, A., and Vincent, N.D.G. (1943). Wind-pressure on buildings including effects of adjacent buildings. Journal of the Institution of Civil Engineers, 20(8), 243–275.

Baskaran, A. (1992). "Review of design guidelines for pressure equalized rainscreen walls". *Internal report n°629, National Research Council of Canada, Institute for Research in Construction,* Ottawa.

Baskaran, B.A., and Brown, W.C. (1992). Performance of pressure equalized rainscreen walls under cyclic loading. *Journal of Thermal Insulation and Building Envelopes*, 16, 183–193.

Bearman, P.W. (1969). On vortex shedding from a circular cylinder in the critical Reynolds number regime. *Journal of Fluid Mechanics*, 37(3), 577–585.

Bearman, P.W. (1972). Some measurements of the distortion of turbulence approaching a two-dimensional bluff body. *Journal of Fluid Mechanics*, 53(3), 451–467.

Bearman, P.W., and Morel, T. (1983). Effect of free stream turbulence on the flow around bluff bodies. *Progress in Aerospace Sciences*, 20(2–3), 97–123.

Bearman, P.W., and Obasaju, E.D. (1982). An experimental study of pressure fluctuations on fixed and oscillating square-section cylinders. *Journal of Fluid Mechanics*, 119, 297–321.

Bearman, P.W., and Trueman, D.M. (1972). An investigation of the Flow around Rectangular Cylinders. *Aeronautical Quarterly*, 23(3), 229–237.

Beaudoin, J.F., Cadot, O., Aider, J.L., and Wesfreid, J.E. (2006). Bluff-body drag reduction by extremum-seeking control. *Journal of Fluids and Structures*, 22(6–7), 973–978.

Behrens, T. (2009). OpenFOAM's basic solvers for linear systems of equations. *Internal report* (Chalmers University).

Belloli, M., Rosa, L., and Zasso, A. (2014). Wind loads and vortex shedding analysis on the effects of the porosity on a high slender tower. *Journal of Wind Engineering and Industrial Aerodynamics*, 126, 75–86.

Bentley, J.P., and Nichols, A.R. (1990). The mapping of vortex fields around single and dual bluff bodies. *Flow Measurements Instrumentations*, 278–286.

Bentum, C. Van, and Geurts, C. (2015). Full scale measurements of pressure equalization on air permeable façade elements, In *Proceedings of the 14th International Conference in Wind Engineering ICWE14* – Porto Alegre, Brazil, 1-12.

Berger, E., and Wille, R. (1972). Periodic Flow Phenomena. *Annual Review of Fluid Mechanics*, 4(1), 313–340.

Bettenhausen, D., Vaglio, J., and DeGanyar, T. (2010). Double-Skin Facade Cavity Dynamics. *Original paper and presentation for the International Conference on Building Envelope Systems and Technologies (ICEBEST)*, Vancouver, Canada, 9-15.

Blocken, B. (2014). 50 years of Computational Wind Engineering: Past, present and future. *Journal of Wind Engineering and Industrial Aerodynamics*, 129, 69–102.

Bosch, G., and Rodi, W. (1998). Simulation of vortex shedding past a square cylinder with different turbulence models. *International Journal for Numerical Methods in Fluids*, 28(4), 601–606.

Briassoulis, D., Mistriotis, A., and Giannoulis, A. (2010). Wind forces on porous elevated panels. *Journal of Wind Engineering and Industrial Aerodynamics*, 98(12), 919–928.

BS-NA-EN1991-1-4:2005, (2005). UK National, Annex to Eurocode 1. Actions on structures. General actions. Wind action. BSI.

Buresti, G. (2012). Elements of fluid dynamics. Imperial College Press, UK.

Carassale, L., Freda, A., and Marrè-brunenghi, M. (2014). Experimental investigation on the aerodynamic behavior of square cylinders with rounded corners. *Journal of Fluids and Structures*, 44, 195–204.

Carey, P.S., and Etheridge D.W. (2001). Leakage measurements using unsteady techniques with particular reference to large buildings, *Building Services Eng. Research and Technology*, 22(2), 69–82.

Chand, I., Bhargava, P.K., and Krishak, N.L.V. (1998). Effect of balconies on ventilation inducing aeromotive force on low-rise buildings. *Building and Environment*, 33(6), 385–396.

Charuvisit, S., Hino, Y., Ohdo, K., Maruta, E., and Kanda, M. (2007). Wind Tunnel Experiement on Wind Pressures Acting on The Scaffolds in Strong Winds. *Journal of Wind Engineering*, , 32(1), 1–10.

Chen, G., Wang, W., Sun, C., and Li, J. (2012). 3D numerical simulation of wind flow behind a new porous fence. *Powder Technology*, 230, 118–126.

Cherry, N.J., Hillier, R., and Latour, M.E.M.P. (1984). Unsteady measurements in a separated and reattaching flow. *Journal of Fluid Mechanics*, 144, 13–46.

Cheung, J.C.K., and Melbourne, W.H. (1986). Wind loading on porous cladding. In *Proceedings of the 9th Australasian Fluid Mechanics Conference*, Auckland, New Zeland.

Chino, N., Iwasa, Y., Mataki, Y., Hagiwara, T., and Sato, H. (1991). Internal pressure of double composite exteriors. *Journal of Wind Engineering and Industrial Aerodynamics*, 38(2–3), 381–391.

Chiu, Y.H., and Etheridge, D.W. (2007). External flow effects on the discharge coefficients of two types of ventilation opening. *Journal of Wind Engineering and Industrial Aerodynamics*, 95(4), 225–252.

Chow, C.L. (2013). Full-scale burning tests on double-skin facade fires. *Fire and Materials*, 37, 17–34.

Chu, C.R., and Wang, Y.W. (2009). Experimental study of the discharge coefficient of internal openings in partitioned buildings. In *Proceedings of the 7th Asia-Pacific Conference on Wind Engineering APCWE-VII,* Taipei, Taiwan.

Cockroft, J.P., and Robertson, P. (1976). Ventilation of an enclosure through a single opening. *Building and Environment*, 11(1), 29–35.

Cooper, K.R. (1988). The use of a forebody plate to reduce the drag and to improve the aerodynamic stability of a cylinder of square cross-section. *Journal of Wind Engineering and Industrial Aerodynamics*, 28(1–3), 271–280.

Da Matha Sant'Anna, F.A., Laneville, A., Trépanier, J.Y., and Lu, Z.Y. (1988). Detailed pressure field measurements for some 2-D rectangular cylinders. *Journal of Wind Engineering and Industrial Aerodynamics*, 28, 241-250.

Dagnew, A.K., and Bitsuamlak, G.T. (2013). Computational evaluation of wind loads on buildings: A review. *Wind and Structures*, 16(6), 629–660.

Doebber, I., and McClintock, M. (2006). Analysis Process for Designing Double Skin Facades and Associated Case Study. In *Proceedings of the 2nd National IBPSA-USA Conference, Simbuild 2006*, Cambridge, 160–167.

Driver, D.M. (1991). Reynolds shear stress measurements in a separated boundary layer flow. *AIAA Paper*, 91, 1787-1991.

EN1991-1-4:2005, (2005). Eurocode 1: Actions on structures – General actions, Part 1-4: Wind actions. CEN.

ESDU80024, (1980). Blockage corrections for bluff bodies in confined flows. *ESDU International Ltd. (Aeronautics A1b or M2a)*. Sponsored by the Institution of National Engineers, 4pp.

Euteneuer, G.A. (1970). Druckanstieg im Inneren von Gebauden bei Windeinfall. *Der Bauingenieur*, 45(6), 214–216.

Fazio, P., and Kontopidis, T. (1988). Cavity pressure in rain screen walls. *Building and Environment*, 23(2), 137–143.

Fung, Y. (1997). Biomechanics: Circulation. *Springer science and business media*, New York, USA, 572p.

Garden, G.K. (1963). Rain Penetration and its Control. *National Research Council of Canada,* CBD-40.

Gerhardt, H.J., and Kruger, O. (1997). Double Skin glass facades - Investigations into the load sharing possibilities. In *Proceedings of the ICBEST'97, International Conference on Building Envelope Systems and Technologies*, University of Bath, Bath, UK, 335-340.

Gerhardt, H.J., and Janser, F. (1994). Wind loads on wind permeable facades. *Journal of Wind Engineering and Industrial Aerodynamics*, 53(1–2), 37–48.

Gerhardt, H.J., and Kramer, C. (1983). Wind loads on wind-permeable building facades. *Journal of Wind Engineering and Industrial Aerodynamics*, 11(1–3), 1–20.

Gerhardt, H.J., and Kramer, C. (1983). Windkräfte an hinterlüfteten Fassaden. Schriftenreihe des Bundersministers für Raumordnung, Bauwesen und Städtebau, Bau- und Wohnforschung, 21pp.

Gerrard, J.H. (1966). The mechanics of the formation region of vortices behind bluff bodies. *Journal of Fluid Mechanics*, 25(2), 401.

Geurts, C., Bentum, C. Van, Bronkhorst, O., and Hulsbosch, C. (2015). Pressure distributions over permeable skins; a sensitivity study. In *proceedings of the 14th International conference on wind engineering ICWE*, Porto Alegre, Brazil.

Giannoulis, A., Stathopoulos, T., Briassoulis, D., and Mistriotis, A. (2012). Wind loading on vertical panels with different permeabilities. *Journal of Wind Engineering and Industrial Aerodynamics*, 107–108, 1–16.

Ginger, J.D., Holmes, J.D., and Kopp, G.A. (2008). Effect of building volume and opening size on fluctuating internal pressures. *Wind and Structures*, 11(5), 361–376.

Guha, T.K., Sharma, R.N., and Richards, P.J. (2010). The effect of envelope flexibility on internal pressure fluctuations in a low rise building with a dominant opening. In *Proceedings of the 11th Americas conference on wind engineering*, San Juan, Puerto Rico.

Gűndoğdu, M.Y., Çarpinlioğlu, M.O. (1999). Present State of Art on Pulsatile Flow Theory. Part 1: Laminar and Transitional Flow Regimes. *JSME International Journal - Series B - Fluids and Thermal Engineering* 42, 384–397.

Hassanli, S., Hu, G., Kwok, K.C.S., and Fletcher, D.F. (2017). Utilizing cavity flow within double skin façade for wind energy harvesting in buildings. *Journal of Wind Engineering and Industrial Aerodynamics*, 167, 114–127.

Hirst, T., Li, C., Yang, Y., Brands, E., and Zha, G. (2015). Bluff body drag reduction using passive flow control of jet boat tail. *SAE International Journal of Commercial Vehicles*, 8(2), 713-721.

Holmes, J.D. (1979). Mean and Fluctuating Internal Pressures Induced by Wind. In *Proceedings of the 5th International Conference on Wind Engineering*, Colorado USA, Vol.1, 435-450, Pergamon Press, Oxford, UK.

Holmes, J.D. (2007). Wind loading of structures. *Taylor & Francis,* 2 Park Square, Milton Park, Abingdon, Oxon OX14 4RN (2nd edition).

Holmes, J.D., and Ginger, J.D. (2009). Codification of internal pressures for building design. In *Proceedings of the seventh Asia-Pacific conference on wind engineering,* November 8-12, Taipei, Taiwan.

Hu, G., Kwok, K.C.S., and Tse, K.T. (2016). Mitigating wind-induced response of a tall building with an innovative façade system. In *Proceedings of the 8th International Colloquium on Bluff Body Aerodynamics and Applications*, Boston, Massachusetts, USA, II, 993–998.

Igarashi, T. (1997). Drag reduction of a square prism by flow control using a small rod. *Journal of Wind Engineering and Industrial Aerodynamics*, 69–71, 141–153.

Inculet, D.R., and Davenport, A.G. (1994). Pressure-equalized rainscreens: A study in the frequency domain. *Journal of Wind Engineering and Industrial Aerodynamics*, 53(1–2), 63–87.

Irminger, J.O.V., and Nökkentved, C. (1930). Wind pressures on buildings. *Ingeniorvidenskabelige Skrifter*, A23.

Irtaza, H., Beale, R.G., and Godley, M.H.R. (2012). A wind-tunnel investigation into the pressure distribution around sheet-clad scaffolds. *Journal of Wind Engineering and Industrial Aerodynamics*, 103, 86–95.

Irtaza, H., Beale, R.G., Godley, M.H.R., and Jameel, A. (2010). Pressure distribution around net clad scaffolds using computation fluid dynamics techniques. *IOSR Journal of Mechanical and Civil Engineering*, 3, 54–62.

Ishida, H. (2003). Double-Skin glass façade - Design method of wind pressure. In *Proceedings of Glass Processing Days*, Tampere, Finland, 253–255.

Jensen, M. (1958). The Model-law for Phenomena in Natural Wind. *Ingenioren, Int.* (Ed. 2).

Johansson, C.H. (1946). The influence of moisture on the heat conductance for bricks. *Byggmastaren*, 7, 117-124.

Johnson, D. A., and King, L. S. (1985). A Mathematically Simple Turbulence Closure Model for Attached and Separated Turbulent Boundary Layers. *AIAA Journal*, 23(11), 1684–1692.

Jones, W.P., and Launder, B. (1972). The prediction of laminarization with a two-equation model of turbulence. *International Journal of Heat and Mass Transfer*, 15(2), 301–314.

Karava, P., and Stathopoulos, T. (2011). Wind-induced internal pressures in buildings with large façade openings. *Journal of Engineering Mechanics*, 138 (4), 358–370.

Karava, P., Stathopoulos, T., and Athienitis, a K. (2005). Wind driven flow through building openings. In *Proceedings of International Conference Passive and Low Energy Cooling for the Built Environment*, Santorini, Greece, 427–432.

Kato, S., Murakami, S., Mochida, A., Akabayashi, S., and Tominaga, Y. (1992). Velocity-pressure field of cross ventilation with open windows analyzed by wind tunnel and numerical simulation. *Journal of Wind Engineering and Industrial Aerodynamics*, 41–44, 2575–2586.

Kawai, H. (2006). Pressure in a cavity of building-high double façade. In *Proceedings of the fourth international symposium on computational wind engineering (CWE2006),* Yokohama, Japan, 741–744.

Kawai, H., Nishimura, H., Suzuki, M., and Oura, Y. (2009). Field Measurement of Wind Pressure on a Double Skin with a Ventilator. In *Proceedings of the 5th European-African conference on wind engineering*, Florence, Italy.

Koenig, K., and Roshko, A. (1985). Experimental study of geometrical effects on the drag and flow field of two bluff bodies separated by a gap. *Journal of Fluid Mechanics*, 156, 167–204.

Kramer, C., Gerhardt, H.J., and Kuster, H.W. (1979). On the wind-loading mechanism of roofing elements. *Journal of Industrial Aerodynamics*, 4, 415–427.

Kramer, C., Gerhardt, H.J., and Scherer, S. (1979). Wind pressure on block-type buildings. *Journal of Wind Engineering and Industrial Aerodynamics*, 4(3–4), 229–242.

Kwok, K., and Bailey, P. (1987). Aerodynamic Devices for Tall Buildings and Structures. *Journal of Engineering Mechanics*, 113(3), 349–365.

Lajos, T. (1986). Drag reduction by the production of a separation bubble on the front of a bluff body. *Journal of Wind Engineering and Industrial Aerodynamics*, 22(2–3), 331–338.

Lander, D.C., Letchford, C.W., Amitay, M., and Kopp, G.A. (2016). The influence of the bluff body shear layers on the wake of a square prism in a turbulent flow. *Physical Review Fluids*, 1, 044406.

Laneville, A., and Yong, L. Z. (1983). Mean flow patterns around two-dimensional rectangular cylinders and their interpretation. *Journal of Wind Engineering and Industrial Aerodynamics*, 14 (1983) 387-398.

Latta, J.K. (1973). Walls, windows and roofs for the Canadian climate. *NRCC 13487, National Research Council of Canada*, Ottawa, Canada.

Launder, B.E., and Sharma, B.I. (1974). Application of the energy-dissipation model of turbulence to the calculation of flow near a spinning disc. *Letters in Heat and Mass Transfer*, 1(2), 131–137.

Lee, B.E. (1975). The effect of turbulence on the surface pressure field of a square prism. *Journal of Fluid Mechanics*, 69, 263–282.

Li, X.X., Liu, C.H., and Leung, D.Y.C. (2008). Large-eddy simulation of flow and pollutant dispersion in high-aspect-ratio urban street canyons with wall model. *Boundary-Layer Meteorology*, 129(2), 249–268.

Lo, L.J., and Novoselac, A. (2012). Cross ventilation with small openings: Measurements in a multi-zone test building. *Building and Environment*, 57, 377–386.

Loncour, X., Deneyer, A., Blasco, M., Flamant, G., and Wouters, P. (2004). Ventilated Double Facades: Classification and illustration of facade concepts. Belgian Building Research Institute (BBRI), 49pp.

Longo, S., Tanda, M.G. (2009). Esercizi di idraulica e di meccanica dei fluidi. Springer-Verlag Italia, 386pp.

Lou, W., Huang, M., Zhang, M., and Lin, N. (2012). Experimental and zonal modeling for wind pressures on double-skin facades of a tall building. *Energy and Buildings*, 54, 179–191.

Loudon, C., and Tordesillas, A. (1998). The Use of the Dimensionless Womersley Number to Characterize the Unsteady Nature of Internal Flow. *Journal of Theoretical Biology*, 191, 63–78.

Lyn, B.D.A., and Rodi, W. (1994). The flapping shear layer formed by flow separation from the forward corner of a square cylinder, *Journal of Fluid Mechanics*, 267, 353-376.

Mannini, C. (2015). Applicability of URANS and DES simulations of flow past rectangular cylinders and bridge sections. *Computation*, 3, 479–508.

Maruta, E., Kanda, M., and Sato, J. (1998). Effects on surface roughness for wind pressure on glass and cladding of buildings. *Journal of Wind Engineering and Industrial Aerodynamics*, 74–76, 651–663.

Marques da Silva, F., Glória Gomes, M. (2008). Gap inner pressures in multi-storey double skin facades. *Energy and Buildings* 40, 1553–1559.

McLaren, F. G., Sherratt, A. F. C., and Morton, A. S. (1969). Effect of free stream turbulence on the drag coefficient of bluff sharp-edged cylinders. *Nature*, 223, 828–829.

Menicovich, D., Lander, D., Vollen, J., Amitay, M., Letchford, C., and Dyson, A. (2014). Improving aerodynamic performance of tall buildings using fluid based aerodynamic modification. *Journal of Wind Engineering and Industrial Aerodynamics*, 133, 263–273.

Menter, F.R. (1992). Improved two-equation k-omega turbulence models for aerodynamic flows. *NASA Technical Memorandum*, (103978), 1–31.

Menter, F.R. (1993). Zonal Two Equation k-w , Turbulence Models for Aerodynamic Flows. *AIAA Journal*, 93–2906, 1–21.

Menter, F.R. (1994). Two-equation eddy-viscosity turbulence models for engineering applications. *AIAA Journal*, 32(8), 1598–1605.

Minor, J.E. (2005). Lessons learned from failures of the building envelope in windstorms. *Journal of Architectural Engineering*, 11(1), 10–13.

Montazeri, H., Blocken, B., Janssen, W. D., and van Hooff, T. (2013). CFD evaluation of new second-skin facade concept for wind comfort on building balconies: Case study for the Park Tower in Antwerp. *Building and Environment*, 68, 179–192.

Munshi, S.R., Modi, V.J., and Yokomizo, T. (1999). Fluid dynamics of flat plates and rectangular prisms in the presence of moving surface boundary-layer control. *Journal of Wind Engineering and Industrial Aerodynamics*, 79(1–2), 37–60.

Murakami, S., and Mochida, A. (1995). On turbulent vortex shedding flow past 2D square cylinder predicted by CFD. *Journal of Wind Engineering and Industrial Aerodynamics*, 54–55, 191–211.

Nakaguchi, H., Hashimoto, K., and Muto, S. (1968). An experimental study on aerodynamic drag of rectangular cylinders. *Journal of the Japan Society of Aeronautical Engineering*, 16(168), 1–5.

Nakamura, Y. (1993). Bluff-body aerodynamics and turbulence. *Journal of Wind Engineering and Industrial Aerodynamics*, 49(1–3), 65–78.

Namiranian, F., and Gartshore, I. S. (1988). Direct measurements of oscillating lift on a rigid square section cylinder in a turbulent stream. *Journal of Wind Engineering and Industrial Aerodynamics*, 28, 209–218.

Narashima, R., and Sreenivasan, K. R. (1988). Flat plate drag reduction by turbulence mainpulation. *Sãdhanã*, 12, 15–30.

Ni, Z., Lu, S., and Peng, L. (2012). Experimental study on fire performance of double-skin glass facades. *Journal of Fire Sciences*, 30(5), 457–472.

Nore, K., Blocken, B., and Thue, J.V. (2010). On CFD simulation of wind-induced airflow in narrow ventilated facade cavities: Coupled and decoupled simulations and modelling limitations. *Building and Environment*, 45(8), 1834–1846.

Obasaju, E.D. (1979). On the effects of end plats on the mean forces on square sectioned cylinders. *Journal of Industrial Aerodynamics*, 5, 179–186.

Oh, J.H., and Kopp, G.A. (2014). Modelling of spatially and temporally-varying cavity pressures in air-permeable, double-layer roof systems. *Building and Environment*, 82, 135–150.

Ohmi, M., and Iguchi, M. (1982). Critical Reynolds Number in an Oscillating Pipe Flow. *Bulletin of the JSME*, 25(200), 165–172.

Oka, S., and Ishihara, T. (2009). Numerical study of aerodynamic characteristics of a square prism in a uniform flow. *Journal of Wind Engineering and Industrial Aerodynamics*, 97(11–12), 548–559.

Okajima, A. (1982). Strouhal numbers of rectangular cylinders. *Journal of Fluid Mechanics*, 123, 379.

Oleszkiewicz, I. (1990). Fire exposure to exterior walls and flame spread on combustible cladding. *Fire Technology*, 26(4), 357–375.

Oleszkiewicz, I. (1991). Vertical separation of windows using spandrel walls and horizontal projections. *Fire Technology*, 27(4), 334–340.

Overend, M., Zammit, K. (2006). Wind loading on cladding and glazed façades. *International Symposium on the Application of Architectural Glass, ISAAG 2006*. 1–10.

Prasad, A., and Williamson, C.H.K. (1997). A method for the reduction of bluff body drag. *Journal of Wind Engineering and Industrial Aerodynamics*, 69, 155–167.

Raisee, M., Jafari, A., Babaei, H., and Iacovides, H. (2010). Two-dimensional prediction of time dependent, turbulent flow aroud a square cylinder confined in a channel. *International Journal for Numerical Methods in Fluids*, (62), 1232–1263.

Ramponi, R., Blocken, B., de Coo, L.B., and Janssen, W.D. (2015). CFD simulation of outdoor ventilation of generic urban configurations with different urban densities and equal and unequal street widths. *Building and Environment*, 92, 152–166.

Richards, P., and Robinson, M. (1999). Wind loads on porous structures. *Journal of Wind Engineering and Industrial Aerodynamics*, 83(1–3), 455–465.

Robertson, A.P., Roux, P., Gratraud, J., Scarascia, G., Castellano, S., Dufresne de Virel, M., and Palier, P. (2002). Wind pressures on permeably and impermeably-clad structures. *Journal of Wind Engineering and Industrial Aerodynamics*, 90(4–5), 461–474.

Rockwell, D.O. (1977). Organized fluctuations due to flow past a square cross section cylinder. *Journal of Fluids Engineering - Transactions of ASME*, 511–516.

Rodi, W. (1997). Comparison of LES and RANS calculations of the flow around bluff bodies. *Journal of Wind Engineering and Industrial Aerodynamics*, 69–71, 55–75.

Rodi, W., Ferziger, J.H., Breuer, H., and Pourquié, M. (1997). Status of large eddy simulation: Results of a workshop. *Journal of Fluids Engineering - Transactions of the ASME*, 119(2), 248–262.

Rousseau, M.Z. (1990). Facts and Frictions of Rainscreen Walls. *Construction Canada 90 03*, 32(2), 40–47.

Sadri, R.M, Floryan, J.M. (2002). Accurate Evaluation of the Loss Coefficient and the Entrance Length of the Inlet Region of a Channel. *Journal of Fluids Engineering*, 124, 685-693.

Schewe, G. (1984). Untersuchung der aerodynamischen Kräfte, die auf stumpfe Profile bei großen Reynolds-Zahlen wirken. *Mitteilung: DFVLR-Mitt.84-19*. DLR Institut fűr aeroelastik : Gőttingen, Germany (in German).

Sharpe, T., and Proven, G. (2010). Crossflex: Concept and early development of a true building integrated wind turbine. *Energy and Buildings*, 42(12), 2365–2375.

Shur, M., Spalart, P.R., Squires, K.D., Strelets, M., and Travin, A. (2005). Three dimensionality in Reynolds-averaged Navier-Stokes solutions around two-dimensional geometries. *AIAA Journal*, 43(6), 1230–1242.

Sick, F., and Erge, T. (1996). Photovoltaics in buildings - A design handbook for architects and engineers. *International Energy Agency, Paris, France*. 280pp.

Soda, A., Mannini, C., and Sjeric, M. (2011). Investigation of unsteady air flow around two-dimensional rectangular cylinders. In *Transaction of FAMENA XXXV-2*, 11–34.

Spalart, P.R. (2000). Trends in Turbulence Treatments. *AIAA Paper 2000-2306, Fluids 2000*, 1-13.

Spalart, P.R., and Allmaras, S.R. (1992). A one-equation turbulence model for aerodynamic flows. *AIAA Paper 92-0439, 30th Aerospace Sciences Meeting and Exhibit*,1-22.

Spalart, P.R. (2001). Young-person's guide simulation grids detached-eddy. *NASA Technical Note CR-2001-211032*, 1-18.

Speziale, C.G. (1998). Turbulence modeling for time-dependent RANS and VLES: A review. *AIAA Journal*, 36(2), 173–184.

Stathopoulos, T., and Wu, H. (1995). Generic models for pedestrian-level winds in built-up regions. *Journal of Wind Engineering and Industrial Aerodynamics*, 54–55, 515–525.

Stathopoulos, T., and Zhu, X. (1988). Wind pressures on buildings with appurtenances. *Canadian Journal of Civil Engineering*, 17, 569–577.

Straube, J. (2001). Pressure Moderation and Rain Penetration Control. In *Proceedings of the Ontario Building Envelope Council (OBEC) Pressure-Equalized Rainscreen (PER) Seminar*, University of Waterloo, Waterloo, Ontario, 1-51.

Sun, Y., and Bienkiewicz, B. (1993). Numerical Simulation of pressure distributions underneath roofing paver systems. *Journal of Wind Engineering and Industrial Aerodynamics*, 46-47, 517–526.

Takeuchi, T. (1990). Effects of geometrical shape on vortex-induced oscillations of bridge tower. *Journal of Wind Engineering and Industrial Aerodynamics*, 33, 359–368.

Tamura, G.T., and Shaw, C.Y. (1976). Studies on exterior wall air tightness and air infiltration of tall buildings. *ASHRAE Transactions,* 82(1), 122–134.

Tamura, T., and Miyagi, T. (1999). The effect of turbulence on aerodynamic forces on a square cylinder with various corner shapes. *Journal of Wind Engineering and Industrial Aerodynamics*, 83(1–3), 135–145.

Teitel, M. (2010). Using computational fluid dynamics simulations to determine pressure drops on woven screens. *Biosystems Engineering*, 105(2), 172–179.

Tominaga, Y. (2015). Flow around a high-rise building using steady and unsteady RANS CFD: effect of large-scale fluctuations on the velocity statistics. *Journal of Wind Engineering and Industrial Aerodynamics*, 142, 93–103.

Trias, F.X., Gorobets, A., and Oliva, A. (2015). Turbulent flow around a square cylinder at Reynolds number 22,000: a DNS study. *Computers and Fluids*, 123, 87–98.

Trung, V.T., Tamura, Y., and Yoshida, A. (2011). Effects of various parapets on wind loading on porous sunshade roof cover sheets for a low-rise building. *Advances in Structural Engineering*, 14(2), 133–150.

UNI-EN12179:2002, (2002). Curtain Walling - Resistance to Wind Load - Test Method.

UNI-EN13116:2002, (2002). Curtain Walling - Resistance to Wind Load - Performance Requirements.

Van Dyke, M. (1982). An album of fluid motion. Stanford, California: The parabolic press.

Van Schijndel, A.W.M., and Schols, S.F.C. (1998). Modeling pressure equalization in cavities. *Journal of Wind Engineering and Industrial Aerodynamics*, 74–76, 641–649.

Vickery, B.J. (1966). Fluctuating lift and drag on a long cylinder of square cross-section in a smooth and in a turbulent stream. *Journal of Fluid Mechanics*, 25(3), 481.

Wang, F., Tamura, Y., and Yoshida, A. (2013). Wind loads on clad scaffolding with different geometries and building opening ratios. *Journal of Wind Engineering and Industrial Aerodynamics*, 120, 37–50.

Wang, F., Tamura, Y., and Yoshida, A. (2014). Interference effects of a neighboring building on wind loads on scaffolding. *Journal of Wind Engineering and Industrial Aerodynamics*, 125, 1–12.

Waldner, R., Flamant, G., Prieus, S., Erhorn-Kluttig, H., Farou, I., Duarte, R., Blomqvist, C., Kiossefidi, N., Geysels, D., Guarracino, G. (2007). Best practice for double skin façades. *WP5 Best Practice Guidelines, BESTFAÇADE*. 157pp.

Wellershoff, F., and Hortmanns, M. (1999). Wind load on double skin facade systems with gaps greater than 15 cm. In *Proceedings of Wind Engineering into the 21th Century*, 1209–1214.

White, F.M., and Corfield, I. (2006). Viscous fluid flow. *McGraw-Hill*, 614pp.

Wilcox, D.C. (1988). Reassessment of the scale-determining equation for advanced turbulence models. *AIAA Journal*, 26(11), 1299–1310.

Wilcox, D.C. (1993). Turbulence modeling for CFD. *DCW Industries, Inc.*, La Cañada, California, USA, 477pp.

Winter, D.C., Nerem, R.M. (1984). Turbulence in pulsatile flows. *Annals of biomedical engineering* 12, 357–369.

Womersley, J.R. (1955). Method for the calculation of velocity, rate of flow and viscous drag in arteries when the pressure gradient is known. *Journal of Physiology*, 127, 553–563.

Wood, A., and Salib, R. (2013). Natural ventilation in high-rise office buildings. *CTBUH Technical Guide*.

Xu, F.Y., Ying, X.Y., and Zhang, Z. (2011). Prediction of unsteady flow around a square cylinder using RANS. *Applied Mechanics and Materials*, 52–54, 1165–1170.

Yokoi, S. (1960). Study on the prevention of fire-spread caused by hot upward current. *Report of the Building Research Institute* No. 34.

Yu, D., and Kareem, A. (1998). Parametric study of flow around rectangular prisms using LES. *Journal of Wind Engineering and Industrial Aerodynamics*, 77–78, 653–662.

Yue, F., Yuan, Y., Li, G., Ye, K., Chen, Z., and Wang, Z. (2005). Wind load on integral-lift scaffolds for tall building construction. *Journal of Structural Engineering*, 131(5), 816–824.

Yun, G.Y., McEvoy, M., and Steemers, K. (2007). Design and overall energy performance of a ventilated photovoltaic façade. *Solar Energy*, 81(3), 383–394.